一維奈米針矩陣的製作與特性分析

Synthesis and Characterization of One-Dimensional Nanotip Arrays

研 究 生：羅鴻鈞　　Student：Hung-Chun Lo

指導教授：呂志鵬　　Advisor：Jih-Perng Leu

國 立 交 通 大 學

材 料 科 學 與 工 程 學 系

博 士 論 文

A Thesis

Submitted to Department of Materials Science and Engineering

College of Engineering

National Chiao Tung University

in partial Fulfillment of the Requirements

for the Degree of

Doctor of Philosophy

in

Materials Science and Engineering

November 2011

Hsinchu, Taiwan, Republic of China

中華民國 一百 年 十一 月

一維奈米針矩陣的製作與特性分析

學生：羅鴻鈞　　指導教授：呂志鵬 教授

陳家富 教授

陳貴賢 博士

林麗瓊 博士

國立交通大學材料科學與工程學系（研究所）博士班

摘　　要

製作高準直性一維奈米結構需要多道製程的配合，除了製作遮罩，還需輔以乾/濕蝕刻等方式來製作，此過程不但耗時耗力，更需要投入大量的經費，本論文在第一部份探討中，以矽甲烷、甲烷為主要反應氣體，在不同材料的晶圓上形成不同結晶相之碳化矽，利用碳化矽具備有極佳的機械特性，在電漿環境中相對的擁有較佳的抗蝕刻能力，進而開發出以一道製程便能製作出針尖半徑為數奈米(Si nanotip: 1~2nm; GaP nanotip: 2~5nm)，且具備高準直性一維奈米結構之技術，由於此電漿反應器所生成之電漿呈現一發散之形狀，因此具備有可大面積製作的優點(目前已經可在 6 吋矽晶圓上製作出均勻之奈米針)。由於在製作過程中碳化矽的形成為成長機制而奈米針卻屬於蝕刻機制下的產物，因此如何在電漿環境中維持這兩種機制的同時進行便是此技術的關鍵。

本論文第二部分的研究內容以一維奈米結構之製備為主軸，搭配上各種不同研究主題所需之後製程，以滿足各個應用研究的需求。首先，我們利用一維奈米針具備有超尖銳的特性進行場發射研究，根據推測，由於此一結構外型具備非

常強的增強因子(根據計算其 β factor 約為 10^3)，加上矽基板與碳化矽遮罩之間能帶的轉換造成電子穿遂能力的增加，也因此經由此一方式製作出來之一維矽奈米針之 turn-on voltage 為 0.35 V/μm，且當施加電場升至 1 V/μm 的環境下，其電流密度可達 3.0 mA/cm^2，藉由此一研究特性的探討，我們發覺到此一維奈米結構由於外型的改變，對其表面電場的分佈也很有可能造成非常大的差異，而此一發現在生物醫學上面的研究也指出對細胞的生長有著明顯不同的影響，因此我們也利用表面改質的方式改變表面電位，並較為深入的探討此一實驗參數改變與神經細胞成長之間的關連性。在進行細胞培養的過程中，我們發現到試片表面的親、疏水特性也扮演著非常重要的角色，因此我們針對不同深寬比的奈米結構進行親、疏水性的研究與探討。

另外，對於一維奈米材料/結構而言，由於具備有非常高的比表面積（蝕刻後/蝕刻前之表面積可增加 10^3 倍），因此若結合上適當的後製程參數的調控，對 DNA 而言，可在 10^{-13}M 的濃度條件下，透過表面增強拉曼光譜儀的掃瞄直接偵測到訊號，這也意味著此一技術將可有效改善目前所使用之疾病檢測方法之極限，以真正達到早期發現、早期治療的目標。

關鍵字：化學氣相沈積、高準直奈米針、一維奈米結構、碳化矽、自組裝乾蝕刻技術

Synthesis and Characterization of One-Dimensional Nanotip Arrays

student：Hung-Chun Lo

Advisors：Dr. Jih-Perng Leu

Dr. Chia-Fu Chen

Dr. Kuei-Hsien Chen

Dr. Li-Chyong Chen

Department（Institute）of Materials Science and Technology

National Chiao Tung University

Abstract

Generally, it requires multiple processes sub or mask writing, dry and/or wet etchings to produce well-aligned 1-D nanostructure. These processed are expensive and take time to manpower for operation. In this thisis work, we developed SMDE techniques to fabricate nanotip arrays in a single process, which is applicable on variour substrate such as Si, GaP, sappire, silica, and metals including Ai and Cu. Detailed characterization and mechanism studies are reported in this work.

The second part of the thesis presents the field emission performance, cell culture property, wetting property, and surface enhanced Raman spectroscopy utilizing the Si nanotip arrays. Significant enhancement/reduction of the above mentioned properties has been observed. It's concluded that nanotip arrays produced by the SMDE process are simple and effective in these applications. Therefore SMDE

provide a generally applicable process to produce.

1-D nanotip arrays on various substrates, which have been demonstrated very effective in field emission and bio-related applications, offer simple and inexpensive technique for various applications.

Key words: chemical vapor deposition (CVD), well aligned nanotip arrays, 1-D nano structure, SiC, self-masked dry etching (SMDE) technology

致　　謝

回顧求學時期，由於許多的師長、親人、朋友的幫助、支持與鼓勵，才能有這本論文的誕生。

在此，感謝中央研究院 原子與分子科學研究所 研究員 陳貴賢博士、國立台灣大學 凝態科學研究中心 研究員 林麗瓊博士、逢甲大學 電子工程學系 教授 陳家富博士、國立交通大學 材料科學與工程研究所 教授 呂志鵬博士、中央研究院 基因體中心 研究員 張瑛芝博士以及國立陽明大學 生醫光電研究所 教授 Dr. Surojit Chattopadhyay 的指導，使得本論文的研究內容具備了多樣性，並在學生面臨困難的時候適時的伸出援手。

當然同時也要感謝中央研究院與交通大學 材料科學與工程研究所先進材料實驗室所有的夥伴，因為你們，我的人生充滿了歡樂、研究充滿了新奇與滿足。

最後感謝我的家人，因為你們的支持與鼓勵才有今天的我。

謹以此論文獻給我的父母、妻子、女兒以及兄姐。

Table of Contents

Abstract (in Chinese).....I

Abstract (in English).....III

Acknoledgement (in Chinese).....V

Table of Contents.....VI

Figure Index.....X

Chapter 1: Introduction

1.1 Growth Model.....4

1.1.1 Vapor-Solid Mechanism.....5

1.1.2 Vapor-Liquid-Solid mechanism.....7

1.1.3 Vapor-Solid-Solid mechanism.....9

1.1.4 Solution-Liquid-Solid mechanism.....10

1.2 Etching Model.....11

1.2.1 Wet Etching.....11

1.2.2 Dry Etching.....14

1.3 Motivation..... 21

Chapter 2: Background

2.1 Electrodeposition.....23

2.2 Electron Beam-Induced Deposition.....28

2.3 Pulsed Laser Deposition.....31

2.4 Sputtering.....36

2.5 Hot-Filament Chemical Vapor Deposition.....41

2.6 Thermal Chemical Vapor Deposition.....43

2.7 Arc Discharge.....45

2.8 Metal Organic Chemical Vapor Deposition……...52

2.9 Molecular Beam Epitaxy……57

2.10 Microwave/RF Plasma Enhanced Chemical Vapor Deposition……...60

2.11 High-Voltage Plasma Enhanced Chemical Vapor Deposition……..62

2.12 Electron Cyclotron Resonance Plasma Enhanced Chemical Vapor Deposition..64

Chapter 3: Experimental Section

3-1 Electron Cyclotron Resonance Plasma Enhanced Chemical Vapor Deposition (ECR-CVD)……..….....68

3-2 Ion Beam Sputtering Deposition (IBSD) Process……..……72

3-3 Metal Organic Chemical Vapor Deposition System (MOCVD)..……...…….75

3-4 Thermal Chemical Vapor Deposition (TCVD)……....78

3-5 High Resolution Scanning Electron Microscope (HR-SEM)……..…....80

3-6 High Resolution Transmission Electron Microscope (HR-TEM)……...82

3-7 Auger Electron Spectroscope (AES)……..…….....84

3-8 Raman Spectroscope……...…….....86

Chapter 4: Synthesis and Mechanism of Nanotip Arrays

4-1 Introduction…….....88

4-2 Materials and Methods……...…..90

4-3 Results and Discussions…….....91

Chapter 5: Electron Field Emission From Well-aligned Nanotip Arrays

5-1 Introduction.....100

5-2 Materials and Methods……...103

5-3 Results and Discussions.....105

Chapter 6: Cell Culture

6-1 Neuronal Viability and Proliferation on Nano-textured Silicon Surfaces

6-1-1 Introduction……...117

6-1-2 Materials and Methods……..120

6-1-3 Results…….……..123

6-1-4 Discussion……...……...134

6-2 Neuron Viability and Proliferation on 1-D Nanomaterials

6-2-1 Introduction…….……..……140

6-2-2 Materials and Methods……..……....142

6-2-3 Result and Discussion…….……...144

Chapter 7: Surface Enhanced Raman Spectroscope (SERS)

7-1 SERS Using Self-Assembled Silver and Gold Nanoparticles on SiNTs

7-1-1 Introduction…….……..…153

7-1-2 Materials and Methods…….....…156

7-1-3 Results and Discussion.....…….....158

7-2 Label Free Sub-Picomole Level DNA Detection with AgNPs decorated AuNT arrays as SERS platform

7-2-1 Introduction……...173

7-2-2 Materials and Methods…….....175

7-2-3 Results and Discussion…….....177

Chapter 8: Geometrically Tuned and Chemically Switched Wetting Properties of Silicon Nanotips

8-1 Introduction…….……...191

8-2 Materials and Methods…….....193

8-3 Results and Discussions……....194

Chapter 9: Conclusion and Future Prospects

9-1 Conclusion.....203

9-2 Future prospects.....205

References and Notes.....206

Figure Index

Figure 1-1 Comparison between wet and dry etching……..18

Figure 1-2 Basic steps in dry etching……...19

Figure 1-3 Typical reactive-ion etching system……...20

Figure 2-1 General setup for electro-deposition process……..27

Figure 2-2 Schematic of a typical pulsed laser deposition system……..……35

Figure 2-3 Schematic of electrodes in a typical magnetron sputtering system……40

Figure 2-4 Schematic of the thermal CVD set-up……44

Figure 2-5 Schematic of Arc Discharge Chamber……51

Figure 2-6 Schematic of a MOCVD system setup……...…56

Figure 2-7 Schematic of an MBE system setup……...…59

Figure 2-8 Schematic of ECR-CVD system……67

Figure 3-1 AX4400 ECR plasma CVD system.....71

Figure 3-2 IBS-250 Ion Beam Sputtering Deposition system……..…74

Figure 3-3 schematic diagram of MOCVD……..…76

Figure 3-4 Schematic diagram of Thermal CVD……..…79

Figure 3-5 Systematically illustration of JSM-6700F HR-SEM……..…81

Figure 3-6 Schematic of JEOL-4000EX……..83

Figure 3-7 Entire setup of AES/ESCA system……...…..85

Figure 3-8 Schematic diagram of HR800 Raman system……..…..87

Figure 4-1 Tilted top-view HRSEM morphologies of the nanotip arrays fabricated by the self-masked process of various substrates: (a) single-crystal silicon (Si); (b) polycrystalline silicon (poly-Si); (c) epitaxial gallium nitride (GaN) film on sapphire; (d) single-crystal gallium phosphide (GaP); (e) sapphire; and (f) aluminum. The insets show their corresponding magnified

images…….....…….....95

Figure 4-2 (a) HRTEM image of the Si nanotip revealing a SiC cap formed on top of the tip. Inset shows the magnified HRTEM image of the interface between Si and SiC cap on which the lattice mismatch of Si/SiC = 4:5 can be observed. (b) HRTEM image of the GaP nanotip with SiC cap also formed on the tip. Inset shows the magnified HRTEM image of the interface between GaP and SiC cap on which the lattice mismatch of GaP/SiC = 1:2 can be observed…….....96

Figure 4-3 High-resolution Auger depth profile at the top of the nanotip showing the composition of the cap to be Si/C = 1:1……..….....97

Figure 4-4 Schematic diagram for the nanotip formation: (a) the reactive gases are composed of silane, methane, argon, and hydrogen; (b) the SiC nanosized clusters are formed from the reaction of SiH_4 and CH_4 plasma and uniformly distributed on the substrate surface; and (c) the unmasked region is etched by Ar and H_2 plasma, whereas the region masked by SiC caps protects the substrate from etching, and hence creates the conical tips.....98

Figure 4-5 Patterned arrays of naotips generated by photolithography process using silicon nitride as the etching resistant….....……..99

Figure 5-1 Typical SEM micrograph of the silicon nanotips. (a) The cross-section view of nanotips of 1μm height with an aspect ratio of 1000. (b) and (c) show the tilted top views of nanotips demonstrating the high density nature of the arrays of 3×10^{10} and 1×10^{11} cm^{-2}, respectively.....111

Figure 5-2 The cross-section TEM micrograph of a SiC-capped Si nanotip. The inset is a magnified lattice image at the interface between the Si and SiC, which confirms the lattice spacing of the aforementioned materials.....112

Figure 5-3 A typical field emission data obtained from silicon nanotips fabricated

monolithically by the ECR dry etching of Si(100) substrate, demonstrating the ultralow turn-on electric fields. The inset presents the emission current data plotted in the Fowler-Nordheim coordinates, wherein the dashed line represents a linear relationship for an ideal field emitter.....113

Figure 5-4 High resolution scanning electron microscopy image of (a) the cross-sectional view of the GaP nanotip array and (b) from the 25° tilted image of ultrasharp GaP nanotip array.....114

Figure 5-5 High resolution transmission electron microcopy image of a single GaP nanotip capped with a SiC core formation on top of the tip.....115

Figure 5-6 Field emission characteristics of the GaP nanotip array. (a) The J-V characteristics of the nanotip array with (I) 30 and (II) 80μm of cathode-to-anode distance. (b) The corresponding Fowler-Nordheim plot from (I) and (II).....116

Figure 6-1 Cross-section view of HR-SEM images of SiNTs with Au coating for different sputtering times: (a) as-grown, (b) 5 min, (c) 10 min, (d) 20 min and (e) 40 min. (scale bar: a. 100nm; b~e. 10nm)……..…..127

Figure 6-2 Cross section HRSEM images of planar Si templates with Au coating for different sputtering times: (a) 5min, (b) 10min, (c) 20min and (d) 40min. (scale bar: 50 nm)……..……..128

Figure 6-3 3-dimensional topographical images, from tapping-mode AFM studies, of planar Si templates with Au-coating for different sputtering times: (a) 5min, (b) 10min, (c) 20min and (d) 40min……..……..….129

Figure 6-4 Dependence of the water contact angles of SiNTs and planar Si surfaces on Au coating time…….....……130

Figure 6-5 Variation of ζ with Au coating time. (a) SiNTs and (b) planar Si surfaces. Corresponding PC12 cell number density is also shown for better visualization of its resemblance with ζ……..……131

Figure 6-6 SEM images of PC12 neuron cells grown for 7 DIV, followed by 7 days of NGF incubation, on the (a) 5min Au coated SiNTs and (b) 5min Au coated planar Si wafer. (scale bar: 10μm). The inset of (a) shows the lamella-like structures that were secreted during cell culture to strengthen the adhesion of the cell-structure interface. (scale bar of insets: 200nm).....……..…132

Figure 6-7 (a) SEM image of PC12 neuron cells after 3 DIV culture, followed by 7 days NGF incubation, on a patterned template having both SiNTs and planar Si. (scale bar: 100μm) (b) The time dependence cell viability ratio of cell counts on Si vs. SiNT in various DIV of culture.....133

Figure 6-8 Schematic illustration of surface roughness effect on cell adhesion and soma shape……...……..……..139

Figure 6-9 The HRSEM of MWCNT fabricated by MWPECVD which was shown that 20 nm in diameter……...…….……..147

Figure 6-10 HRSEM shows the good viability of PC12 cell on MWCNT and highly cross-linked neurite outgrowth……...……..148

Figure 6-11 Shows the high quality of GaNNW with several um and ~50nm in length and diameter which can be observed in (a) and (b), respectively.....149

Figure 6-12 The SEM image shows the well proliferation phenomenon with extended neurite outgrowth and (b) shows the CL spectra of the interface of uptake GaNNW and cell body…….....……..…….150

Figure 6-13 HRSEM shows the viability of PC12 cell cultured on silica nanowire. The separate state and circular shape figured out the poor viability and proliferation of PC12…….....151

Figure 6-14 HRSEM image of individual PC12 on silica nanowire……..……..152

Figure 7-1 Scanning electron micrographs showing (A) cross-sectional view of the as-grown silicon nanotips; cross-section images of silicon nanotips covered with silver sputtered for (B) 1 min, (C) 3 min, (D) 5 min, (E) 10 min, and (F) 20 min scale bar of all inset: 20 nm) in IBS….....…167

Figure 7-2 (A) Raman spectra of Rhodamine 6G drop-coated on as-grown silicon nanotips; SERS spectra of different concentrations of Rhodamine 6G drop coated on silicon nanotips covered with different amounts of self-assembled silver nanoparticles (B) 1 x 10^{-6} M, (C) 1 x 10^{-7} M, (D) ~1 x 10^{-10} M. Inset in figure 7-2D shows the background-subtracted Raman spectra for Rhodamine 6G dispersed on silicon nanotips covered silver coating for 10 and 20 min by IBS. Silicon signal and the three most intense Rhodamine 6G Raman lines are marked by arrows.....168

Figure 7-3 Raman spectra of BPE drop coated on as-grown silicon nanotips; SERS spectra of different concentrations of BPE drop coated on silicon nanotips covered with different amounts of self-assembled silver nanoparticles (B) 1 x 10^{-6} M, (C) 1 x 10^{-8} M, and (D) ~1 x 10^{-9} M.....169

Figure 7-4 Atomic force microscope image of a flat crystalline silicon surface covered with silver sputtered in the ion beam system for 10 min.....170

Figure 7-5 Background-subtracted SERS spectrum of Rhodamine 6G, normalized with respect to the 520 cm^{-1} signal from silicon, on (blue line) flat crystalline silicon covered with sputtered silver (as in figure 7-4), and (red

line) silicon nanotips covered with self-assembled silver nanoparticles (as in figure 7-1E)…….....…….171

Figure 7-6. Aging of SERS spectra (background subtracted) of Rhodamine 6G (1 x 10^{-6} M) on silicon nanotips covered with self-assembled silver nanoparticles (as in figure 7-1E)……..….....…..172

Figure 7-7 A schematic of the pathway for generating the SERS platform. Step 1: the as-grown silicon nanotip array template; Step 2: Au coating of the SiNT array to generate the AuNT array for efficient DNA immobilization; Step 3: immobilization of DNA molecules on the AuNT array; Step 4: silver nanoparticle (AgNP) deposition for efficient Raman signal enhancement.....183

Figure 7-8 Cross-section high resolution scanning electron microscopy (HR-SEM) images of (a) as-grown SiNTs, (b) low magnification of Au coated SiNTs, (c) high magnification of Au coated SiNTs; cross-section SEM images of AuNTs covered with AgNPs sputtered for (d) 5, (e) 10 and (f) 20 min by IBSD system…….....…….....184

Figure 7-9 Raman scattering spectrum of 1.2nM of (a) Rhodamine 6G adsorbed on SiNT and SERS spectrum of (b) Rhodamine 6G adsorbed on AuNTs. SERS spectrum of hybridized A and T, on AuNT, at (c) 1.2nM and (d) 12mMconcentrations. (e) Raman spectrum of hybridized ds-A + T (12mM concentration) on planar Si. (f) The Raman spectrum of bulk A and T powder dispersed on planar silicon wafer. The symbols ■ and ▲ represent Raman bands of adenine and thymine, respectively….....185

Figure 7-10 Raman scattering spectrum of the (a) as-grown AuNTs. SERS spectra of thiolated ss-A hybrized with ss-T (1.2nM) obtained on AuNTs decorated

with AgNPs sputtered for (b) 0 (bare AuNTs), (c) 5, (d) 10 and (e) 20 min. The symbols ■ and ▲ represent Raman bands of adenine and thymine, respectively…….....……186

Figure 7-11 SERS spectra of thiolated ss-A hybrized with ss-T, on the optimized substrates (as in figure 7-8e), with concentrations of (a) 1.2nM, (b) 12pM and (c) 120 fM…….....……..187

Figure 7-12 Time decay of the SERS spectrum. Aging of SERS spectrum of 1.2nM of hybridized ds-A with T on AuNTs decorated with AgNPs sputtered for 10 mins (optimized substrate, as in figure 7-8e)…….....……188

Figure 7-13 SERS spectra of individual *ss*- and hybridized *ds*- DNA on the AgNP decorated AuNT platform. Background subtracted SERS spectra of *ss*- and hybridized *ds*- nucleotides, with 1.2 nM concentrations, measured on the optimized substrate (as in figure. 7-8e): a) Individual thiolated *ss*-A (A), *ss*-T (T) and hybridized A with T (A+T), and b) individual thiolated *ss*-C (C) , *ss*-G (G) and hybridized C with G (C+G). The top plot (A+C) in (a) shows SERS spectrum of thiolated *ss*-A with non-complimentary *ss*-C (without thiol) after washing. SERS spectra of optimized substrate (AuNT+AgNP) is the background for all the spectra shown in (a) and (b)…….....……189

Figure 7-14 Decay of SERS signals of DNA. Decay of SERS signals of thiolated *ss*-A, T, C and G (1.2 μM each) immobilized on AgNP decorated AuNTs (optimized substrate) as a function of time (Days). Intensity of the 1300, 1359, 1279, and 652 cm^{-1} line is taken as the reference for A, T, C, and G, respectively, (see figure 7-13) in this experiment. The error bar measures the scatter of the data. The data is normalized by setting the mean of the scatter on day 0 to 100 %.....190

Figure 8-1 Tilted view SEM images of SiNTs grown at different temperatures: (a) 250 °C. (b) 400 °C. (c) 600 °C and (d) 700 °C. The inset in each shows the cross-sectional SEM images and the corresponding optical photograph of a water droplet indicating the contact angle. Scale bars for (a)-(d) are 100 nm and those in the inset are 200 nm.....199

Figure 8-2 Advancing, receding and intrinsic water contact angles as a function of aspect ratios (α) of the silicon nanotips. An optical photograph of a water droplet indicating the contact angle is shown for the two extreme α values. A reference value of the water contact angle at 48° for a polished silicon wafer is indicated by the dashed line.....200

Figure 8-3 Advancing, receding and intrinsic water contact angles as a function of inter-tip distance (β) of the silicon nanotips. A cross-sectional SEM image and corresponding optical photograph of a water droplet indicating the contact angle is shown for the two different β values. A reference value of water contact angle at 48° for polished silicon wafer is indicated by the dashed line.....201

Figure 8-4 (a) Cross-sectional SEM image of a TiO_2 coated polished silicon wafer. (b) Tilted view SEM image of a TiO_2 coated silicon nanotip. The inset shows an optical photograph of a water droplet indicating the contact angles on the respective substrates.....202

Chapter 1. Introduction

Nanotechnology is emerging as a major discipline that is driving applications in a broad spectrum of fields through diverse strategies and architectures. Analytical (bio) chemistry, medical diagnostics [1-1], and environmental science [1-2] are undergoing revolutionary changes through the introduction of nano-scale materials and systems. Higher sensitivity and shorter response times are two main advantages of using nano-systems for analytical purposes. Furthermore, the current trend is towards the realization of miniaturized analytical systems such as lab-on-chip devices, where complete analytical stages will be integrated on just a single chip [1-3]. A major consequence will be the possibility to perform analysis and diagnostics on a desktop device or close to the patient in hospitals [1-4]. Nano-structures are ideally suited for such devices, since they can be integrated easily as active elements on micro-scale chips along with other preprocessing stages [1-5]. Unlike microelectronics applications - where billions of nano-devices must be prepared on a cm-sized chip to be competitive with conventional devices - the analytical applications require just a few active nano-sensors to be integrated on a chip, which makes them highly viable for a variety of applications.

The two-, one-, or zero-dimensional systems overwhelmed the number of scientific journals that published them. The one dimensional systems, however, took the major share of activity releasing the whiskers, tips, tubes, wires, rods, belts, brushes, and so on. It would be a mammoth task to even review the set of morphologies observed in any single dimension, zero-, one-, or two. A more realistic attempt will involve the discussion of a single interesting morphology in a particular dimension. Nanostructured coatings offer great potential for various applications due to their superior characteristics that are not typically found in conventional coatings. Because

of the novel properties and various potential applications, nano crystalline materials, with typical grain sizes < 10 nm, are attracting increasing attention from researchers all over the world. Because of the small grain size of these materials and consequently the large volume fraction of atoms in or near the grain boundaries, these materials exhibit properties that are often superior and sometimes completely new, in comparison with those of conventional coarse-grained materials. These include increased strength/hardness, enhanced diffusivity, improved ductility/toughness, reduced density, reduced elastic modulus, higher electrical resistivity, increased specific heat, higher coefficient of thermal expansion, lower thermal conductivity, increased corrosion and wear resistance and superior soft magnetic properties. However, a full understanding of the structures, thermal stability and properties of these novel materials has not yet been achieved. A number of issues and properties are still to be addressed.

Nano crystalline materials are single-phase or multiphase polycrystals, the crystal size of which is of the order of a few (typically 1-100) nanometers in at least one dimension. Thus, they can be equiaxed and are termed nanostructure crystallites (three-dimensional (3D) nanostructures), or they can have a lamellar structure and are termed layered nanostructures (two-dimensional (2D) nanostructures), or they can be filamentary (one-dimensional (1D) nanostructures). Additionally, zero-dimensional (0D) atom clusters and cluster assemblies are considered. The length and width are much greater than the thickness in layered nano crystals, and the length is substantially larger than the width or diameter in filamentary nanocrystals. Nano crystalline materials may contain crystalline, quasi-crystalline or amorphous phases and can be metals, ceramics or composites.

Among the above materials, most attention has been paid to the synthesis, consolidation and characterization of the 3-D nanostructured crystallites followed by

those of 2-D layered nanostructures. While the former are expected to be used in applications based on their high strength, improved formability and soft-magnetic properties, the latter are intended for electronic applications. Relatively few investigations have been carried out on the 0-D clusters and 1-D filamentary nanostructures.

In principle, any method capable of producing polycrystalline materials with very fine grains can be used to produce nano crystalline materials. If a phase transformation is involved, e.g. liquid to solid or vapor to solid, then steps have to be taken to increase the nucleation rate and decrease the growth rate during the formation of the product phase. Nano crystalline materials can be synthesized by a number of techniques with the starting material existing either in the vapor, liquid or solid state. Inert gas condensation, in which the evaporated material is quenched onto a cold substrate, was the first technique used to synthesize nano crystalline metals and alloys. Subsequently, electro-deposition processing, plasma processing and physical and chemical vapor deposition have also been used.

Among these techniques, both of bottom up and top down processes were generally applied in synthesis of 1-D nanostructures which will be briefly demonstrated. Before we go through the fabrication method of 1-D nanostructure, the mechanism and model of both of growth and etching will be briefly introduced in the following.

1.1 Growth Model

The growth model of 1D nanostructure could be traced back to 1950's, when metal whiskers were prepared and the vapor-solid (VS) growth mechanism was proposed by Sears et al [1-6]. Later on, growth of Si whiskers by the so-called vapor-liquid-solid (VLS) mechanism was reported by Wagner et al [1-7]. One dimensional nanostructure were reported in the 1980's and received wide attention in the 1990's [1-8~1-10]. In the early stages of 1D nanostructure research, the observation of whisker structures was more or less at the macro-scale because of the lack of micro-structural characterization tools, and the explanations of the growth mechanisms were somewhat qualitative. Two terms, alloy droplet and alloy particle, can be used interchangeably in describing the liquid phase in the growth of 1D nanostructures by the VLS mechanism. Basically, these two terms were used to indicate the same meaning: the catalyst. As we will discuss later, the catalyst may neither be a pure liquid phase nor be a pure solid phase. And the vapor-liquid-solid mechanism might, under certain situations, be a vapor-solid-solid one.

1.1.1 Vapor-Solid mechanism

In a VS growth process, usually a solid precursor sublimes to generate a vapor which is subsequently transported to a target substrate to form the solid phase 1D nanostructure. Since in this process only vapor and solid phases are involved, the name vapor-solid growth mechanism came out accordingly. Growth of crystals from a vapor phase was studied with a long history, and some theoretical models are still valid for guiding the growth of nanoscale crystals. In this growth model, the growth proceeds with the help of defects, including screw dislocations, stacking faults, steps and kinks without the guidance of metal alloy droplets. Analogous to the liquid droplets in the VLS mechanism which we will detail in the next section, the defects play the role of effective collecting sites for incoming atoms and the axial growth takes place preferentially wherein. Since the defects cannot be as effective as the alloy droplets in guiding the growth of 1D nanostructure because the capturing efficiency for the defects is smaller than unity, it is not surprising that the growth rate by a VS mechanism is much smaller than that by a VLS one. Consistently, VS growth is more influenced by thermodynamics than VLS growth is. In a free mode VLS growth, the 1D structure will grow mostly in a favorable crystallographic orientation that is not necessarily the thermodynamically most stable configuration, while for a VS growth the crystallographic orientation will be averaged according to statistical distribution (Wulff Theorem) under thermodynamic equilibrium conditions, which means that under the VS growth mechanism, equilibrium thermodynamics plays a certain role in determining the growth rate and final morphology of the nanostructures. However, kinetic considerations are also relevant to VS growth when controlled growth is pursued.

VS mechanism was originally proposed and theoretically modeled by Burton,

Cabrera, and Frank (BCF theorem) [1-11~1-12], and later elaborated by Sears et al. [1-13~1-14] in the middle of last century. Since then, many whiskers of metals and semiconductors have been synthesized via this mechanism [1-15~1-17], and the growth processes of the whiskers have also been explained successfully using these models [1-18~1-24].

The theories for VS mechanism were based on the operation of a screw dislocation at the tip of a growing whisker as the source of growth steps. Although screw dislocations had not been confirmed universally and even been criticized for several decades, recently, two groups of researchers have indeed observed the operation of screw dislocations in growing lead chalcogenide nanostructures [1-25~1-27]. By using the Eshelby model [1-28], Jin et al. calculated the Burgers vector of the screw dislocation in their PbS nanowires, which was in good agreement with the geometric calculations from the crystallography of PbS [1-25]. Other defects such as edge dislocations, stacking faults, and twin crystals could also provide the growth steps [1-29, 1-30]. It is well-known that the final shape of a crystal which grows at thermal equilibrium conditions was determined by Wulff theorem; namely, the crystals are bound with surface planes of minimum total surface free energy [1-31~1-33]. However, the growth of whiskers in reality takes place under non-equilibrium conditions; thus, the final morphology of the crystals may deviate greatly from what Wulff theorem predicts, which means that the growth behavior of various planes is manifested kinetically [1-34]. This case is especially true for VS mechanism. As we mentioned previously, for VS mechanism thermodynamics plays a more important role than for VLS mechanism. This is the reason that in VS growth 1D nanostructure is mostly well faceted, whereas in VLS growth they are not.

1.1.2 Vapor-Liquid-Solid mechanism

VLS mechanism has a clear indication of phases involved during the growth, namely, a vapor phase, a liquid phase, and a solid phase are involved in the growth sequence. Generally, three processes are involved in VLS growth of D nanostructures, firstly, the precursors impinge a substrate in a vapor phase; then, the growing atoms form alloys with metal particle catalysts in a liquid phase; finally, the growing materials precipitate from the alloy droplets in a solid phase. Kinetically, there are four steps for VLS mechanism:

(1) Diffusion of precursor molecules in the reaction chamber;

(2) Adsorption and cracking of the precursor followed by incorporation of the atomic species into the alloy droplets;

(3) Diffusion of the atoms through the droplets; and

(4) Precipitation of the growing atoms at the liquid–solid interface and incorporation into the 1D nanostructure [1-35].

Many experimental parameters are closely related to the first step, however, the importance of the first step was underestimated in the past and sometimes it was even omitted from the four steps wrongfully. It was a controversial topic regarding which of the four steps is the rate determining one. It was assumed that the diffusion step could not be rate determining, since the diffusion through the liquid alloy droplet is simply too fast [1-36], however, this assumption might not be true. Concerning the other two steps, Bootsma and Gassen favored step two [1-37], whereas Givargizov believed that the incorporation of the growing atoms into the 1D nanostructures at the liquid–solid interface is the rate determining step [1-35]. It is clear that under a steady state growth condition, the flow of precursor materials through the vapor-liquid-solid sequence has to be continuous. Therefore, some kinds of interactions between the

neighboring steps are necessary, and none of the four steps can be dealt as an independent process. Variation of any of the four steps will have an influence on other steps, and if the response can not be justified, the growth will deviate from the steady growth regime. Either a new steady state is obtained or the growth terminates.

For VLS mechanism, it is well-known that a metal alloy droplet is needed to guide the growth of the 1D nanostructure, and the function of which is similar to a catalyst for a chemical reaction. However, the catalyst is not necessarily metal. Any elements that could alloy with the growing material and satisfy the requirements for VLS mechanism are candidates as catalysts. Recently, metalloid particles have indeed been reported to guide the growth of ZnO nanowires [1-38]. Both the size and the shape of the growing material can be controlled by the alloy droplet. In some special cases, even the orientation of the material follows the crystallographic interface matching between the growing material and the alloy droplet when it is in a solid state [1-39]. In general, the alloy droplet surface is assumed to be ideally rough, such that all the impinging vapor molecules are captured. The word 'capture' has richer meaning than a simple sticking does. According to Parker [1-40], the sticking efficiency of any surface, no matter solid or liquid surfaces, is approximately unity for the elements other than H_2 and He. For a perfect flat solid surface, the sticking atoms either re-evaporate into the vapor phase or relocate to a favorable site with steps, kinks, or defects. In contrary, the sticking atoms on a droplet surface will immobilize and incorporate into the alloy droplets. In addition, atoms that impinge on the substrate still have a chance to diffuse to the alloy droplet if the diffusion length is long enough. The contribution to growth from direct impingement of atom on the alloy droplet surface is not of dominance because the surface area of the alloy droplet is far smaller than the side surface of the nanowires.

1.1.3 Vapor-Solid-Solid mechanism

As the name indicated, vapor-liquid-solid growth, the alloy particle should be in a liquid alloy state with the grown material; however, controversies do exist over the state of the alloy particle [1-41~1-44]. Both liquid and solid states have been observed for the alloy particle [1-45~1-47]. For example, Samuelson et al. confirmed that Au catalyst particles did not melt in the temperature range during directing the growth of GaAs nanowires by electron diffraction measurements, consistent with the fact that nanowires could grow at a temperature well below the eutectic point of the alloy [1-48]. However, Harmand et al. reexamined the growth situation of GaAs nanowires at a higher temperature and deduced that the catalyst was in a liquid phase also by electron diffraction measurements [1-46]. A recent article resolved the conflict and demonstrated that both liquid and solid states of the alloy particle can guide the growth of 1D nanostructure, and these two states can even coexist in a synthesis run [1-49]. Mohammad in a recent work further proposed the vapor-quasisolid-solid mechanism aiming at unify the vapor phase growth mechanisms [1-50]. Whatever the state the alloy particle is in, it acts as a favorable capturing site for impinging atoms with 100% sticking ratio.

1.1.4 Solution-Liquid-Solid mechanism

As mentioned, vapor phase mechanism aroused lot of rules to fabricate 1-D nanostructures. Among these fabrication theories, another mechanism so called solution-liquid-solid was also captured scientific eye to manipulate nanostructures because of the cheap with high fabrication throughput. In this section, the briefly illustration will be focused on this mechanism.

1.2 Etching Model

1.2.1 Wet Etching

Since the early works by Uhlir [1-51] and Turner [1-52], Si nanostructure has been generally fabricated by the electrochemical etch of mono-crystalline silicon in ethanoic HF solutions, although stain etching in HF/HNO3 solutions has also been used for specific applications [1-53]. Some other techniques have been proposed, including vapor phase etching [1-54], spark processing [1-55], and chemical etching in organic solvents [1-56]. The electrochemical method has been demonstrated to be easily scalable to process up to 800 wafers aiming at the production of large area homogeneous Si based layers [1-57], rendering this technique suitable for industrial optics or solar cell applications of Si nanostructure, for example. This is the most widely used and versatile method for the fabrication of Si nanostructure with feature sizes in the nanometer range.

Although the mechanism responsible for the electrochemical dissolution of silicon in HF-based solutions has not been satisfactorily explained yet, the most widely accepted model for p-type Si was proposed by Allongue et al. [1-58]. Initially, the surface Si atoms are passivated with hydrogen [1-59]. The weak Si–H bonds are broken and substituted with Si-OH bonds, taking two holes in the process. In the next step, F- ions replace OH- groups, yielding Si-F bonds. These ionic bonds induce a strong polarization on the Si atoms, weakening their back bonds with the other Si atoms. The weakened Si-Si bonds are then attacked by HF molecules, tearing the Si atom apart from the bulk, and leaving the remaining Si atoms (now at the surface) bound to H atoms. The process then continues from the beginning until it is interrupted.

The previously described reaction mainly depends on the availability of holes to

initiate the process. The silicon/electrolyte interface can be regarded as a Schottky diode, in which holes arising from bulk Si reach the electrolyte crossing the spatial charge region by thermo-ionic effect [1-60]. Surface irregularities due to missing Si atoms produce a concentration of current lines at the pore tips, lowering the barrier height and enhancing the process there. As a consequence, the porous structure is depleted of carriers, becoming more resistive [1-61]. Additionally, as the silicon structures become smaller, the semiconductor band gap widens due to quantum confinement effects [1-62]. This effect becomes prominent when the confinement reaches the exciton Bohr radius (6 nm in the case of silicon). These two effects enhance the accumulation of holes at the pore tips, thus enhancing the dissolution process at these points and promoting the in-depth growth of pores. Another key consequence of such growth mechanism is that the already formed porous structure is not further affected by the continuation of the etching process, which is of tremendous importance for the fabrication of homogeneous Si nanostructures, especially for large thicknesses.

Given that during the dissolution process of bulk silicon the availability of holes plays a decisive role, it becomes apparent that such parameters as current density and doping level have a great influence on the resulting structure and properties of Si nanostructures. Other parameters such as electrolyte composition (mainly HF concentration), crystalline orientation, or process temperature, also influence the reaction kinetics and hence the morphology of Si nanostructures. Even the presence of light during the process has an important effect on the final structure; it provides the required holes for Si nanostructures formation in the case of n-type silicon, and reduces the typical feature size in the case of p-type Si wafers, as a consequence of the increased hole concentration given by the creation of electron-hole pairs. As a result, an ample variety of structures, porosity, and pore morphology may be achieved

depending on the fabrication parameters [1-63].

As previously stated, the silicon skeleton is depleted of carriers after pore formation [1-62, 1-64], which means that the etching process takes place only at the pore tips without affecting the porous structure already formed. Accordingly, a change in the etching parameters only affects the structure currently being formed, resulting in a new layer of different characteristics beneath the already formed one and yielding a bi-layer structure. This process may be repeated several times resulting in complex multilayer structures. The most extended method for the fabrication of multilayer structures consists on changing the applied current density with time, i.e., by alternatively switching the anodization current between low and high values a stratified structure of low- and high-porosity layers, respectively, is obtained [1-63, 1-65]. In a similar way, alternate light intensities can be used to obtain multilayer structures in n-type silicon [1-66]. A more precise method, but also considerably more complex and expensive, consists on the etching under constant conditions of epitaxially grown wafers with given doping profiles. Given the high sensitivity of the etching process to the dopant level [1-67], a multilayer structure is obtained following the initial dopant depth profile.

1.2.2 Dry Etching

In pattern transfer operations, a resist pattern is defined by a photolithographic process to serve as a mask for etching of its underlying layer (Figure 1-1a). Most of the layer materials (e.g., SiO_2, Si_3N_4, and deposited metals) are amorphous or polycrystalline thin films. If they are etched in a wet etchant, the etch rate is generally isotropic (i.e., the lateral and vertical etch rates are the same), as illustrated in Figure 1-1b. If h_f is the thickness of the layer material and l the lateral distance etched underneath the resist mask, we can define the degree of anisotropy (A_f) by

$$A_f \equiv 1 - l/h_f = 1 - R_l\, t/R_v t = 1 - R_l/R_v$$

where t is time and R_l and R_v are the lateral and vertical etch rates, respectively. For isotropic etching, $R_l = R_v$ and $A_f = 0$.

The major disadvantage of wet etching in pattern transfer is the undercutting of the layer underneath the mask, resulting in a loss of resolution in the etched pattern. In practice, for isotropic etching, the film thickness should be about one third or less of the resolution required. If patterns are required with resolutions much smaller than the film thickness, anisotropic etching (i.e., $1 \geq A_f > 0$) must be used. In practice, the value of A_f is chosen to be close to unity. Figure 1-1c shows the limiting case where $A_f = 1$, corresponding to $l = 0$ (or $R_l = 0$).

To achieve a high-fidelity transfer of the resist patterns required for ultra-large scale integration (ULSI) processing, dry etching methods have been developed. Dry etching is synonymous with plasma-assisted etching, which denotes several techniques that use plasma in the form of low-pressure discharges. Dry-etch methods include plasma etching, reactive-ion etching (RIE), sputter etching, magnetically enhanced RIE (MERIE), reactive-ion-beam etching, and high-density plasma (HDP) etching.

Plasma is a fully or partially ionized gas composed of equal numbers of positive and negative charges and a different number of un-ionized molecules. Plasma is produced when an electric field of sufficient magnitude is applied to a gas, causing the gas to break down and become ionized. The plasma is initiated by free electrons that are released by some means, such as field emission from a negatively biased electrode. The free electrons gain kinetic energy from the electric field. In the course of their travel through the gas, the electrons collide with gas molecules and lose their energy. The energy transferred in the collision causes the gas molecules to be ionized (i.e., to free electrons). The free electrons gain kinetic energy from the field, and the process continues. Therefore, when the applied voltage is larger than the breakdown potential, sustained plasma is formed throughout the reaction chamber.

Plasma etching is a process in which a solid film is removed by a chemical reaction with ground-state or excited-state neutral species. The process is often enhanced or induced by energetic ions generated in a gaseous discharge. Plasma etching proceeds in five steps, as illustrated in Figure 1-2: (1) the etchant species is generated in the plasma, (2) the reactant is then transported by diffusion through a stagnant gas layer to the surface, (3) the reactant is adsorbed on the surface, (4) a chemical reaction (along with physical effects such as ion bombardment) follows to form volatile compounds, and (5) the compounds are desorbed from the surface, diffused into the bulk gas, and pumped out by the vacuum system.

Plasma etching is based on the generation of plasma in a gas at low pressure. Two basic methods are used: physical methods and chemical methods. The former includes sputter etching, and the latter includes pure chemical etching. In physical etching, positive ions bombard the surface at high speed; small amounts of negative ions formed in the plasma cannot reach the wafer surface and therefore play no direct role in plasma etching. In chemical etching, neutral reactive species generated by the

plasma interact with the material surface to form volatile products. Chemical and physical etch mechanisms have different characteristics. Chemical etching exhibits a high etch rate, and good selectivity (i.e., the ratio of etch rates for different materials) produces low ion bombardment–induced damage but yields isotropic profiles. Physical etching can yield anisotropic profiles, but it is associated with low etch selectivity and severe bombardment-induced damage. Combinations of chemical and physical etching give anisotropic etch profiles, reasonably good selectivity, and moderate bombardment-induced damage. An example is reactive-ion etching (RIE), which uses a physical method to assist chemical etching or creates reactive ions to participate in chemical etching.

Plasma reactor technology in the IC industry has changed dramatically since the first application of plasma processing to photo-resist stripping. A reactor for plasma etching contains a vacuum chamber, pump system, power supply generators, pressure sensors, gas flow control units, and endpoint detector. Each etch tool is designed empirically and uses a particular combination of pressure, electrode configuration and type, and source frequency to control the two primary etch mechanisms—chemical and physical. Higher etch rates and tool automation are required for most etchers used in manufacturing.

RIE has been extensively used in the microelectronic industry. In a parallel plate diode system (Figure 1-3), a radio frequency (RF), capacitively coupled bottom electrode holds the wafer. This allows the grounded electrode to have a significantly larger area because it is, in fact, the chamber itself. The larger grounded area combined with the lower operating pressure (<500 mTorr) causes the wafers to be subjected to a heavy bombardment of energetic ions from the plasma as a result of the large, negative self-bias at the wafer surface. The etch selectivity of this system is relatively low compared with traditional barrel etch systems because of strong

physical sputtering. However, selectivity can be improved by choosing the proper etch chemistry.

Compare to RIE process, ECR plasmas have the highest electron density because of the plasma localization due to the external magnetic field. Besides, the high vacuum process can also contribute high mean free path to allow the charged redical accumulate enough energy for chemical/physical reaction under low temperature. The dissociation of process gases would be more efficient in such a plasma environment as opposed to those without the magnetic field and the resultant cyclotron resonance condition.

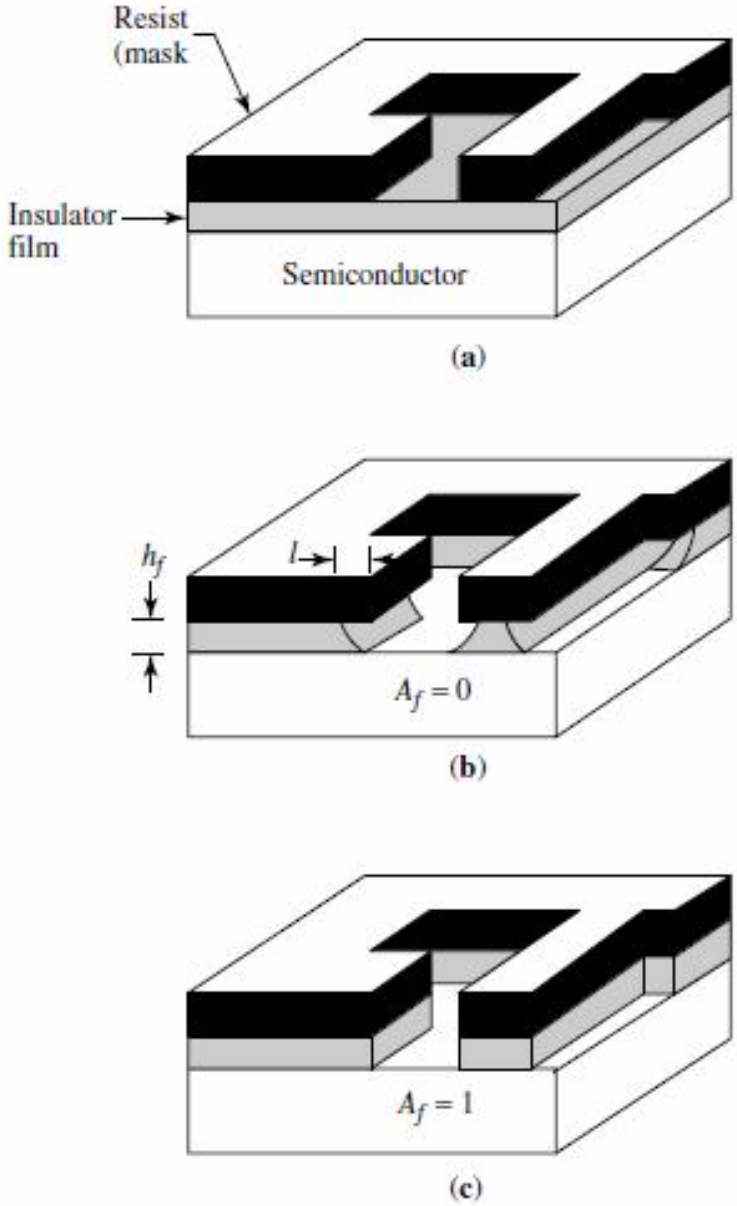

Figure 1-1. Comparison between wet and dry etching: (a) resist pattern; (b) isotropic etching; (c) anisotropic etching.

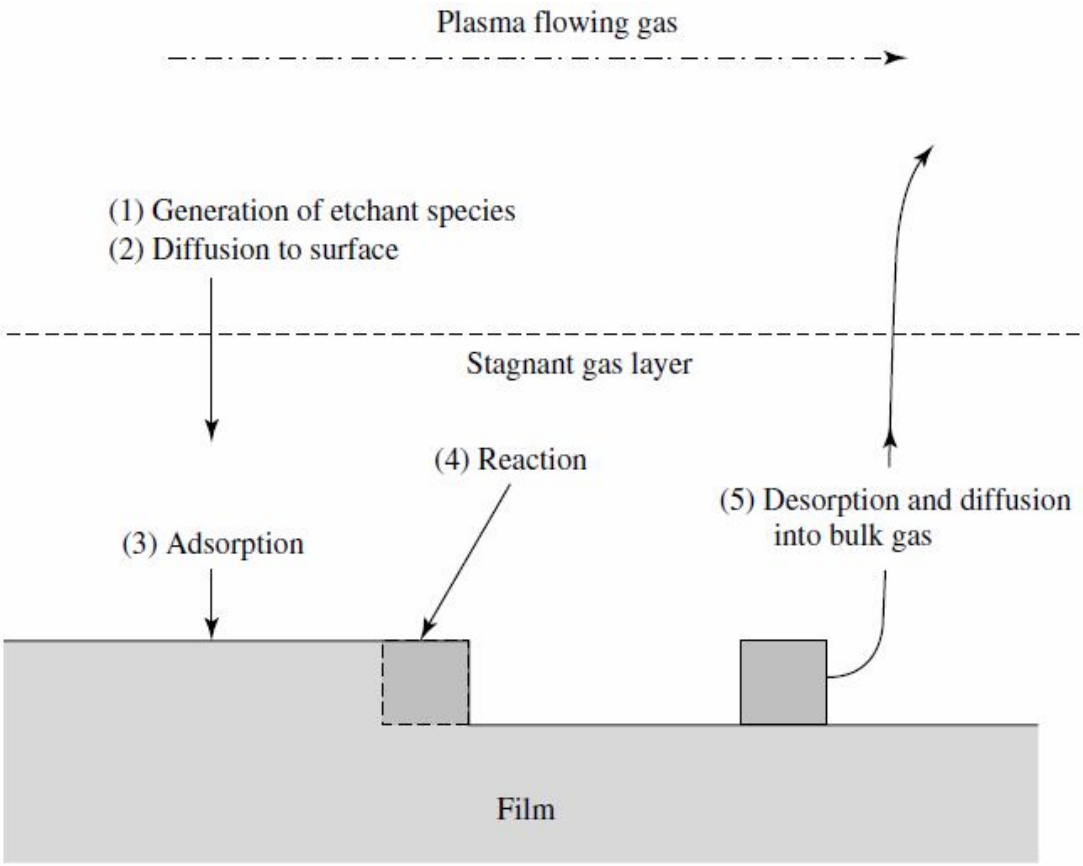

Figure 1-2. Basic steps in dry etching.

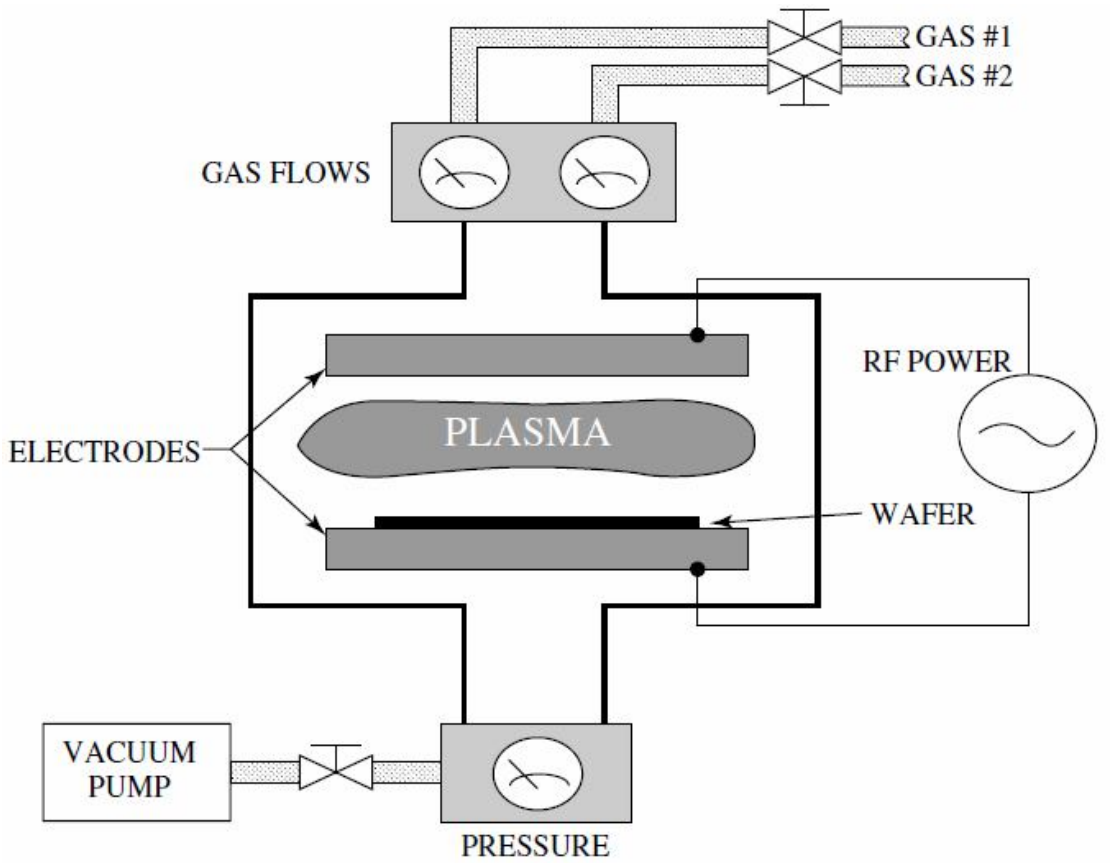

Figure 1-3. Typical reactive-ion etching system.

1.3 Motivation

For 1-D nanostructure fabrication, E-beam lithography (EBL) is a popular choice to identify the nano-pattern using the nano-mask of 1-D structure. However, the high cost and low throughput are always the constraint for the development of such kind of application. Depending on the material types, the high temperature requirement for synthesis also limits the growth of 1-D structure. In this thesis, the unique Self Masked Dry Etching (SMDE) technique was successfully applied to fabricate the well-aligned nanotip arrays via electron cyclotron resonance (ECR) plasma reactor. The most attractive advantages of this fascinating technology are the ease in operation (one-step manipulation) and relatively low temperature (~200°C) requirement.

Because of the unique well-controlled technique with well-characterized mechanism, we have successfully achieved the well-aligned Si nanotip arrays on a large-scale Si wafer with good uniformity. Here, my motivation was to manipulate the similar 1-D nanostructures to the other commercially available wafer substrates, such as poly Si, GaN, GaAs, GaP, glass, aluminum, copper, etc., which can support lot of applications in industrial circle. Inevitably, we could successfully modify and employ the developed concept/technique, so called SMDE technique, to achieve the nanotip array of various materials, depending on the substrate used, with ultra sharp apex radius. The study has established the potential of the SMDE technique for wide applications in industry.

The research work was not only limited to the fabrication and structural manipulation of 1-D nanostructures, but also to establish and demonstrate the characterizations and hence the possible applications that would be strongly influenced by the nanotip or array structures. Study have revealed that the unique but easy control on the SMDE technique could direct the well-controlled manipulation of

the nanotip or array structures, and hence their properties.

According to the electron microscopy (both of TEM and SEM) study, the nanotip arrays with ultra sharp apex (~1nm in apex radius) exhibited excellent beta factor. Appropriate aspect ratio and nanotip number density could effectively lower down the turn-on voltage, and hence the field emission property. The study was then planned to investigate the effect of aspect ratio and various type of Si wafer on the field emission property.

Per following the investigation of field emission, the unique electrical property of nanotip arrays has inspired us to investigate the electric-sensitive neuron cell proliferation using the nanotip arrays as templates. The initial idea on this topic was to define a pattern to guide the neuron cell proliferation and its neurite growth. From the finding of this research, the enormous difference (~1000 times) in cell proliferation rates on two surfaces, with and without 1-d nanostructures, indicated that the well-defined template could effectively control the cell proliferation and neurite outgrowth.

My last but important investigated direction was to establish the well-aligned template with large surface area created by SMDE process as a potential candidate for optical sensing. Combined with apposite post treatment (metal nanoparticle decoration), the template of nanotip arrays could be easily adapted for bio-molecule detection via surface enhanced Raman spectroscopy technique.

Chapter 2. Background

2.1 Electrodeposition

Electrodeposition is a unique technique in which a variety of materials can be processed including metals, ceramics and polymers. Electrochemical strategies offer important advantages and unique possibilities in the development of nanomaterials and nanostructures. Recently, novel ED technologies have evolved into an important branch of nanotechnology. Using this technique, it is possible to obtain pore-free NC metal specimens in a single step process [2-1, 2-2]. The co-deposition of ceramic materials with metals and polymers has created opportunities for the preparation of novel hybrid nanomaterials and nanostructures that cannot be obtained by other methods. Figure 2-1 shows a general schematic diagram of the ED process. To obtain enhanced characteristics of any nano-coating, it is essential to optimize the bath (electrolyte) composition as well as the deposition parameters in addition to selecting appropriate anode and cathode materials with a suitable coating. Similarly, optimized parameters and bath composition are paramount in the ED of any new coating or material. Recent research has been focused on demonstrating the feasibility of co-depositing various nanomaterials and the development of novel electrochemical strategies. Nano-hybrids have been combined resulting in advantageous properties compared with those of individual materials and exhibit novel and advanced properties not achievable in single phase materials.

The technique used for the synthesis of nano crystal materials is determined by the ease of the process, its economic viability, its scalability and the desired purity of the end product. Most of the techniques referred to previously produce the nano crystal material in the powder form. The application of nano crystal materials requires that these powders are consolidated to their full density with minimal porosity, and this is

not easy to achieve. Full densification with complete inter-particle bonding requires the exposure of the powder to high temperatures and pressures for extended periods of time, which is likely to coarsen the micro-structural features. The retention of the material in the nano crystal state, however, warrants that the powder is not exposed to high temperatures for longer periods of time; this may not result in complete densification. Thus, successful consolidation to full density requires innovative methods of consolidation. However, since nano crystal materials have a large fraction of the atoms in the grain boundaries, the diffusivity of nano crystal materials is much higher than that of a coarse-grained material of same composition. This allows the full consolidation of nano crystal materials at temperatures 300 to 400 ℃ lower than those required for the coarse-grained materials. The successful consolidation of nano crystal powders has been achieved by electro-discharge compaction, plasma-activated sintering, shock consolidation, hot isostatic pressing (HIP), ceracon processing, hydrostatic extrusion, strained powder rolling and sinter forging [2-3]. Consolidation is not required if the powder can be used as it is (e.g. in slurries, as catalysts or for coating purposes). It is critical to synthesize nanosized powders in a clean environment, and powders that are susceptible to contamination by oxygen and moisture must be protected during storage and transport. However, the nanostructured materials produced by ED and amorphous crystallization that lead to the direct fabrication of high-density bulk materials are not subject to these concerns.

The synthesis of nanomaterials requires an atomistic deposition process and extreme control over the deposition. Vapor deposition techniques have been used almost exclusively to produce these materials. The fact that electrochemical deposition, also being an atomic deposition process, can be used to synthesize nano-composites, has generated a great deal of interest in recent years. The obvious advantages of this century-old process of ED are as follows:

a. Rapidity

b. Low cost

c. Free from porosity

d. High purity

e. Industrial applicability

f. Potential to overcome shape limitations or allows the production of free-standing parts with complex shapes

g. Higher deposition rates

h. Produce coatings on widely differing substrates

i. Ability to produce structural features with sizes ranging from nm to μm

j. Easy to control alloy composition

k. Ability to produce compositions unattainable by other techniques

l. The possibility of forming of simple low-cost multilayers in many different systems, e.g. Cu/Ni, Ni/Ni–P etc.

m. No post deposition treatment

The formation of nuclei on an electrode substrate was extensively studied on the basis of macroscopic thermodynamic considerations. The nucleation of nanostructures on the electrode substrate during ED is affected by the crystal structure of the substrate, specific free surface energy, adhesion energy, lattice orientation of the electrode surface and crystallographic lattice mismatch at the nucleus-substrate interface. The final size distribution of the electrodeposited material, however, strongly depends on the kinetics of the nucleation and growth. The ED process involves either instantaneous or progressive nucleation. In the case of instantaneous nucleation, all the nuclei form instantaneously on the electrode substrate and subsequently grow with increasing time of ED. In contrast, the number of nuclei that form is a function of the time of ED in progressive nucleation. These nuclei gradually

grow and overlap; therefore, progressive nucleation produces zones of reduced nucleation rate around the growing stable nuclei.

The ED technique consists of an electrochemical cell and accessories for applying a controlled current at a certain voltage. The cell usually contains a reference electrode, a specially designed cathode and an anode or counter electrode. The cathode substrate on which ED of the nanostructure takes place can be made of either nonmetallic or metallic material. Using the surface of the cathode as a template, various desired nanostructures or morphologies can be synthesized for specific applications. Such a template-assisted ED process can be broadly divided into two types: active template-assisted and restrictive template-based ED.

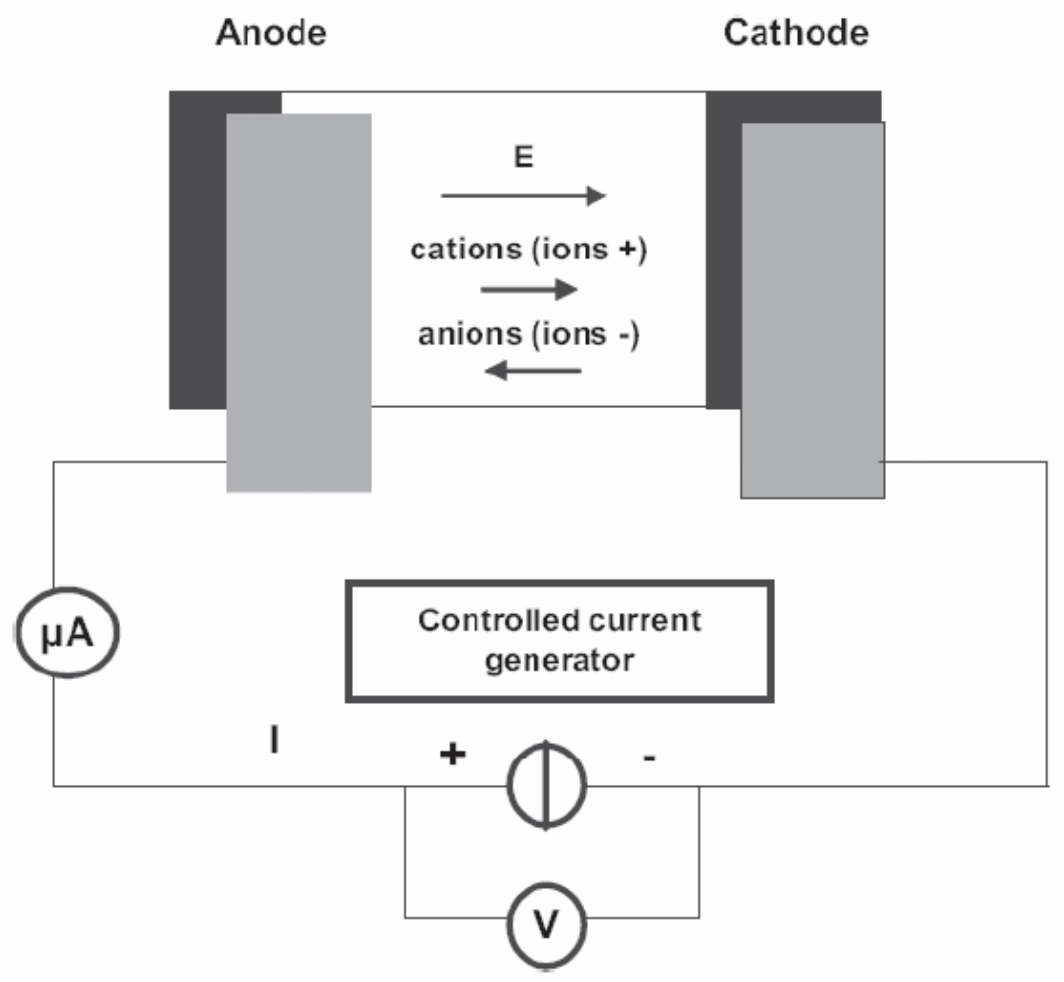

Figure 2-1. General setup for electro-deposition process.

2.2 Electron Beam-Induced Deposition

Electron beam induced deposition of nanostructures is quite popular due to the process control and its compatibility with silicon device technology. It requires special mention and some discussion in detail because the technique could produce magnificent tip structures in desired locations. To top it all, this process is analogous to the chemical vapor deposition (CVD) technique.

This selective area electron beam-induced deposition technique utilizes an e-beam to induce a chemical reaction for appropriate precursor molecules (organometallic in most cases) on the substrate surface that already has a thin adsorbed layer of the same precursor. The reaction is carried out with the precursor gas flowing and products are immobilized on the area addressed by the e-beam. The operating beam voltage is generally between 2–40 kV, the beam current is near 50 pA, and the beam diameter is<10 nm at 30 kV at a working distance of 12 mm. The beam diameter decreases and thus the resolution increases with increasing beam voltage. A computer control pattern generator helps in positioning the beam at desired locations on the sample surface. This kind of e-beam deposition is particularly suited for high resolution atomic force microscopy (AFM) tip synthesis because the e-beam can be focused onto a cantilever supported tip and a smaller tip can be generated on it. 1-D gold nanoscale AFM tips have been generated on conventional AFM tips by the use of a dimethyl-gold complex as a precursor [2-4, 2-5]. The exposure of the adlayer on the sample surface to the finely focused e-beam decomposes the adlayer. This enables continuous adsorption of the additional organometallic gas molecules in this addressed area only. The e-beam is stationary for a finite period of time during which a tip shank structure appears. The tip heights can be increased with prolonged reaction time and can reach 4 μm. The aspect ratio can be in excess of 20 and the apex

diameter <50 nm. The beam voltage and exposure time can be varied to generate different lengths and diameters of the tip structure. Tips of many metals, for example, gold [2-6, 2-7], molybdenum [2-8], cobalt [2-9], platinum [2-10], and tungsten [2-11] have been reported along with carbon [2-12].

Recently, finer tips have been prepared working at a much higher accelerating voltages of 200 kV and beam currents in excess of 0.5 nA [2-11, 2-13, 2-14]. Monte Carlo simulations of the tip growth using 20 and 200 keV electrons have been demonstrated. Along with growth normal (tip, upside length) to the sample surface these tungsten tips protrude inside (root, downside length) of the sample surface as well. They show the variation of the upside length, downside length (negative), and the root diameter as a function of the number of electrons used for irradiation at each energy (20 and 200 keV). The simulation results appear to agree well with the experimental findings. The root grows faster during the initial stages of irradiation whereas the tip or upside growth is slow. The root growth saturates after some time after which the upside length increases nearly linearly with the impinging electrons. These facts are common for both low and high energy e-beam irradiation, the difference being only in the dimensions of the resultant tips. The yield for the higher energy electrons (200 keV) is lower and so takes a longer time or a higher number of electrons for the same volume of deposit compared to the 20 keV electron case. However, control of the morphology, achieving a smaller lateral width and a higher aspect ratio, is easier to accomplish using 200 keV electrons. The major advantage of this technique is its accurate addressability, which is essential for several applications such as scanning probe microscopy (SPM). However, the drawback is its inefficiency in generating wide area arrays. Apart from the temporal factor, the minimum spacing achievable between two e-beam deposited lines is limited to ~50 nm whereas each deposited line may only be 30 nm wide and 50 nm thick. The resolution of this

technique is dependent on several factors including beam diameter, energy, gas pressure, material, nature of the organometallic precursor used, nature of material deposited, pattern aspect ratio, and spatial extent of beam activated surface chemistry. The technique will continue as a major force in technology development, especially in the generation of SPM tips.

2.3 Pulsed Laser Deposition

The process of PLD (see figure 2-2) can generally be divided into four steps: (1) laser ablation of the target material and creation of plasma; (2) dynamic of the plasma; (3) deposition of the ablation material on the substrate; (4) nucleation and growth of the film on the substrate surface. [2-15]

The ablation of the target material upon laser irradiation and the creation of plasma are very complex processes. The removal of atoms from the bulk material is done by vaporization of the bulk at the surface region in a state of non-equilibrium and is [2-16] caused by a coulomb explosion. In this stage the incident laser pulse penetrates into the surface of the material within the penetration depth. This dimension is dependent on the laser wavelength and the index of refraction of the target material at the applied laser wavelength and is typically in the region of 10 nm for most materials. The strong electrical field generated by the laser light is sufficiently strong to remove the electrons from the bulk material of the penetrated volume. This process occurs within 10 ps of an ns laser pulse and is caused by non-linear processes such as multi-photon ionization which are enhanced by microscopic cracks at the surface, voids, and nodules, which increase the electric field. The free electrons oscillate within the electromagnetic field of the laser light and can collide with the atoms of the bulk material thus transferring some of their energy to the lattice of the target material within the surface region. The surface of the target is then heated up and the material is vaporized. This laser energy could be equivalent to dozens of eV per atom. The remaining energy should be enough to surpass the melting and ionizing points, resulting in excited plasma over a very small volume. This inevitably leads to an expulsion of target atoms away from the surface in a highly forward directed plasma plume.

In order to prevent the target from being asymmetrically deprived of material, which could result in a change in plume direction, the target can be rotated slowly. This partially corrects the problem, and also improves target utilization.

Another common effect, which was a fact for every deposition in this work, is that when the target is ablated by the beam, the chemical composition is altered. This sometimes results in a more metallic composition on the very surface of the target. If this [2-17] metal happens to reflect ultraviolet light, the amount of energy absorbed will be progressively less with each turn.

The material expands in the form of plasma parallel to the normal vector of the target surface towards the substrate due to Coulomb repulsion and recoil from the target surface. The spatial distribution of the plume is dependent on the background pressure inside the PLD chamber. The density of the plume can be described by a $\cos(\theta)n$ with a shape similar to a Gaussian curve, where n can vary from approximately 4 to 30, and θ is measured with respect to the normal of the surface [2-18].

The nucleation process and growth kinetics of the film depend on several growth parameters including:

(1) Laser parameters - several factors such as the laser fluence [J/cm^2], laser energy, and ionization degree of the ablated material will affect the film quality, the stoichiometry, and the deposition flux. Generally, the nucleation density increases when the deposition flux is increased [2-19].

(2) Substrate surface temperature - The surface temperature has a large affect on the nucleation density. Generally, the nucleation density decreases as the temperature is increased.

(3) Substrate surface - The nucleation and growth can be affected by the surface preparation (such as chemical etching), the miscut of the substrate, as well as the

roughness of the substrate.

(4) Background pressure - Common in oxide deposition, an oxygen background is needed to ensure stiochiometrically transfer from the target to the film. If, for example, the oxygen partial pressure is too low, the film will grow off stoichiometry which will affect the nucleation density and film quality.

Atoms adhere to the surface due to attractive forces with electrochemically compatible and/or similar atoms. The exact nature of the bonding depends once again on the type of material. Since atoms adhere to the surface, this process is called adsorption, and the accumulated atoms themselves may be called adatoms. These adatoms interact with the top substrate atoms, and with each other.

The substrate in most cases needs to have a higher temperature than room temperature. Otherwise, the surface may be too cold, and adatoms may not have enough kinetic energy to arrange freely to a stable equilibrium. This may result in the film being completely amorphous or highly defective, even though the stoichiometry should suggest [2-20] a more stable configuration. Once the adatoms are on the surface of a heated substrate, several things may occur. They may, and probably will nucleate with each other. The opposite may occur, called dissociation, which happens due to thermal vibration.

Adatoms may diffuse around the surface until they find a stable configuration. The adatoms may even evaporate from the substrate itself. There are several models that describe the possible growth mechanisms when substrates are being continuously bombarded with new atoms. These models can be divided as various general types [2-21]:

(1) Simple growth mode - It can assume that every atomic site in the substrate is equivalent, and may hold one adatom. The atoms are absorbed into an immobile state, which in turn can absorb another atom. Since there is no interaction between sites, this

should result in a distribution of randomly piled up stacks of adatoms. This is the model that roughly resembles a substrate that is too cold during the deposition [2-22].

(2) Frank-van der Merwe growth model - In this model the dominant factor is the total surface energy of the configuration, meaning that each site is not independent of their neighbor. Therefore, the most electrochemically stable stacking of adatoms is the one with least surface area. Adatoms will then arrange each other over one single mono-layer at a time. In order for this to begin, the adatom-surface interaction must have a much stronger than adatom-adatom interactions [2-23].

(3) Volmer-Weber growth model - If the adatom-adatom interactions are much stronger than the interactions with the substrate surface, this must lead to the formation of 3-dimensional adatom clusters. In comparison to the Frank-van der Merwe model, many layers should stack up in order to unite all the separate islands over the substrate. Only high temperature and surface energy equilibrium may be able to produce a flat surface on the resulting film.

(4) Stranski-Krastanov growth model - If the adatom, like in the Frank-van Merwe model, have a much stronger attraction towards the surface than toward each other, then the first few atomic layers of the film will also be stacked up one single layer at a time. This model on the other hand predicts that once the atoms are stacked up to a certain point above the substrate, maybe even a single monolayer, the adatoms start to pile up and eventually start growing as separate three-dimensional islands similar to the Volmer-Weber model.

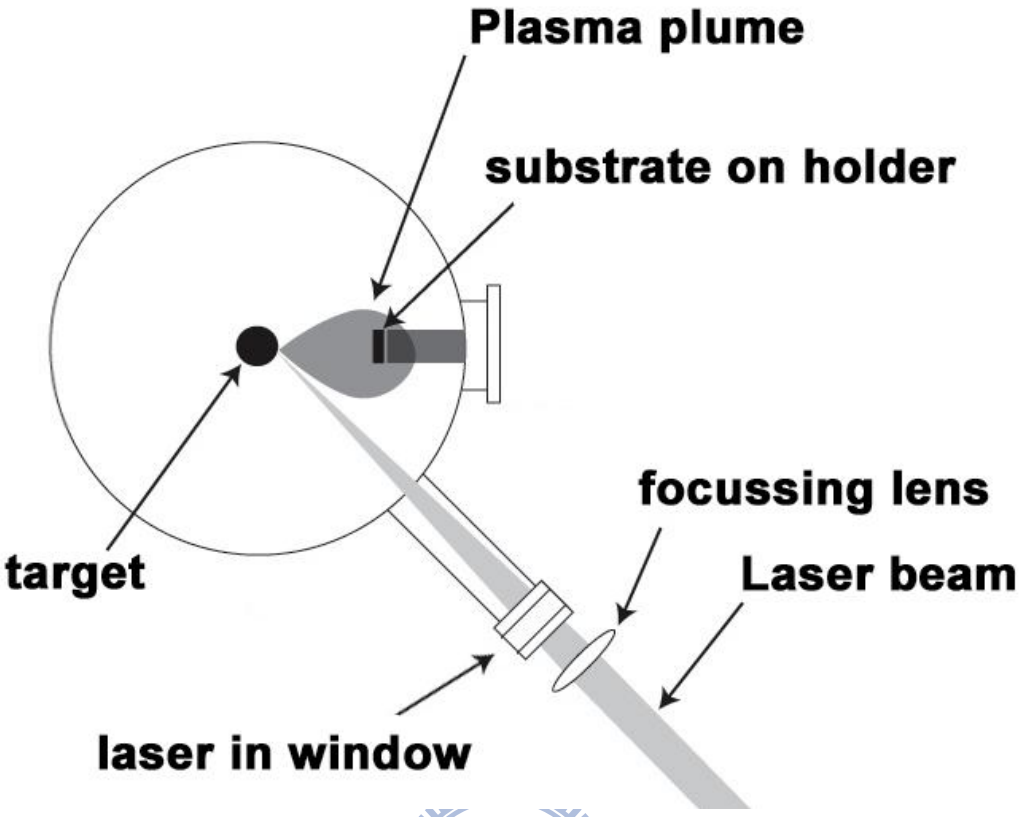

Figure. 2-2 Schematic of a typical pulsed laser deposition system

2.4 Sputtering

The mechanism of sputtering is often called knock-on sputtering. The elementary event is an atomic collision cascade. The incident ions bombard the atoms in the target, causing the ejection of the atoms. The history of sputtering dates back to 1877 when sputtering was used to coat mirrors. Sputtering has many advantages compared to other thin films fabrication techniques, including high deposition rate, the ability to produce insulating and metallic materials, uniformity of thickness, good adhesion to most surfaces, and maintaining the stoichiometry of the target composition [2-24]. As a result, sputtering has become one of the most versatile techniques in thin film fabrication in both industry and research labs. Meanwhile, sputtering provides an alternative way for nanowire synthesis.

The sputtering process consists of the following stages, (1) ionization of sputtering gas, usually an inert gas, such as argon; (2) acceleration of ions towards the target; (3) collision between the ions and the atoms in the target; (4) the ejection of atoms from the target; (5) deposition of sputtered atoms onto the substrate.

The electrons in the plasma acquire energy from the applied electric field and collide with the gas molecules. When the energy of the electrons Ee is lower than 2 eV, the collisions are elastic. At Ee higher than 15 eV, the collisions result in ionization, which sustains the plasma by producing positive ions and new free electrons, as described by the following equation

$$A+e^- \rightarrow A^{++}+2e^-$$

where A is the gas molecule. When Ee is between 2 eV and 15 eV, a variety of inelastic collisions take place, which result first in the excitation in the gas molecule. The relaxation of an electronically excited state is practically instantaneous ($\sim 10^{-8}$) in most cases and is accompanied by the emission of a UV or visible photon, which

gives the plasma its glow.

The condition of self-sustained plasma depends on the geometry of the sputtering chamber, gas pressure, and the voltage between the electrodes. The mean free path, the mean distance that a particle traverses in a gas between collisions with the gas molecules, is an important parameter.

Normally the gas pressure is less than 10^{-1} torr, in which gas can be treated as ideal gas. Hence, the mean free path of molecule in molecule-molecule collision lm can be expressed as

$Lm = RT\sqrt{2}\pi\alpha 2PNA$

where α is the diameter of the gas molecule. Different types of sputtering require different gas pressure, which can be as low as $5x10^{-5}$ Torr for magnetron sputtering and as high as 100 mTorr for a simple DC diode sputtering system.

Over the years, several types of sputtering have been employed for the deposition of thin films by sputtering. The simplest is "diode" direct current (DC) sputtering, in which the material to be deposited (target) is connected to a negative voltage and the substrate is mounted on the anode facing the target. A DC voltage of the order of 1-5 kV is applied across the cathode (target) and the anode with current density 1-10 mA/cm^2.

The plasma is sustained with a gas pressure of 10-100 mTorr. At pressures below 10 mTorr, the plasma cannot be self-sustained because of insufficient ionizing collisions. If the gas pressure is too high, the ions are slowed by inelastic scattering and will not have enough energy to produce secondary electrons when they hit the target. During the deposition of the films using diode sputtering, substantial number of inert gas molecules is known to be trapped in the films. In addition, the deposition rate for DC sputtering is very low.

An alternative method to increase the ionization at low pressure is to supply

additional electrons from a source other than the target. This is called the triode sputtering. The extra electron source is a hot cathode, usually a heated tungsten filament, which can withstand ion bombardment for a long time. The density of ions in the plasma is controlled by adjusting the electron emission current of the hot filament. This method allows sputtering at a pressure of the order of 1 mTorr, much lower than that in the diode sputtering. The limitation of this technique is the complexity of power supplies and the difficulty in producing uniform sputtering from large flat targets [2-24].

The most important and widely used sputtering technique today is magnetron sputtering, which has made significant progress since its development in early 1970s. It has a number of advantages over the conventional sputtering techniques, particularly with respect to high deposition rate, low operating pressures, and much better overall quality of the films.

Figure 2-3 is the schematic diagram of the electrodes in a typical magnetron sputtering system. The target is clamped to a planar cathode backed by permanent magnets and soft magnetic materials (e.g. Fe) that produce a toroidal magnetic field with field lines above and approximately parallel to the cathode surface. Usually, the permanent magnets are typically Nd-Fe-B magnets, which can produce a magnetic field of a few hundred Gauss near the cathode surface. In order to have higher sputtering efficiency, the top layer of the cathode is made as thin as possible, e.g. 0.125 mm, to achieve high magnetic field on the cathode surface. Some sputter source manufacturers offer exposed magnets in order to maximize the magnetic field above the target. The voltage applied to the target produces an electric field approximately perpendicular to the magnetic field near the cathode surface. The secondary electrons in the region where electric (E) and magnetic (B) fields are nearly perpendicular are trapped into toroidal orbits, thus, greatly increase the ionization efficiency.

Most magnetron sputtering systems operate in the pressure ranging from 1 to 20 mTorr and a cathode voltage of a few hundred volts. The sputtering rates are primarily determined by the ion current density at the target. The deposition rates of the films are affected by the ion current density, target-substrate distance, gas pressure, target material, and sputtering gas composition.

The plasma is confined above the target by the magnetic field, but small amounts of ions can still bombard other parts of the sputtering gun. To alleviate this problem, the gun cover and the shield are electrically grounded. To prevent the side of the gun from bombardment by ions, the ground shield (also the top cover) is very close to the gun, with spacing around 1-3 mm. Therefore no ions will be present between the gun and the grounded shield and the gun is protected from the sputtering process.

Finally, a combination of triode and magnetron sputtering can further increase the ionization efficiency. With an additional cathode electron source added to magnetron sputtering system, extra electrons increase the plasma density. The deposition rates can be up to 10 times higher than that of the conventional magnetron sputtering at the same voltage. The pressure can also be greatly reduced to as low as 0.05 mTorr at full power. At such a low pressure, the mean free path of Ar molecules, is 1 m. The atoms from the target can reach the substrate without scattering from the gas molecules.

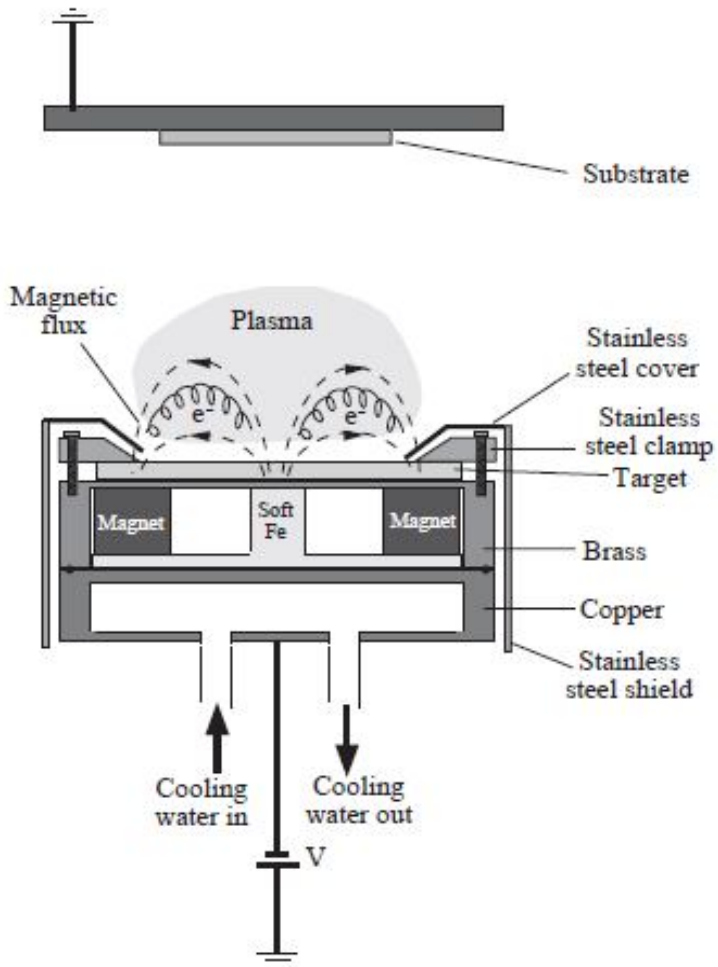

Figure. 2-3 Schematic of electrodes in a typical magnetron sputtering system

2.5 Hot-Filament Chemical Vapor Deposition

This technique employs a tungsten filament heated to a high temperature of about 2000°C and involves the thermal dissociation of the process gases. Depending on the mean free path of the products, radicals or ions, they are deposited or condensed on to a substrate placed nearby. However, this technique has never been used independently to generate nanostructures, such as nanotips, in an active way. That is, given an already existing tip structure or mold, hot filament-CVD can only coat its surface to alter the composition of the tip. The basic function of the technique is limited to that of coating.

A typical example has been the formation of conical diamond tips for AFM applications [2-26]. Anisotropically etched silicon tips with pre-defined shapes were taken as the starting material. Low pressure chemical vapor deposited silicon nitride was then deposited on both sides of the silicon wafer. A conformal coating would be produced over the tip section. The back side of the wafer was patterned and successively etched in a KOH bath (anisotropic etching) and HF, HNO_3, and acetic acid solution (isotropic etching) to remove the silicon underlying the silicon nitride. CVD diamond was then deposited from the backside by the hot filament-CVD technique to fill up the silicon nitride mold. In the next step, the silicon nitride mold was removed by wet etching in a HF/peroxide/de-ionized water mixture. The diamond tip can then be transferred onto a support for AFM applications. The resultant diamond tip reproduces the shape and radius of curvature of the initial silicon tips. There are numerous reports on coating metallic or silicon tips by either diamond or silicon nitride or amorphous carbon by the hot filament-CVD process for different applications purpose. Growth of polycrystalline diamond, by hot filament-CVD, at the end of silicon whiskers was reported by Givargizov et al. [2-27] and Zhirnov et al.

[2-28]

However, there is a report [2-29] in which a D.C. plasma-assisted hot filament-CVD was used to generate a high density of silicon and silicon nitride cones using N_2, H_2 and methane precursor gases. The carbonized tungsten filament was heated to about 2000°C and a negative bias (-450 V) was applied to generate a plasma between the substrate (Si (100)) and a Ta mesh held above it. The substrate temperature was about 700-800°C. 2-3 μm long cones having 0.5 μm widths at half height, 22° apex angle and 10^6-10^7/cm^2 density were obtained [2-29]. A similar report [2-30] of Si nanotips produced by the same technique and gaseous precursors has been made in which a much lower temperature of 190°C for the filament and -600 V as the bias was used. Si tips with 22° apex angle and 10^8/cm^2 density were still obtained [2-30].

2.6 Thermal Chemical Vapor Deposition

Thermal-CVD (see figure 2-4) usually uses a horizontal tube (quartz for example) held in a single or multiple zone furnace whose temperature can be controlled between 30-2000°C. The tube can have pumping options depending on the actual requirements and a range of inert or reactive gas inlets. The ends of the tube are O-ring sealed for vacuum purposes. Thermal-CVD will mostly involve evaporation of compressed solid or powder precursors, held in a ceramic boat, in the presence or absence of a reactive gas. However, an inert or reactive carrier gas is always used to carry the vapors to the reaction and condensation zone. The substrates are generally placed in a lower temperature region to facilitate condensation. The temperature gradient and the actual temperature at the deposition zone, substrate type, and gas pressure will dictate the morphology and quality of the products. This technique is probably the easiest and cheapest to generate nanostructures. Nanowires, nanobelts, nanotubes, and nanotips have all been synthesized successfully by this technique. Group III-nitrides and group II-VI compound semiconductor nanostructures are the more famous products of this technique. However, the simplicity of the process helps maintaining a wide spectrum of material that thermal-CVD can produce. Nanotube morphologies of MoS_2 [2-31], $MoSe_2$ and WSe_2 [2-32], In_2O_3 [2-33], SiO_2 [2-34], AlN [2-35] and many more have been reported. Nanorod morphologies are not scarce and those of ZnO [2-36], GeO_2 [2-37], GaN [2-38] and AlN [2-39, 2-40] can be found. Thermal-CVD grown nanowires are widespread. Take for example, those of GeO_2 [2-41], SnO_2 [2-42], In_2O_3 [2-43], β–Ga_2O_3 [2-44], InN [2-45, 2-46], and GaN [2-47]. A slightly different category such as nanobelt or ribbonlike morphology can also be grown [2-48~2-52]. Interesting morphologies such as nanosprings, nanohelices, and nanospirals can also be grown by thermal-CVD [2-53].

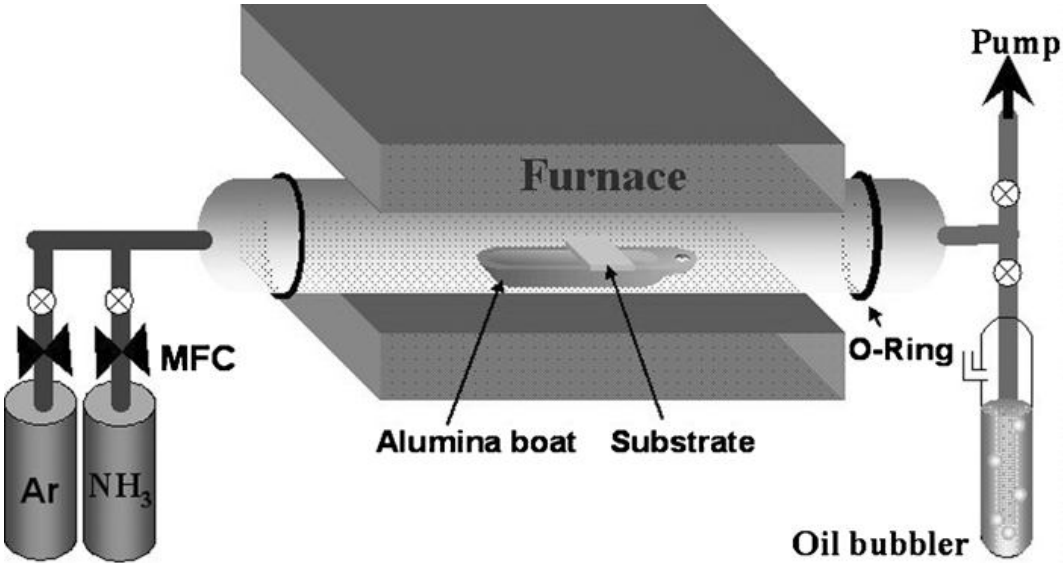

Figure. 2-4. Schematic of the thermal CVD set-up. A quartz tube held horizontally in a furnace with both ends sealed with O-rings. The inlet is connected to the carrier and reactant gases and the outlet is connected to the pump and oil scrubber. The ceramic boat and the substrate is also shown. MFC: Mass flow controller.

2.7 Arc Discharge

It was one of the types of stationary electric discharge in gases and first observed between two carbon electrodes in air by V. V. Petrov in 1802 and independently by H. Davy in 1808-09. As shown in figure 2-5 [2-54], the luminous current channel of this discharge is bent into the shape of an arc; hence the name “arc discharge”.

The formation of an arc discharge is preceded by a short transient process in the space between the electrodes (the discharge gap). The duration of the transient process (stabilization time of the discharge) is usually about 10^{-6} to 10^{-4} sec, depending on the pressure and the type of gas, the width of the discharge gap, and the condition of the electrode surfaces. The arc discharge is produced by ionizing the gas in the gap (for example, by means of an auxiliary, so-called triggering, electrode). In other cases it is produced by heating one or both electrodes to a high temperature or by moving them apart after they have been touching for a short time. An arc discharge may also be developed as a result of an electrical breakdown of the discharge gap during a brief, sharp increase of the voltage between the electrodes. If the breakdown occurs when the gas pressure is close to atmospheric pressure, then the transient process that precedes the arc discharge is called a spark discharge.

Arc discharges are characterized by a great variety of forms. A discharge can take place at virtually any gas pressure, from less than 10^{-5} mm of mercury up to hundreds of atmospheres; the potential difference between the electrodes may have any value between several volts and several thousands of volts (a high-voltage arc discharge), and it may be DC or AC. However, AC half-cycle is usually much greater than stabilization time of the arc discharge, which makes it possible to regard each electrode as a cathode during one half-cycle and as an anode in the next. The distinctive features of all forms of arc discharge (which are closely associated with the

nature of the electron emission from the cathode in this type of discharge) are the small cathode fall and the high current density at the cathode. The cathode fall is generally of the order of the ionization potential for the working gas, or even lower (1-10 volts), and the current density at the cathode ranges from 10^2 to 10^7 A/cm^2. At such a high current density the current strength in an arc discharge is usually also high (on the order of 1-10 A or more), in some forms it reaches many hundreds and thousands of amperes.

A fundamental difference between an arc discharge and other types of stationary electrical discharges in a gas is the nature of the elementary processes that occur at the cathode and in the region near it. Whereas secondary electron emission takes place in a glow discharge and in a negative corona discharge, in an arc discharge electrons are emitted from the cathode as a result of thermionic and auto electronic emission processes (the latter is also called tunnel emission). When only the first of these processes occurs in an arc discharge, the discharge is called thermionic. The intensity of the thermionic emission is a function of the cathode temperature; consequently, in order to have a thermionic arc discharge, the cathode or individual portions of it must be heated to a high temperature. This is achieved by connecting the cathode to an auxiliary energy source (an arc discharge with an external heater or with artificial preheating). A thermionic arc discharge takes place when the cathode temperature is raised sufficiently by the impact of the positive ions that form in the discharge gap and are accelerated by the electric field toward the cathode. However, in an arc discharge without artificial preheating, the thermionic emission intensity is frequently too small to maintain the discharge and the auto electronic emission process plays an important role. The combination of these two forms of emission is known as thermo-auto-electronic emission.

Auto electronic emission from a cathode requires the presence of a strong electric field near the cathode's surface. Such a field is created by the space charge of positive ions at a distance from the cathode of the order of the mean free path for the ions (10^{-6} to 10^{-4} cm). Calculations indicate that auto electronic emission cannot maintain an arc discharge independently and is always accompanied to some extent by thermionic emission. Because of the complexity of studying the processes in the thin layer near the cathode at high current densities, sufficient experimental information regarding the role of auto electronic emission in an arc discharge is not yet available. Theoretical analysis cannot yet explain satisfactorily all the phenomena observed in the various forms of arc discharges.

The layer in which the electrical field that produces auto electronic emission is developed is so thin that it does not create a large potential drop at the cathode. However, for the field to be strong enough, the density of the space charge of the ions at the cathode and thus the density of the ion current must be great. Thermionic emission also can take place with ions of low kinetic energy at the cathode (that is, with a small cathode fall), but under these conditions a high current density is required, since the greater the number of ions bombarding the cathode, the more intensely it is heated. Thus, the distinctive features of arc discharges (the small cathode fall and the high current density) are due to the characteristics of the processes near the cathode.

The discharge gap of an arc discharge is filled with plasma that consists of electrons, ions, and neutral and excited atoms and molecules of the working gas and of the electrode materials. The mean energies of the various kinds of particles in the plasma may differ. Consequently, in speaking of the temperature of an arc discharge, a distinction is made between the ion temperature, the electron temperature, and the

temperature of the neutral component. When these temperatures are all equal, the plasma is called isothermal.

An arc discharge with artificial preheating of the cathode is called non-self-sustaining, since the discharge cannot be maintained by its own energy: when the external heat source is disconnected, the arc is extinguished. A discharge is easily ignited without auxiliary ignition electrodes. An increase in the voltage of this arc discharge at first increases its current to a value determined by the intensity of the thermionic emission from the cathode at a given heater temperature; then, up to some critical voltage, the current remains almost constant (the so-called free mode). When the voltage exceeds the critical value, the nature of the cathode emission changes: the photoelectric effect and secondary electron emission begin to play an essential role in it (the energy of the positive ions becomes high enough to dislodge electrons from the cathode). This leads to an abrupt increase in the discharge current, and the discharge passes into the restricted mode.

Under certain conditions an arc discharge with artificial preheating continues stable operation when the voltage between electrodes decreases to values that are not only smaller than the ionization potential of the working gas but also lower than its minimum excitation potential. This form of arc discharge is a low-voltage arc. Its existence is due to the development close to the cathode of a potential maximum that exceeds the anode potential and is close to the first excitation potential of the gas, as a result of which step ionization becomes possible.

Self-sustaining arc discharge is maintained by the energy of its own discharge. On refractory cathodes (tungsten, molybdenum, or graphite) the arc discharge is purely thermionic in nature; the bombardment of the positive ions heats the cathode to a very

high temperature. In such an arc discharge, the material of a fusible cathode is rapidly vaporized; the vaporization cools the cathode, and its temperature does not attain the values at which the discharge can be maintained by thermionic emission alone auto electronic emission takes place along with it.

A self-sustaining arc discharge can exist both at extremely low gas pressures (the so-called vacuum arcs) and at high pressures. The plasma of a self-sustaining low-pressure arc discharge is notable for its non isothermal quality: the ion temperature is only slightly above the temperature of the neutral gas in the space surrounding the discharge region, whereas the electron temperature reaches tens of thousands of degrees and, in narrow tubes and at high currents, hundreds of thousands of degrees. This is explained by the fact that the more mobile electrons, receiving energy from the electrical field, are not able to transfer it to the heavy particles in their rare collisions.

In a high-pressure arc discharge the plasma is isothermal (more accurately, it is quasi-isothermal, because although the temperatures of all the components are equal, the temperatures in different parts of the arc-discharge column are not the same). This form of arc discharge is characterized by a substantial current strength (10 to 10^3 A) and a high plasma temperature (of the order of 10^4 K). The highest temperatures are achieved in such an arc discharge when the arc is cooled by a stream of liquid or gas, the current channel of a “cooled arc” becomes thinner and is heated more intensively at the same current strength. It is this form of an electric discharge that is called an electric arc, the arc discharge is bent by the action on the current channel of streams of gas that are either directed from outside or are convection streams produced by the discharge itself.

A self-sustaining arc discharge on fusible cathodes is distinguished by the fact that thermo-auto-electronic emission of electrons occurs only in small portions of the cathode (the so-called cathode spots). The small dimensions of these spots (less than 10^{-2} cm) are caused by the pinch effect, which is the constriction of the current channel by its own magnetic field. The current density in a cathode spot depends on the cathode material and may reach tens of thousands of A/cm^2. Therefore intensive erosion takes place in cathode spots and jets of vaporized cathode materials fly out of them at a velocity of the order of 10^6 cm/sec. Cathode spots are also formed during arc discharge on refractory cathodes if the pressure of the working gas is less than about 10^2 mm of mercury (mm Hg). At higher pressures the thermionic emission of an arc discharge with chaotically shifting cathode spots is transformed into a thermionic arc discharge without a cathode spot.

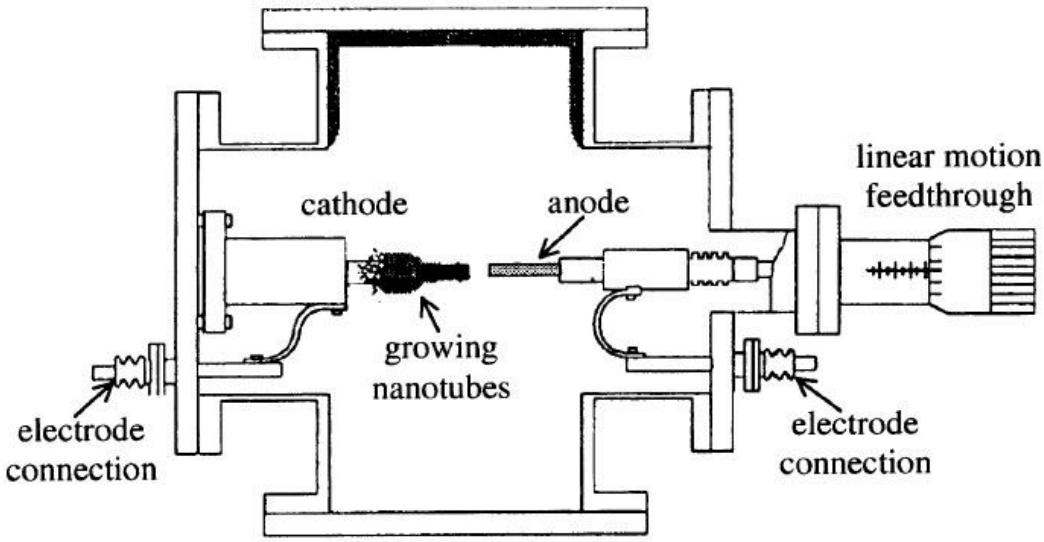

Figure 2-5. Schematic of Arc Discharge Chamber

2.8 Metal Organic Chemical Vapor Deposition

Metal organic chemical vapor deposition (MOCVD), also known as metal organic vapor phase epitaxy (MOVPE), is a chemical vapor deposition method in which the surface reaction of metal organics and metal hydrides, both in vapor phase, take place on a heated substrate.

Since its invention in 1968, MOCVD has become a dominant epitaxial growth technique in the compound semiconductor industry [2-55]. Epitaxy refers to a special case

Most MOCVD systems consist of three parts, gas handling system, reactor, vacuum and exhaust system, as shown in figure 2-6.

(1) Gas handling system: Gas is introduced via devices known as 'bubblers'. In a bubbler a carrier gas (usually nitrogen or hydrogen) is bubbled through the metal organic liquid, which picks up some metal organic vapor and transports it to the reactor. The amount of metal organic vapor transported depends on the rate of carrier gas flow and the bubbler temperature, and is usually controlled automatically and most accurately by using a Piezocon type vapor control system. The mixing of volatile alkyl and hydride compounds in the gas handling system is achieved within a manifold that first stabilizes the flows, then mixes them and selectively directs them either to the reaction chamber or into the vent (waste). The manifold is designed to uniformly mix metal organic and hydride sources prior to reaching the growth zone.

(2) Reactor: The reactor chamber is usually made of quartz or stainless steel and contains the susceptor on which the substrate wafer is resting. The susceptor can be heated using one of the following three methods: RF induction heating, radiative (lamp) heating, or resistance heating. The shape of the reactor chamber is carefully designed and engineered to eliminate the development of vortices and dead volumes.

The growth parameters (e.g., pressure, temperature, and total gas flow) are chosen such that a laminar flow free of convection is realized. This is generally easier to do by operating at low pressure. By doing so, one ensures that a stable, reproducible, and uniform growth process is achieved.

(3) Vacuum and exhaust system: MOCVD system for GaAs and InP use toxic materials like AsH_3 and PH_3. The exhaust gases still contain some non-reacted AsH_3 and PH_3, which need to be converted to liquid or solid wastes for recycling (preferably) or disposal.

In MOCVD system, crystal growth process is governed by law of thermodynamic and kinetic processes. Thermodynamics determines the driving force for the overall growth reaction while kinetics defines the rates at which various steps occur. In this growth process, one or more of the Group III constituents are transported to the reaction zone in the form of metal alkyls, while the Group V constituents are usually transported as hydrides. Binary compound is the simplest case which involves a reaction of the vapors of a volatile metal organic compound and a gaseous hydride, given by

$$RnM+XHn \rightarrow XM+nRH\uparrow$$

where R is an organic radical (tertiary-butyl-, methyl- or ethyl-radical), M and X are the constituent Group III and V species respectively for the deposited solid.

During the epitaxial growth, the group V concentration is always kept in excess compared to group III concentration due to its higher volatility. As a result, the growth rate is limited and controlled by the concentration of group III alkyl elements. Like most CVD process, the growth regimes of the MOCVD process can be defined

in three regions [2-56].

The alkyl pyrolysis efficiency profile is steep at the growth temperature below 500°C. This implies that the growth is reaction-rate limited at temperature < 500°C. For substrate temperature of 500°C and higher, the alkyl pyrolysis efficiency attains unity. The growth regime of this temperature range (500°C - 800 °C) is mass transport limited [2-57, 2-58]. For temperature above 800°C, the gas phase pyrolysis of hydrides become important and solid particulate can be formed before reaching the substrate. This is known as parasitic spontaneous nucleation or pre-reaction. Moreover, when temperature approaches the congruent temperature of III-V alloys, the semiconductor begin to decompose into its constituent gas phase. This reduces the growth rate and an increased vapor pressure from the constituent source is needed to maintain smooth surface morphology.

Under condition of excess group V hydrides and while in mass transport limited growth regime, the growth rate of binary alloy is given by [2-59]:

$$Rg = M_A P_A F_A / kTdAAe$$

where M_A, P_A, F_A, k, and T are molecular weight , vapor pressure, and flow rates of alkyl metal, respectively; k, T, and Ae are Boltzmann constant, bubbler temperature, and effective area of growth chamber respectively. Generally, the rate of growth can be estimated by using a simple formula as [2-59]:

$$Rg = P_A F_A / 22400(B_A - P_A)$$

where P_A, F_A and B_A are alkyl vapor pressures (Torr), alkyl-hydrogen flow rate (cm^3/min), alkyl bubbler pressure (Torr) respectively; the unit of growth rate is mol/min.

The Surface morphology of III-V compound semiconductor strongly depends on V/III ratio. As a rule of thumb, the higher V/III ratio, the smoother is the crystal morphology. However, increasing V/III ratio also reduces the surface mobility of

group III gives rise to non-stoichiometric structure and causes point defects in the epitaxial layer [2-60]. In a typical system, PH3/AsH3 and V/III ratios are in the range of 25-50 and 40-100 respectively. As we discussed previously, the decomposed efficiencies of alkyl metals and hydrides strongly depend on the growth temperature profile, so the optimal PH_3/AsH_3 or V/III ratio is a function of the substrate temperature.

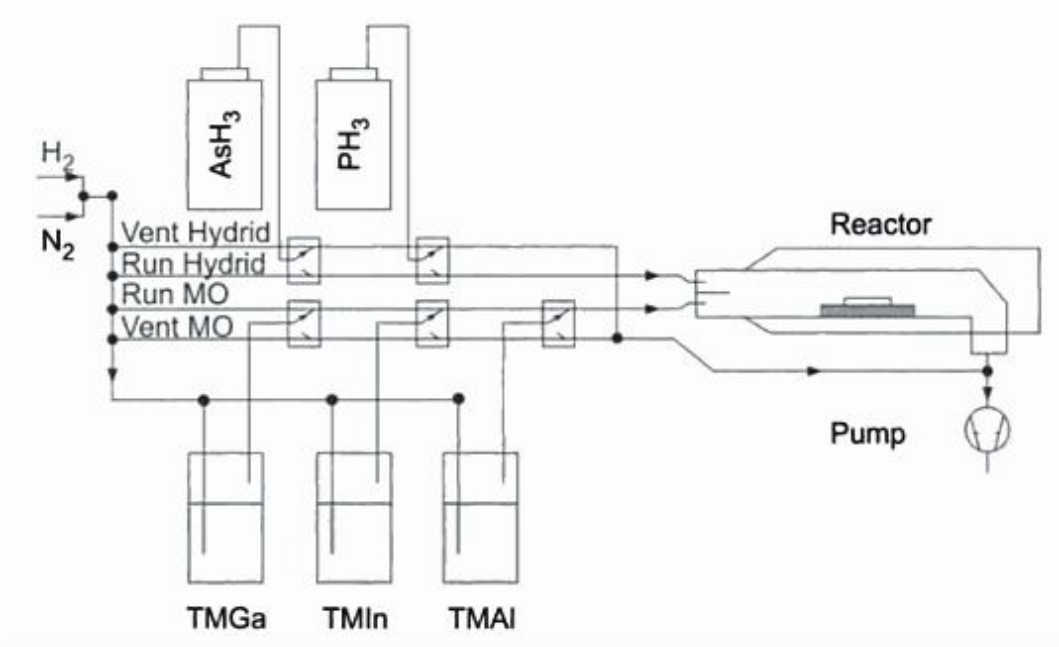

Figure. 2-6 Schematic of a MOCVD system setup

2.9 Molecular Beam Epitaxy

Molecular beam epitaxy (MBE) is an advanced technique for the growth of thin epitaxial layers and nanostructures of compound semiconductors, Si, Ge and other materials [2-46]. For MBE system, the growth is conducted under an ultra-high vacuum of 10^{-8} ~ 10^{-9} Pa. Under such a high vacuum, O_2, CO_2, H_2O, and N_2 contamination on the growing surface can be neglected. This makes it possible to reduce the growth rate down to nm/min, so that precise control of the growth thickness is possible. Another important advantage of MBE is that in-situ monitoring of the growing surface is possible. Reflection high-energy electron diffraction (RHEED) is one of the most powerful tools used to see the flatness and atomic structure of the surface during growth. MBE can produce high-quality single crystal layers with very abrupt interface, monolayer control of thickness, precise doping and compositional accuracy. Because of the high degree of control and flexibility using MBE, it is a valuable tool in the development of sophisticated, magnetic and photonic devices [2-47, 2-48].

The schematic of typical MBE system is shown in figure 2-7. An MBE system is basically made up of five parts: (1) an ultra-high vacuum chamber equipped with wafer transfer and rotation mechanism, (2) a heated sample mount, (3) source cells, (4) in-situ monitoring tools, which are used to monitor the initial surface cleaning and successive growth, and (5) pumps, which provide and keep the UHV necessary for growing high-quality materials.

Source cells can be effusion cells, which generate component fluxes by evaporating or subliming high purity source materials, or gas cells, which generate component hydride or plasma flues controlled by a mass flow controller. The hydrides decompose at the substrate surface and incorporate into grown materials without extra

hydrogen atoms. Growth from hydrides, the substrate surface will be covered by hydrogen and this makes surface reaction kinetics different from the cases without surface-H coverage. In hydride gas source growth, source hydrogen desorption is normally the rate limiting step, as it is believed in Si growth from disilane (Si_2H_6).

The in situ monitoring tool include reflection high-energy electron diffraction (RHEED), which provides information about substrate surface configuration and flatness; pyrometry, which provides in situ growth temperature calibration; and residual gas analyzer (RGA), which provides information about chamber vapor composition for chamber leakage detection and growth monitoring. More complex MBE systems may also contain Auger electron spectroscopy (AES), electron energy-loss spectrometry (EELS), and low energy electron diffraction (LEED), which provided composition and chemical status analysis, localized vibration modes of adsorbed molecules as well as surface phonon analysis, and two dimensional surface configuration analyses, respectively.

The pumps include ion pumps, cryo pumps, turbo pumps, and a liquid nitrogen cryo-shroud, which is maintained below nitrogen boiling point and surround the hot source furnaces and inner growth space to decrease chamber outgasing.

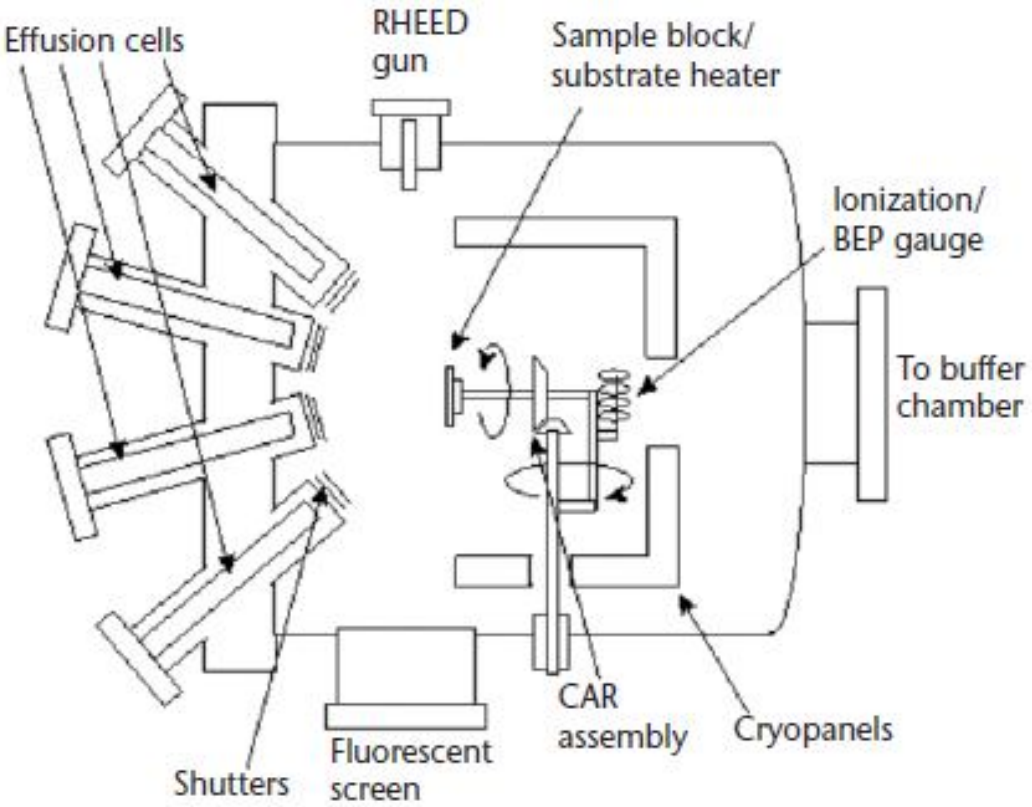

Figure. 2-7 Schematic of an MBE system setup

2.10 Microwave/RF Plasma Enhanced Chemical Vapor Deposition

Microwave PECVD uses microwave radiation to initiate plasma. A typical process uses a 2-3 GHz source with output power between 600W to 1 kW, which is comparable to a microwave oven with a frequency of 2.4 GHz and similar power range.

A catalyst of ferric nitrate [2-64], cobalt [2-65], nickel, or layered aluminum and iron [2-66] is deposited on a substrate of silicon (or Alumina [2-64]). The sample is placed on a graphite susceptor and heated, most often by a radio-frequency (RF) inductive coil, to a temperature between 800 to 900°C. This range of temperatures has been shown to be necessary in the growth of carbon nanotubes by microwave PECVD. After the chamber is pumped down to the mTorr ($1x10^{-3}$) base pressure range, the precursor gasses, controlled by mass flow controllers, are introduced in a specified ratio. The most commonly used gas mixtures are Acetylene (C_2H_2) with Ammonia (NH_3) [2-65] and Methane (CH_4) with Hydrogen (H_2). Acetylene is usually mixed in the 1:4 ratio with ammonia. Gas ratios for the Methane/Hydrogen mixture have varied dramatically in recent years, with the majority of the gas changing from Methane (60% of total in 1998) [2-64] to Hydrogen (80% of total in 2002) [2-66]. The alignment of carbon nanotubes has also improved, with the results changing from soot and randomly ordered nanotubes (resembling the results from early arc-discharge methods) to fields of uniformly aligned CNTs. The chamber pressure has also decreased over time (from 15 to 3 Torr), which when combined with the changing chemistry, results in approximately the same quantity of Hydrogen present in the chamber, while the amount of Methane is greatly decreased.

Carbon nanotube growth can occur in the absence of a plasma if the other growth

conditions are present. As shown in the experiment by Bower et al. (2000) [2-65], once the precursor gas is no longer energized, the carbon nanotubes can continue to grow. However, further CNT growth in these conditions is not aligned as it was previously, and the growth mechanism is shifted to conventional CVD. This resulting growth occurs at the same temperature (825°C) as the plasma enhanced growth occurred, but at tremendously reduced rate (150 nm/min compared to the plasma enhanced 6000 nm/min).

The field of carbon nanotube growth by microwave plasma enhanced CVD has progressed considerably in a relatively short period of time. Early results were similar to that of arc-discharge, the nanotubes produced were tangled and randomly oriented [2-64] but were grown over the total surface of the sample, not just at the cathode. Recent results have shown that carbon nanotubes can be grown on a variety of substrate contours parallel to the normal of the surface [2-65].

2.11 High-Voltage Plasma Enhanced Chemical Vapor Deposition

The process of plasma enhanced chemical vapor deposition is similar to that of thermal CVD. A cleaned substrate (usually silicon or glass) is coated with a metal that has been shown to act as a catalyst for CNT growth, such as Ni, Fe, Co etc., using various deposition methods (evaporation, sputtering, etc.). The coated samples are placed into the PECVD reactor, which is then pumped down to a low base pressure (~1mTorr). Simultaneously, the substrate is heated to a temperature shown to produce carbon nanotubes (450 to 700°C depending on process and chemistry [2-67, 2-68]). The decrease in required substrate temperature for CNT growth compared to other growth methods is thought to be a result of the energy added to the system from the high-voltage plasma. The carbon containing and reacting gasses are introduced into the chamber through a network of mass flow controllers to regulate the flow rate and gas composition of the mixture. The high voltage causes an ionization avalanche resulting in plasma formation, which acts to decompose the gas into its components. The exact growth mechanism of CNT formation is not exactly known, however it is thought that carbon enters into the catalyst until it is supersaturated. Finally, the carbon is precipitated out of the catalyst in the form of a carbon nanotube.

This method has more variables than the other techniques and allows for independent control of growth parameters. It has been shown that substrate temperature, catalyst thickness, chamber pressure, precursor flow rate, gas ratio, order of gas introduction, applied high voltage and current, and electric field orientation have effects on nanotube growth rate, diameter, and alignment.

A comprehensive study of the effect on nanotube growth of changing a single parameter and holding the others constant was performed by Han et al. in 2002 [2-67].

This work provided insight into the complex, interdependent system of growth parameters and a starting point for successfully growing nanotubes.

The decrease in nanotube diameter is suggested to be caused by enhanced hydrogen etching from dissociated NH_3 due to increased plasma intensity. The increased growth rate is a function of increased amounts of C_2H_2 being dissociated and absorbed into the catalyst.

The nanotubes grown at 120 standard cubic centimeters per minute (sccm) of NH_3 resembled nanofibers with coarse structure and short length. The growth rate increased slightly with higher flow rates of ammonia. Above 240 sccm of NH_3, the CNT density decreased while the diameter remained constant. This behavior is thought to be the result of the etching effects of ammonia. Results from other groups indicate that the use of NH_3 is critical for nanotube formation. Without it, the catalyst forms an amorphous carbon layer that prevents CNT growth.

The average nanotube diameter for both growth runs was approximately 90 nm [2-67]. This indicates that the rate of growth is a function of total flow rate, while carbon nanotube diameter is more dependent on the gas ratio.

Finding the optimal balance of parameters for growth of well aligned multiple wall carbon nanotubes requires tuning the process to grow CNTs with a designed diameter at a high rate of growth. Based on the results from the above experiments, a starting recipe for carbon nanotubes of approximately 75 nm diameter should include: NH_3 to C_2H_2 ratio of 4 to 1 with total flow of 300 sccm, sample temperature of approximately 450°C, and a plasma intensity of 605V at 0.12 A DC.

2.12 Electron Cyclotron Resonance Plasma Enhanced Chemical Vapor Deposition

As shown in figure 2-8, ECR plasmas have the highest electron density because of the plasma localization due to the external magnetic field. The dissociation of process gases would be more efficient in such a plasma environment as opposed to those without the magnetic field and the resultant cyclotron resonance condition. ECR plasmas constituted of gases that produce precursors for etching as well as deposition, have been used for nanotip fabrication on a range of substrates [2-69]. The basic mechanism is etching of the substrates through a self-assembled nano-mask. This technique of nanotip fabrication in the ECR plasma has been termed a "self masked dry etching" or SMDE technique [2-69]. Here, the plasma of H_2, Ar, CH_4, and SiH_4 gas mixture was ignited in an ECR condition and a range of substrates such as Si, poly-Si, GaN, GaP, sapphire, glass, copper, aluminum has been used. SiC, generated in the gas phase, deposits on these substrates and acts as etch resistant nano-masks. Subsequent etching by the Ar/H_2 gas mixture produces the tips. The tip composition is that of the substrate material with only a SiC cap at the apex for a Si tip. The tip lengths and densities are functions of plasma parameters such as gas flow rates, substrate temperatures, and reaction time. The etching properties of the substrates are also important. For example, amorphous materials are difficult to etch into a uniform nanotip. Although glass has been etched into the rough nanotip morphology, the length and density are not that well controlled. Crystalline substrates that exhibit preferential etching directions are better suited for this particular purpose.

The substrate temperature plays an important role in determining the length of the nanotips. On Si, the nanotips lengths were observed to be decreasing with increasing temperature [2-70]. 250°C substrate temperature produced the longest Si nanotips

whereas 800°C produced no noticeable nanotips at all. An Arrhenious plot of the length of the Si nanotips as a function of substrate temperature yielded two distinct slopes. The activation energy in these two linear regimes could be calculated and correlated with the etching efficiency in the two temperature zones. Physically speaking, it has been observed that with increasing substrate temperature the density of the SiC particles increased. As the process temperature was increased, methane dissociation became more efficient at the vicinity of the silicon substrate and instead of well separated SiC nanomasks, a continuous layer of SiC or a carbon rich SiC layer was formed above 700°C. The formation of a SiC layer decreased the etching rate of silicon and finally inhibited further lengthening of nanotips. The rate constants for dissociation of CH_4 were enhanced by two orders of magnitude from 1×10^9 at 250°C to 1×10^{11} at 700°C, whereas the rate constants for the dissociation of SiH_4 increased from 1×10^{12} at 250°C to 3×10^{12} at 700°C. Moreover, at a process temperature of 700°C, the dissociation rate constants for CH_4 are only one order smaller than that of SiH4, which would predict an efficient pathway for the formation of SiC. Above 700°C, the thin film of SiC was detected by both X-ray Photoelectron Spectroscopy (XPS) and Fourier Transform Infra-Red (FTIR) spectroscopy. This opposed any etching of the substrate and the formation of the nanotips was inhibited [2-70].

The general applicability of this plasma-based SMDE technique is quite unique and can, in principle, be applied to any kind of substrates. The plasma parameters need only to be optimized to get the tip morphology. The tips are monolithic to the parent substrate and always aligned in an array because of the etching-based fabrication method. Large area fabrication of nanotips is also not a problem; 6” Si wafers have been used to generate nanotips of reasonable uniformity. However, there is a concern about uniformity when using amorphous or metallic substrates, especially copper. As these nanotips were etched out from the substrate itself, and not grown as in

deposition techniques, the integrity of the nanotips is unmatched. There is no substrate- nanostructure interface, which can go a long way in helping device structures and simplifying their analysis.

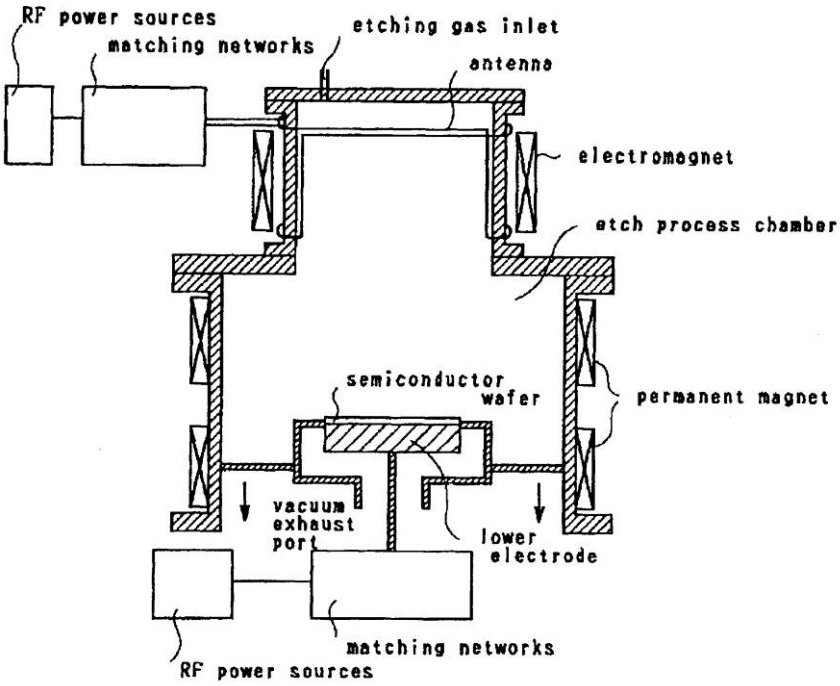

Figure. 2-8 Schematic of ECR-CVD system.

Chapter 3. Experimental Section

3-1 Electron Cyclotron Resonance Plasma Enhanced Chemical Vapor Deposition (ECR-CVD):

ECR plasmas have the highest electron density because of the plasma localization due to the external magnetic field. The dissociation of process gases would be more efficient in such a plasma environment as opposed to those without the magnetic field and the resultant cyclotron resonance condition. ECR plasmas constituted of gases that produce precursors for etching as well as deposition, have been used for nanotip fabrication on a range of substrates. The basic mechanism is etching of the substrates through a self-assembled nano-mask. This technique of nanotip fabrication in the ECR plasma has been termed a “self-masked dry etching” or SMDE technique

The AX4400 ECR plasma source is a high performance electron cyclotron resonance (ECR) plasma source designed for sub-micron feature-width semiconductor etching and high purity, low-temperature, plasma enhanced chemical vapor deposition (PECVD) applications. It may be used for both and isotropic etching.

As illustrated in figure 3-1, the components in an AX4400 are: (1) a source of 2.45 GHz microwave radiation, (2) a coupler to produce the desired microwave field pattern, (3) a vacuum window to admit the microwaves into the process chamber, (4) a source of process gases, and (5) a magnet system capable of generating at least 875 Gauss in the desired plasma volume. The source is mounted on a process chamber which contains the work piece and is connected to vacuum gas handling equipment for process pressure control.

Since the ECR source performs equally well in etching and deposition processes, it can be used to perform both types of operations in sequence in the same process chamber merely by using different gas sources and by varying system control

parameters.

The AX4400 ECR source generates uniformly distributed, high density plasma with very high ion content. It does so by exciting a process gas with 2.45 GHz microwave energy in a strong magnetic field within a high-vacuum chamber. In regions where the field strength is approximately 875 Gauss, electron cyclotron resonance occurs. The geometry of the microwave coupler and window, the means for introducing and distributing the process gas, and the regulation/control of the magnetic and microwave fields are key factors in achieving high efficiency and a uniform, dense plasma. All are features of the AX4400 source design.

The nanotips were fabricated using an electron cyclotron resonance (ECR) plasma reactor, which is comprised of gases such as hydrogen (H_2), argon (Ar), methane (CH_4), and silane (SiH_4) (10% in helium) with a typical flow rates of 8, 5, 1, and 0.2 sccm, respectively. Plasma etching of the Si(1 0 0) substrate produced highly aligned uniform silicon nanotip arrays with the tip diameter typically in the nanometer scale (~1nm) and the tip length in the micrometer scale (~1μm). The tip density can be controlled to range between 10^6 and $10^{11}cm^{-2}$. Each nanotip seems to be protected by a cap at the tip-head. The major physical features of the nanotips, e.g., the aspect ratio and the packing density, could be controlled by adjusting the etching parameters such as substrate temperature, applied microwave power, etc. Typical process temperature was 200°C, relatively lower than that for the aforementioned CNT growth.

Electrons within the plasma are partially confined in the radial direction by the magnetic field. However, since the average lifetime of electrons in the plasma is less than that of the relatively slow moving ions, a net positive space potential results. This positive space potential is highest in the dense plasma that exists within the ECR source and falls off in the region near the substrate. The resulting potential gradient accelerates ions out of the ECR chamber to a kinetic energy of 10 to 20eV before they

strike the substrate surface.

Because of the ECR principle, the AX4400 achieves high throughput at relatively low pressures and temperatures - thus minimizing damage and contamination of the substrate. The AX4400 is also compatible with a wide range of inert and reactive process gases.

The AX4400 ECR source is supplied as a complete, pre-tested, complement of system components ready for assembly and direct mounting on a mating flange or spool piece of the user's vacuum chamber.

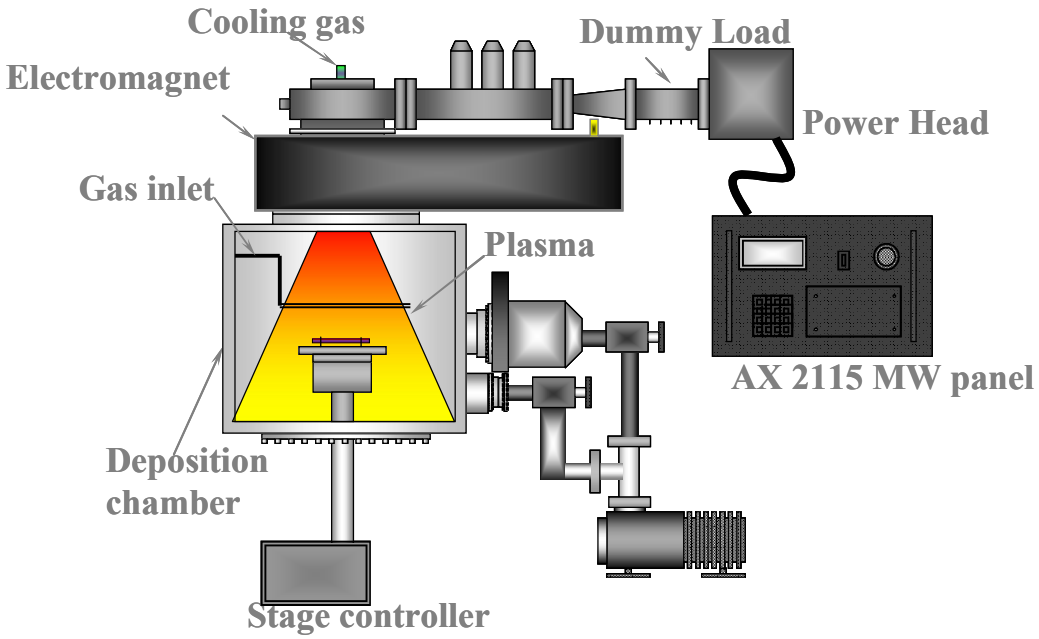

Figure. 3-1 AX4400 ECR plasma CVD system

3-2 Ion Beam Sputtering Deposition (IBSD):

Due to the high performance and uniformity of the nanoparticle and thin film deposition, the IBSD system (IBS-250, commonwealth scientific corp.) was used. The diameter of this Kaufman-type ion source is 64 mm (2.5”), while the length for a flange-mounted installation is 127mm (5.0”). In a freestanding installation, an additional 50mm (2.0”) should be allowed for the wiring and gas-feed tube behind the socket.

A variety of ion-optics designs are available for the 3cm source. Using two-grid graphite optics with argon, ion beam currents up to 100mA can be generated at 1000eV (a beam voltage of 1000V). The low-energy capability is excellent, with beam currents over 20mA possible at 300eV using two-grid graphite optics. Using one-grid optics, beam currents up to at least 30mA are possible at 50eV.

The plug-in approach is well suited to the use of a single ion source in any one of several vacuum chambers, as long as sockets are provided in these chambers. It is also well suited to the use of two ion sources alternately in a single socket, permitting a vacuum chamber to be operated with one source while maintenance is carried out on the other source. The reproducibility of the beam profile is important when a 3cm is used with multiple sockets, or multiple 3 cm sources are used with a single socket.

The 3cm ion source is fabricated primarily of stainless steel and alumina. There are small parts made of other vacuum compatible materials. The anode minimizes target contamination with ion source materials, while the overall design is well suited to high-vacuum operation, including high temperature baking cycles.

The entire IBSD system we used to fabricate nanoparticle and thin film was shown in figure 2-2. The optimized parameters of operation we used were 3sccm argon gas flow rate, $6x10^{-6}$Torr in base pressure, $4x10^{-4}$Torr to $4x10^{-4}$Torr in operating pressure.

The deposition temperature of the substrate was maintained at room temperature and the tunable rotating target holder can make the uniform sputtering yield of the target under the ion beams exposure. According to the electron microscopy (EM, HRSEM and HRTEM) images, the uniform nano-sized particles and ultra thin continuously thin film (in several nanometer range) can be observed.

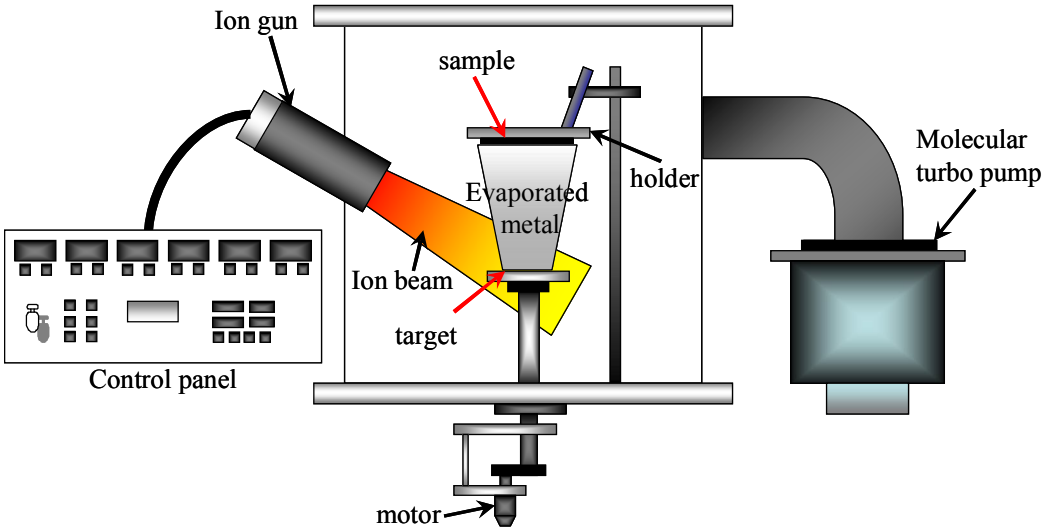

Figure. 3-2 IBS-250 Ion Beam Sputtering Deposition system

3-3 Metal Organic Chemical Vapor Deposition:

For the past few years, MOCVD has become a commonly used technology for production of Ⅲ-Ⅴ compound semiconductor optoelectronic devices and electronic devices. The achievement of growing ultra-bright blue light emitting diodes by MOCVD makes this technology be a leading candidate for manufacturing optoelectronics devices. Briefly, MOCVD process relies on vapor transport of the group Ⅲ alkyls combined with group Ⅴ hydrides into heated substrate. At the heated substrate, the molecules pyrolyze to produce the group Ⅲ and the group Ⅴ elements needed for formation of the desired Ⅲ-Ⅴ semiconductors and subsequent reaction. Because these precursor molecules are so unstable at the growth temperature and the Ⅲ-Ⅴ solid is so stable, the thermodynamic driving force for MOCVD typically is enormous. MOCVD is sometimes described as a highly non-equilibrium process.

The first MOCVD system design for GaN growth was developed by Maruska and Tietjen. Soon after, Manasevit applied this technique to grow GaN onto sapphire substrates. The choice of sapphire substrate results from the facts that no bulk GaN substrates are available and a very stable material is required to deal with the high temperature required for GaN growth. Metal organic group Ⅲ sources are either liquids, such as trimethylgallium (TMGa), triethylgallium (TEGa), trimethylaluminum (TMAl) and triethylaluminum (TEAl), or solids such as trimethylindium (TMIn). For Ⅲ-Nitrides growth, ammonia (NH_3) is most commonly gaseous hydride source. Doping materials can be metal organic precursors such as dimethylzinc (DMZn), cyclopenta-dienyl-magnesium (Cp_2Mg) and hydrides of silence (SiH_4) or disilance (Si_2H_6).

In this study, we use MOCVD (homemade) by VLS mechanism to achieve the growth of various 1-D InN nanostructures. Samples used in this study were all grown

on gold (catalyst)-coated (0 0 1)-oriented Si substrates and the indium and nitrogen sources were trimethylindium (TMIn) and ammonia (NH_3), respectively. In the experiment, we take TMIn into the thermostat and hold temperature at 10℃. We use high degree of purity N_2 gas to be carrier gas and dilute TMIn. In the chamber, the environment is low pressure. The model of system can see figure 3-3 using pyrolytic boron nitride (PBN) to heat sample.

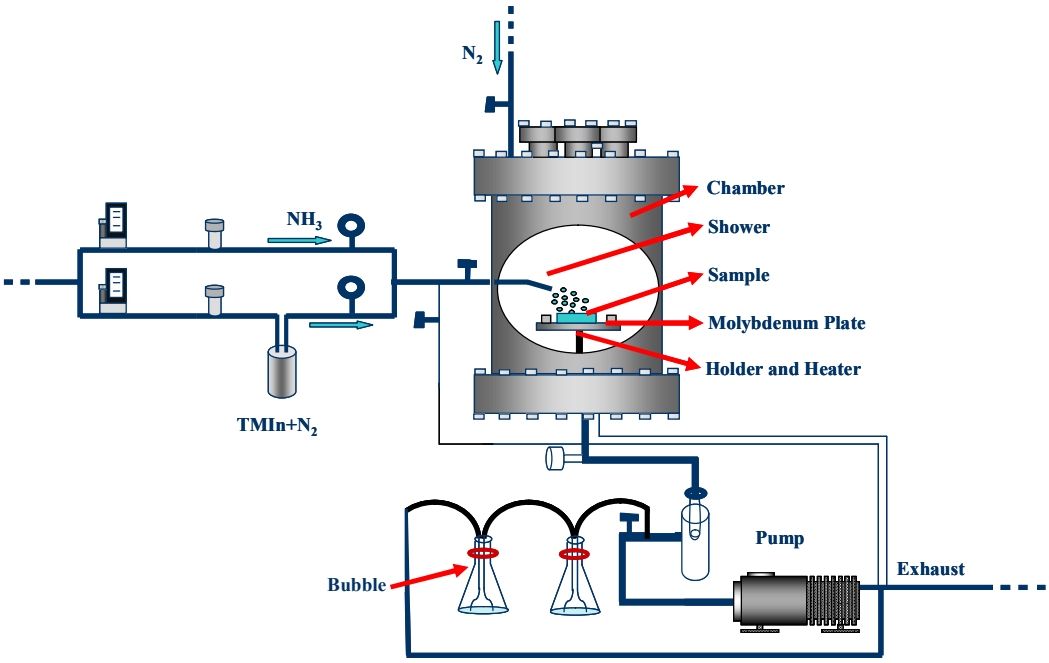

Figure. 3-3 schematic diagram of MOCVD

3-4 Thermal chemical vapor deposition (Thermal-CVD):

In a typical CVD process, the wafer (substrate) is exposed to one or more volatile precursors, which react and/or decompose on the substrate surface to produce the desired deposition. The volatile byproducts are always formed during deposition, which can be removed by gas flow in the reaction chamber. According to the references reported, there are several types of processes were employed to fabricate the 0-D, 1-D and 2-D structure of III-nitride materials.

(1) Thermal CVD (TCVD): shown in figure 3-4.

(2) Low-pressure CVD (LPCVD).

(3) Plasma-Enhanced CVD (PECVD)

A four-stage growth process is proposed to explain the formation of GaN nanowires as follows: (1) Ga and Ga_2O_3 powder was uniformly mixed. (2) Increasing temperature to form Ga_2O via Ga and Ga_2O_3 mixture. (3) Vaporizing Ga_2O semi-product under processing temperature to deposit onto the catalyst coated substrate via VLS mechanism in N_2 environment.

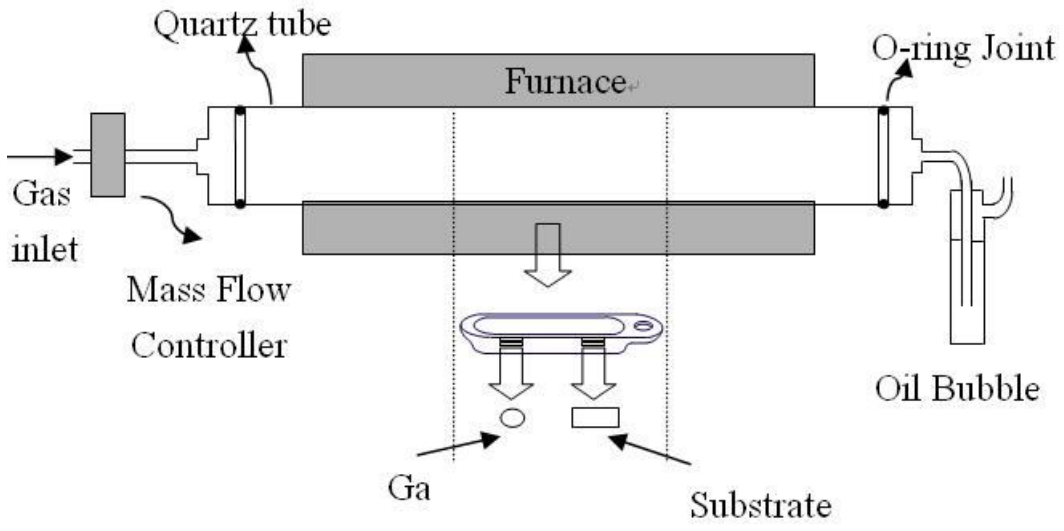

Figure. 3-4 Schematic diagram of Thermal CVD

3-5 High Resolution Scanning Electron Microscope (HR- SEM)

The JSM-6700F is a high-resolution scanning electron microscope, which employs a field-emission gun for the electron source and state-of-the-art computer technology for the image-display system, shows in figure 3-5.

A combination of a conical field emission gun and semi-inlens objective lens results in a high-resolution image; a 1280 X 1024 pixel high-definition display system enables a fine flicker-free image even in slow-scan conditions and makes it possible to operate the SEM in a lighted room; and mouse/panel/keyboard operation with on-screen menu bar and condition-setting windows offers easy and smooth operations in all stages from condition setting to image observation.

Employing the Windows NT operating system provides high networking performance as well as easy and smooth operations in all stages from condition setting to image observation and filing with the JEOL-specific graphic user interface. The JSM-6700F is a super intelligent PC-SEM that can flexibly cope with the development of the computer technology.

When the electron probe illuminates the specimen, secondary electrons, backscattered electrons, transmitted electrons, characteristic X-rays, and so forth are emitted from the specimen surface. In order to detect these as signals or for other research purposes, the JSM-6700F can accommodate a variety of optional attachments. By effectively combining these attachments, we can fully expand the scope of application of this instrument, allowing multiple information to be drawn out of the surfaces of the specimen.

Figure. 3-5 systematically illustration of JSM-6700F HR-SEM

3-6 High Resolution Transmission Electron Microscope (HR-TEM)

Among TEMs, the JEOL-4000EX shows in figure 3-6 across the full range from routine analysis to sub-nanometer research. Their high performance, flexibility, wide range of signals and ease of use ensure a vast increase of productivity in advanced materials research.

High-resolution imaging provides insight in crystal structures, microstructures, defects and interfaces at an unprecedented atomic level. The JEOL-4000EX's highly stable lens currents, high tension and mechanical design provide the ultimate in high-resolution performance on a routine basis. The three objective-lens versions allow tailoring of resolution and tilt to specific fields of investigation, with each lens version combining the highest tilt and best point resolution currently available. The dedicated HR-TEM mode incorporates a two-channel electro-magnetic image shift to keep the illumination centered exactly on the field of view.

Figure 3-6 schematic of JEOL-4000EX

3-7 Auger Electron Spectroscope (AES)

The AES analysis was used to characterize the composition of the nanostructure. As shown in figure 3-7, the multiple electron spectroscopy for chemical analysis was employed to analyze the surface composition and the electron structure of the interfaces of nanostructure.

In this system, dual anode of aluminum and magnesium were used as X-ray light source, the maximum energy of 15kV can be created as high as 400W. The energy of aluminum anode and magnesium anode were 1486.6eV and 1253.6eV, respectively, was used to sputter the element of the surface. Multi-channel detector with spherical capacitor analyzer of 10-360 type was used to collect the signals of Auger electron backscattered from surface. Resolution (△E/E) of this analyzer was 0.1~0.8%.

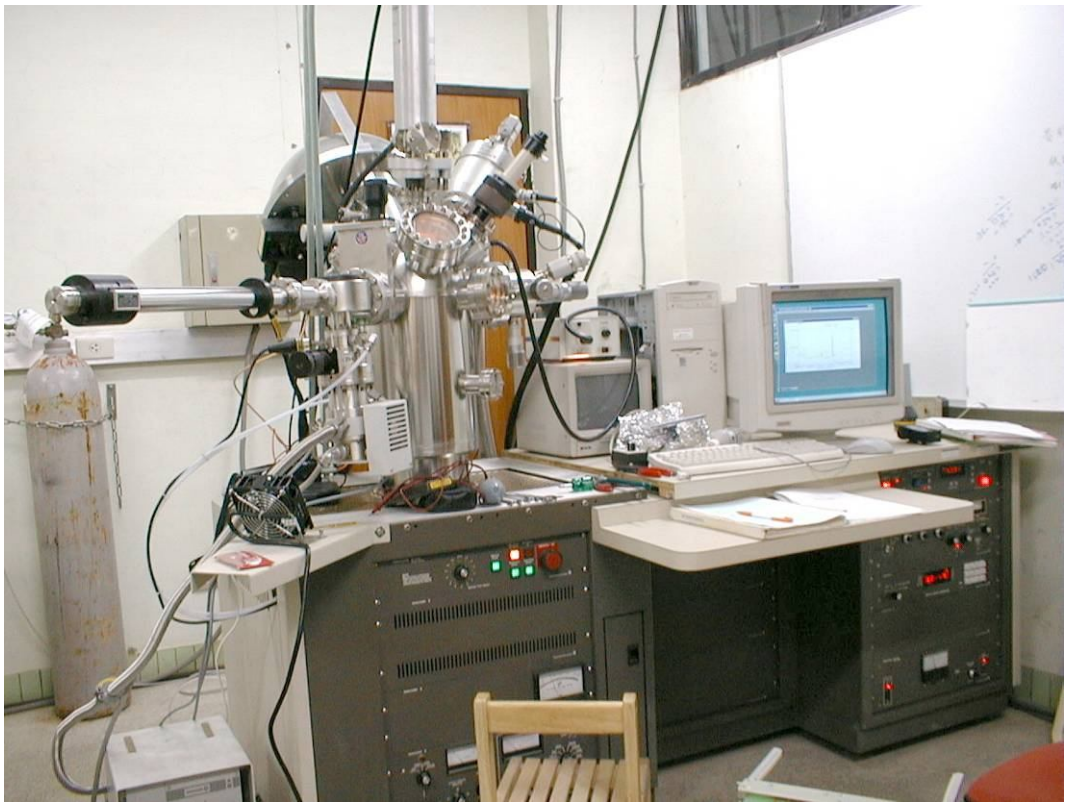

Figure. 3-7 Entire setup of AES/ESCA system

3-8 Raman Spectroscope

As shown in figure 3-8, the HR800 is an integrated Raman system. The microscope is coupled confocally to an 800mm focal length spectrograph equipped with two switcheable gratings. The software used in this system was LabSpec5 which was a general data acquisition and data analysis based on open NexGen module architecture, enables different data acquisition modes (e.g. single spectrum, multidimensional data set, video image etc.). In the picture below shows the main parts of the instrument as they can be seen when the cover was taken off. The excitation wavelength is supplied by an internal HeNe 20mW laser mounted on the back of the instrument.

An entrance for another external laser beam is also placed on the back side (laser wavelength available includes virtually any laser within 440-800nm). The laser is totally reflected by the notch towards the sample under microscope and the Raman scattering is totally transmitted through the notch filter towards the confocal hole and entrance slit of the spectrograph can be accessed in the higher part of the instrument. If the HR800 is a “line scanning” model, the entrance optics also contains the scanner and projection optics for the canned line on the sample onto the slit of the spectrograph. Raman scattering can also be entered via a fiber optics probe. The fiber optic entrance is situated also on the back side of the instrument. The laser is coupled to another fiber optic going to the probe using the 10X objective of the microscope. The spectrograph is the box under the entrance optic of the instrument and forms a spectrum on cooled one or nitrogen cooled one, with 15 or 16 bit dynamic range, size 1024 X 256 or 2000 X 800.

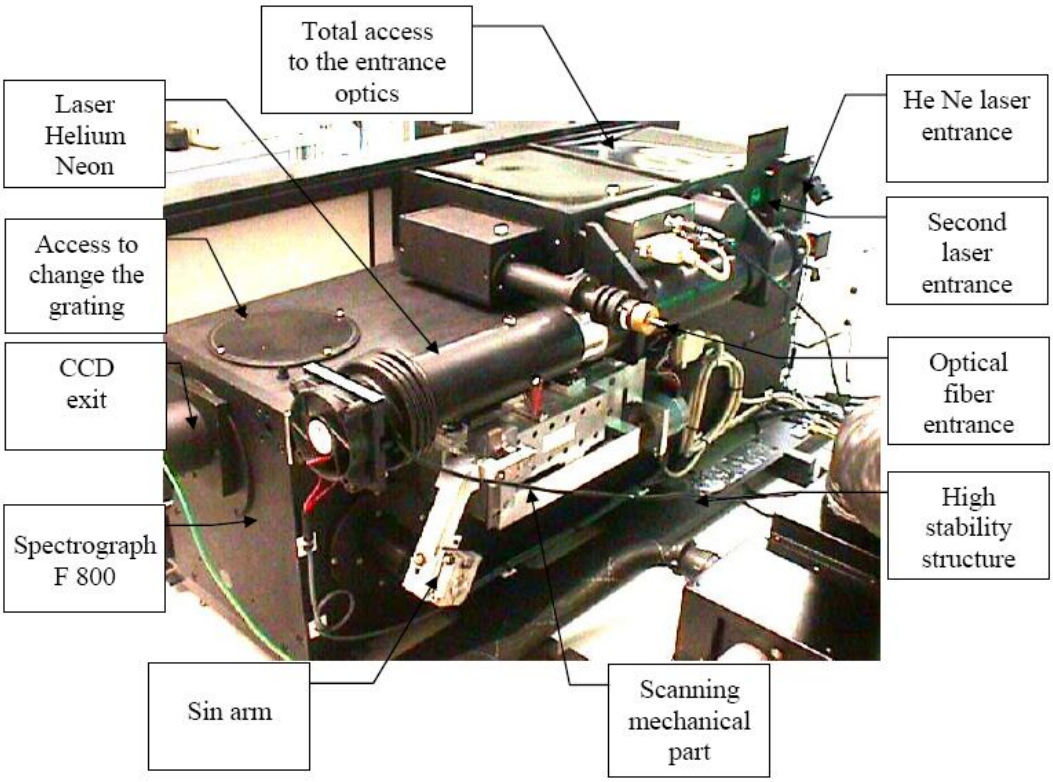

Figure. 3-8 Schematic diagram of HR800 Raman system

Chapter 4. Synthesis and Mechanism of Nanotip Arrays:

4-1 INTRODUCTION:

Nanoscaled tips have been demonstrating their unique usefulness in different applications such as high-efficiency field emission [4-1], near-field optical microscopy [4-2, 4-3], high-resolution atomic force microscopy and atomic-resolution scanning tunneling microscopy [4-4~4-6]. Sharper tip (i.e., smaller apex of the tip) gives stronger field enhancement for increased field emission current [4-7] and better spatial resolution in scanning probe microscopy [4-8, 4-9]. Currently, field emission from microand nanotips as well as other one-dimensional nanomaterials have been widely investigated [4-10~4-14]. Optimum field emission performance can be obtained by adjusting the size and spacing of the tips or nanostructures so as to maximize the enhancement of the local electric field of individual emitter and the collective emission current from an ensemble of emitters [4-15~4-17]. In addition to the applications mentioned above, nanotips are being explored for different purposes in solar cells [4-18], optoelectronics [4-19~4-20] and bio/chemical sensing devices [4-21~4-23]. However, a number of crucial technological hurdles block the way for actual realization of these developmental works. Those include uncontrolled growth of nanotips and incompatibility of the nanofabrication process with the well-established silicon process technology. Accordingly, an efficient nanofabrication process capable of delivering tip morphologies over large areas and on varied substrates and still compatible with existing process technologies will significantly advance research in nanotechnology.

Until now, optical lithography has been playing the major role in fabricating sharp tips but limited to 50 nm in radius [4-2, 4-11~4-12]. Electron-beam or

focused-ion-beam lithography can produce tips with smaller radius. However nanolithography has the physical limitation in tip radius [4-24] typically about 15 nm. Dry etching of the substrates pretreated with heterogeneous nanomasks is one of the efficient techniques for nanofabrication. Whether in reactive ion etching (RIE) of substrates such as GaN [4-25] or Si [4-26], or in Ar ion beam sputtering of substrates (e.g., Si) [4-27], nanomask fabrication poses the main challenge toward obtaining nanotips. Nevertheless, the aforementioned processes can be applied successfully only to certain limited substrates.

4-2 MATERIALS AND METHODS:

In this section, we report a one-step and self-masked dry etching (SMDE) technique for fabricating uniform and high-density nanotip arrays over a large area in a cost-effective manner, using a Seki high-density electron cyclotron resonance (ECR) plasma reactor. The pre-cleaning of the substrate by hydrogen (H_2) plasma, followed by simultaneous process of self-masking and reactive etching of the unmasked area for nanotip formation, was done in the reaction chamber in one step and without interrupting the vacuum. Reactive gases comprising of argon (Ar), H_2, methane (CH_4), and silane (SiH_4) (10%, diluted in helium) with typical flow rates of 3, 8, 2, and 0.2 sccm, respectively, were activated by a microwave power of typically 1200 W at a chamber pressure of 5.8 mTorr, during the nanotip fabrication process. Nanotip arrays were etched out from a variety of substrates maintained at a temperature between 100°C to 250°C, as measured by a two-color optical pyrometer.

4-3 RESULTS AND DISCUSSION:

Figure 4-1 shows the tilted top-view high-resolution scanning electron microscope (HRSEM) images of nanotip arrays formed by the SMDE technique on various substrates, e.g., single-crystal silicon (Si), polycrystalline silicon (poly-Si), gallium nitride (GaN), gallium phosphide (GaP), sapphire, and aluminum (Al). Nanotips were found to be well aligned and uniformly distributed over the entire surface with a high density for all the samples.

In case of single crystalline 6 in. Si wafers, Si nanotip density as high as 1.5 X $10^{11}/cm^2$ was obtained with a high aspect ratio of ~50. Similar geometric features of the nanotips as observed on all substrates with different crystal orientation, as demonstrated in figure 4-1, suggest no orientation dependence of the etching process involved and recognizes a general applicability of the SMDE process in the field of nanotip fabrication, apart from its simplicity and compact process steps. Further structural investigation was carried out by using high-resolution transmission electron microscope (HRTEM). Typical HRTEM images of the nanotips of crystalline silicon and GaP are shown in figure 4-2a and figure 4-2b, respectively.

In both cases, ~1 nm apex radius of the tip was obtained, which can be compared favorably to the finest tip reported so far. More interestingly, a cap has been identified at the top of the tip with lattice spacing different from that of the body of the tip. Figure 4-2a shows the Si nanotip substrate with a lattice spacing of 3.15 Å and the cap with a lattice spacing of 2.58 Å, which is close (2.38% deviation) to the literature data of 2.51 Å for (111) d spacing of 3C-SiC [4-28]. HRTEM study of the GaP nanotips sample revealed a similar cap structure. As shown in figure 4A-2b, the cubic GaP structure exhibits a (200) lattice spacing of 2.726 Å at the bottom of the tip, whereas the cap exhibits a lattice spacing of 1.82 Å, which is close to (0.55% deviation) the

literature data of 1.83 Å for (102) d spacing of 2H-SiC [4-29].

To confirm this, a high resolution Auger depth profile was performed on the cap and a Si/C = 1:1 stoichiometry was identified from the composition data presented in figure 4-3. Accordingly, the formation of a SiC cap, acting as the nanomask, is believed to be instrumental in the fabrication of the nanotip arrays not only for Si but also for non-Si substrates. The dashed lines in the inset of figure 4-2a and 4-2b indicate the interface between SiC cap and etched substrates. It appears that the SiC caps were formed on Si and GaP substrates in a "heteroepitaxial" manner. A lattice matching relationship of 4:5 with a 5° angle for Si and SiC (or 1:2 with 41° angle for GaP and SiC) was observed.

Figure 4-4 illustrates the schematic description of the nanotip formation. The gas-mixture consisting of SiH_4, CH_4, Ar, and H_2 present in the ECR plasma is supposed to react and play two different roles: formation of SiC nanomasks and etching of the substrate to develop nanotips (figure 4-4a). It is believedthat in the ECR plasma, SiC nanosized clusters are formed from the reaction of SiH_4 and CH_4 plasma [4-30] and uniformly distribute themselves over the substrate surface (figure 4-4b). Meanwhile, Ar and H_2 plasma are responsible for the physical etching and chemical etching, respectively, of the substrates. The SiC nanoclusters deposited on the substrate then act as nanomasks against etching, because of their higher hardness and chemical inertness. Under the protection of a high density of SiC caps, formation of high density and high aspect ratio nanotip arrays can be realized (figure 4-4c).

This one-step approach, promoting the occurrence of SiC ("bottom up") and dry etching of substrates ("top down"), enables the fabrication of various nanotips without choosing a specific substrate or pretreating with a specific heterogeneous etching resistant as used in conventional methods. Studies that use masks developed by pretreating the substrates have no control on the size of the masks grown. In

comparison, the SMDE process possesses a control on the size and density of the SiC clusters simply via the process parameters of the high-density plasma environment, such as process temperature, gas pressure, and composition, which translates into crucial control of the tip morphologies and densities. For example, the high-temperature environment favors the formation of SiC masks at such high densities so as to cover the entire substrate surface inhibiting the nanotip formation. Such detailed dependence of morphology on experimental conditions will be discussed in a separate paper.

The mechanism underlying the self-assembly of nanomasks is unclear, however, symmetry and lattice mismatch between the substrate and the mask material are likely to play a role.[4-31] After the simultaneous formation of SiC nanoclusters and etch-active reagents in the plasma, selforganization of nanomasks appears to be a concerted process involving both the substrate and the mask; their lattice mismatch of different dimensions may lead to the differences in the geometrical features of nanotips, including their surface density, while preparing nanotips using different substrates.

We would like to pay special emphasis to the applicability of the SMDE technique to a series of materials. The slight difference in morphology of post-etching structures on different materials is in fact a drawback for all etching processes. In SMDE technique, we have a combination of physical and chemical dry etching process. The resultant shape would be affected by the inherent difference in physical hardness and chemical reactivity of the substrate with the plasma. Consequently, we successfully combined photolithography with SMDE technique to form silicon nitride patterned arrays of nanotips as shown in Figure 4-5, which demonstrated the potential of the SMDE technique in device applications.

Quantum confinement effects in Si as well as compound semiconductors arising

from reduction in dimensions have been widely investigated.[4-32~4-35] The study of the optoelectronic properties of these nanotips relative to their bulk counterparts is ongoing and will be reported in a separate paper. The field emission property of such sharp nanotip arrays in a simple diode structure reveals an ultralow turn-on field (defined as the field at which an emission current density of 10 uA/cm^2 is obtained) of 0.35 V/um.[4-36] Further studies on gate controlled field emission devices such as that shown in figure 4-5 is underway. Meanwhile, we have applied our nanotips as a template for metallic nanoparticulate growth for surfaceenhanced Raman scattering (SERS) study, and an enhancement factor as high as 10^6-10^8 for Rhodamine 6G was observed.

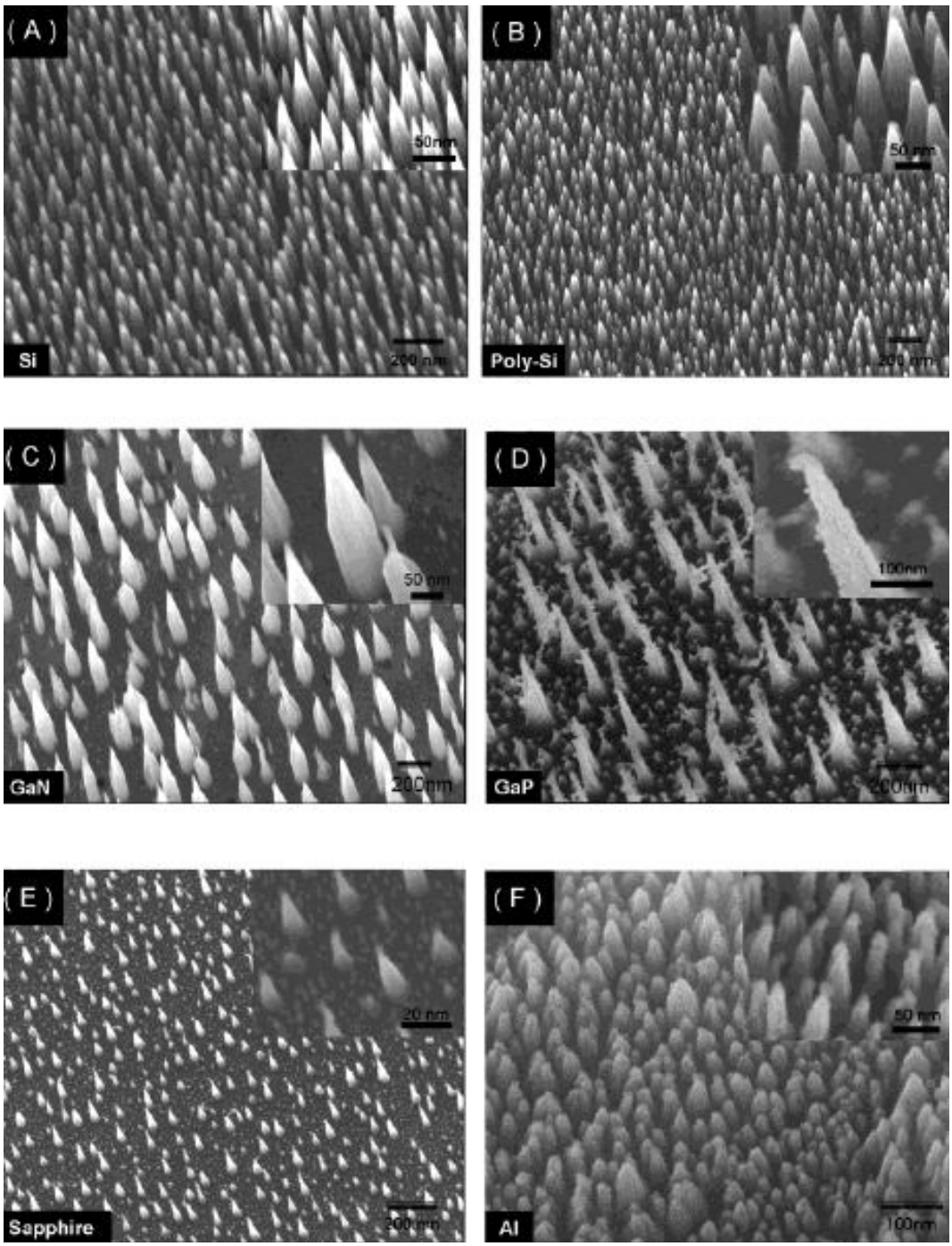

Figure 4-1. Tilted top-view HRSEM morphologies of the nanotip arrays fabricated by the self-masked process of various substrates: (a) single-crystal silicon (Si); (b) polycrystalline silicon (poly-Si); (c) epitaxial gallium nitride (GaN) film on sapphire; (d) single-crystal gallium phosphide (GaP); (e) sapphire; and (f) aluminum. The insets show their corresponding magnified images.

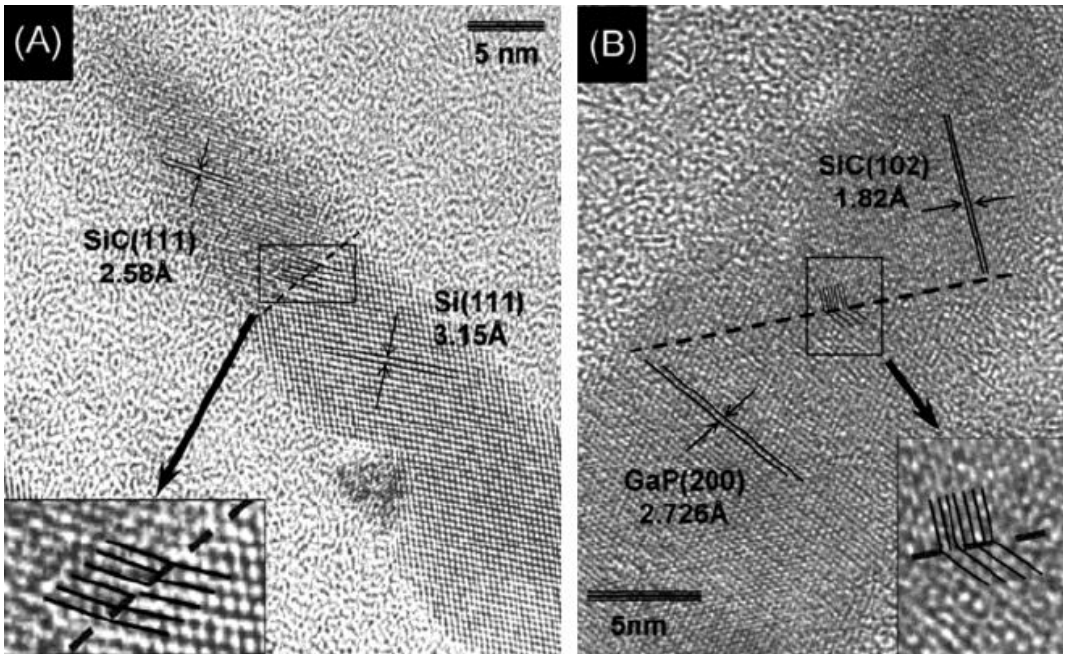

Figure 4-2 (a) HRTEM image of the Si nanotip revealing a SiC cap formed on top of the tip. Inset shows the magnified HRTEM image of the interface between Si and SiC cap on which the lattice mismatch of Si/SiC = 4:5 can be observed. (b) HRTEM image of the GaP nanotip with SiC cap also formed on the tip. Inset shows the magnified HRTEM image of the interface between GaP and SiC cap on which the lattice mismatch of GaP/SiC = 1:2 can be observed.

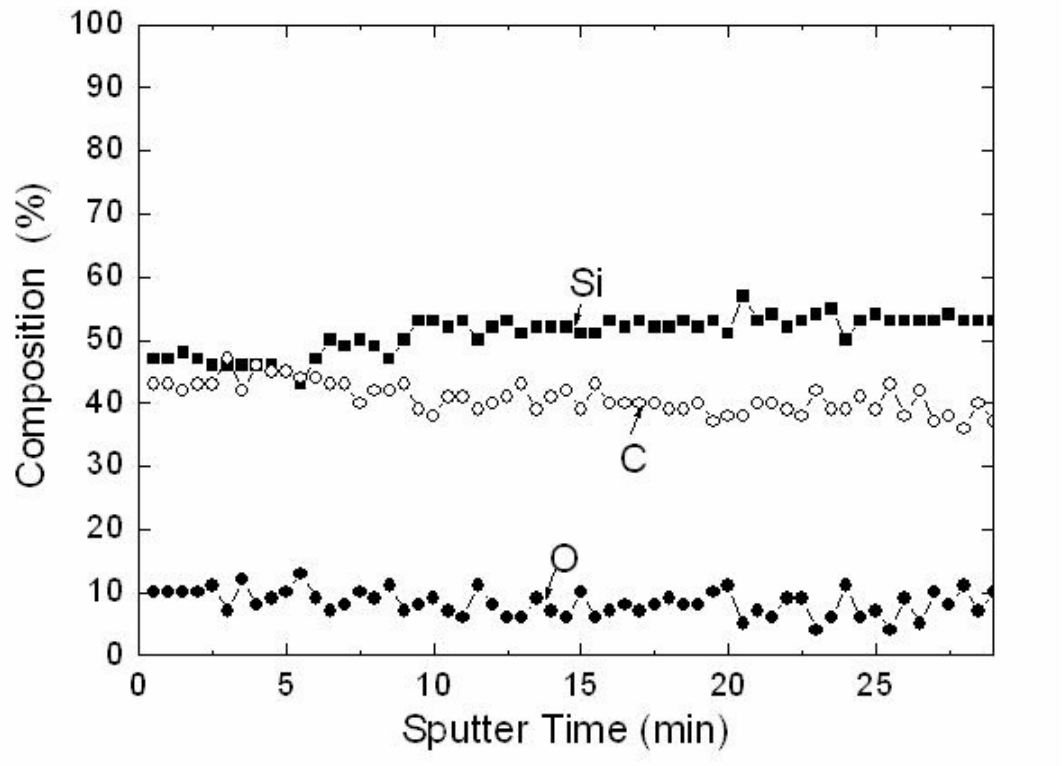

Figure 4-3 High-resolution Auger depth profile at the top of the nanotip showing the composition of the cap to be Si/C = 1:1.

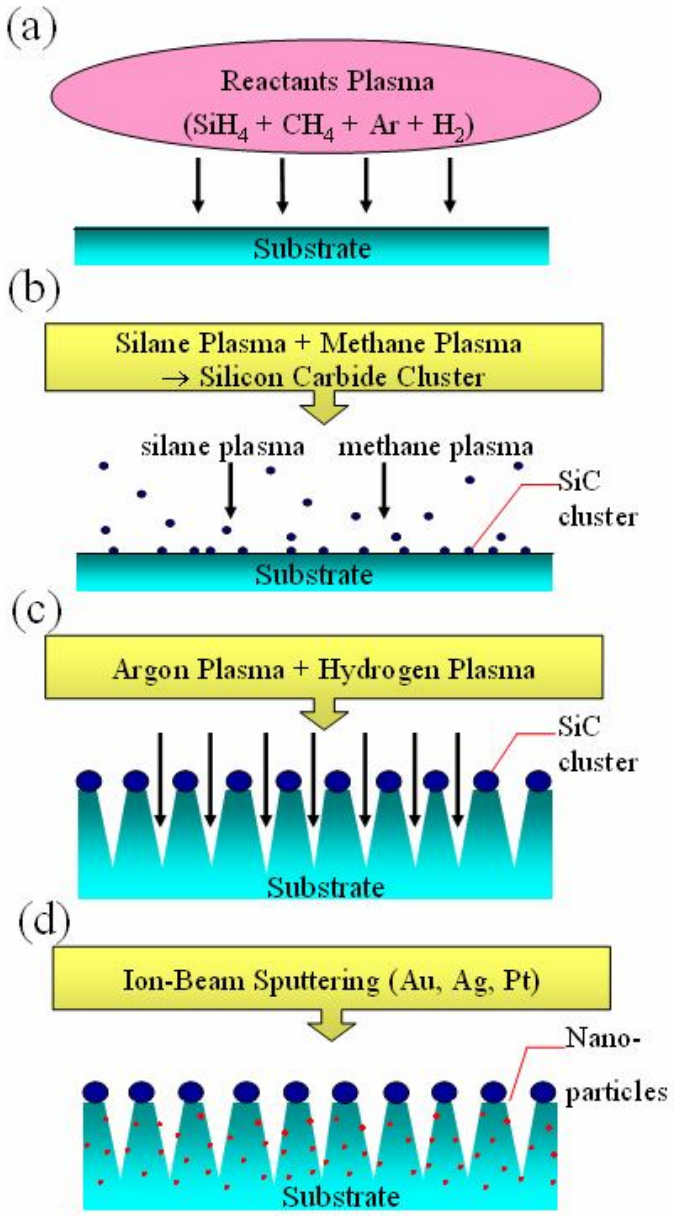

Figure 4-4. Schematic diagram for the nanotip formation: (a) the reactive gases are composed of silane, methane, argon, and hydrogen; (b) the SiC nanosized clusters are formed from the reaction of SiH_4 and CH_4 plasma and uniformly distributed on the substrate surface; and (c) the unmasked region is etched by Ar and H_2 plasma, whereas the region masked by SiC caps protects the substrate from etching, and hence creates the conical tips.

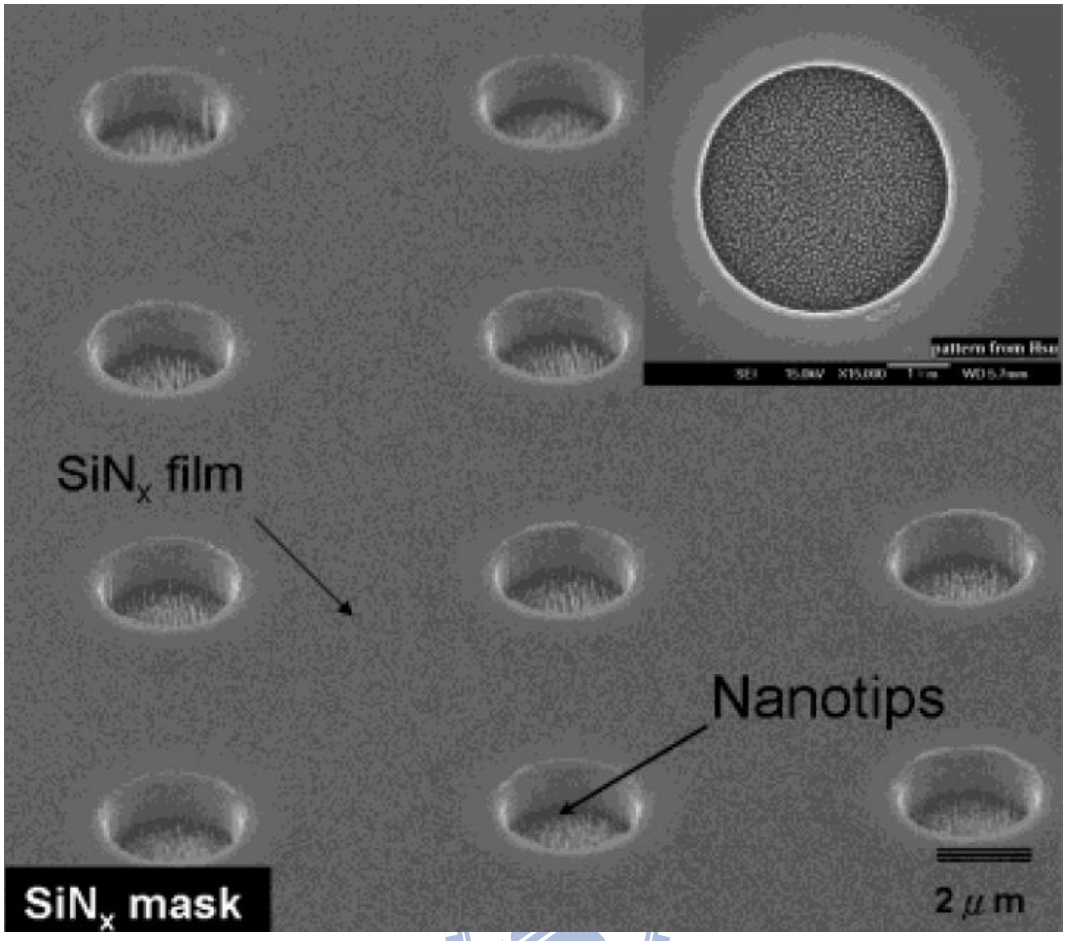

Figure 4-5 Patterned arrays of naotips generated by photolithography process using silicon nitride as the etching resistant.

Chapter 5. Electron Field Emission From Well-aligned Nanotip Arrays

5-1 INTRODUCITON:

Structures with at least one dimension between 1 and 100 nm are called nanostructures. They have steadily attracted growing interest due to their fascinating properties, as well as novel characteristics originating from their morphologies [5-1~5–9]. Nanostructures can be divided into zero-dimensional (0D when they are uniform), one-dimensional (1D when they are elongated), and two-dimensional (2D when they are planar) based on their shapes. The recent emphasis in the nanomaterials research is put on 1D nanostructures at the expense of 0D and 2D ones, perhaps due to the intriguing possibility of using them in a majority of short-term future applications.

There is a large number of new opportunities that could be realized by down-sizing currently existing structures to the nanometer scale (100 nm), or by making new types of nanostructures. The most successful examples are seen in microelectronics, where ‘‘smaller’’ has always meant a greater performance ever since the invention of transistors: e.g. higher density of integration, faster response, lower cost, and less power consumption [5-1]. Inorganic semiconductor nanostructures are ideal systems for exploring phenomena at the nanoscale and studying the dependence of functional properties on size and dimensionality.

Field-emission (FE), is one of the main features of nanomaterials and nanostructures, and is of great commercial interest in displays and other electronic devices. In the case of a nanostructure, it has the advantage of faster device turn-on time, compactness and sustainability, as compared to conventional bulky technologies. Recent progress in the synthesis and assembly of nanostructures has resulted in a

considerable increase in the current density and lowering of the turn-on voltage for a variety of nanomaterials. Field-emission, also known as Fowler–Nordheim tunneling, is a form of quantum tunneling in which electrons pass from an emitting material (which is negatively biased) to the anode through a barrier (vacuum) in the presence of a high electric field. This phenomenon is highly dependent both on the properties of the material and the shape of the particular cathode, and the materials with higher aspect ratios and sharp edges produce higher field-emission currents.

The current density (J) produced by a given electric field (E) is described by the Fowler–Nordheim equation:

$$J = (A\beta^2E^2/\varphi)\exp(-B\varphi^{3/2}/\beta E) \quad (1)$$

$$I = S * J,\ E = V/d \quad (2)$$

$$\ln(J/E^2) = \ln(A\beta^2/\varphi) - B\varphi^{3/2}/\beta E \quad (3)$$

where A and B are constants, ($A = 1.54*10^{-6}$ A eV V^{-2}, $B = 6.83*10^3$ $eV^{-3/2}$ V mm^{-1}), S is the emitting area, V is the applied potential, I is the emission current, β is the field enhancement factor, d is the distance between a sample and the anode and φ is the work function of the emitting materials. The field enhancement factor, β, is related to emitter geometry, its crystal structure, and the spatial distribution of emitting centers. β can be expressed as β = h/r, where h is the height and r is the radius of curvature of an emitting center. Thus, materials with elongated geometry and sharp tips or edges can greatly increase an emission current. The emission occurs from the tip of an emitter. The emitter can have different emission currents depending upon the tip geometry such as, (i) round tip, (ii) blunt tip and (iii) conical tip.

Since the discovery of carbon nanotubes (CNTs), much attention has been paid to exploring the prospects of inorganic semiconductor nanostructures as field-emitters due to their low work functions, high aspect ratios, high mechanical stability, and high conductivity etc [5-10~5-13]. A CNT may have an aspect ratio as high as 1000, which

leads to effective field enhancement at the apex of a nanotube. This provides a great opportunity for using such materials to obtain electron emission based devices at rather low applied potential [5-14]. However, to achieve high structural quality of these CNT and improved field emission performance, the process temperature of CNT growth has to be maintained at above 600°C. On the other hand, field emitters utilizing lithographically etched silicon tips usually require extremely small tip to gate spacing to achieve the required emission current density because of its high turn-on field of several tens of V/mm [5-15, 5-16]. A gross reduction in tip diameter and increased packing density of the field emitter tips is required for a major advancement in this field. In this letter, we report the fabrication process of high-density (10^9–$3*10^{11}$ cm^{-2}) silicon nanotips at low temperatures (~200°C) suited for integration into the state-of-the-art silicon technology. Furthermore, high field emission current density has been achieved at ultralow electric field. Here, two kinds of inorganic semiconductor nanotips, such as Si, GaP, were focused on their corresponding field-emission behavior.

5-2 MATERIALS AND METHODS:

The one-step fabrication of semiconductor nanotip arrays using a large area etching technique has been demonstrated using single crystal silicon substrate and silicon carbide films. Therefore, we use GaP wafers with a similar technique to prepare these nanotip arrays. A 1.5 kW AsTex AX2115 microwave source and an AX4400 electromagnet were employed to generate the high-density electron cyclotron resonance (ECR) plasma. The plasma is composed of a mixture of semiconductor-grade gases, silane (SiH_4), methane (CH_4), argon (Ar), and hydrogen (H_2), with typical flow rates of 0.2, 3, 3, and 8 SCCM (SCCM denotes cubic centimeter per minute at STP), respectively. The gas mixture at a pressure of 3.2 mTorr was ionized directly by a microwave energy source (typically 1200 W) under a high electro-magnetic field (875 G). Without any pretreatment or any catalyst coating, the reaction begins on a pure Si/GaP substrate in the size of 1 x 2 cm^2 cut from a Si/GaP wafer. The substrate temperature for fabricating Si/GaP nanotip arrays can vary between 150 and 800°C, and can be detected by a thermocouple attached directly to the substrate holder. The Si/GaP nanotip array with a SiC cap starts developing under the active etching and codeposition of the high-density plasma.

High resolution scanning electron microscopy (HRSEM, JEOL JSM-6700 field emission scanning electron microscope) and high resolution transmission electron microscopy (HRTEM, JEOL JEM-3000F) were used to study both the morphological and structural aspects of the bare Si/GaP nanotip array distribution, respectively. The field emission measurement system we used was a laboratory-assembled vacuum chamber pumped by a turbo molecular pump (Alcatel, ATP-400). A Windows-based data acquisition program combined with a Keithley 237 power supply was used to detect the field emission currents with voltages in this study. To estimate the reliable

current density versus applied field (J-V) results, the pressure of measurement was maintained under 5 x 10^{-7} Torr regime.

5-3 RESULTS AND DISCUSSION:

Field Emission behavior of SiNTs

Plasma etching of the Si(100) substrate produced highly aligned uniform silicon nanotip arrays with the tip diameter typically in the nanometer scale (~1 nm) and the tip length in the micrometer scale (~1 mm). The tip density can be controlled to range between 10^6 and 10^{11} cm^{-2}, as the typical ones shown in figure 5-1. Each nanotip seems to be protected by a cap at the tip-head. The major physical features of the nanotips, e.g., the aspect ratio and the packing density, could be controlled by adjusting the etching parameters such as substrate temperature, applied microwave power, etc. Typical process temperature was 200°C, relatively lower than that for the aforementioned CNT growth.

To verify the formation of SiC clusters as the nanomasks, which is suggested by the nanobeam Auger analysis as mentioned earlier, high-resolution transmission electron microscopy (HRTEM) was also employed to acquire the direct evidence of the tip structure. As shown in figure 5-2, the HRTEM image of the nanotip shows clear Si(111) lattice spacing of 3.14 Å, and the cap of the tip with a lattice spacing of 2.58 Å. The cap is confirmed to be SiC since the 2.58 Å lattice spacing is within 97% of the 2.51 Å d spacing of a cubic phase SiC(111) [5-17], and thereby presented a clear evidence for the formation of the SiC nanomasks in the process.

The results discussed so far demonstrate that silicon nanotips are produced by the anisotropic (crystallographic orientation independent) dry etching of the crystalline silicon substrate by the ECR plasma. The SiC clusters produced by the gas phase reactions of SiH_4, CH_4, and H_2 in the plasma could be uniformly and densely distributed on the substrate. These SiC clusters deposited on the silicon substrate then act as nanomasks, during the subsequent etching process, to form the nanotip array.

The Ar ion from the plasma plays the dominant role in the formation of nanotips by dry physical etching through selective sputtering process while atomic-H, created in high density by the ECR condition, contributes to the dry chemical etching of the silicon surface. Two competing mechanisms, namely the formation of the SiC nanomask on the surface [5-18] and the preferential etching of the unmasked silicon [5-19], coexist during this process and proceed simultaneously in the plasma, forming the nanotips. Microfabricated pure silicon field emitters are inherently chemically reactive. The contaminants act as tunneling barriers resulting in a larger effective work function leading to emission instabilities. Silicon carbide, being chemically very stable, happens to be attractive as a coating material for silicon emitters. However, the growth of SiC on a nanometer scale Si emitter surface is especially challenging because of the 20% mismatch in lattice parameter between Si and SiC [5-20]. The one step fabrication technology, under consideration here, eliminates the need for any further encapsulation of the Si emitters. Figure 5-3 shows a typical field emission result for SiC capped nanotips on a p-type Si substrate. A high current density of 3.0 mA/cm^2 at an applied field as low as ~1.0 V/mm has been achieved. The samples were transferred in air from the ECR processing chamber to the field emission chamber without additional treatment. The field emission chamber is evacuated by a turbo molecular pump to 5×10^{-7} Torr for the measurement. In the measurement the emission current was limited under 3.0 mA/cm^2 as shown in the figure to avoid damaging the emitter tips. The Fowler-Nordheim (F-N) plot depicted in the inset of figure 3 deviates from linear relationship for an ideal field emitter at high electric field. This phenomenon can be attributed to the non-uniformity of the emitter length with fewer discrete long nanotips while the majority of them are shorter ones as shown in figure 5-1. The discrete long nanotips are subjected to less electrical screening effect than the majority shorter ones. Therefore, a smaller slope of the F-N fit at low electric

field since the emission was mainly contributed from the long nanotips and a larger slope was observed at high electric field as emission was dominated by the large number of the short nanotips. The turn-on field for the nanotips, defined as the electric field required extracting a current density of 10 mA/cm^2 from the tip, is found to be ~0.35 V/mm, which is much lower than other reported materials. The low turn-on field in the reported nanotip arrays can be attributed to the extreme sharpness (therefore, large field enhancement factor) of the nanotips as well as negative electron affinity effect from wide band gap materials [5-21] such as the aforementioned SiC cap. It should be noticed that a p-type substrate produced much higher field emission current than an n-type one, which will be reported separately. Silicon based nanotip field emitters operational at ultralow electric fields opens up several possibilities for versatile field emission applications. Field emission displays based entirely on silicon technology, in particular, can thus be realized to produce the next generation displays. Further experiment to fabricate diode- and triode-type emitter is underway to achieve the goal.

Lowering of the operational voltage has multiple effects on the performance of the emitter arrays. The low voltage operation reduces the emitter driving input power and thereby maximizes the power gain and the emission efficiency of the device. In addition, low-voltage operation improves the transconductance of the emitter arrays for any given operating current. The total transconductance of the emitter array again increases effectively with the emitter packing density. Moreover, both smaller tip diameter and larger aspect ratios are advantageous in improving the field enhancement factor at the tip and thereby increasing the transconductance. The lowest possible inter electrode capacitance and the highest possible transconductance maximizes the cutoff frequency at which a field emission electrode could be operational in a miniaturized vacuum device. On going emitter array fabrication

technology can successfully extend the limits with respect to emitter tip packing density, sharpness of the nanotips and a low voltage operation (at an ultralow electric field of ~1.0 V/μm).

Field Emission behavior of GaPNTs

Figures 5-4a and 5-4b show typical HRSEM cross sectional and 25° tilted images of GaP nanotips, respectively. The SEM image (figure 5-4a) indicates that the nanotips fabricated by ECR-CVD are 2 and 80 nm in diameter at the apex and bottom of the nanotips, respectively. They are 900 nm in height, which gives an aspect ratio approaching 11.25. The 25° tilted plane view SEM image, as shown in figure 5-4b, exhibits a uniform distribution with a high density of 2 x 10^{11} /cm^2 of the GaP nanotip array. Compared to porous n-GaAs fabricated using the anodic wet etching method [5-22], the well-aligned high aspect ratio GaP nanotip array is a good candidate for field electron emission applications. The HRTEM image, as shown in figure 5-5, clearly demonstrates the heterostructure aspects of the individual SiC capped GaP nanotip distribution. The HRTEM image shows the GaP structure with a (200) lattice spacing of 2.73 Å at the body of the nanotip array. The structure on the top of the tip with a lattice spacing of 1.82 Å is a close match to the literature report of the 2H-SiC (102) structure. The SiC nanoprotectors were formed on the GaP substrate using a combination of dissociated silane and methane gases. Subsequently, etching progresses on the GaP substrate under an argon and hydrogen plasma environment. The particular etching mechanism and the detailed structural identification of the nanotip array have been discussed in a separate article [5-23].

The field emission property was measured in a high vacuum system with a base pressure of 5 x 10^{-7} Torr. Figure 5-6a (I) shows the J-V characteristics of the GaP nanotip array with the cathode-to-anode distance of 30μm. The current density was 10 μA/cm^2 at an applied voltage of 255 V, which corresponds to an applied turn-on field of 8.5 V/μm. The F-N plot of curve I was shown in figure 5-6b (I), depicting the linear behavior typical of field emission action. Subsequent to the above measurement of 30μm cathode-to-anode distance, we changed the cathode-to-anode distance to

80μm to compare the field emission characteristics with the 30μm one. The results of a field emission measurement in the 80μm cathode-to-anode distance configuration are shown in figure 5-6a (II). The applied turn-on voltage required to extract a current density of 10μA/cm^2 was 8.875 V/μm, which is close to that measured with a 30μm cathode-to-anode gap. Such differences in turn-on voltage using various cathode-to-anode distances were also observed in other types of cold cathode emitters, such as CNTs [5-24], nanowires [5-25], and carbon nitride (C_xN_y) film [5-26]. As shown in figure 5-6b (II), although the anode-cathode spacing was increased, the representative F-N measurement also possessed linear activities for a typical field emission behavior. The reproducibility of the J-V characteristic and the nature of the F-N plot were repeatedly confirmed. Hence, GaP is established as a potential field emitter in the same queue as those of carbon nanotubes and other 1D nanostructures.

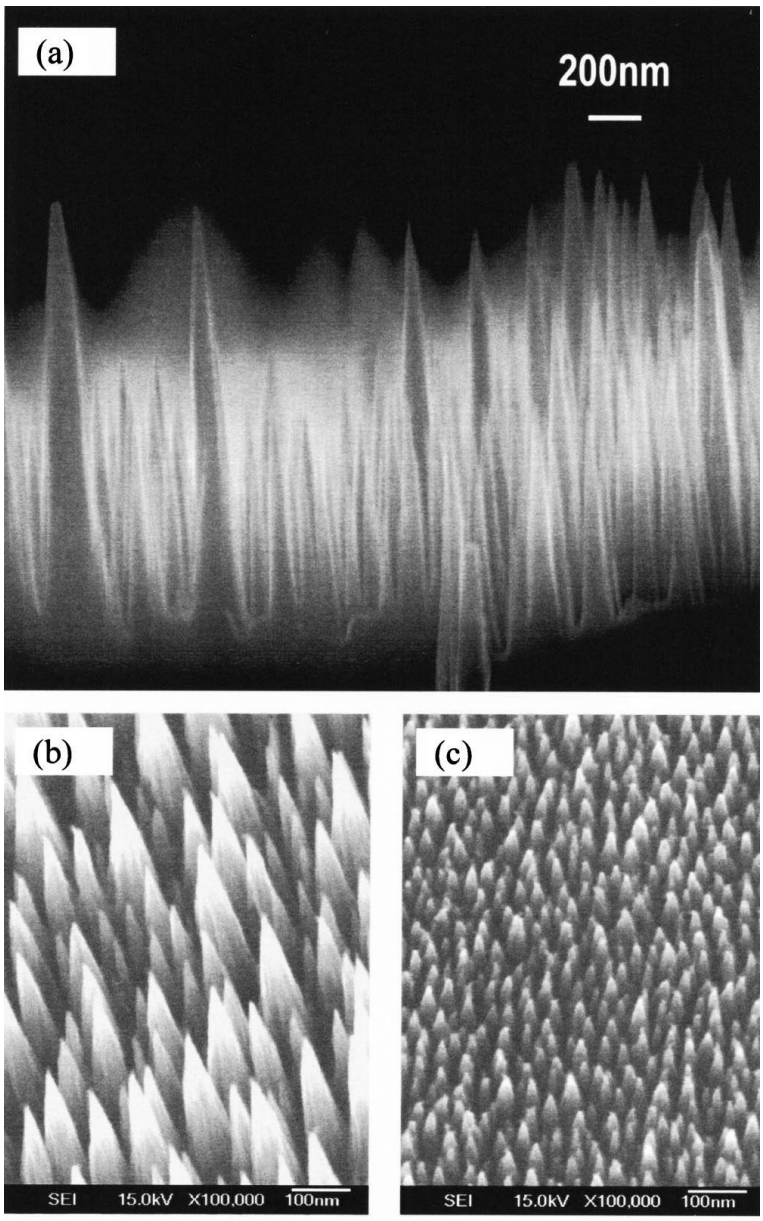

Figure 5-1. Typical SEM micrograph of the silicon nanotips. (a) The cross-section view of nanotips of 1μm height with an aspect ratio of 1000. (b) and (c) show the tilted top views of nanotips demonstrating the high density nature of the arrays of 3 x 10^{10} and 1 x 10^{11} cm^{-2}, respectively.

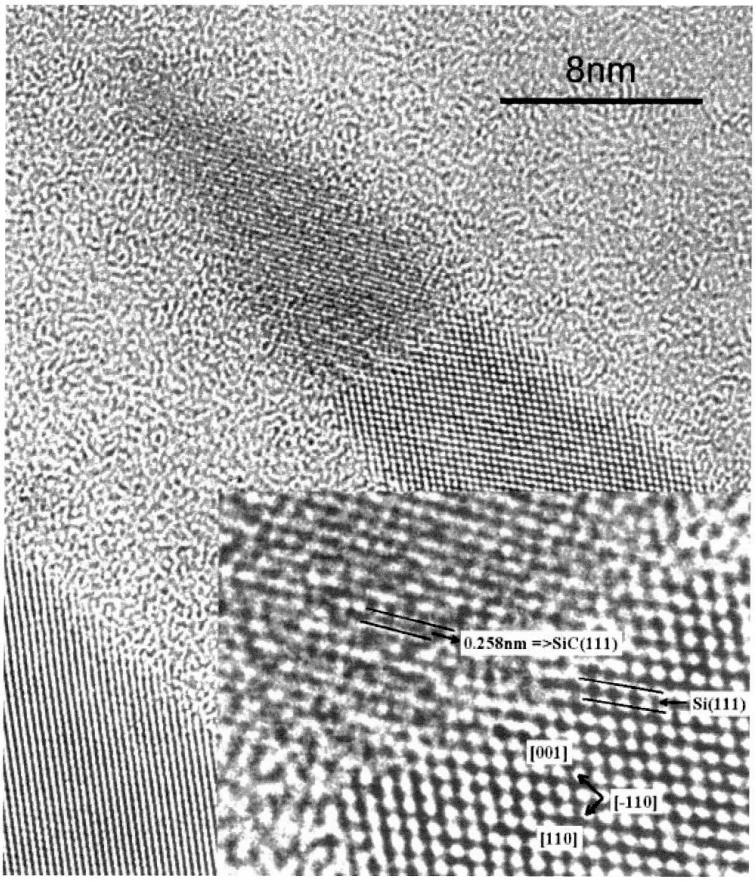

Figure 5-2. The cross-section TEM micrograph of a SiC-capped Si nanotip. The inset is a magnified lattice image at the interface between the Si and SiC, which confirms the lattice spacing of the aforementioned materials.

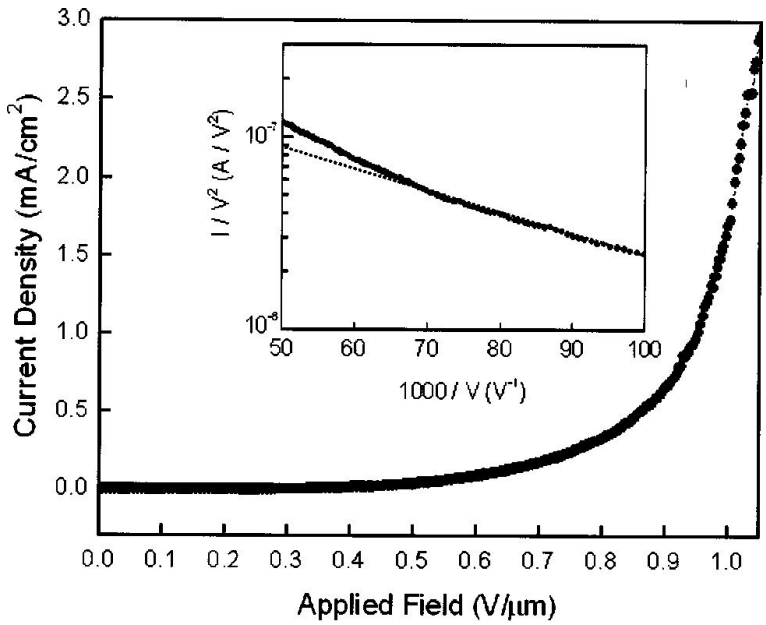

Figure 5-3. A typical field emission data obtained from silicon nanotips fabricated monolithically by the ECR dry etching of Si(100) substrate, demonstrating the ultralow turn-on electric fields. The inset presents the emission current data plotted in the Fowler-Nordheim coordinates, wherein the dashed line represents a linear relationship for an ideal field emitter.

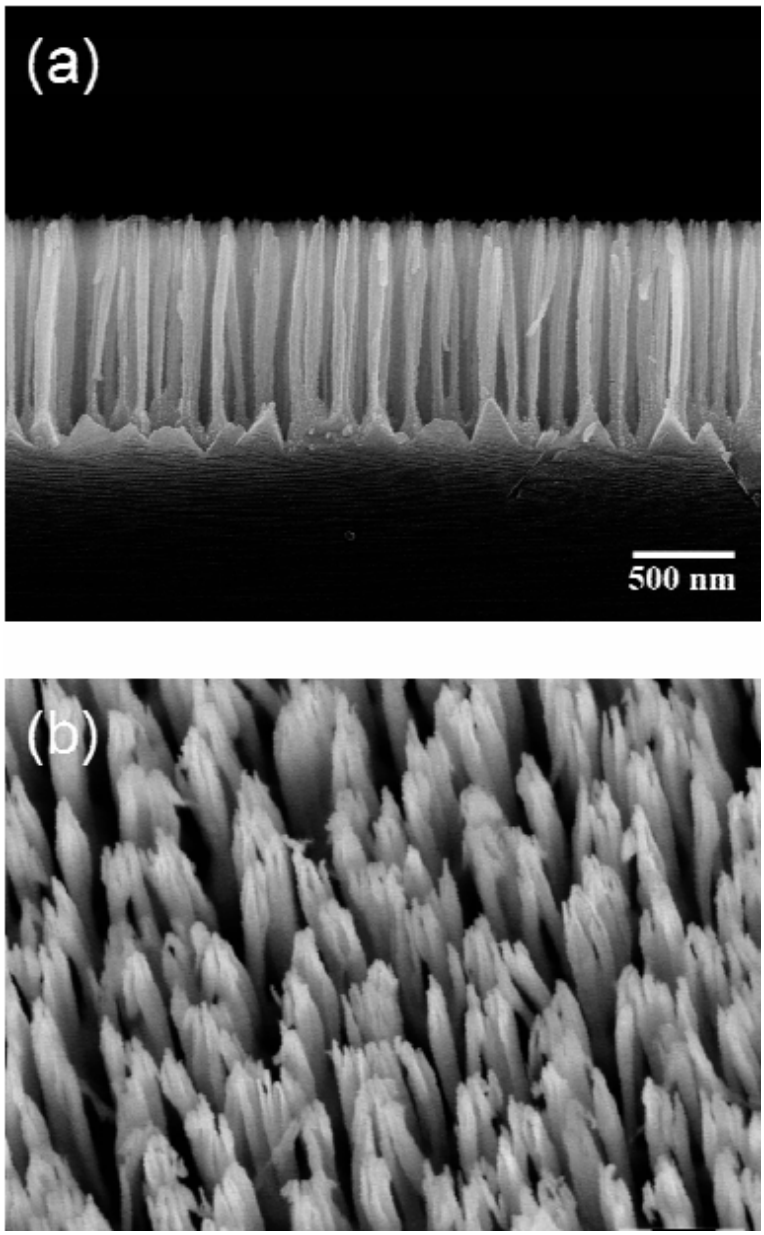

Figure 5-4. High resolution scanning electron microscopy image of (a) the cross-sectional view of the GaP nanotip array and (b) from the 25° tilted image of ultrasharp GaP nanotip array.

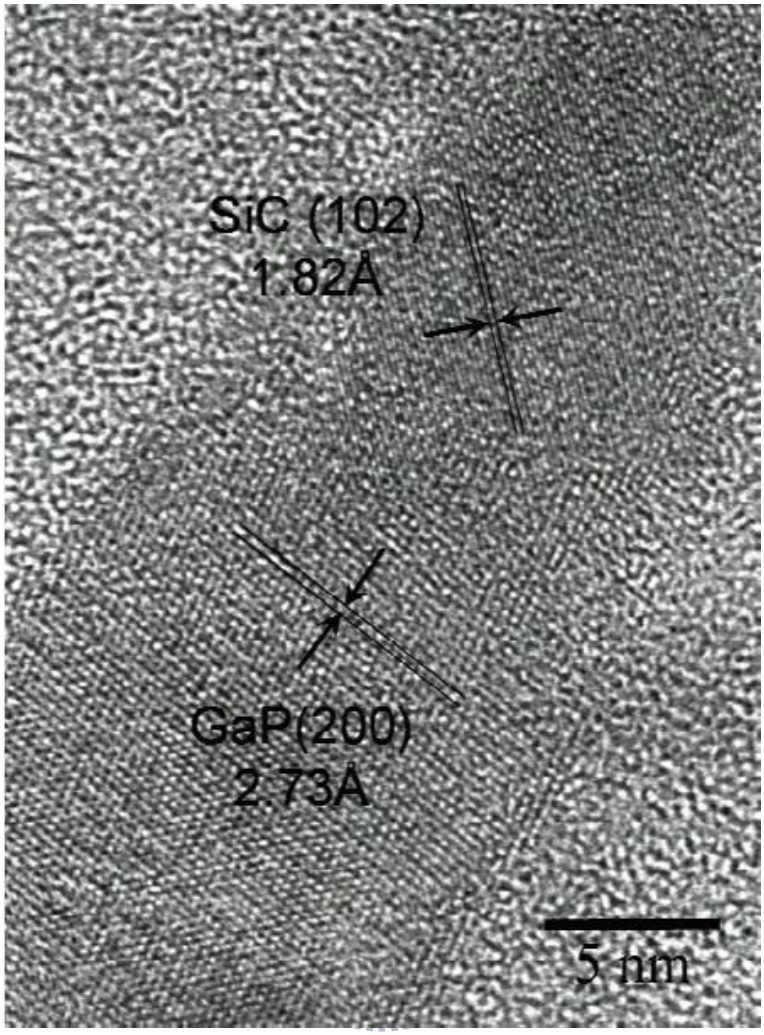

Figure 5-5. High resolution transmission electron microcopy image of a single GaP nanotip capped with a SiC core formation on top of the tip.

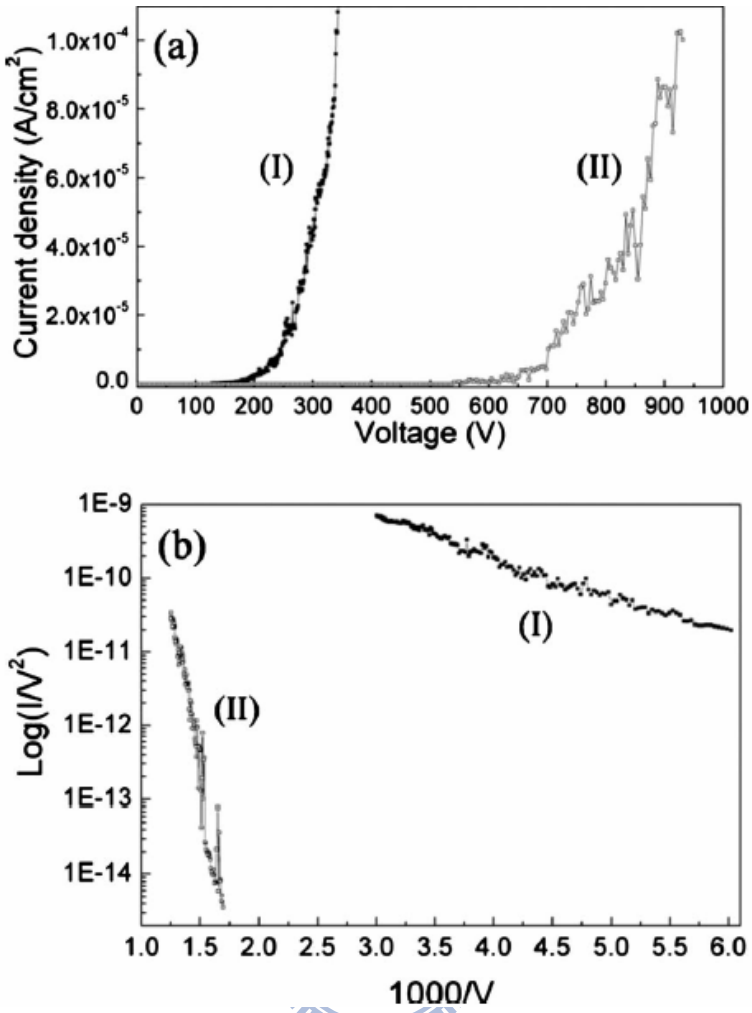

Figure 5-6. Field emission characteristics of the GaP nanotip array. (a) The J-V characteristics of the nanotip array with (I) 30μm and (II) 80μm of cathode-to-anode distance. (b) The corresponding Fowler-Nordheim plot from (I) and (II).

Chapter 6. Cell Culture

6-1 Neuronal Viability and Proliferation on Nano-Textured Silicon Surfaces

6-1-1 INTRODUCTION:

Progress in bionanotechnology has shown great promise in promoting the quality of human life. The combination of materials science and biology has been explored in many critical research areas such as gene delivery [6-1], viability improvement of mammalian stem cells [6-2], guided cell growth [6-3], designing of biochips for stimulation and signal collection [6-4], powerful bio-molecular detection [6-5], and high resolution DNA sensors [6-6]. In theory, three-dimensionally dispersed nanostructures could provide larger surface area, enabling enhanced biological signal collection. For the application of neural prosthesis, nanostructured silicon (Si) wafers have successfully exhibited biocompatibility with central neural cells (substantia nigra) [6-7] and primary hepatocytes [6-8]. Recently, one dimensional structures like Si nanowires have also been used to improve the viability mammalian stem cells [6-2]. Other novel materials like carbon-based nanotubes and nanofibers have been demonstrated to support fibroblast growth and the outgrowth of neuronal processes, and were explored as scaffoldings for neuronal circuits and drug delivery devices [6-9~6-11]. However, compared to the conventional elemental Si template based biotechnology, it is more challenging to achieve significant development in case of nanostructures made from either Si-based compounds (including silicon oxide and silicon nitride) or other novel materials [6-10~6-13]. Additionally, these materials are limited by several technical challenges in nano-sized device-fabrication, such as the uncontrollable manipulation of nanomaterials with poor uniformity, weak interfacial

adhesion with templates, relatively low throughput, and incompatibility of nanofabrication processes with well-established silicon processing technology.

In parallel to materials-oriented research, tremendous efforts have also been made to explore the effect on cell viability and proliferation of surface properties of templates, such as hydrophilicity [6-14], roughness [6-7], and the presence of residual static stress/strain [6-15]. Earlier studies on the importance of hydrophilicity have demonstrated the positive effect of hydrophilic surfaces on cell adherence [6-16] or neuronal culture [6-14] of rat pheochromocytoma (PC12) cells. Simultaneously, surface roughness was also found to strongly influence the adherence and viability of central neural cells [6-7]. In a different approach, F. Haq et al. [6-15] established the synergistic effect of strain level and strain rate on the development and orientation of neurite-extension on micro-textured silicone templates. Surface charge and its effects on cell proliferation have also drawn considerable attention [6-17]. However, most studies were concerned about the direct effect of the surface charge of the template upon the cells. The in situ effects on the ionic distribution of culture-medium, during the course of cell culture, have not been reported to date, but the positive influence of the distribution of ions, like potassium (K^+) or calcium (Ca^+), on cell proliferation have been well established [6-18~6-20]. These various studies show that a clear understanding of the cell-template interaction is necessary for the successful application of materials in template-based biotechnology.

In this study, standard Si-based processing technology was chosen as a model platform to generate templates for a detailed study of the influence of template surface structure and electrical properties on the viability of a directed cell culture. Semiconductor-compatible, well-controlled, one-step processes like self-masked dry etching (SMDE) [6-21] and ion beam sputtering deposition (IBSD) [6-22] were employed to manipulate and control the mechanical and electrical properties of the

surface of two series of biocompatible Si templates that were selected as model systems commercially available, planar Si wafers and silicon nanotip arrays (SiNT) fabricated on the same wafer [6-23]. PC12 cell lines were chosen as a primary model of a neuronal cell culture system because they are important in the study of *in-vitro* actions of Nerve Growth Factor (NGF), a natural complex [6-24]. Building on previous research from our group, SMDE was used to fabricate SiNT templates. The contrast in the cell density and soma of PC12 on SiNT versus planar templates was characterized with HR-SEM. IBSD was used to modify the template surfaces via the controlled deposition of gold (Au). Effect of Au deposition (thickness) on the template properties, such as surface roughness, hydrophilicity, and surface charge, were characterized with AFM, contact angle goniometry, and a streaming potential measurement of the zeta potential, respectively. Here the study was mainly focused on the detail investigation on the contribution of three abovementioned surface properties on cell viability and proliferation which can definitely explore the insight of cell-attachment behavior.

6-1-2 MATERIALS AND METHODS:

Materials. Two sets of templates were used in this study: planar Si wafers and nanofabricated SiNTs, both with and without Au coating. The Si wafers were purchased from SDIC, USA and were 100 mm in diameter, 500±25 μm in thickness, single-side CMP (chemical mechanical planarization) polished, (100)-oriented and test grade quality Si. After ultrasonic cleaning in methanol and acetone for 10 min, hydrofluoride acid was used to remove the native oxide on the Si surface prior to further surface-modification. SiNTs were fabricated by the SMDE technique using an electron cyclotron resonance microwave plasma enhanced chemical vapor deposition (ECR-MWPECVD) method, as described previously [6-21~6-23]. The feed gases (silane and methane) were activated by microwave power from a 1500W AsTeX AX2115 microwave source and a single AX4400 electromagnet at a microwave power of 1200W. The SMDE process occurred with a template temperature of 200°C at 3.2 mTorr pressure.

Gold nanoparticles (AuNPs) were deposited on both planar Si and SiNTs templates by the IBSD method, employing a 3-cm Kaufman-type ion source that created Ar^{+} ions from a 3 sccm flow of Ar, which impinged on the Au target at a 45° angle of incidence. The process was run at ambient temperature and ~3×10^{-4} mTorr pressure, with the Au sputtering time used as the control parameter.

Cell Culture. Cultures of PC12 cells, with an initial concentration of 2×10^{5} cells/mL, were freshly prepared with a culture medium that consisted of 85% Dulbecco's Modified Eagle Medium (GIBCO, Cat. No. 12100-046), 10% horse serum (GIBCO, Cat. No. 26050-088) and 5% fetal bovine serum (GIBCO, Cat. No. 15240-062). To ensure the adherence of the PC12 cells on the nano-textured templates, maximum 7 days *in-vitro* (DIV) plating was applied.

Characterizations. The initial cell density data has been estimated by using fluorescence microscopy. However, later SEM was used exclusively as a characterization tool for microscopic observation of cell adhered on Si-based templates, Since the Si is optically opaque in nature. It is highly possible that the sample preparation of cells for SEM-observation can lead to various kinds of artifacts, hence our initial efforts have been dedicated for the optimization of proper sample preparation procedure (data not shown here), which is described as follows. First, the templates with adhered cells were washed with phosphate buffer saline (PBS) solution and then treated with 2% glutaraldehyde in PBS for 60 min at $4^{o}C$, under visible light in an isolated environment. After thorough washing with PBS and deionized water the samples were dehydrated by rinsing several times with graded ethanol solutions that had increasing ethanol concentrations. Finally, the samples were subjected to 100% ethanol, and subsequently dried with a critical point dryer (Tousimis PVT-3B, Japan).

A JEOL JSM-6700F field emission HR-SEM and an Asylum MFP-3D-BIO AFM were used for topographical observation of cells and templates. Prior to HRSEM observation, the samples were subjected to Pt coating (for 60 s). Repeated HRSEM images (with 500x magnification) were taken from at least 6 randomly chosen regions to quantify the average and error in estimation of the cell number density. The AFM was operated in tapping mode to determine the surface roughness of the templates, with an average taken from measurements of at least 5 different locations. The contact angle of the templates was averaged from goniometric measurements of 3 randomly selected locations, using a Kyowa (model CA-D) goniometer.

The streaming potential measurement technique, with an Anton Parr BI-EKA detector, was used to determine the zeta potential (ζ), the electrical potential existing at the shear plane of a material when in contact with a solution, of the templates. Pressure, ranging from 0 to 200 mbar as measured by a strain-gauge type transducer,

was applied to one end of the template to control the fluid-flow. A Pt electrode was used to determine the charge generated across the template. ζ was calculated according to method of Smoluchowski [6-25]:

$$\Delta U/\Delta p = (\varepsilon_r \bullet \varepsilon_0 \bullet \zeta) / (\eta \bullet \kappa),$$

where ΔU is the variation in the streaming potential, Δp is the pressure difference across the fiber plug, ε_0 is the vacuum permittivity, and ε_r, η and κ represent the permittivity, viscosity, and conductivity of the electrolyte, respectively. To deduct the potential effect from the tunnel, which is made with poly (methyl methacrylate) (PMMA), the value of ζ was corrected as follows:

$$\zeta_{real} = 2\zeta_{measured} - \zeta_{PMMA}$$

To avoid the strong pH-dependence of ζ, $\zeta_{measured}$ was determined in 1 mM KCl solution at pH of 7.0±0.2, a typical pH value for culture medium.

6-1-3 RESULTS:

Nanotip Fabrication and Coating. SiNTs were formed on a set of silicon wafers to investigate the effect of surface roughness and nanostructures on neuronal cell viability. The fabrication of the SiNTs by ECR-MWPECVD proceeded as previously described in the literature [6-21~6-23] resulting in a dense array of Si nanopillars, as shown in the HR-SEM images in figure 6-1a. The as-grown SiNTs had a very sharp tip that formed a ~10° angle, with an apex having a radius of ~1 nm. The nanopillars were ~1 μm in height. From low-magnification SEM observation, the typically number density of nanotips was found to be as high as 10^{11} cm^{-2}, as reported earlier [6-23].

Both the flat silicon wafer and the SiNTs were coated with Au to study the effect of surface chemistry, charge, and energy on the viability of the neuronal cells. The results of the Au coating on the SiNTs can be seen in the HR-SEM images in figures 6-1b-e. After 5 min of Au deposition, AuNPs roughly 3-8 nm in size were uniformly formed on the SiNTs. After a total deposition time of 10 min, the density and size of the AuNPs on the SiNTs increased to 8-14 nm, and the AuNPs appeared to completely coat the SiNTs (figure 6-1c). After 20 min total deposition time, the Au nanoclusters began to agglomerate (figure 6-1d), and after a total deposition time of 40 min, the surface of the Si nanopillars was completely covered. At that point, the Au had coalesced to the point that nanoclusters were no longer present.

In contrast to the Au coating on the SiNTs, Au coating on planar Si surfaces always led to a smooth, uniform coverage of Au, even for 5 min of Au deposition (see Supporting Information, figure 6-2a). Au deposition for t = 5, 10, 20 and 40 min resulted in the formation of Au films with thicknesses of 6, 12, 29, and 40 nm, respectively (see complete series in Supporting Information, figure 6-2). Further

evidence of the lack of nanostructure in the Au coating on the planar Si wafers was provided by AFM studies, which showed no significant increase in the average surface roughness (R_{rms}) with Au deposition (see complete series in Supporting Information, figure 6-3). The R_{rms} of the Au-coated Si wafer was 1.0±0.15, 0.24±0.10, 0.66±0.09 and 0.45±0.08 nm for coating times of 5, 10, 20 and 40 min, respectively. These R_{rms} values were effectively equivalent to that of the bare Si wafer (R_{rms} = 0.32±0.06 nm).

Surface Characterizations. Prior to assessing the affect of the planar and nanostructured surfaces on neuronal cell viability, their contact angle and ζ values were determined. The contact angle of water on the template provided an assessment of the surface energy of the template. As shown in figure 6-4, the contact angle reaches a plateau value at 10 min of Au coating. The plateau value that was reached was consistent with previous Au contact angle values reported in the literature [6-30]. In contrast, the contact angle on SiNTs increased with coating time up to 20 min, and achieved a higher contact angle than was observed on the Au-coated planar templates. Additional Au coating of the SiNT templates led to a decrease in the contact angle below the plateau value of the Au-coated silicon wafer.

To further characterize the surface properties of the templates, we analyzed ζ, which provides a measure of the surface charge of the solid in a given solution. For the planar templates, the initial 5 min of Au coating caused ζ of the template to jump from -18 to -11 mV, as shown in Figure 3b. Additional Au coating led to an asymptotic decrease of ζ, reaching a steady value of -16 mV after 20 min of coating. The change of ζ for the SiNTs as a function of Au coating time qualitatively mirrored that of the planar template, but the ζ values of the SiNTs were consistently more negative than the ζ values of the corresponding planar Si wafer (figure 6-5).

Neuronal Cells on Surfaces. After characterization of the surface properties of the series of planar and nanotip templates, portions of the same batch of PC12 were simultaneously and independently incubated on each template to develop the cell cultures. Several distinguishable features were observed between the two series of templates under HR-SEM inspection. On the planar template, the PC12 cells were flat and firmly attached, possessed a smooth membrane, and had roughly 2-5 extended neurites per neuron (figure 6-6b). In contrast, the PC12 cells were balled up, appeared to be only weakly adhered to the SiNT template, and had no neurites (figure 6-6a). The HR-SEM images also revealed on the SiNT templates the growth of lamella-like structures between the secretion and the neighboring nanotips (inset, figure 6-6a).

In addition to characterizing the structure of the PC12 cells, we also used the HR-SEM images to determine the cell number density (N_n) on each template as a function of Au coating time (t), as shown in Figure 3. Comparison of the graphs shows that the planar templates (figure 6-5b) had Nn values that were 3 orders of magnitude greater than the SiNT templates (figure 6-5a). The maximum N_n values of for the Au-coated planar and SiNT templates were ~230 kcells/cm^2 and ~250 cells/cm^2, respectively. These N_n values can be compared to the initial N_n of the PC12 solution (~200 kcells/cm^2) to show the relative viability of the cells on the different templates, as well as the proliferation of the PC12 cells on the planar templates. Besides the difference in magnitude of N_n for the planar and SiNT templates, the other important observation was that both sets of templates showed a nonlinear trend in cell number density (N_n) as a function of Au coating time (t). Initially, Au-coating led to a sharp increase of N_n, which reached a maximum value after 5 or 10 min of Au coating for the planar or SiNT templates, respectively. Longer t led to a decline in the N_n value, although N_n on the Au coated templates was not as small as N_n for uncoated templates, regardless of the coating time used in this study.

The knowledge of the optimal t to achieve large values of N_n was used to make a direct comparison of PC12 viability on planar versus SiNT templates. A set of patterned templates that had both planar and SiNT regions was Au coated for 5 min and then used for PC12 cell cultures. A series of cultures were treated for 1, 3, and 7 DIV, and then incubated with NGF for 7 days. The contrast of the cell cultures on planar versus on SiNT templates after 3 DIV with and subsequent incubation can be seen in figure 6-7a.

The planar section of the template possessed a relatively large number of neurons with dense and long neurite outgrowth (>150 μm), whereas almost no PC12 cells could be observed on the SiNT section of the template. The few cells that could be found on the SiNT section of the template were close to the Si/SiNT border, and had a circular shape without any neurite extension, similar to figure 6-6a. The Si:SiNT ratios of the cell counts as a function of culture plating time are presented in the graph in figure 6-7b. The ratio of cell counts increased from 1 after the first 18 hours of culture to 10 or 1000 for 3 or 7 DIV cultures, respectively, while it was nearly 1 after first 18 hours culture.

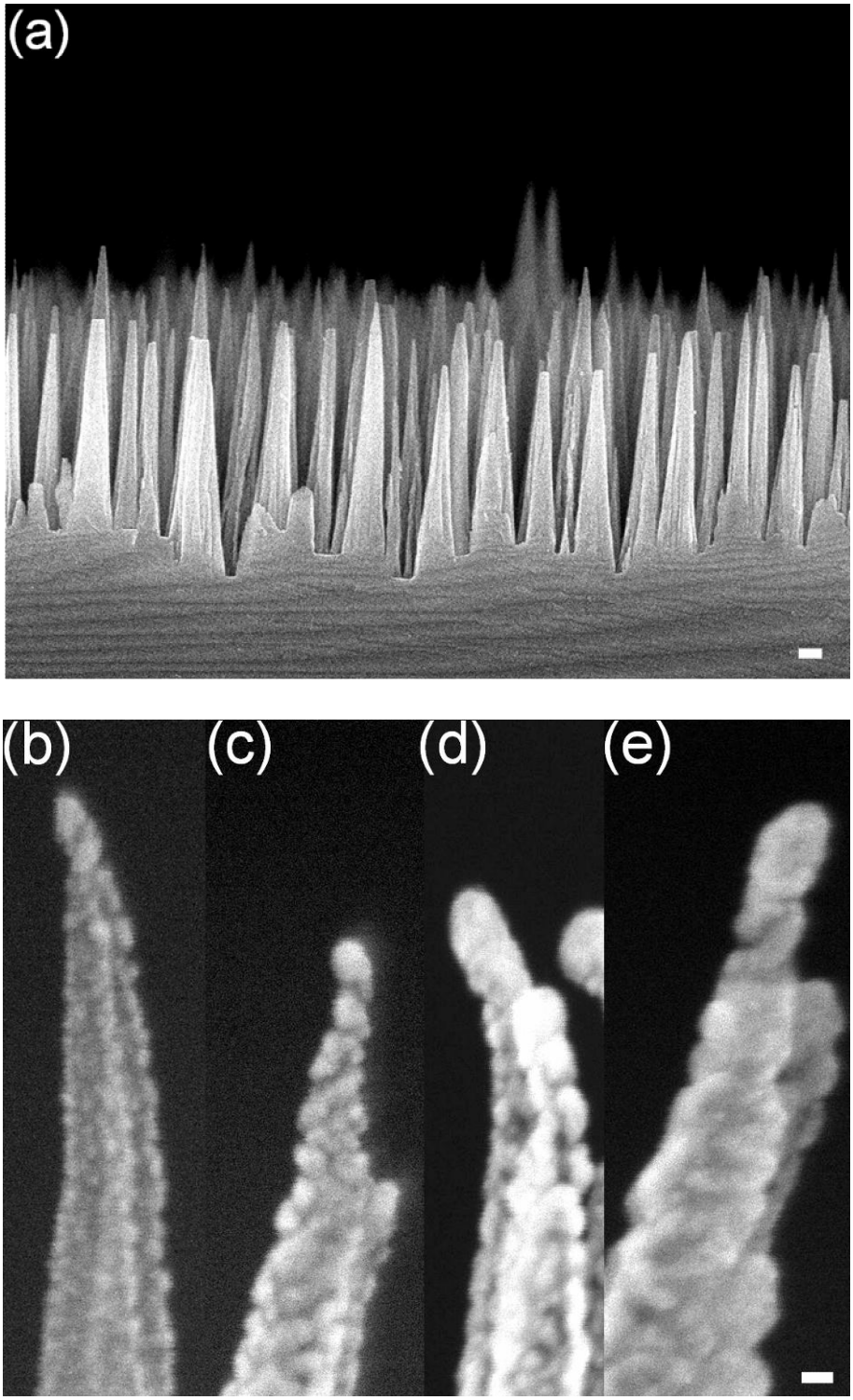

Figure 6-1. Cross-section view of HR-SEM images of SiNTs with Au coating for different sputtering times: (a) as-grown, (b) 5 min, (c) 10 min, (d) 20 min and (e) 40 min. (scale bar: a. 100nm; b~e. 10nm)

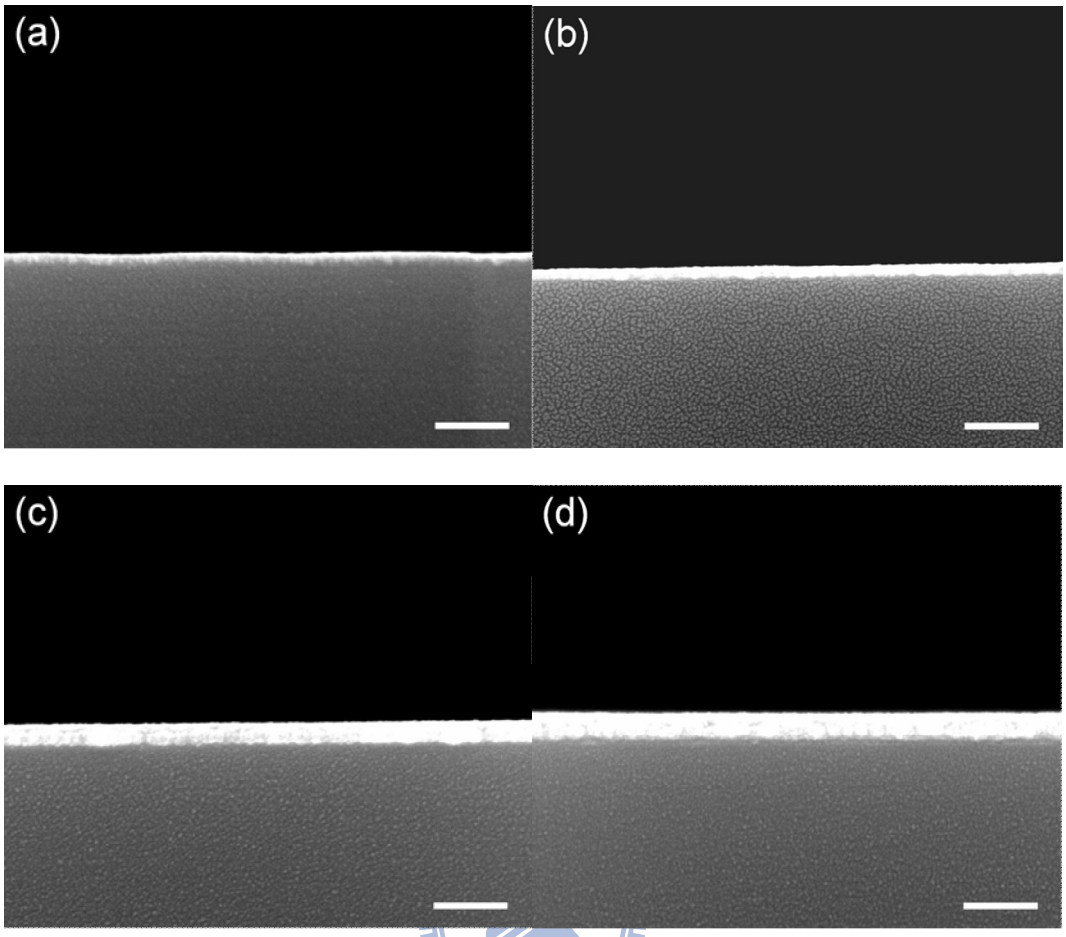

Figure 6-2. Cross section HRSEM images of planar Si templates with Au coating for different sputtering times: (a) 5min, (b) 10min, (c) 20min and (d) 40min. (scale bar: 50 nm)

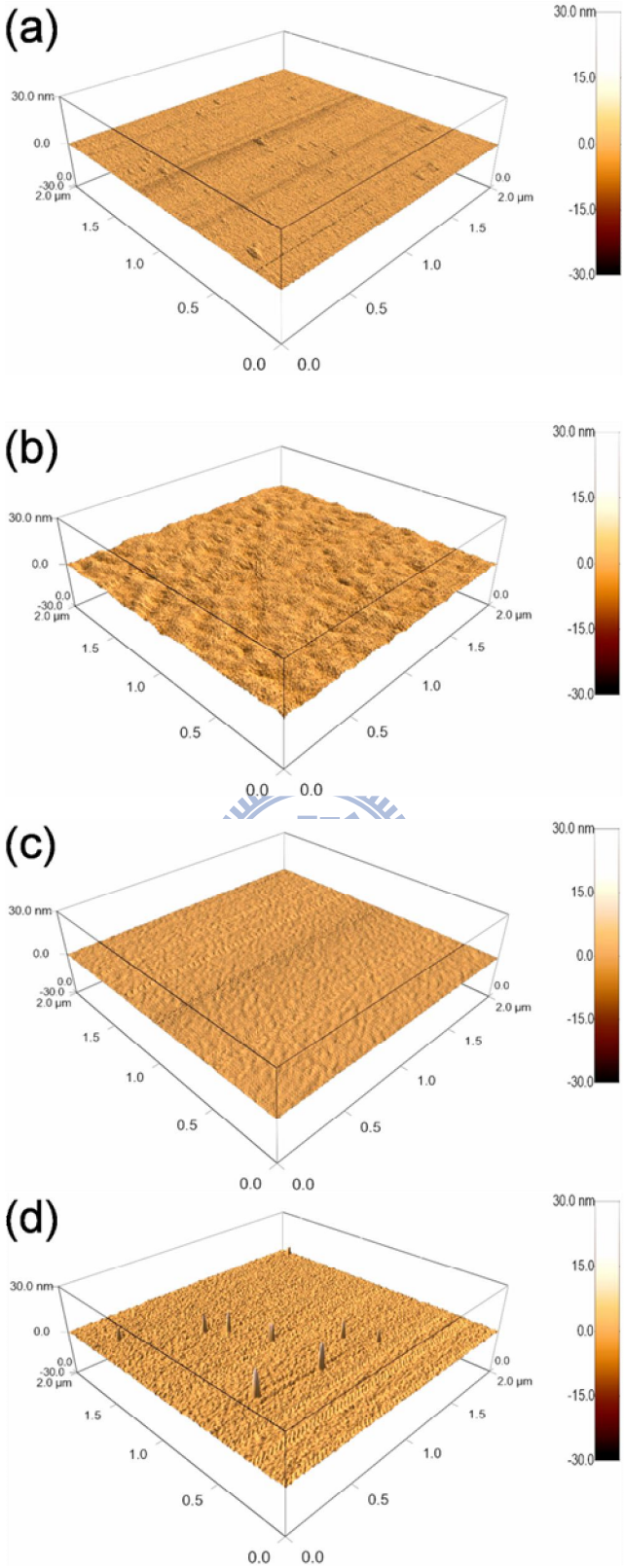

Figure 6-3. 3-dimensional topographical images, from tapping-mode AFM studies, of planar Si templates with Au-coating for different sputtering times: (a) 5min, (b) 10min, (c) 20min and (d) 40min.

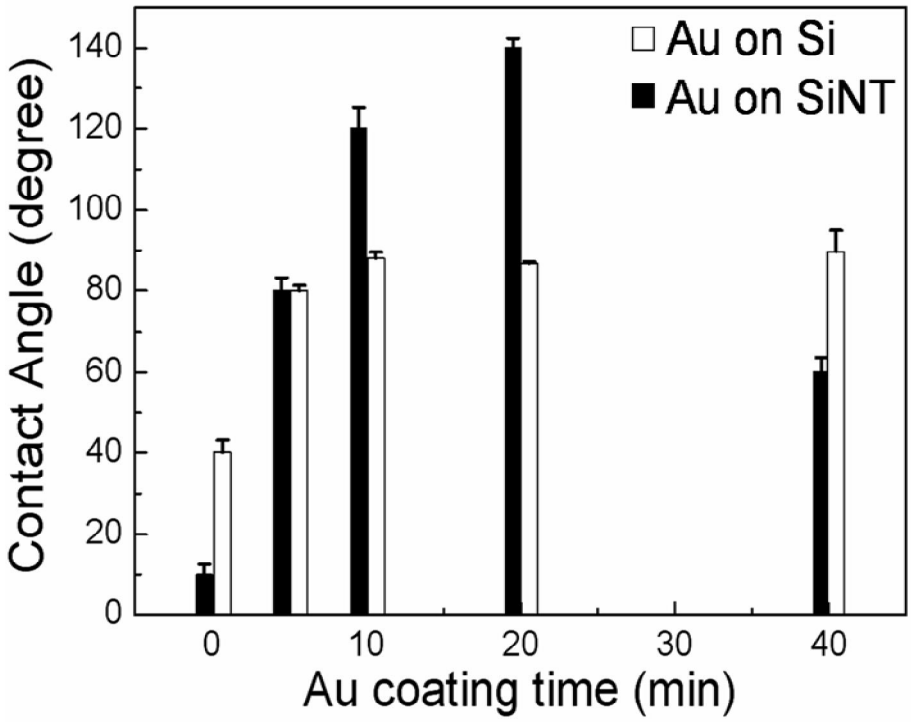

Figure 6-4. Dependence of the water contact angles of SiNTs and planar Si surfaces on Au coating time.

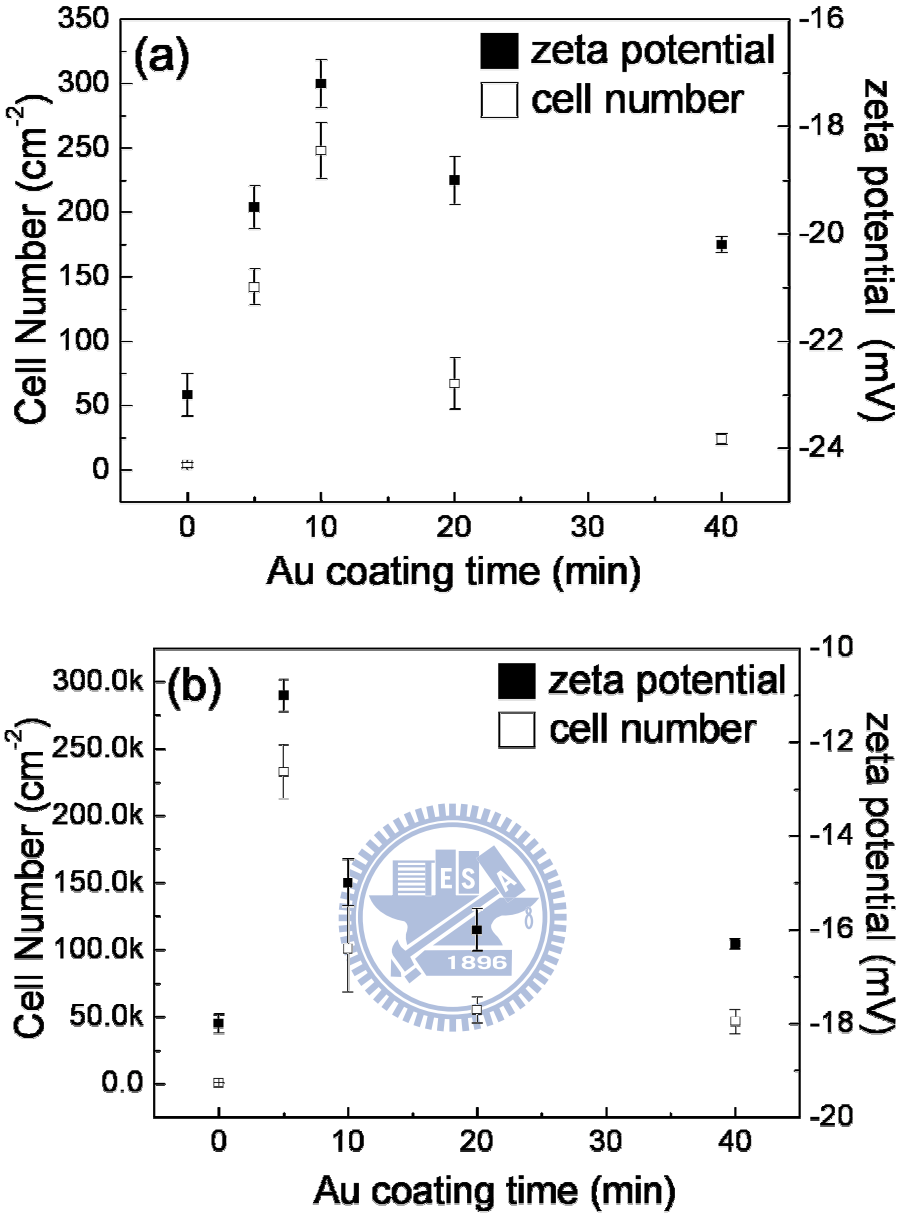

Figure 6-5. Variation of ζ with Au coating time. (a) SiNTs and (b) planar Si surfaces. Corresponding PC12 cell number density is also shown for better visualization of its resemblance with ζ.

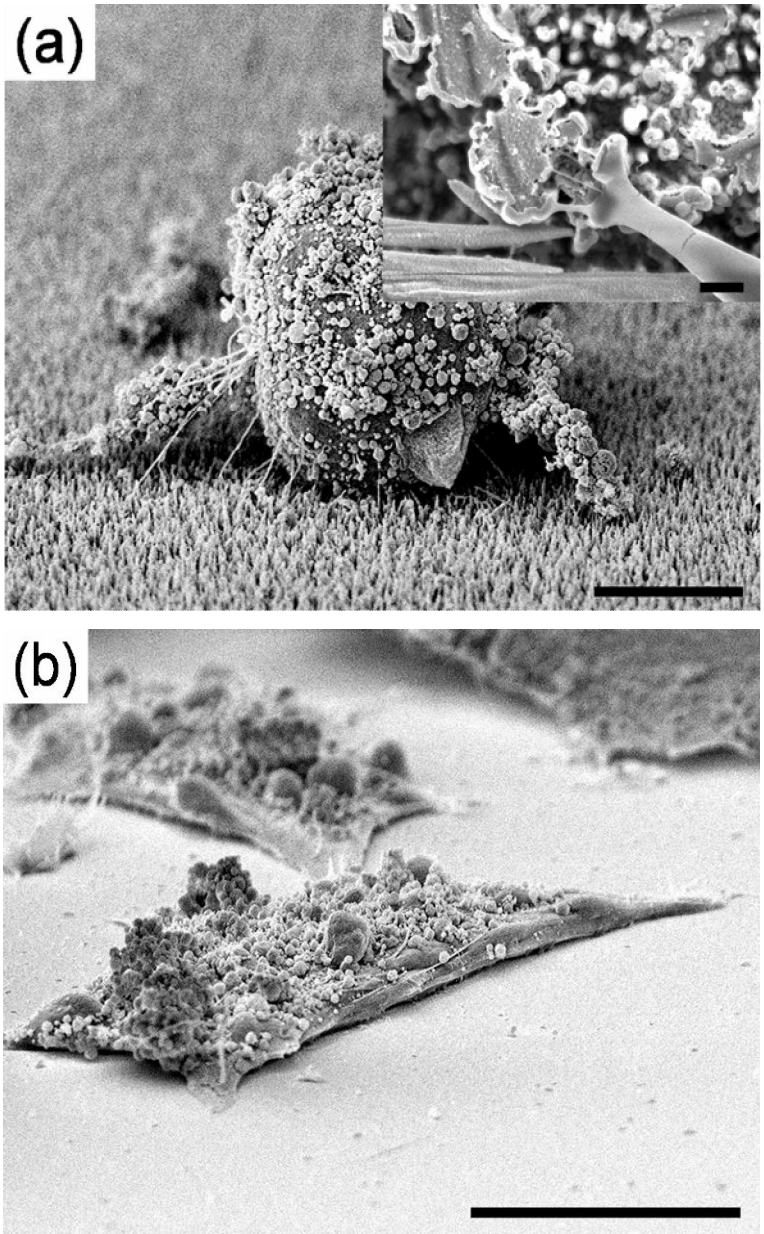

Figure 6-6. SEM images of PC12 neuron cells grown for 7 DIV, followed by 7 days of NGF incubation, on the (a) 5min Au coated SiNTs and (b) 5min Au coated planar Si wafer. (scale bar: 10μm). The inset of (a) shows the lamella-like structures that were secreted during cell culture to strengthen the adhesion of the cell-structure interface. (scale bar of insets: 200nm).

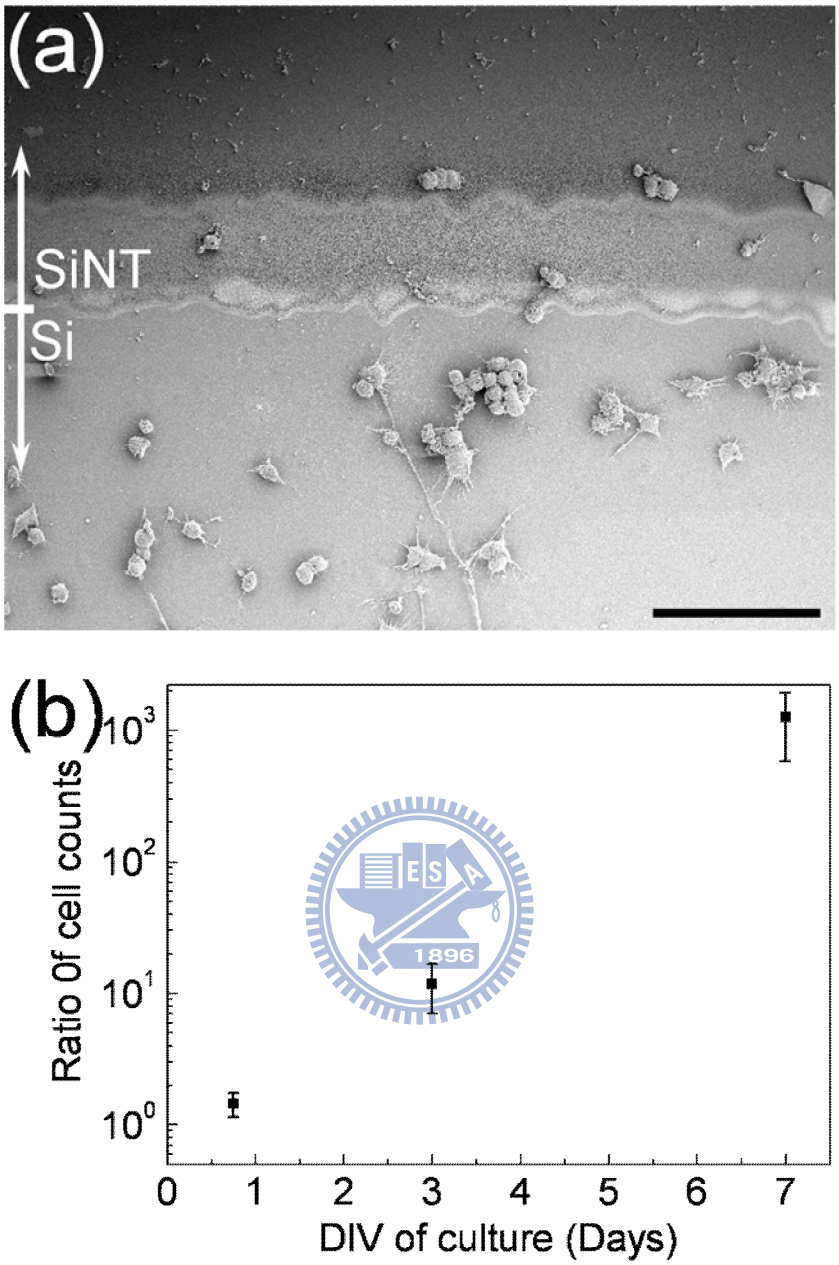

Figure 6-7. (a) SEM image of PC12 neuron cells after 3 DIV culture, followed by 7 days NGF incubation, on a patterned template having both SiNTs and planar Si. (scale bar: 100μm) (b) The time dependence cell viability ratio of cell counts on Si vs. SiNT in various DIV of culture.

6-1-4 DISCUSSION:

The results shown in figures 6-5 and 6-7 point to two primary factors that affected cell viability and proliferation. The primary factor affecting cell viability was the structure of the surface: SiNT vs. planar. The planar template exhibited profound neurite outgrowth and had N_n values that were 1000-fold greater than on the SiNT templates. In terms of proliferation of PC12, given this dramatic difference in N_n, it is only appropriate to discuss PC12 proliferation with respect to the planar templates. Additionally, the cells on the planar template exhibited significant neurite outgrowth. The effect of the Au coating was also significant, but the strength of this effect varied with coating time. We characterized the zeta potential and wetting behavior of the templates in an attempt to understand the physical processes underlying the effect of the SiNTs and the Au coating.

Effect of Surface Structures. Previous research has shown that moderate surface roughness (on the optimal scale of $20 < R_{rms} < 50$ nm) can have a significant effect on neuronal adhesion and its subsequent viability on a template [6-7]. In the work here, the typical notion of surface roughness could not be applied when comparing the vastly different surface structures of SiNTs and the planar wafers. Additionally, on the SiNTs themselves, the dimensions of the SiNTs (tip separation of ~100 nm and base separation of ~10 nm) were too small to be measured by the cantilever tip of the AFM. Instead, to compare the roughness of the SiNT and the planar templates we employed the Wenzel roughness factor (γ), which is defined as the ratio of the actual (rough) area to the geometrical (planar) area [6-26]. Considering the conical-shape of SiNTs and using dimensions determined from SEM and AFM studies, the γ values of the SiNT and planar template were estimated to be ~157 and ~2, respectively. This

quantitative difference supports the clear difference of the two templates that is observable in figure 6-1.

The impact of the different surface structures can be examined in terms of the interfacial energy between the PC12 soma and the template, as illustrated in figure 6-8. Because the soma would try to adapt a shape or profile that was complementary to the surface profile of SiNTs template, the resulting cell membrane exhibited roughness and ruffles (figure 6-6a). It can be imagined that the cells on the nanotips could not achieve sufficient contact area (figure 6-8b) as compared with the cells on planar Si (figure 6-8a), and hence could not compensate their own body weight with the interfacial force, which is proportionate to the cell-template contact area. As a result, the cell adhesion, and therefore cell viability, would drastically decrease on SiNTs templates.

The presences of lamellar structures (inset, figure 6-6a) also support the surface energy argument. These lamellar structures can be viewed as additional anchors for the cells, or as means for the cells to achieve the maximum interfacial energy by expanding the contact area (figure 6-8b). In contrast, the cells adhered on the planar Si templates were able to spread their soma much more easily (figure 6-4b) to achieve the maximum contact area (figure 6-8a), and hence a greater interfacial energy.

Although the surface structure has a significant impact on cell viability when comparing the vastly different structures of planar templates and SiNTs, the effect of surface structure becomes insignificant when the roughness variation of the surface is negligible when compared to the size of the PC12 cells. The planar Si templates with or without Au-coating always exhibited smooth surfaces ($R_{rms} \leq 1$ nm). Similar to the planar templates, the Au-decorated SiNTs templates also possessed a negligible difference (below ±1 nm, as measured by SEM) in roughness compared to the uncoated SiNTs. Thus, within a given type of template (SiNT or planar Si), surface

roughness could be ignored as a controlling factor for the difference in cell viability observed with different Au-coating times.

Effect of Surface Charges. Within a given type of template, the Au coating time t had the same general effect on both ζ and N_n, as shown in figure 6-5. The effect of t on ζ can be understood in terms of the physical structure of the as-grown and Au coated SiNTs. Initially, the presence of surface defects, created by ECR-MWPECVD plasma etching, contributed more negative surface-charges and hence resulted in a low ζ value. Additionally, it can be assumed that a higher concentration of negatively charged surface ions would be present on the SiNTs surfaces due to their high surface area/volume ratio. After a brief Au coating, positive charges on the AuNP surfaces could compensate for the negative charges originally present on the SiNT surface. As the Au coating continues, the surface of the SiNTs is eventually covered by AuNPs, and the ζ measurement would only detect the charge associated with the AuNPs. In the case of the planar template, only 5 min of Au coating was required to reach a uniform Au coating of the template. In the case of the rougher SiNT template, 10 min of Au coating was required before reaching a uniform Au coating of the template. Beyond the point of uniform Au coverage, ζ decreased with longer t for both templates. In the case of the planar template, we can assume that longer t eliminated defects in the continuity of the Au coating. In the case of the SiNT templates, the decrease in ζ matched the tendency of the AuNPs to agglomerate, as shown in figure 6-1d-e. Agglomeration would provide conducting paths, through which the active charges on Au surface, created during the Au sputtering process, could be passivated.

Because ζ can be viewed as representing the surface charge of the template, the correlation of ζ and N_n can be understood in terms of surface charge, which has been shown previously to interfere with cell adhesion [6-17]. However, at present the exact mechanism behind the relationship of surface charge and cell adhesion is not

completely understood. In this study, less negative values of ζ, corresponding to reduced negative surface charge, always correlated with high N_n. One possible explanation of this correlation is that the surface charge of the template could influence the ionic concentration in the neighboring fluid, and the negatively charged surface would trap positive ions (e.g. K^+, Ca^+ etc) from the culture-medium. These trapped positive ions could form a layer of immobile cations, which would dominate over the diffuse layer in the absence of any kinetic process, and hence reduce the cation concentration in the bulk phase of the culture. According to Gallo et al. [6-27] elevated extracellular K^+ concentrations, or other Ca elevating stimuli, promote long term survival of rat cerebellar granule neurons in dissociated cultures. The Ca influx also has lead, by indirect mechanisms, to activation of the ubiquitous mitogen-activated protein kinase pathway [6-28], which is a critical intermediate in long term cellular responses such as proliferation and differentiation [6-29]. In the work here, the surfaces with higher negative charge could trap higher concentration of cations, thus having a greater negative impact on cell proliferation. The negative effect would be acute for the SiNTs templates because they have a larger reactive area than the planar Si.

Effect of Surface Wetting Properties. The contact angle data (figure 6-4) show that both the planar and SiNT templates switched from hydrophilic to hydrophobic with Au coating. Initially, the uncoated SiNTs were more hydrophilic, as evidenced by their lower contact angle, than the planar Si, which matched our previous work with SiNTs [6-22]. The inherent hydrophobic nature of the metallic Au surface resulted in a reduction of hydrophilicity of the template, as observed for both planar Si and SiNTs. The phenomenon was more prominent in the case of the SiNT templates on which AuNPs were formed instead of a thin film. Previous research has shown that the hydrophobic nature of Au is particularly acute for nanoparticles due to

their large surface area/volume ratio [6-22]. It is typical for NPs to exhibit physical properties that are dominated by their surface area. The hydrophobicity of the SiNT template increased with t until the agglomeration of the AuNPs (figure 6-1d, t = 40 min). In the work here, when the AuNPs agglomerated, the ratio of the Au surface area to volume decreased, and consequently the hydrophobicity declined. In contrast, Au coating of the planar templates led to the formation of uniform thin films, and the contact angle of the coated, planar templates remained constant after reaching a maximum value.

While there was a significant change in contact angle with t, this change did not seem to have a direct impact on N_n. The trend in N_n matched neither the wetting behavior trend nor the affinity for cell proliferation in hydrophilic environments that has been reported in the literature [6-14]. By comparing figures 6-4 and 6-5, it can be readily observed that the most hydrophilic surfaces had the lowest values of N_n. In addition, for Au coated planar templates, N_n decreased with longer t despite any significant change in hydrophilicity. Finally, the huge difference in N_n between SiNT templates and planar templates cannot be explained on basis of their wetting properties.

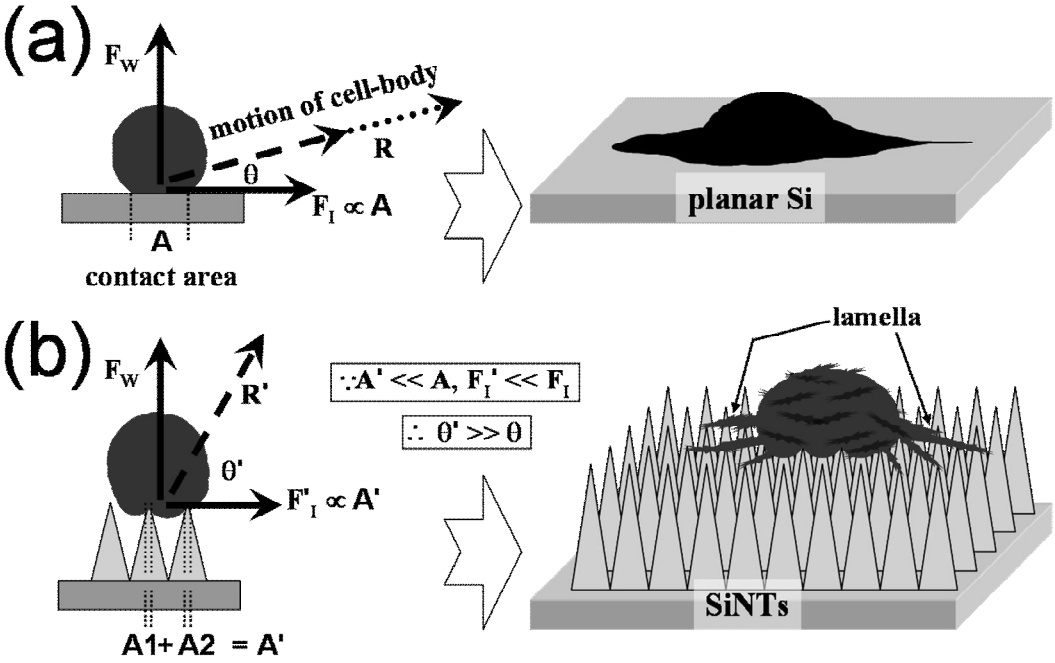

Figure 6-8. Schematic illustration of surface roughness effect on cell adhesion and soma shape: (a) cell on planar Si template, (b) cell on SiNTs. F_W: force due to weight of the cell body. F_I: interfacial force, which is proportionate to the contact area. R: resultant force, along whose direction the cell body will spread. Compared to the cells on planar Si (a), those on SiNTs (b) will suffer due to small contact area ($A' \ll A$), hence F_I' will be small ($F_I' \ll F_I$). Consequently, the angle of R, will be large, i.e. cell-body cannot spread horizontally to achieve the larger A, and as a result the cells on SiNTs will either deform or perish. The growth of lamella may improve cell adhesion (b).

6-2. Neuron viability and proliferation on 1-D nanomaterials:

6-2-1 INTRODUCTION:

The development of nanotechnology is penetrating biology and medicine at a remarkable speed [6-31]. Nanotechnology is poised to provide new tools to measure and understand bio-systems [6-32, 6-33], bring insights to challenges in biotechnology and biomedicine [6-34, 6-35], and offer building components for advanced biomaterials [6-36, 6-37]. One area that will significantly benefit from the development of nanoscale engineering is the technology for neural medicine in its many manifestations [6-38]. The reasons are descript below.

(1) Nanomaterials were originally developed and still have the most widespread applicability for electronics and information processing, which makes their functionalities quite similar to those of neural system.

(2) The neural tissue is highly complex in its anatomy, functional structuring, and information processing, which frustrates the applications of current technologies and requires the change of technological paradigm.

(3) The central nervous system is difficult to access and has heterogeneous cellular and molecular environment, which, in turn, means that size reduction of any devices to interact with neurons is required to create the least possible interference with and disruption to the central nervous system's functionality.

One-dimensional nanostructures such as III-nitride (e.g. GaN and InN), oxide and CNT were aroused more and more attention in cell culture field because of their unique properties of physical, chemical, electical and mechanical behavior [6-39~6-42]. Among these nanomaterials, CNT was attracting lot of attention because

of the strong, flexible, conduct electrical current [6-43~6-45] and can be functionalized with different molecules [6-46~6-47] properties that may be useful in basic and applied cell culture research. Furthermore, III-nitride materials were also explored for biology field because of the good chemical stability, high hardness and tunable electric properties for biocompatibility, good cavity candidate and excitation of bias enhanced cell proliferation. Due to its unique properties, III-nitride field-effect transistor devices have been developed for a variety of microelectronic and high-temperature gas sensor applications. In addition, III-nitride based materials are emerging as the important materials for the optical devices in the visible wavelengths [6-48~6-49]. These devices are essential for full-color display and pickup head in high-definition-digital-video-disk systems. Such advantages make III-nitride materials good candidate in integrating electronics and biological system to develop a microelectrode array for replacing degenerated cells in biomedical applications.

6-2-2 MATERIALS AND METHODS:

Materials. Four sets of nanomaterials were used in this study: multi-walled carbon nanotube (MWCNTs), gallium nitride (GaN) nanowire, indium nitride (InN) nanowire and silica (SiO_2) nanowire. For controlling the structural dispersion, metal particle coated Si wafer was used to grow MWCNT, InN nanowire and SiO_2 nanowire, in the mean time, the noble metal coated GaN thin film deposited sapphire was tuned to grow GaN nanowire. In entire deposition method, vapor-liquid-solid (VLS) mechanism was employed to control the structural and morphological change. MWCNT and SiO_2 nanowire were fabricated by the VLS technique using a microwave plasma enhanced chemical vapor deposition (MWPECVD) method. The feed gases (silane, methane, nitrogen and argon) were activated by microwave power from a 6000W AsTeX A-5000 microwave source at a microwave power ranging from 1000 to 3000W. The VLS process occurred with a template temperature of ~1000°C at several tens Torr pressure. For InN nanowire growth, the feed gases (TMIn and NH_3) were reacted in the home-made MOCVD system. After Au nanoparticle decorated by IBSD reactor, the gases were activated by increasing the temperature of stage to ~600°C. Furthermore, thermal CVD was employed to deposit GaN nanowire at ~950°C after Au catalyst coated by IBSD system.

Au and Fe catalyst were deposited on both Si and epi-GaN grown sapphire wafer by the IBSD method, employing a 3-cm Kaufman-type ion source that created Ar^+ ions from a 2 sccm flow of Ar, which impinged on the Au target at a 45° angle of incidence. The process was run at ambient temperature and ~2×10^{-4} mTorr pressure, with the fixed Au sputtering time in 10 minutes.

Cell Culture. Cultures of PC12 cells, with an initial concentration of 2×10^{5} cells/mL, were freshly prepared with a culture medium that consisted of 85%

Dulbecco's Modified Eagle Medium (GIBCO, Cat. No. 12100-046), 10% horse serum (GIBCO, Cat. No. 26050-088) and 5% fetal bovine serum (GIBCO, Cat. No. 15240-062). To ensure the adherence of the PC12 cells on the nano-textured templates, maximum 7 days *in-vitro* (DIV) plating was applied.

Characterizations. The initial cell density data has been estimated by using fluorescence microscopy. However, later SEM was used exclusively as a characterization tool for microscopic observation of cell adhered on Si nanostructure-based templates. Since the Si is optically opaque in nature. It is highly possible that the sample preparation of cells for SEM-observation can lead to various kinds of artifacts, hence our initial efforts have been dedicated for the optimization of proper sample preparation procedure, which is described as follows. First, the templates with adhered cells were washed with phosphate buffer saline (PBS) solution and then treated with 2% glutaraldehyde in PBS for 60 min at $4^{o}C$, under visible light in an isolated environment. After thorough washing with PBS and deionized water the samples were dehydrated by rinsing several times with graded ethanol solutions that had increasing ethanol concentrations. Finally, the samples were subjected to 100% ethanol, and subsequently dried with a critical point dryer (Tousimis PVT-3B, Japan).

A JEOL JSM-6700F field emission HR-SEM was used for topographical observation of cells and templates. Prior to HRSEM observation, the samples were subjected to Pt coating (for 60 s). Repeated HRSEM images (with 500x magnification) were taken from at least 6 randomly chosen regions to quantify the average and error in estimation of the cell number density.

6-2-3 RESULT AND DISCUSSION:

In this section, the 1-dimensional nanostructures such as multi-wall carbon nanotube (MWCNT), gallium nitride nanowire (GaNNW), and silica nanowire (SiO_2NW) were used as the template to cultivate the rat pheochromocytoma (PC12) cells.

Multi-wall carbon nanotube (MWCNT):

The dense MWCNT was fabricated on iron (Fe) coated, by IBSD process, silicon wafer by Astex MWPECVD. According to the SEM image (figure 6-9), the diameter of MWCNT was 20 nm.

Compare to the other planar Si surfaces, the number density of PC12 on MWCNT demonstrate 100-fold higher. In the meantime, the average neurite density of each cell and the length of neurite can be detected as 4μm and ~100μm, respectively. This observation shows that the pure CNT can be a good template for cell culture. As shown in figure 6-10, the dense cell number with well spread and extended neurite shape can be observed and also the connection of neurite outgrowth was highly cross-linked. This result figured out the MWCNT grown by MWPECVD can be a good medium for cell culture and/or gene/drug delivery.

Gallium Nitride nanowire (GaNNW)

The ion beam sputtering deposition pretreated Au thin film was used to grow GaNNW via thermal CVD. As presented in figure 6-11a, the uniformly coated GaNNW was observed and the diameter (shown in figure 6-11b) was presented in ~50nm. In this case, length of several um GaNNW template was used to cultivate PC12 cell. Since the first publication of PC12 cultivated on GaN wafer published in

2006 in Biomaterials [6-50], they present the substrate surface microstructure was played the very important role in determining neuron-substrate interactions and influencing cell survival and neurite outgrowth. Hence, the 1-D GaNNW was then used as cell culture template to check whether 1-D nanostructure can affect cell growth or not which was shown as below.

As shown in figure 6-12a, the PC12 cultivated GaNNW template was not shown a higher cell density compared to planar GaN wafer, however, the similar result can be observed. According to the SEM image (figure 6-12a), neuron cell seems like to proliferate on this kind of 1-D nanostructure and the extended neurite outgrowth behavior was also observed. The interesting phenomenon of GaNNW can be uptake by neuron cell which the biocompatibility of 1-D GaN nanostructure can be announced. CL was also used to identify the uptake nanostructure was GaN structure which was shown as figure 6-12b. The peak position of 365 and 453nm was contributed by GaNNW which can be identified; nevertheless, the unknown peak of 498nm was still need to be checked.

Silica nanowire (SiO_2NW):

Figure 6-13 shows the viability of PC12 when silica nanowire was used as the template. According to the presented image, the circular shape and fewer number density of PC12 cell was obtained after 7 DIV culture followed by 7 DIV culture with Nerve Growth Factor (NGF). This observation indicates that our silica nanowire was not a suitable template for neuron cell culture.

However, the other reports show that the 1-dimensional silica nanostructure can be the candidate template for mammalian cell culture [6-51] and/or the medium for drug/gene delivery [6-52]. Hence we proposed that i) the high aspect ratio and low

density of our nanostructure (~20nm in diameter and ~8μm in length) make neuron cell can not stand well, ii) the mechanical properties of silica nanostructure thin film was not suitable for cell culture. The first proposition is possible because the sparse silica nanowire will affect the cell to stand unstable on it, therefore the proliferation and neurite outgrowth of cell can be inhibited. Furthermore, the hardness of template can strongly affect the viability of cell is well known, hence the total hardness of 1-dimensional silica thin film can make it soft because of the low density growth of silica nanowire and then decreasing the viability of PC12 cell.

In addition, the uptake of silica nanowire was also catch the attention which was shown in figure 6-14. The secretion of protein was gave a force to drive the silica nanowire face to the cell body which can be observed. However, the cell was stop to migrate and proliferate because of the soft structure of the silica nanowire top surface. This observation also illustrated the poor surface of silica nanowire for cell viability. We supposed that the shorter nanowire length might solve this situation to enhance the cell viability and proliferation.

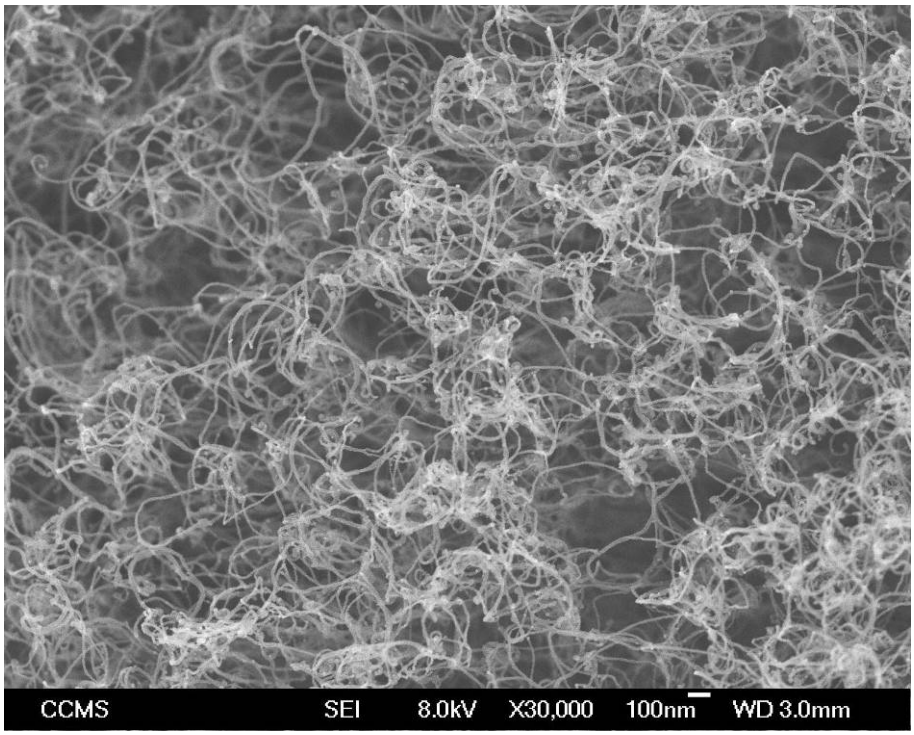

Figure 6-9. The HRSEM of MWCNT fabricated by MWPECVD which was shown that 20 nm in diameter.

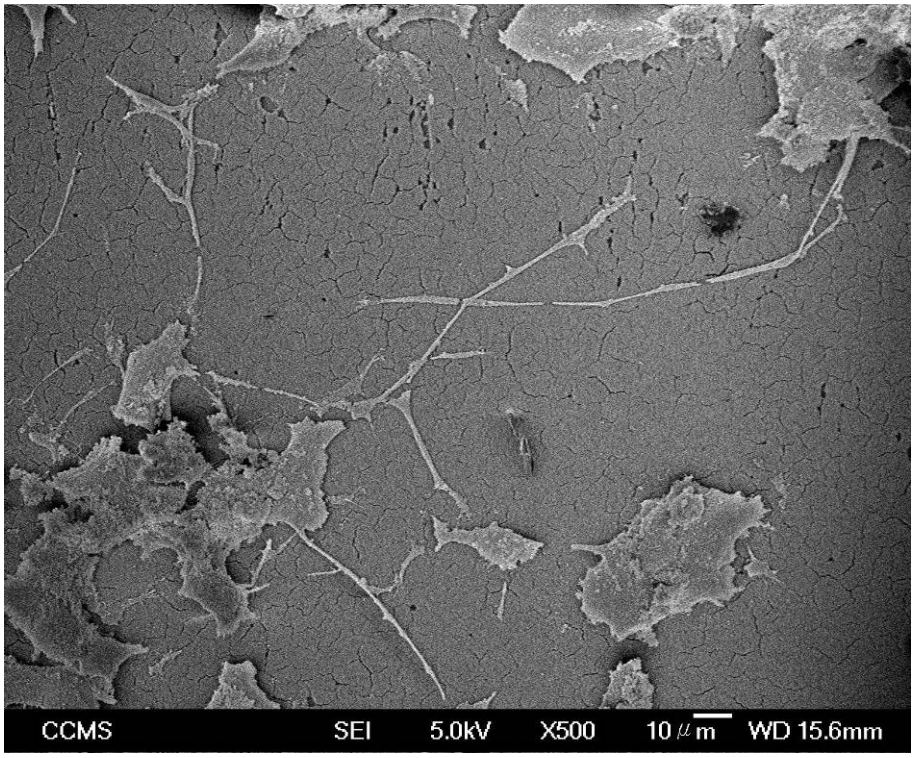

Figure 6-10. HRSEM shows the good viability of PC12 cell on MWCNT and highly cross-linked neurite outgrowth.

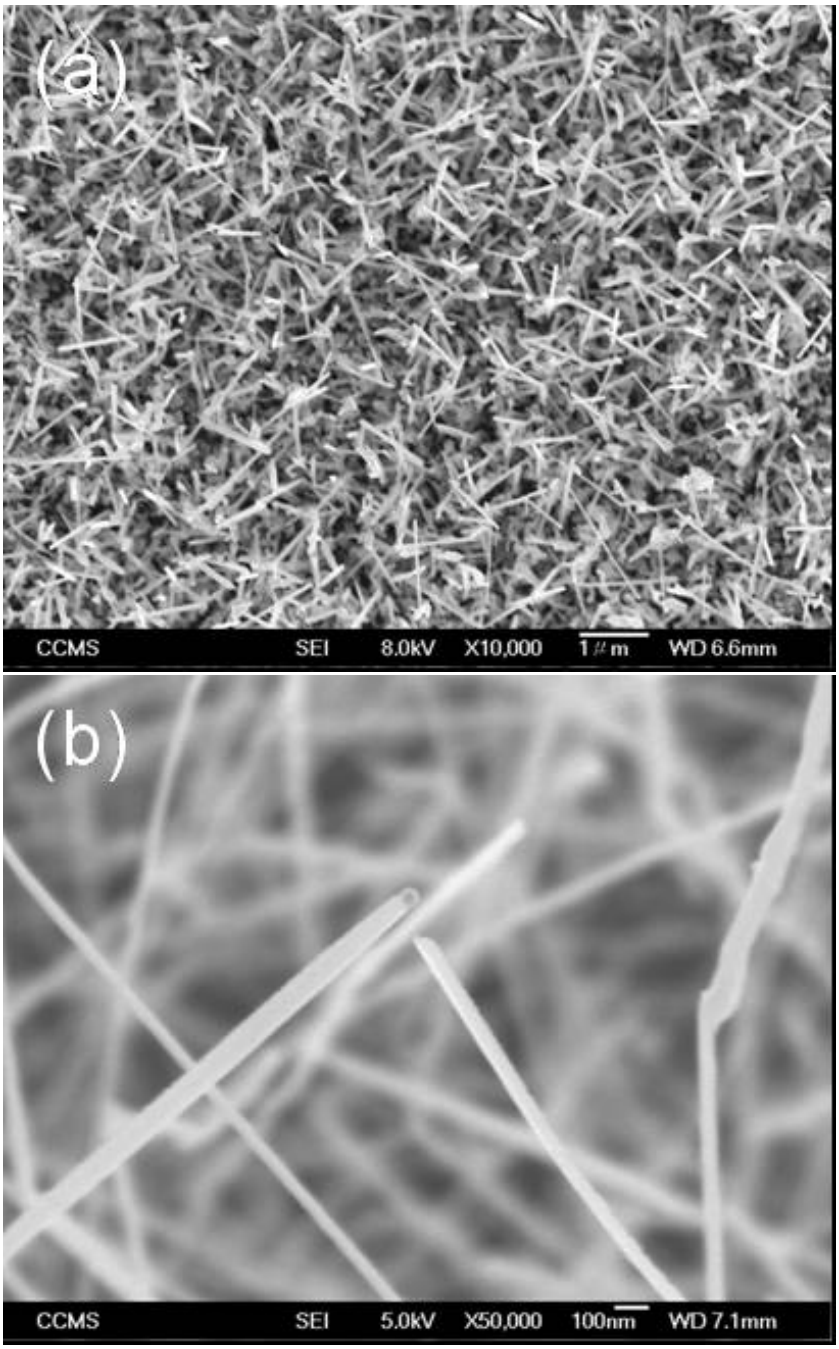

Figure 6-11. shows the high quality of GaNNW with several um and ~50nm in length and diameter which can be observed in (a) and (b), respectively.

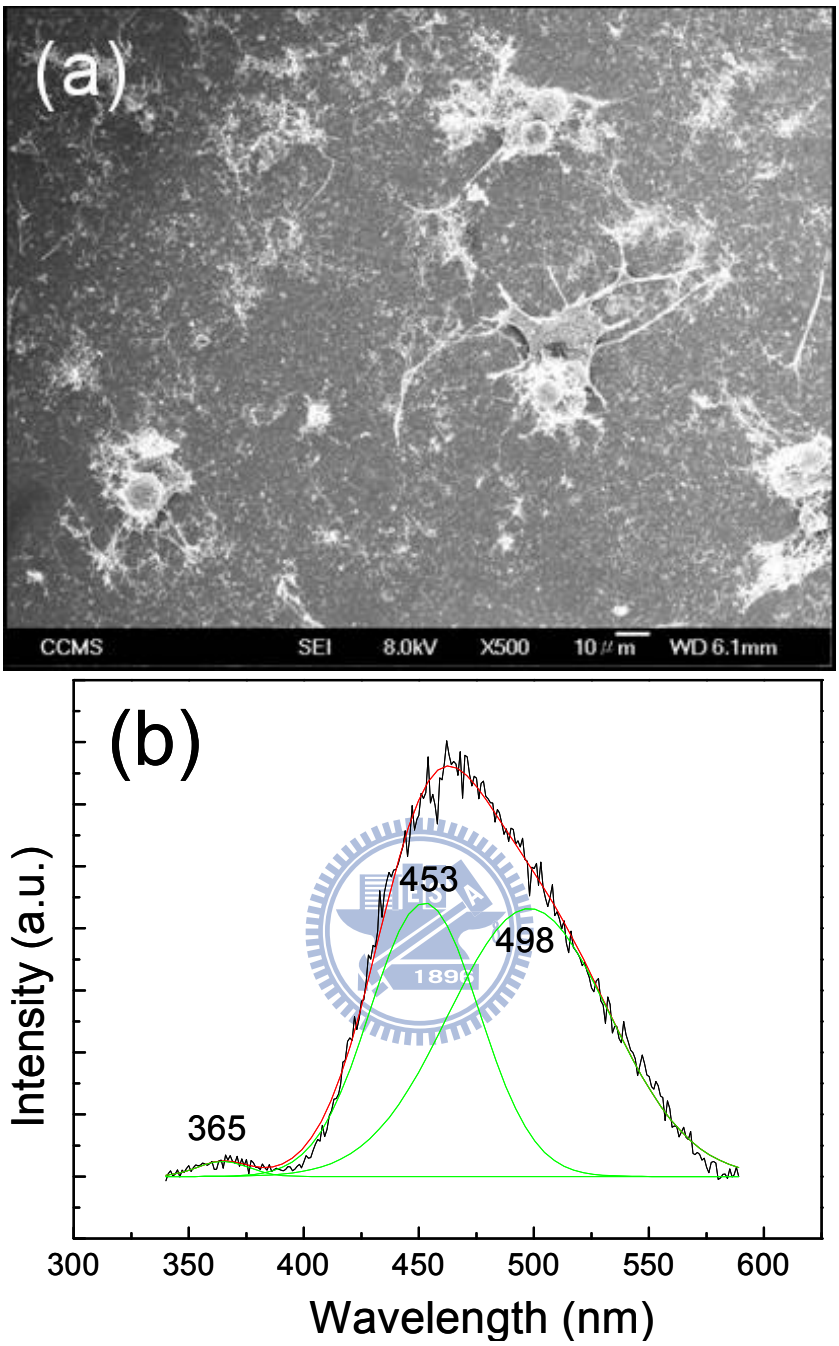

Figure 6-12. the SEM image shows the well proliferation phenomenon with extended neurite outgrowth and (b) shows the CL spectra of the interface of uptake GaNNW and cell body

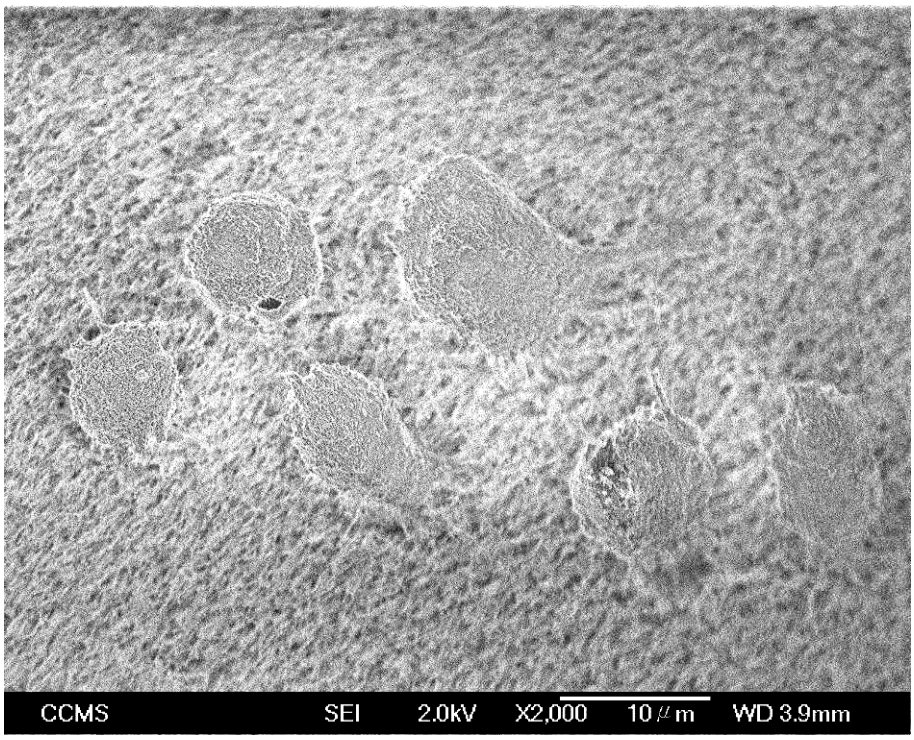

Figure 6-13. HRSEM shows the viability of PC12 cell cultured on silica nanowire. The separate state and circular shape figured out the poor viability and proliferation of PC12.

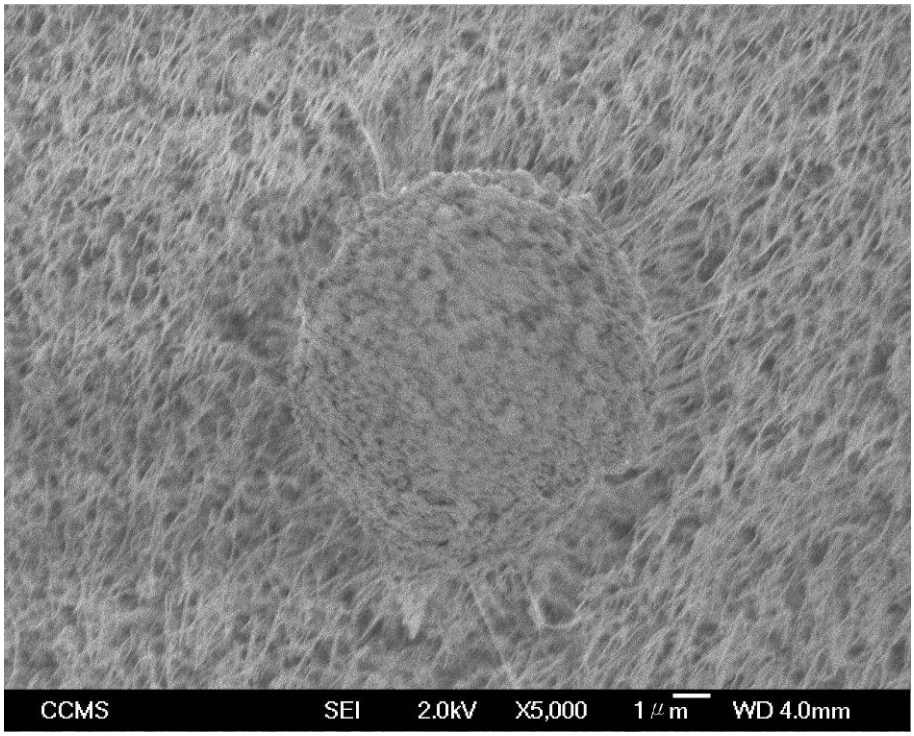

Figure 6-14. HRSEM image of individual PC12 on silica nanowire.

Chapter 7. Surface Enhanced Raman Spectroscopy

7-1. SERS Using Self-Assembled Silver and Gold Nanoparticles on SiNTs

7-1-1 INTRODUCTION:

Surface-enhanced Raman spectroscopy (SERS) has evolved as a powerful and sensitive tool for detection and identification of a wide range of adsorbate molecules down to the limit of single molecule detection [7-1~7-3]. Due to the low scattering cross section (10^{-30} cm^2/molecule), Raman spectroscopy was much inferior to fluorescence spectroscopy, which had a larger cross section (10^{-16} cm^2/molecule), for trace detection. Using specially prepared rough metallic surfaces the otherwise weak Raman signals can be enhanced by several orders making detection possible [7-4]. This enhancement can be as large as 10^{14} [7-1]. Hence, SERS has the capability to unite the sensitivity of fluorescence with the rich structural content inherent to Raman spectroscopy. This extraordinary enhancement is believed to be predominantly due to two mechanisms: a long-range classical electromagnetic (EM) effect and a short-range chemical effect [7-5]. The respective contributions of the mechanism to the overall SERS enhancement are debated, but the EM effect is believed to be a few orders more than that due to the chemical effect. Nie and Emory [7-1] showed that the commonly observed enhancement of the order of 10^6 may have been only an ensemble average over several hundred nanoparticles, whereas a few of these SERS active metallic particulates, called hot particles, can actually give an enhancement of about 10^{15}. At this level of enhancements, SERS, with the richness of molecular

information, supersedes laser-induced fluorescence experiments that carry molecular information only at low temperatures.

Even as we lack a complete quantitative understanding of the fundamentals of SERS, the progress in application developmental research has been remarkably fast and successful. Probing single molecules [7-6~7-8] or nanostructures [7-9, 7-10] and development of nanoscale chemical sensors [7-11, 7-12] utilizing SERS independently or in conjunction with liquid chromatography was made possible. The first step for achieving such advanced stages of application development was the fabrication of proper substrates which are SERS active and provide high enhancement factors. The first substrate on which SERS was observed was electrochemically roughened silver (Ag) electrode [7-4]. Since then Ag films produced by Tollens reaction [7-13] or by vapor-deposition methods [7-14, 7-15] have been commonplace. Nitric-acid-etched Ag foils [7-16], or Ag photodeposited on anatase TiO_2 substrates [7-17] are also relatively easy to prepare. Self-assembled Ag or Au colloid particles on polymer-coated substrates and silver particles layered onto etched polymer substrates has also been used as SERS active substrates [7-14]. These substrates demonstrate enhancement factors of 10^3-10^6 which can be further enhanced by resonance effects. However, most of these techniques, apart from photolithography [7-18], involve wet chemical etching and thus cannot be readily integrated into existing silicon device technologies. Achieving nanometer-size metal prints is several years down the line even for lithographic techniques [7-18, 7-19]. However, a special tip-induced SERS aiding in nanoscale chemical analysis has been demonstrated which does not require a substrate fabrication [7-20]. SERS active substrate generation techniques compatible with silicon device technology are important since only then can it have a wider scope in applications such as micro-electromechanical systems

(MEMS). In this paper we report a dry etched nanostructured substrate on which silver nanoparticles, with less than 10nm diameter, can be self-assembled at an extremely high density that readily exhibits the surface enhancement. The dry etching technique is compatible with the existing silicon device technology and requires no chemical modification. Moreover, these substrates are stable and reproducible as far as SERS signals of analytes are concerned. In this study, standard Si-based processing technology was chosen as a model platform to generate templates for a detailed study of the influence of template surface structure and electrical properties on the viability of a directed cell culture. Semiconductor-compatible, well-controlled, one-step processes like SMDE [7-21] and IBSD [7-22] were employed to manipulate and control the mechanical and electrical properties of the surface of two series of biocompatible Si templates that were selected as model systems commercially available, planar Si wafers and silicon nanotip arrays (SiNT) fabricated on the same wafer [7-23]. PC12 cell lines were chosen as a primary model of a neuronal cell culture system because they are important in the study of in-vitro actions of Nerve Growth Factor (NGF), a natural complex [7-24]. Building on previous research from our group, SMDE was used to fabricate SiNT templates. The contrast in the cell density and soma of PC12 on SiNT versus planar templates was characterized with high resolution scanning electron microscopy (HR-SEM). IBSD was used to modify the template surfaces via the controlled deposition of gold (Au). Effect of Au deposition (thickness) on the template properties, such as surface roughness, hydrophilicity, and surface charge, were characterized with atomic force microscopy (AFM), contact angle goniometry, and a streaming potential measurement of the zeta potential, respectively. Here the study was mainly focused on the detail investigation on the contribution of three abovementioned surface properties on cell viability and proliferation which can definitely explore the insight of cell-attachment behavior.

7-1-2. MATERIALS AND METHODS:

A high-density electron cyclotron resonance (ECR) plasma discharge of silane (SiH_4), methane (CH_4), hydrogen (H_2), and argon (Ar) gas mixture was used to etch out these silicon nanotips from a bare untreated crystalline silicon wafer. A detailed description of the nanotip formation can be found elsewhere [7-21]. In short, severe plasma (Ar and H_2) etching of the silicon substrate partially masked by silicon carbide nanoparticles, originating from CH_4 and SiH_4 plasmas, resulted in a uniform array of aligned silicon nanotips. The aspect ratio and the packing density of these nanotip arrays can be controlled by adjusting the etching parameters such as substrate temperature, microwave power, etc. Each silicon tip had a cap at its apex that was characterized to be silicon carbide (SiC) by auger electron spectroscopy (AES) and high-resolution transmission electron microscopy (HRTEM). The high-resolution scanning electron microscope (HRSEM) images shown in Figure 1 were taken using a FESEM.

The nanotips were coated with silver by the ion-beam sputtering (IBS) process. A base pressure of 6 x 10^{-6} Torr was achieved in the sputtering chamber that contained a high-purity silver target, mounted on a rotating stage, and the silicon nanotip substrates were held about 10-15 cm away from the target. An argon (Ar) ion beam (Ar flow rate of 2 sccm) was accelerated toward the silver target using a Commonwealth Scientific (CS) IBS controller. The sputtered silver was collected on the substrate, kept at room temperature, for different durations of time. The working pressure was about 5 x 10^{-4} Torr. Flat crystalline silicon substrates were also coated with silver by IBS and used for comparison purposes. These silver-coated flat silicon substrates were scanned with a Solver line P-47 SPM-MDT to image the resultant silver islands and particles.

Commonly used molecules for SERS experiments such as Rhodamine 6G and trans-1,2-bis(4-pyridyl)ethylene (BPE) (TCI, Tokyo, Japan) were then dispersed by drop coating onto these substrates, in measured quantities, from their solution (in methanol) and dried. They were then used for the Raman measurements using a Renishaw-2000 micro Raman spectroscope. Single accumulations with integration times of 5s were used to collect the spectra in a backscattered mode. A 532nm laser with a source intensity of 100 mW was used with a probe beam diameter of 1 um. Different concentrations (10^{-6} to 10^{-10} M) of Rhodamine 6G and BPE were used and their Raman spectra were taken on these specialized substrates.

7-1-3 RESULTS AND DISCUSSION:

The formation of silicon nanotips, by a process named self-masked dry etching (SMDE), has been depicted schematically elsewhere [7-21]. Arrays of aligned silicon nanotips with a tip diameter typically in the range of 2 nm, base diameter of 100 nm, and tip length of 1nm can be obtained using the electron cyclotron resonance (ECR) plasma chemical vapor deposition (CVD) technique [7-21]. Figure 7-1a shows the cross-section scanning electron micrograph (SEM) of the as grown silicon nanotips [7-21] without any metal particles on them. The inset shows a plane view SEM of the as-grown nanotips. The tip density could be as high as 10^{11} cm^{-2}, as shown in figure 7-1a. Assuming all the nanotips are touching each other at the bottom, the surface area can be quantified at 150 m^2cm^{-3}, which is as good as the high-porosity porous silicon.

These substrates were then coated with silver (Ag) by Argon ion beam sputtering (IBS) using silver target at room temperatures. Due to the surface energy difference between the silicon nanotips and that of silver they self-assembled to form nanoparticles on these nanotips. The size of these nanoparticles was always between 4 and 10 nm with a rather small departure from the mean value. The density of these particles, under optimized IBS time, was also very high and could be found throughout the entire surface of the nanotips. Figure 7-1b-f depict the SEM images of the silicon nanotips coated with different ion beam sputtering times using silver targets. As evident from the pictures, with lower silver sputtering times, between 1 and 5 min, the silver nanoparticles were scattered near the apex of the nanotips only with a random low-density distribution (figure 7-1b-d). From the sputtering time of 5 min onward the nanoparticles developed throughout the entire surface of these nanotips with a higher and uniform density (figure 7-1e). In the optimized condition, for 10 min IBS time, high density of monodispersed Ag nanoparticles could be

obtained throughout the entire surface of these nanotips. This ensured a rather high density of nanoparticles that could be packed over a unit area of the substrate in comparison to the flat silicon or other polymer substrates normally used for SERS. Such high packing density of these nanoparticles would help maintain the reproducibility levels since the probability of attachment of an analyte molecule in unit probe area would increase manifold. Longer Ag sputtering time will, however, encourage agglomerated clusters leading to the formation of a conformal thin film of Ag on these silicon nanotips (figure 7-1f) instead of the well-separated monodispersed nanoparticles. The density of the metallic nanoparticles could be controlled easily by the sputtering time only, allowing a small dispersion of the particle size. This renders these substrates ideal systems for verifying theoretical modeling of SERS.

The effect of silver coating time on the surface-enhanced signal is demonstrated in figures 7-2 and 7-3. Surface-enhanced Raman signals of Rhodamine 6G (figure 7-2) and BPE (figure 7-3) were collected from silicon nanotip substrates coated with 0 min (uncoated), 1, 3, 5, 10, and 20 min of silver using IBS. Different concentrations of Rhodamine and BPE were dispersed on these differently coated substrates. Figure 7-2a shows the Raman spectra collected from uncoated silicon nanotips for three different concentrations of Rhodamine 6G adsorbed on these substrates. A broad fluorescence band and only the silicon signal from the nanotips at 520 cm^{-1} could be observed with all three different concentrations of Rhodamine 6G used. However, with the silver coating on these silicon nanotip substrates, the surface-enhanced Raman signals were readily observed on a fluorescent background. It is to be noted that one of the analytes used in this study, namely Rhodamine 6G, has electronic resonance in the visible and our probe laser (532 nm) may excite resonance effects contributing to the Rhodamine signals. But to maintain a uniform terminology over the entire text, the term SERS has been retained. The enhancement factors were

calculated from the ratio of the SERS cross-section of adsorbed analytes to the RS cross-sections of bulk analytes1 through the calculation of the total number of Raman photons (NR) from the recorded count. NR is calculated as follows:

(NR) X (collection efficiency) X (optical throughput) X (CCD efficiency) X (gain) = recorded count

where collection efficiency (in %) is that of the objective of the microscope, optical throughput is the total transmission (in %) of the optical path involved in the detection, which, along with the detector efficiency and gain can be calculated for a particular Raman spectroscope. The recorded count being known from the Raman spectrum, NR, is estimated.

The number of analyte molecules (N_M) can be calculated as follows: since the number density ($10^{11}/cm^2$), the base radius (50 nm) and length (1 μm) of the nanotips are all determined from HRSEM measurements, we can calculate the number of nanotips, approximately 1000, in the probe area. The surface area of the nanotips can be found out assuming the nanotips as regular cones of fixed height (1μm long) and base radius of 50 nm. Using a fixed volume of analyte solution (10 μL) of fixed concentration, N_M in the probe volume can be estimated by assuming homogeneous dispersion (the assumption of homogeneous distribution is supported from the fact that our nanotips were hydrophilic having very low water contact angles) of the molecules over the entire sample area (5 mm X 5 mm). This has been estimated to be 2×10^5 molecules in the probe volume for an analyte concentration of 1×10^{-6} M. We assumed 100% dye molecules taking part in the SERS process to estimate the "minimum" enhancement factor in our case using

$(F(\text{photons}/\text{cm}^2\cdot\text{sec}))\ X\ (N_M)\ X\ (\sigma_R^*) = N_R$

where F is the incident photon flux and σ_R^* is the SERS cross section. Basically, this methodology of enhancement factor calculation is identical to what was reported by Nikoobakht et al. [7-22], assuming 100% adsorption. A lower adsorption (less than 100%), will give rise to a lower N_M taking part in the Raman process and hence, a higher enhancement. An estimation of the enhancement factors using careful geometrical analysis and consideration of surface coverage and adsorption isotherms have produced large errors of 30-50% [7-19, 7-23]. Here the quoting of a "minimum" enhancement by considering 100% adsorption seems more reasonable.

The intensities of the Raman signals were markedly higher for higher concentrations (10^{-6} M) of Rhodamine 6G used (figure 7-2b) and merely visible for lower concentrations approaching 10^{-10} M (figure 7-2d). However, unambiguous signals of the three most intense Rhodamine 6G Raman frequencies can be found even at the lowest concentrations (inset, figure 7-2d) which may not be too obvious in figure 7-2d itself.

Similarly when BPE was used as the analyte, there was no SERS signal from the uncoated silicon nanotip substrates, with only a broad fluorescence and the silicon signal at 520 cm^{-1} being observed (figure 7-3a). For the highest concentration of BPE used (~1 X 10^{-6} M) even the silicon signal was suppressed. However with silver coating on the substrates, the SERS signals could be readily obtained for all three concentrations of analytes used in this study (figure 7-3b-d).

Figures 7-2 and 7-3 both show the Raman signals on a broad fluorescent background. The fluorescent background observed in most spectra indicates that a fraction of analytes were adsorbed on bare silicon instead of the metallic sites which would have quenched the fluorescence. The nanotips coated with silver for 10 min

yielded the largest SERS signals independent of the concentrations. Several groups have investigated the variation of the SERS intensity with analyte concentrations and inferred a linear dependence [7-22, 7-24]. However, they differ on the range of this linear regime, spanning 10^{-10} to 10^{-6} M in concentration in some case24 and only 10^{-5} to 10^{-4} M [7-19] in some. This indicates a system-dependent variation of the SERS intensity with analyte concentration. We observed that the integrated intensity, say, of the 1650 cm^{-1} line of Rhodamine 6G does not increase linearly with its molar concentration. An increase of 4 orders in concentration saw an increase of 5 X 10^2 in the SERS intensity (plot not shown). Intuitively, a linear variation of the SERS intensity with the analyte concentration is expected assuming that the SERS active sites increase linearly with the analyte concentration, and the SERS active and inactive sites all have the same adsorption energy (consistent with the Langmuir isotherm) [7-19]. But SERS active sites have higher affinity for adsorbates than the inactive sites [7-23]. This is the reason for the blinking of SERS signal probably arising out of the thermally activated diffusion of analyte molecules between SERS inactive and active sites [7-25]. A nonlinear increase in SERS active particles, hence SERS intensity, was also observed with molecular concentration by Michaels et al. [7-26]. The sub-linearity in our case may be a result of (i) nonlinear increase in SERS active sites with the increase in analyte concentration [7-26], (ii) the rough morphology of our substrate scattering (over a much larger solid angle than that projected by our objective lens) or re-absorbing the Raman photons predominantly at the higher concentrations, or (iii) the extremely low surface coverage [7-19] regimes in our experiments.

It has been mentioned that a silver coating time around 10 min produced the best enhancements. At longer silver coating times, since they produced a continuous thin film on the nanotips, the enhancements were relatively small. Again at small silver

coating times, say 1 min, the density of the nanoparticles was not sufficiently high to guarantee a strong and reproducible SERS signal. This can be interpreted from the modeling of Garcia-Vidal and Pendry [7-27]. They showed from a model study that the efficiency of an SERS active substrate is maximum when the separation, d, between the metallic particles is equal to their diameter, 2R, (assuming half cylindrical particles), i.e., the particles just touching each other. To satisfy this modeling condition, we need to have a high density of nanoparticles on our substrate. This condition is close to what we have for the nanotips covered with silver sputtered for 10 min in the IBS system. With lesser silver coating times, we observed scattered nanoparticles which simulates the modeling condition of $d > 2R$, and with higher silver coating times (20 min or more) we approach the modeling condition of $d < 2R$, both of which will amount to reduced SERS activity of the nanoparticles. Gunnarsson et al. [7-18] also demonstrated through their electron beam lithographically prepared substrates that SERS activity increases manifold with decreasing particle separation. This could be related to the electromagnetic coupling effects between the silver nanoparticles [7-28]. However it should be mentioned here that the silver particles used by Gunnarsson et al.18 are of the size 200 nm, much larger than what was used in this study. Although in that study they mentioned that the effect of interparticle separation far outweighs the effect of particle size itself. Talking of interparticle coupling, a situation very similar to the present case was reported by Maxwell et al. [7-29] where the SERS intensity was shown to increase as a function of "particle coverage" and ultimate saturation of SERS signal above 1 monolayer. The lack of particle-particle interaction as a result of longer interparticle separation implying lower particle coverage (substrates shown in figure 7-1b and c), produced relatively weak SERS intensities, but with increasing particle coverage (figure 7-1e), stronger SERS intensity was observed. However, with increased sputtering times, the

3-dimensional particle formation breaks down promoting a 2-dimensional film (figure 7-1f), our observation is a decreased SERS intensity that matches well with the reported SERS intensity normalized to the particle coverage [7-29]. The current technique of Ag particle generation, apart from being friendly to silicon technologies, can also produce substrates on which such models [7-27] can be verified.

There are several reports [7-30, 7-31] on the growth of silver on flat crystalline silicon that generally demonstrates a Stranski-Krastanov or a modified Stranski-Krastanov growth mode, where 3-dimensional Ag islands grow on a thin 2-dimensional Ag wetting layer. However, we are less cognizant about the growth of silver on rough silicon surfaces, such as these nanotips. To identify the advantage of using a rough silicon nanotip morphology to generate SERS-active Ag nanopaticles, flat crystalline silicon substrates and silicon nanotips both were identically coated with silver for 10 min (that yielded the best SERS signals) using IBS technique and matched for the surface enhancement effects using Rhodamine 6G as an analyte. The silver-coated flat silicon surfaces had larger silver nanoparticles of >20 nm diameters sparsely (interparticle distances of ~100 nm) distributed on agglomerated Ag islands (figure 7-4) as expected for a Ag coverage exceeding 1 monolayer.30 This is both qualitatively and quantitatively different to the high density of nearly monodispersed Ag nanoparticles observed for the nanotips substrates. An effort to mimic the effective thickness or the surface coverage of the Ag layer as observed on silicon nanotips, by decreasing the Ag sputtering time on flat silicon substrates, will produce a 2-dimensional wetting layer [7-30] (for a coverage below 1 monolayer) devoid of particle formation required for SERS.

Figure 7-5 shows the background fluorescence subtracted SERS spectrum, normalized to the intensity of silicon signal at 520 cm^{-1}, for Rhodamine 6G on flat crystalline silicon (as in figure 7-4) and silicon nanotips coated with 10 min of silver

by IBS (as in figure 7-1e). The background removal was done by pixel imaging of the spectrum or alternatively by using mathematical software to fit the background with a polynomial and using a suitable scaling factor to match the SERS spectrum and generating the particular background after specifying the Raman peak positions of the analytes. Figure 7-5 only distinguishes the SERS activity of differently self-assembled Ag morphologies generated on silicon nanotips against a control sample of flat silicon. Clearly the silicon nanotip substrates showed higher enhancements (~10^8), by about 2 orders of magnitude, in comparison to the silver coated flat silicon substrates (3 X 10^6). This is attributed to several factors. The silicon nanotips with silver particles were found to be hydrophilic, whereas the silver-coated flat silicon substrates were found to be hydrophobic in our experiments. Such difference in the wettability of these substrates definitely arose due to the difference in surface roughness in these two substrates apart from other possible chemical contributions. The removal of any surface hydrogen from the nanotip surface during the plasma etching may be one such chemical contribution. The same volume of analyte molecules dispersed uniformly over the whole surface area of the nanotip substrate reproducibly produced SERS spectra, whereas the same volume of analyte on the flat silicon substrate was confined to a small area only, outside which no SERS spectra could be obtained. This resulted in an excess population of analyte molecule per unit probe volume on the flat silicon substrate. This, apart from the difference in SERS count (figure 7-5), was taken into account while calculating the enhancement factors. Other than this, the larger particle size and interparticle separation of silver particulates on the flat silicon substrate in comparison to the silicon nanotips would affect SERS activity.

The stability of these substrates was tested by measuring the Raman activity with time. These substrates can give Raman signals even three months after they were drop

coated with the analytes. figure 7-6 shows the aging of SERS spectrum for Rhodamine 6G (1 x 10^{-6} M) on silicon nanotips substrates coated with silver (as in figure 7-1e). There is a reduction in the SERS intensity over a period of 3 months but still the analyte detection is clear and unambiguous, which is required for analytical studies.

Electrochemically roughened silver electrodes are not stable for SERS; their activity started decreasing after the preparation itself and the activity may last for few days [7-32]. Silver foil roughened with nitric acid etching generally stays active for a week, whereas the silver film produced by Tollen's reaction is not stable. Photo-deposited silver films are stable over few weeks [7-32]. Such instabilities may result from desorption of analytes from the SERS active sites or a decay in the activity of the metal nanoparticles in the scattering process, among other probable reasons such as photo-bleaching. However, from the high density of the silicon nanotips and resultant high packing density of the mono-dispersed metal nanoparticles on them, an initial explanation of the stability may be statistical in nature whereby a significant fraction of active analytes on active SERS centers still exist. However, further studies are required to know the reason for such stability in this case, or rather the root cause for instabilities in all the SERS active systems. Viewed in the wider perspective these new SERS active substrates can be termed quite stable.

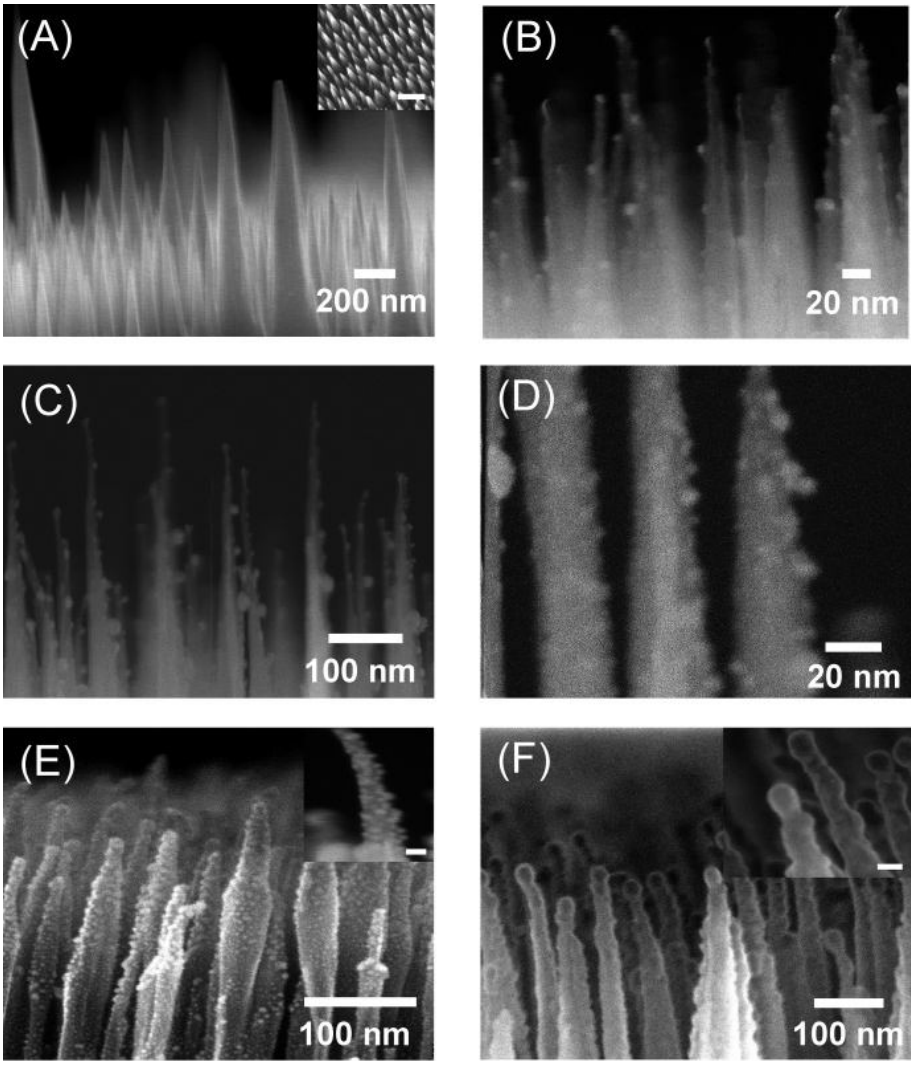

Figure 7-1. Scanning electron micrographs showing (a) cross-sectional view of the as-grown silicon nanotips (inset shows the top view of the as-grown nanotips; scale bar 200 nm); cross-section images of silicon nanotips covered with silver sputtered for (b) 1 min, (c) 3 min, (d) 5 min, (e) 10 min (inset showing a single tip with the silver nanoparticles; scale bar 20 nm), and (f) 20 min (inset showing a magnified image of the silicon tip covered in a silver film; scale bar 20 nm) in IBS.

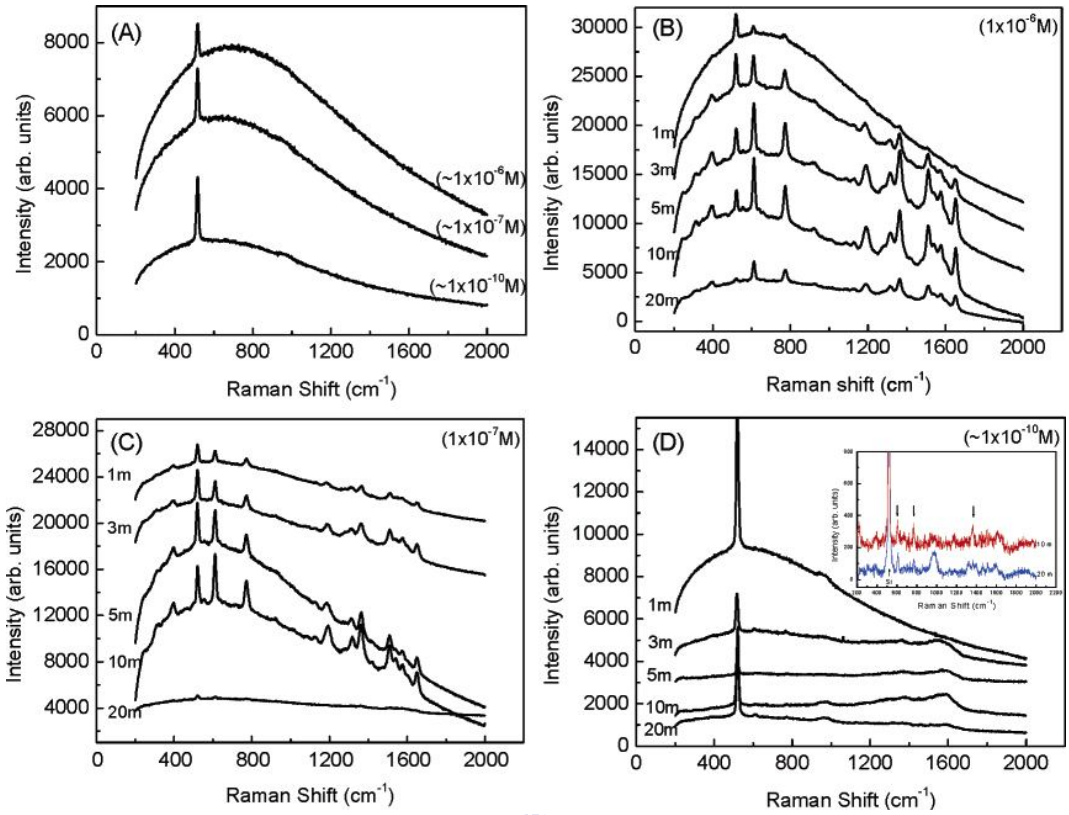

Figure 7-2. (a) Raman spectra of Rhodamine 6G drop-coated on as-grown silicon nanotips (the concentration of Rhodamine 6G is marked on each curve); SERS spectra of different concentrations of Rhodamine 6G drop coated on silicon nanotips covered with different amounts of self-assembled silver nanoparticles (b) 1 x 10^{-6} M, (c) 1 x 10^{-7} M, (d) ~1 x 10^{-10} M (the numbers mentioned on each curve in figure 7-2b-d denote silver sputtering times). Inset in figure 7-2d shows the background- subtracted Raman spectra for Rhodamine 6G dispersed on silicon nanotips covered silver coating for 10 and 20 min by IBS. Silicon signal and the three most intense Rhodamine 6G Raman lines are marked by arrows.

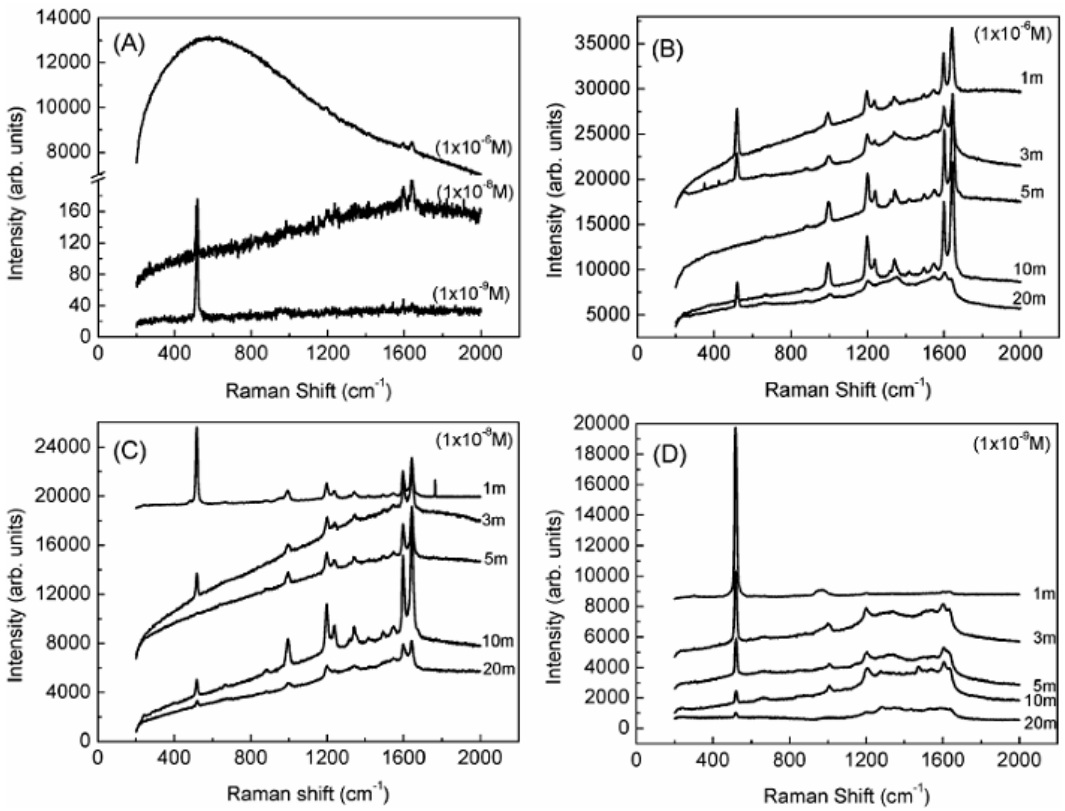

Figure 7-3. Raman spectra of BPE drop coated on (a) as-grown silicon nanotips (the concentration of BPE is marked on each curve); SERS spectra of different concentrations of BPE drop coated on silicon nanotips covered with different amounts of self-assembled silver nanoparticles (b) 1 x 10^{-6} M, (c) 1 x 10^{-8} M, and (d) ~1 x 10^{-9} M (the numbers mentioned on each curve in figure 7-3b-d denote silver sputtering times).

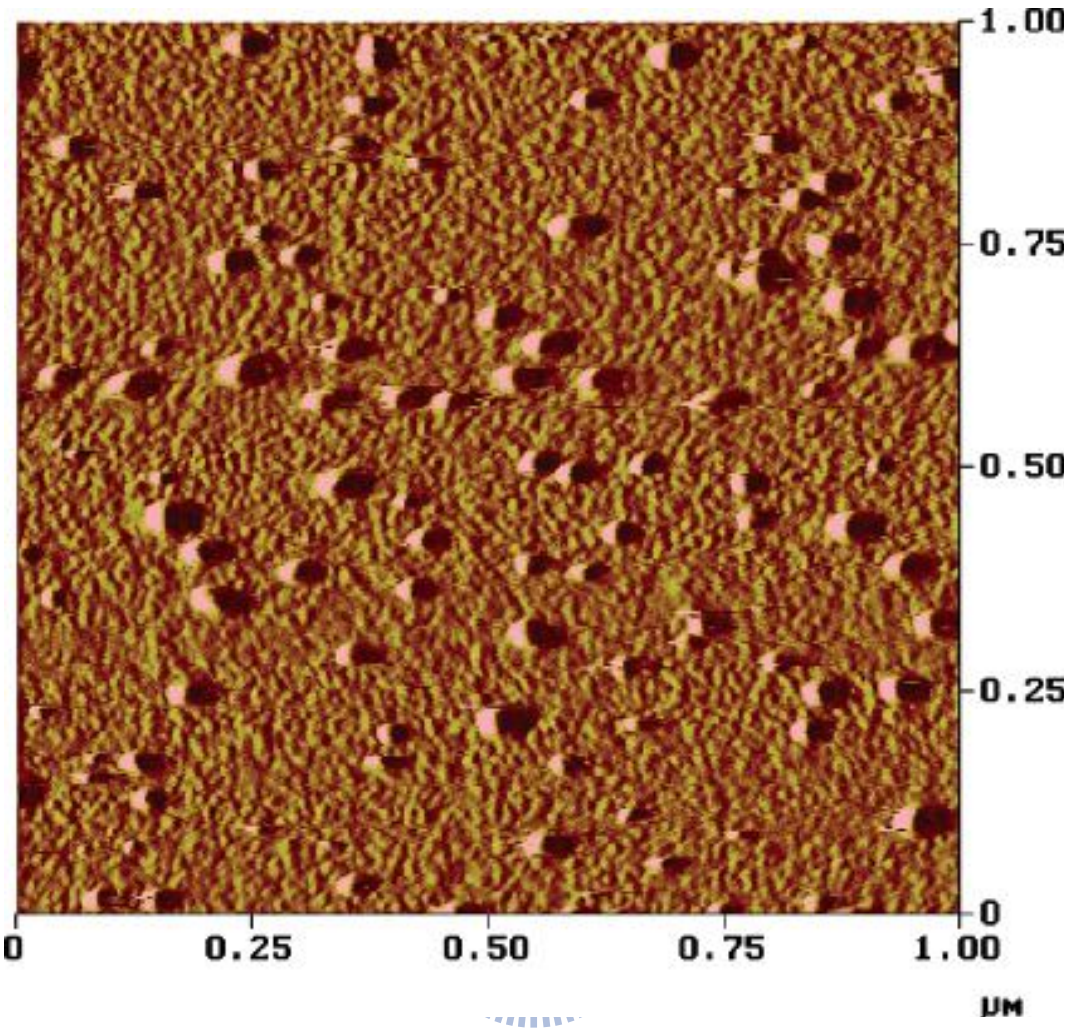

Figure 7-4. Atomic force microscope image of a flat crystalline silicon surface covered with silver sputtered in the ion beam system for 10 min.

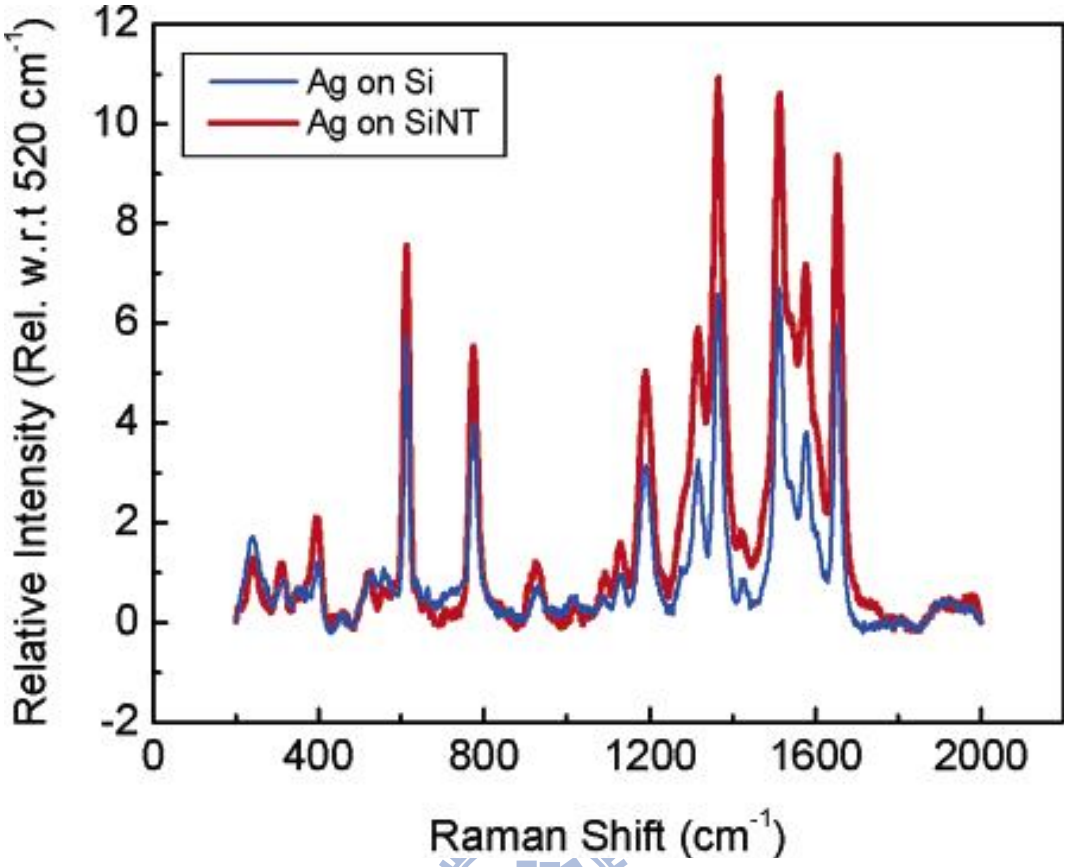

Figure 7-5. Background-subtracted SERS spectrum of Rhodamine 6G, normalized with respect to the 520 cm^{-1} signal from silicon, on (blue line) flat crystalline silicon covered with sputtered silver (as in figure 7-4), and (red line) silicon nanotips covered with self-assembled silver nanoparticles (as in figure 7-1e). Estimated number of analyte molecules in unit SERS probe area is higher by several tens in the case of flat crystalline silicon.

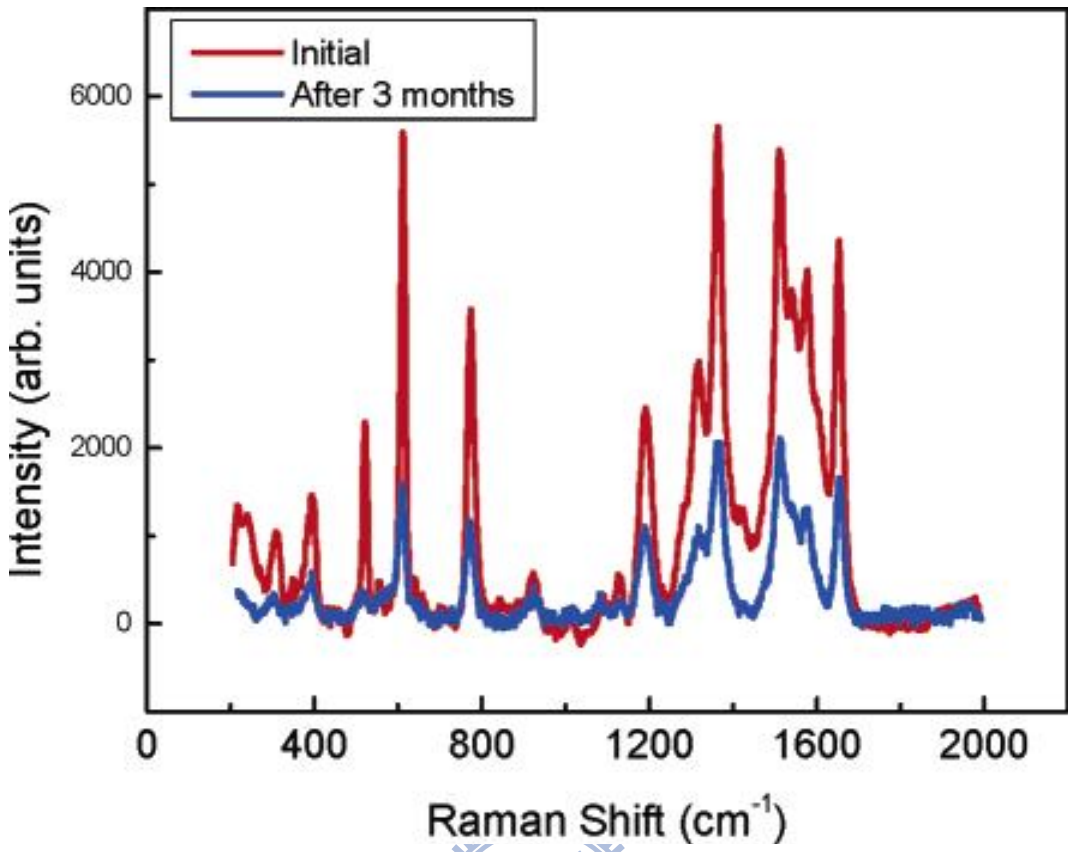

Figure 7-6. Aging of SERS spectra (background subtracted) of Rhodamine 6G (1 x 10^{-6} M) on silicon nanotips covered with self-assembled silver nanoparticles (as in figure 7-1e).

7-2. Label free sub-picomole level DNA detection with Ag NPs decorated AuNT arrays as SERS platform

7-2-1 INTRODUCTION

Surface enhanced Raman scattering (SERS) has developed into a frontline tool for chemical analysis and sensing [7-33], since its discovery [7-45], owing to an improved scattering cross-section over the conventional spontaneous Raman process and its efficacy at room temperatures. The enhancement of the Raman scattering cross-section (>10^6) is believed to be due to a surface plasmon aided stronger electro magnetic coupling at the analyte site [7-58, 7-59]. However, another school of thought attributes the enhancement to a chemical charge transfer effect, though it could only predict a theoretical enhancement of the Raman scattering cross-section to the tune of 10^2 [7-58]. Apart from the range of organic and inorganic molecules successfully detected using SERS, the technique is becoming increasingly important for bio-sensing [7-64, 7-65]. Fodor et al. [7-46] used a pulsed ultraviolet (UV) laser to enhance the signals from the mononucleotide of adenine (A), thymine (T), cytosine (C) and guanine (G) with limited success. Silver nanoparticle (AgNP) aided SERS was well established for the detection of the nonfluorescent bio-species, such as DNA and fluorescent biomarkers [7-35, 7-43, 7-44, 7-51, 7-52, 7-62, 7-63, 7-66, 7-69]. However, Ag did not participate as well as Au in bio-immobilization. For this purpose, gold (Au) plays a major role in establishing the Au-S (gold-sulphur) bond to efficiently immobilize the thiolated bio-species on the substrate, but lost out on the enhancement, and hence sensitivity, of the SERS process against Ag. Conventional detection techniques, such as fluorescence, yielded detection limits of 10^{-13}M from dye labeled-DNA sequences dispersed in AgNP containing buffer solution [7-43, 7-44, 7-51, 7-69]. However, those are indirect detection schemes in the solution phase. The

use of Au nanostructures to obtain high immobilization was also employed to detect labeled-DNA sequences through SERS [7-35, 7-52, 7-62, 7-63]. These detection schemes were limited by the complex sample preparation and relatively low enhancement factors compared to AgNP, as discussed before [7-62]. For increased reliability, measurements using solid substrates were also reported [7-35, 7-66].

A recent development, tip enhanced Raman spectroscopy (TERS), has demonstrated detection of low concentration nonfluorescent analytes such as DNA [2, 7-42, 7-49, 7-60] and fluorescent biomarkers [7-41]. This near-field technique, an emerging competitor of SERS for detection purposes, demonstrated significantly high spatial resolution and sensitivity by tuning the gap between the apex of the cantilever tip and the substrate. However, challenges, such as fabricating uniform TERS tips, nano-scale heating and mismatch between topography and optical signal, remain for the development of this technique [7-68]. Being excellent otherwise, TERS can also be prohibitively expensive and complicated for routine measurements compared to SERS.

We demonstrate here a simple SERS platform that uses AgNP decorated Au nanotips (AuNTs) array that incorporates the immobilization efficiency of Au and enhanced Raman scattering efficiency of the AgNPs (figure. 1) for label-free, high-sensitivity DNA detection. In addition, we demonstrate high and tunable three dimensional packing densities of the AgNPs that could maximize the SERS enhancement and increase its stability.

7-2-2 MATERIALS AND METHODS:

In this study, a semiconductor compatible electron cyclotron resonance microwave plasma enhanced chemical vapor deposition (ECR-MWPECVD) and an ion beam sputtering deposition (IBSD) system was used to fabricate the silicon nanotip (SiNT) arrays and the Au/Ag coated nanostructure, respectively. The high density ECR plasma of silane (SiH_4), methane (CH_4), hydrogen (H_2) and argon (Ar) gas mixture was used to fabricate (top down process) the well aligned SiNTs from commercial 6 inch single crystalline silicon wafers (figure 7-7, step 1). The detailed description of the SiNT formation is published elsewhere [7-40, 7-48, 7-54]. The IBSD technique used a Kaufman type ion source and its application to the deposition of noble metals (bottom up process) could be found elsewhere [7-38, 7-39]. As shown later, surface modification of the SiNTs via an Au thin film (figure 7-7, step 2) aids in high efficiency DNA immobilization (figure 7-7, step 3), and subsequent deposition of AgNPs (figure 7-7, step 4) ensures superior sensitivity Raman measurement.

The AuNT substrates were incubated with single strand (ss) probes (p-DNA) for 24 h at 4°C for immobilization (figure 7-7, step 3). Thiol-modified p-DNA (MDBio) with a 20-base sequence, 5'-HS-(CH2)6-AAAAAAAAAAAAAAAAAAAA-3', was diluted to 10mM with 2x saline sodium citrate (SSC) buffer. Before hybridization procedure, Cleland's Reductacryl reagent (EMD Biosciences) was added to prevent the aggregation of the p-DNA and the mixture, of p-DNA and reducing agent, was then filtered via MicroSpinTH G25 column (GE Healthcare) at 3000rpm for 2min. A specific 20-base ss-oligonucleotide, 5'-TTTTTTTTTTTTTTTTTTTT-3', complementary to the p-DNA, was selected as the target (t-DNA). Duplex buffer solution (Integrated DNA Tech.) was further added to reach a final concentration of 10mM, prior to hybridization studies. After each of the above-mentioned steps, the

sample was washed carefully in de-ionized water, followed by drying in nitrogen flow, in order to avoid the physisorption (or non-specific binding) of chemicals in solution or p-DNA on the AuNTs surface. Similar technique was adopted for the ss-C and G nucleotides. No fluorescent labels or Raman dyes were used.

High resolution field emission scanning electron microscope (JEOL JSM-6700 FESEM) was used to study the structure and morphology of the bare SiNTs, AuNTs and the AgNPs density distribution. Raman spectroscopy measurements were carried out in a Jobin Yvon LabRAM HR800 micro Raman spectroscope system. A 632nm He-Ne laser (beam diameter ~1.5μm) with a power density of 4.5mW/μm^2 and acquisition time of 60 s was used.

7-2-3 RESULTS AND DISCUSSION:

In this study, a top-down self-masked dry etching (SMDE) technique was developed to create the SiNTs template (figure 7-7, step 1) over a large area (~ 28 sq. inch) at 200°C process temperature [7-48, 7-54]. These SiNTs had apex diameters typically in the range of ~2-5 nm, bottom diameters of 100-200 nm, aspect ratio around 10-12 (using base diameter of 100 nm) and tip density of 10^{11} cm^{-2}. Conformal Au coating, by IBSD, of these SiNTs resulted in theAuNTarray that closely resembled the features of the SiNT template (figure 7-7, step 2). Post DNA immobilization, controlled sputtering of Ag, on these AuNTs, resulted in the bottom-up growth of self assembled AgNPs (figure 7-7, step 4) whose number density, or their average inter-particle distances, could be easily controlled as a function of the sputtering time. Figure 7-2 shows the SEM images of plain SiNTs (figure 7-8a), Au thin film coated AuNTs (figure 7-8b and c), and AgNPs decorated AuNTs (figure 7-8d-f). Direct DNA immobilization on AgNP decorated SiNTs (without the Au thin film) was found unsuitable since a fraction of the physisorbed AgNPs along with the DNA strand would be washed away during sample preparation yielding lower Raman signals. Compared with the other cylindrical 1-D nanostructures, the well aligned AuNTs template supports the NP loading without any shadow effect due to its conical morphology, just like its underlying SiNTs template [7-39]. Figure 7-8b depicts the well aligned AuNTs with high uniformity, aspect ratio and density. Assuming all the nanotips touching each other at the bottom, the real surface area can be quantified to be around 225m^2 cm^{-3} [7-67], which is as good as high-porosity porous silicon [7-37, 7-55].

IBS deposition of Au for 60 min at room temperature on the SiNTs yielded the AuNTs (figure 7-8b and c). Comparing the bare and Au-coated SiNTs, the thickness

of the Au layer was estimated to be around 10nm at the apex. The thiolated DNA species were then immobilized onto the AuNTs surface followed by the AgNPs deposition. The density of AgNPs, produced on the AuNTs, corresponding to Ag sputtering times of 5, 10 and 20 min are shown in figure 7-8d-f, respectively. The size of these NPs varied between 3 and 10nm in diameter. For sputtering times of 5min and above, the AgNPs developed throughout the entire surface of the AuNTs (figure 7-8d). High density, with 1-2nm inter-particle distance, and uniformly dispersed AgNPs were observed at an optimized sputtering time of 10 min (figure 7-8e). Longer sputtering times, say 20 min, resulted in agglomerated clusters leading to the formation of an Ag thin film on the AuNTs (figure 7-8f).

We began, by studying the SERS activity of the AuNTs vis-à-vis the bare SiNTs. We used a standard analyte, Rhodamine 6G (R6G), with a concentration of 1.2nM on SiNTs and AuNTs and various concentrations of adenine and thymine on AuNT for this purpose (figure 7-9). The results indicate that R6G absorbed on SiNTs yielded no Raman bands for the analyte (figure 7-9a). The second order Raman band for Si (at 980cm^{-1}) dominates the spectrum. In contrast, the AuNTs shows finger print R6G Raman bands at ~610, 780, and ~1600cm^{-1} (figure 7-9b). This indicates that the AuNTs are SERS active, at least for R6G which has a Raman scattering cross-section between ~10^{-30} and 10^{-22} cm^2/mol [7-56, 7-59, 7-61]. However, lower concentrations (1.2nM) of DNA could not be detected on the AuNTs (figure 7-9c). In contrast, at a higher concentration (1.2 x 10^{-2} M) rich Raman signals from DNA (adenine and thymine mononucleotide) could be observed from the AuNTs (figure 7-9d). Similar DNA dispersion on bare silicon wafers did not yield any Raman signals (figure 7-9e). This does show limited SERS activity of the AuNTs. In comparison to figure 7-9d, measured at 12mM, bulk DNA powders dispersed on silicon showed strong and rich Raman signals (figure 7-9f). However, figure 7-9d-f cannot be compared to obtain a

SERS enhancement factor since, among other reasons [7-53], the non-SERS cross-section of the DNA used is unknown. The results in figure 7-9d-f indicate that either (i) the DNA molecules have significantly lower Raman scattering cross-section than R6G, and/or (ii) the surface plasmon in the AuNTs is too weak to excite the Raman signals from the DNA. The first proposition is reasonable since R6G is a laser dye with strong Raman scattering cross-section [7-56, 7-61]. The second proposition is also reasonable since the polarizability, and hence the surface plasmon generation, is weaker in the metal thin films than the rough nanostructured counterparts. Since Au is indispensable for DNA immobilization, an extension of the substrate design was necessary to observe any reliable detection of DNA species through Raman spectroscopy. Accordingly, the additional AgNP decoration of the AuNT was employed to induce a stronger enhancement of the SERS signal from the DNA.

Raman spectrum from the bare AuNTs (figure 7-10a) and SERS spectra from the DNA immobilized AuNTs (figure 7-10b) were compared with those having different amounts of AgNPs deposited on the DNA molecules (figure 7-10c-e). SERS signals of poly (A) and poly (T) sequences with 1.2nM concentration were reliably detected only from the AgNPs coated AuNTs (figure 7-10c-e). DNA Raman signals from AuNTs (Ag coating time of 0 min, figure 7-10b) showed no reproducible Raman signals. This clearly demonstrates the contribution from the AgNPs.

Weak DNA Raman signals, from the 5 and 20 min grown AgNPs (as in figure 7-8d and f, respectively), appeared mostly within 700-1650cm^{-1} (figure 7-10c and e). The assignment of the peaks to the vibration modes of A and T is indicated in figure 7-10d [7-42, 7-46, 7-49, 7-50]. Enhanced SERS signal of the DNA chains (figure 7-10d) could only be obtained from the 10 min grown AgNPs which are uniformly dispersed and have higher density (figure 7-10e) compared to others shown in figure 7-10. The peaks, in the SERS spectra of the ss-A and T, are now better resolved and more

intense for easy identification and assignment (figure 7-10d) [7-42, 7-49, 7-60]. AuNT substrates with Ag films, obtained with longer duration (20 min) sputtering, yielded very weak Raman signals (figure 7-10e). This is attributed to the difficulty in polarizing the Ag thin films, compared to the nanometric Ag particles, and hence a lowering of the surface plasmon strength upon laser irradiation. The suppressed SERS signal in figure 7-10e may also be due to the masking of the DNA molecules underneath the Ag film.

Density of the metal NPs are more critical than its size with regard to cross-section enhancement as pointed out by Garcia-Vidal and Pendry in their calculation [7-47]. We refer to their work to explain why the sparse AgNPs (figure 7-8d) or the Ag thin film (figure 7-8f) did not yield high enhancements as in the case of the high density AgNPs (figure 7-8e) [7-47]. They predicted that the SERS enhancement will go to a maximum when the central separation, d, between the metallic particles (Ag in this case) is equal to the particle diameter (2r), or in other words, when the adjacent AgNPs are touching each other. This is the theoretical recipe for SERS 'hot-spots' provided by Garcia-Vidal and Pendry [7-47], though experimental isolation of a 'hot-spot' is still illusive. Single molecule detection schemes had to rely on SERS 'hot-spots' whose enhancement factors were estimated about million times higher than an average SERS active metal site with enhancement factors of 10^6-10^8 [7-36, 7-51, 7-57, 7-59]. This ideal condition for maximum SERS enhancement, or socalled 'hot-spots', is close to what we have for the AuNTs covered with AgNPs grown for 10 min (figure 7-8e; d~2.5r). This is our optimized SERS platform. Longer Ag deposition time, d~2r or shorter Ag coating times (5 min or less), d~2r dramatically decreased the SERS activity of the metal. Our experimental results are in agreement with their calculations. At this point, it is essential to point out that this technique may not be limited to the A and T nucleotides only, but can well be extended to C, G and

their hybridized double strands (ds-) also (see figure 7-13).

It is only natural to argue that the above results of DNA detection could also be obtained on a planar Au film instead of the high aspect ratio AuNTs used as the platform. Qualitatively, a similar result is expected before we consider the following facts. AgNPs with ~10nm size and controllable density could not be grown on Au thin films due to severe agglomeration effect leading to island formation [7-50]. AuNTs, with high roughness, impart a suitable surface energy so that Ag self-assembles as AgNPs, with controllable density and dimension, on it. Modification of the AuNT surface with DNA molecules may add to the effect that helps create the AgNPs. However, even the bare silicon nanotips can self-assemble AgNPs without the help of any DNA coverage [7-39]. Secondly, AuNTs, with high surface area, can generate a high packing density of AgNPs in three dimensions (3D) (see figure 7-7, step 4) instead of a 2D packing of islands obtainable on a thin film. This is a key distinction of this nanotips platform as against the lithographically prepared planar SERS platforms. The 3D packing of the AgNPs ensures that even with the laser tightly focused to ~1.5μm spot, it could actually excite a larger number density of AgNPs and hence achieve a significant SERS signal from the adsorbed analyte. However, the SERS signal of the DNA clearly arises from its electromagnetic interaction with the AgNPs and not due to an increased number density of DNA adsorbed on the rough nanotips. This is because bare AuNTs, with high immobilization efficiency, did not produce any enhanced SERS signal of the DNA (figure 7-9c) compared to figure 7-10.

Figure 7-11 shows the SERS signals from different concentrations of hybridized ds-DNA on the optimized AgNPs coated AuNTs (as in figure 7-8e). The high SERS enhancement of the AuNT array based sensing platform enabled DNA detection down to 1.2×10^{-13}M concentration. The 1168cm^{-1} Raman fingerprint signals of the A and

T species and 1300cm^{-1} of the T species [7-42, 7-49, 7-50] were clearly resolvable at the lowest concentration. The integrated intensity of the 1300cm^{-1} line of T (see figure 7-14), as a function of concentration, shows a variation similar to what the Langmuir isotherm would predict and is nearly linear over the 120fM to 10nM range.

Lastly, any practical sensor platform must demonstrate a reasonable stability, given the fact that surface enhanced Raman signals are known to decay within hours of preparation. The stability of the current platform was tested by measuring the Raman activity with time. Individual ss-DNA, with 10^{-6}M concentrations, immobilized on our optimized platform showed 50-65% remnant intensity (of the strongest Raman line) after 144 h of storage in ambient desk-top conditions (see figure 7-14). The data in figure 7-14 contains a scatter of five similar experiments on different pieces of the same substrate. Hence, the scatter is a measure of the reproducibility of the substrates. Even low concentrations (1.2 nM) of hybridized ds-DNA can retain up to ~40% of the initial intensity of a particular Raman line even after 3 weeks of the immobilization when conserved under normal desktop conditions on the optimized substrates (figure 7-12). These results demonstrate outstanding stability characteristics enabling clear and unambiguous detection.

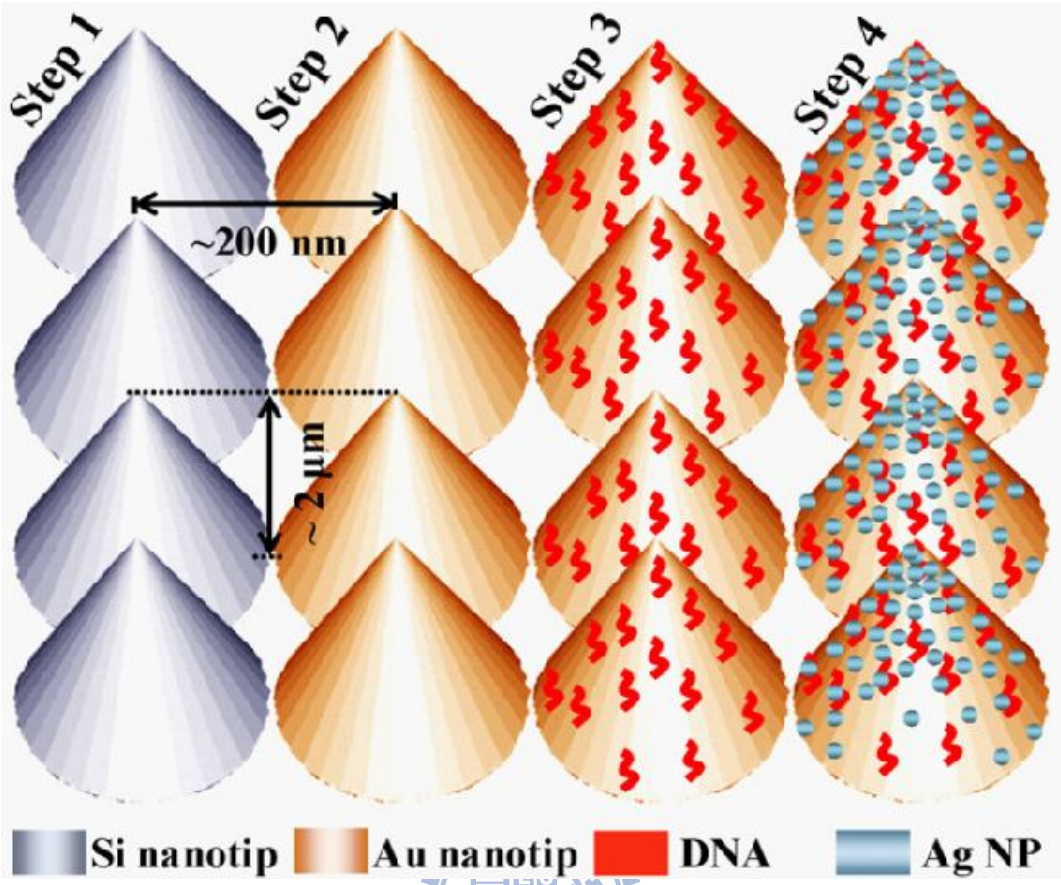

Figure. 7-7. A schematic of the pathway for generating the SERS platform. Step 1: the as-grown silicon nanotip array template; Step 2: Au coating of the SiNT array to generate the AuNT array for efficient DNA immobilization; Step 3: immobilization of DNA molecules on the AuNT array; Step 4: silver nanoparticle (AgNP) deposition for efficient Raman signal enhancement.

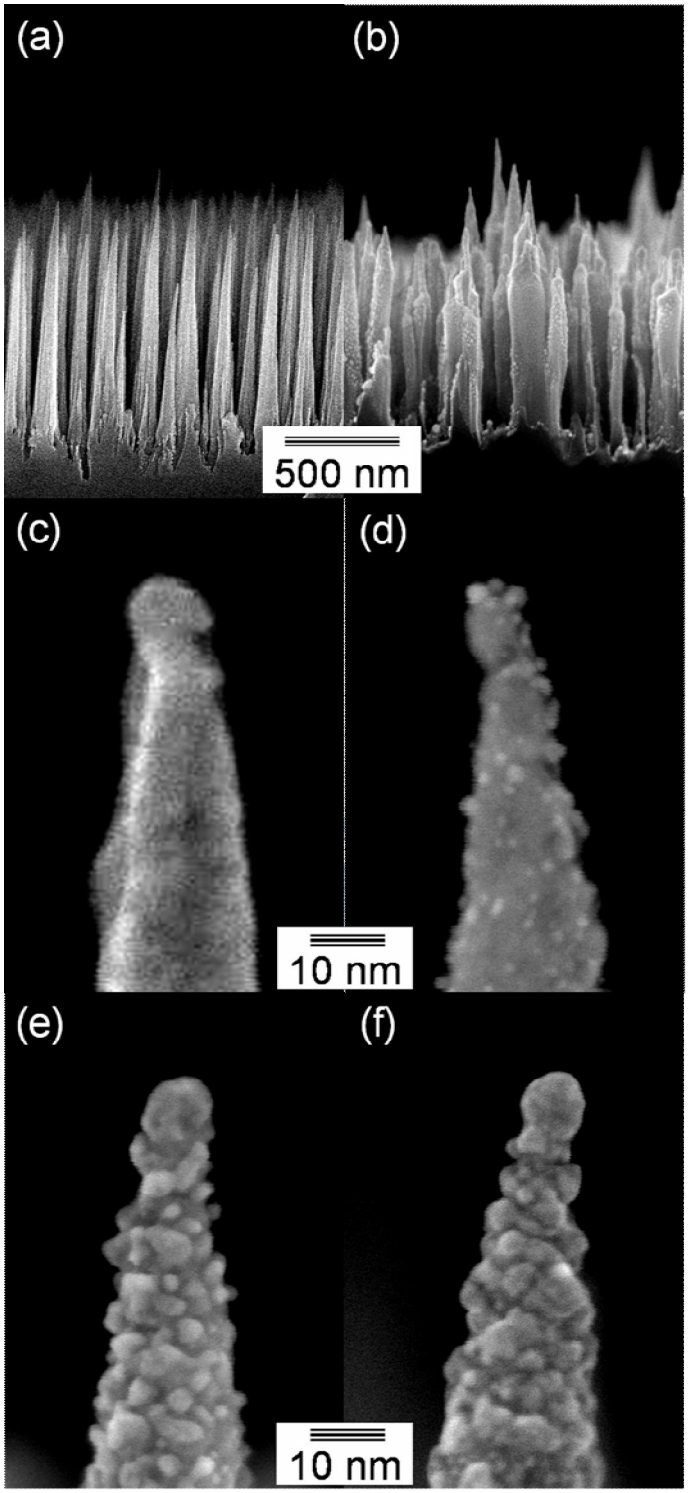

Figure. 7-8. Cross-section high resolution scanning electron microscopy (HR-SEM) images of (a) as-grown SiNTs, (b) low magnification of Au coated SiNTs, (c) high magnification of Au coated SiNTs; cross-section SEM images of AuNTs covered with AgNPs sputtered for (d) 5, (e) 10 and (f) 20 min by IBSD system.

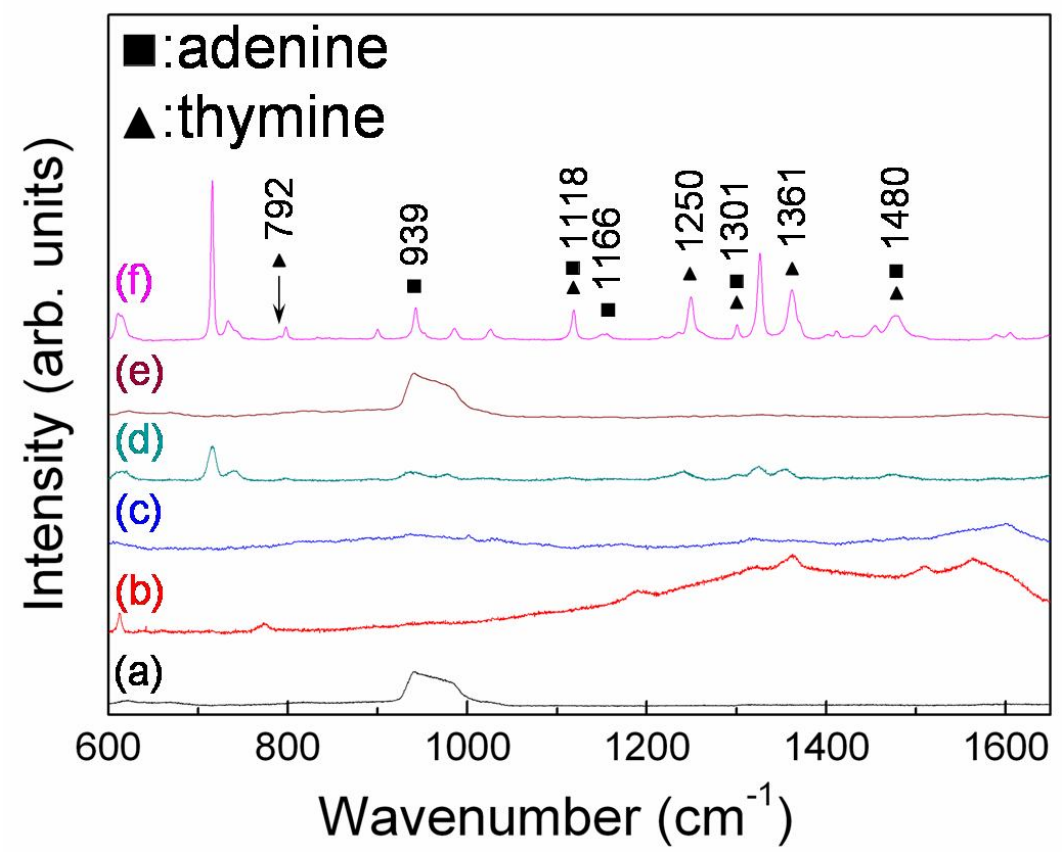

Figure. 7-9. Raman scattering spectrum of 1.2nM of (a) Rhodamine 6G adsorbed on SiNT and SERS spectrum of (b) Rhodamine 6G adsorbed on AuNTs. SERS spectrum of hybridized A and T, on AuNT, at (c) 1.2nM and (d) 12mM concentrations. (e) Raman spectrum of hybridized ds-A + T (12mM concentration) on planar Si. (f) The Raman spectrum of bulk A and T powder dispersed on planar silicon wafer. The symbols ■ and ▲ represent Raman bands of adenine and thymine, respectively.

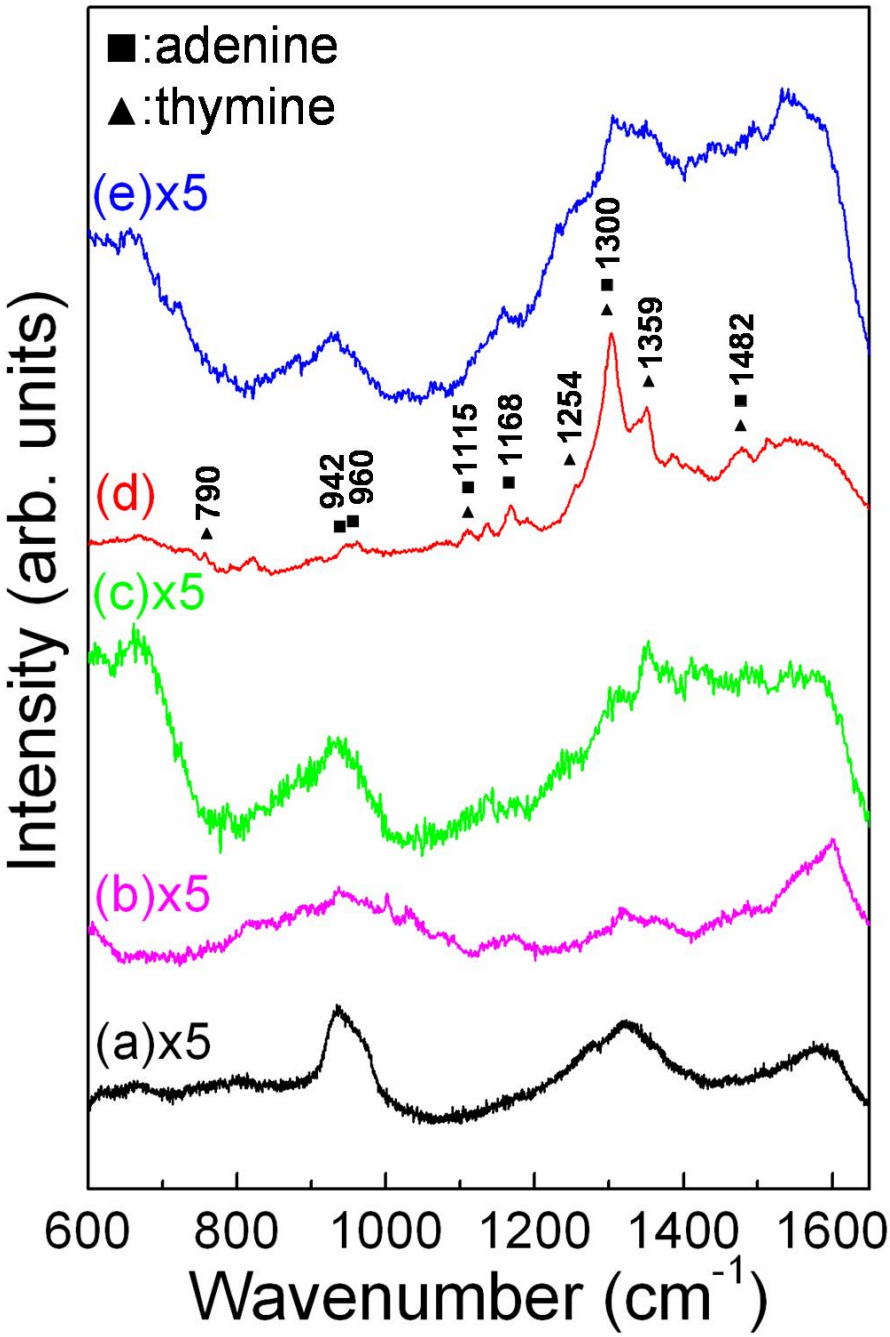

Figure. 7-10. Raman scattering spectrum of the (a) as-grown AuNTs. SERS spectra of thiolated ss-A hybrized with ss-T (1.2nM) obtained on AuNTs decorated with AgNPs sputtered for (b) 0 (bare AuNTs), (c) 5, (d) 10 and (e) 20 min. The symbols ■ and ▲ represent Raman bands of adenine and thymine, respectively.

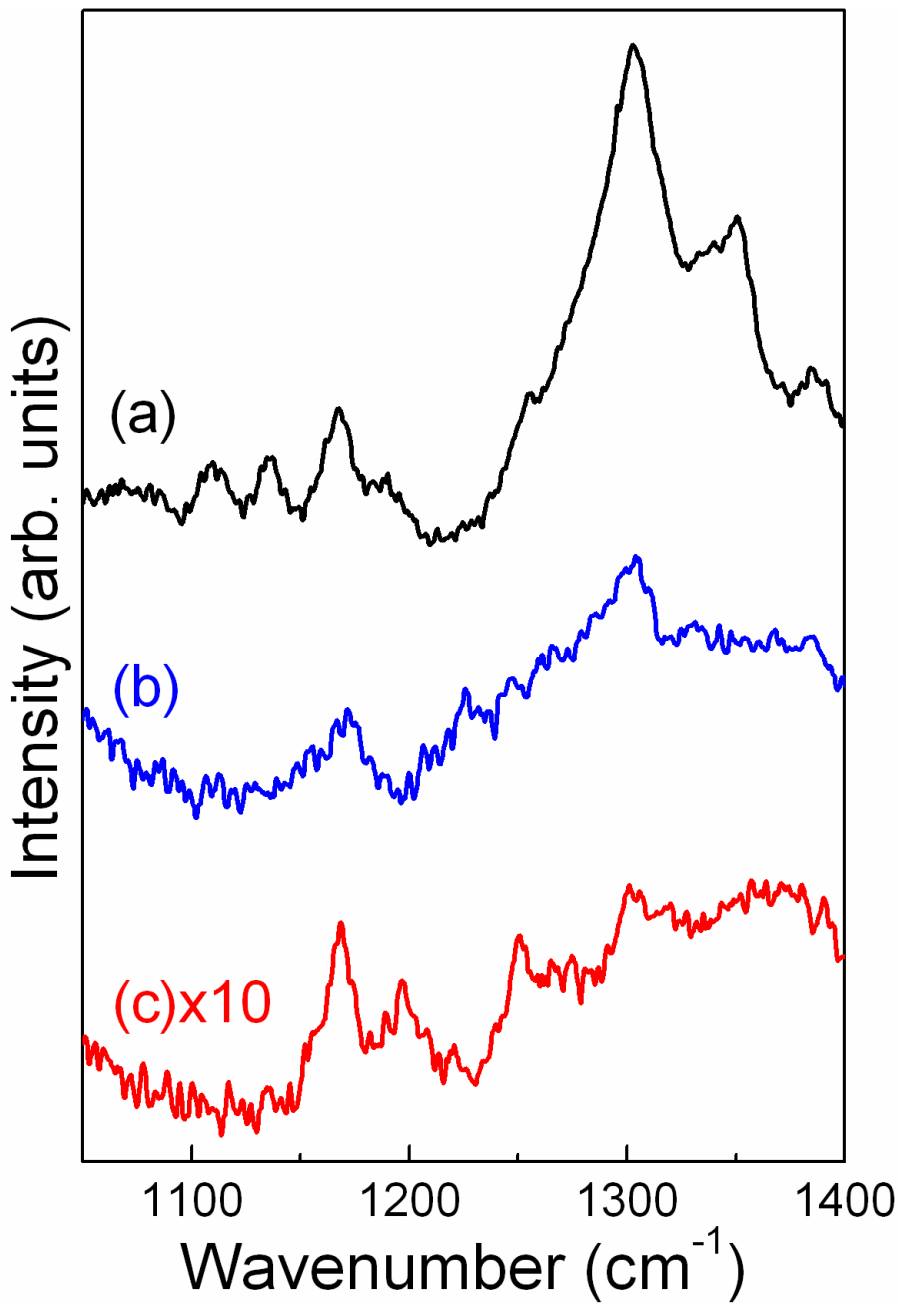

Figure. 7-11. SERS spectra of thiolated ss-A hybrized with ss-T, on the optimized substrates (as in figure 7-8e), with concentrations of (a) 1.2nM, (b) 12pM and (c) 120 fM.

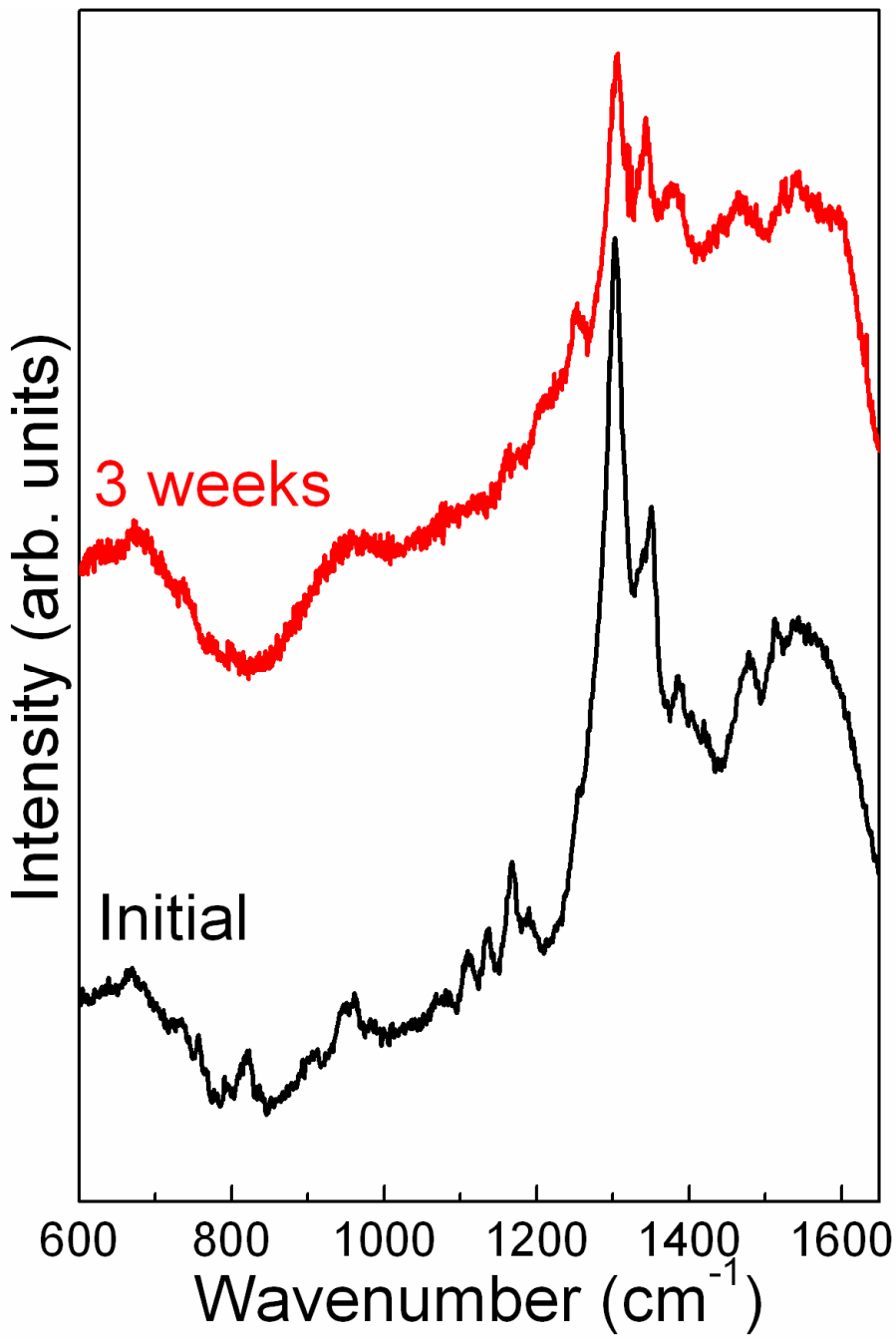

Figure. 7-12. Time decay of the SERS spectrum. Aging of SERS spectrum of 1.2nM of hybridized ds-A with T on AuNTs decorated with AgNPs sputtered for 10 mins (optimized substrate, as in figure 7-8e).

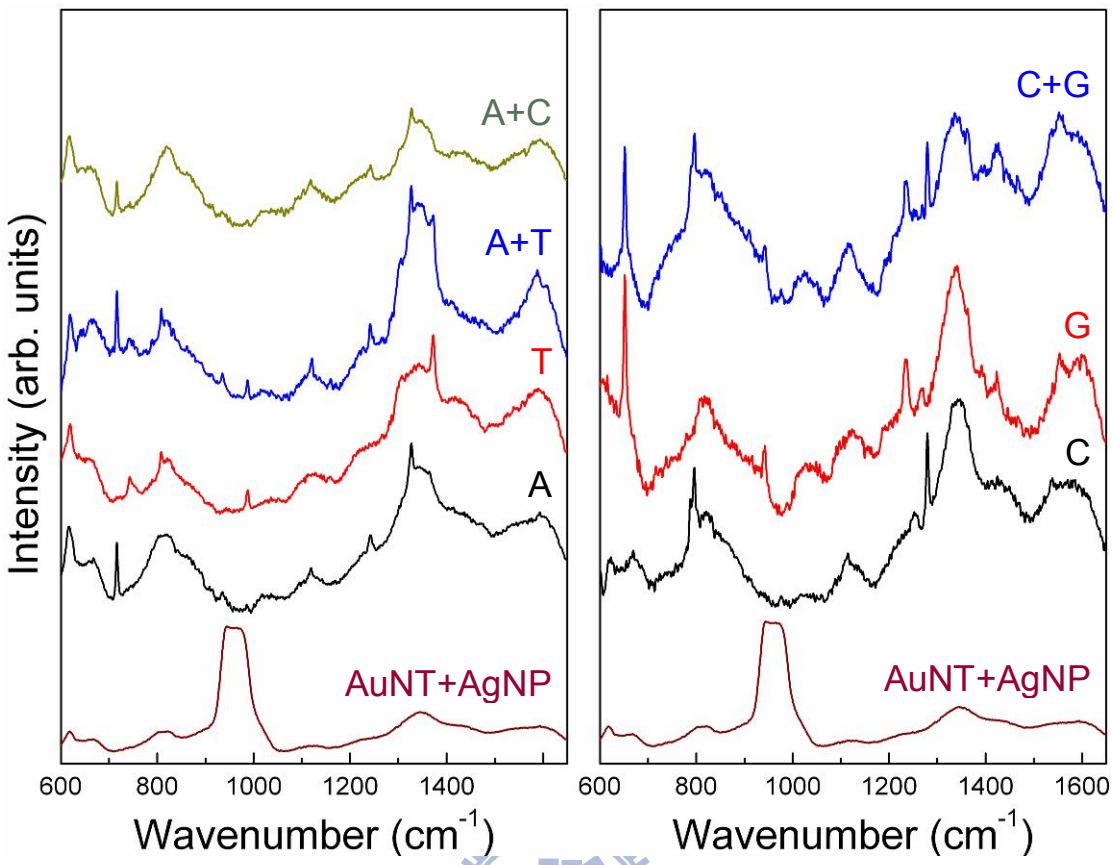

Figure. 7-13. SERS spectra of individual *ss*- and hybridized *ds*- DNA on the AgNP decorated AuNT platform. Background subtracted SERS spectra of *ss*- and hybridized *ds*- nucleotides, with 1.2 nM concentrations, measured on the optimized substrate (as in figure. 7-8e): a) Individual thiolated *ss*-A (A), *ss*-T (T) and hybridized A with T (A+T), and b) individual thiolated *ss*-C (C) , *ss*-G (G) and hybridized C with G (C+G). The top plot (A+C) in (a) shows SERS spectrum of thiolated *ss*-A with non-complimentary *ss*-C (without thiol) after washing. SERS spectra of optimized substrate (AuNT+AgNP) is the background for all the spectra shown in (a) and (b).

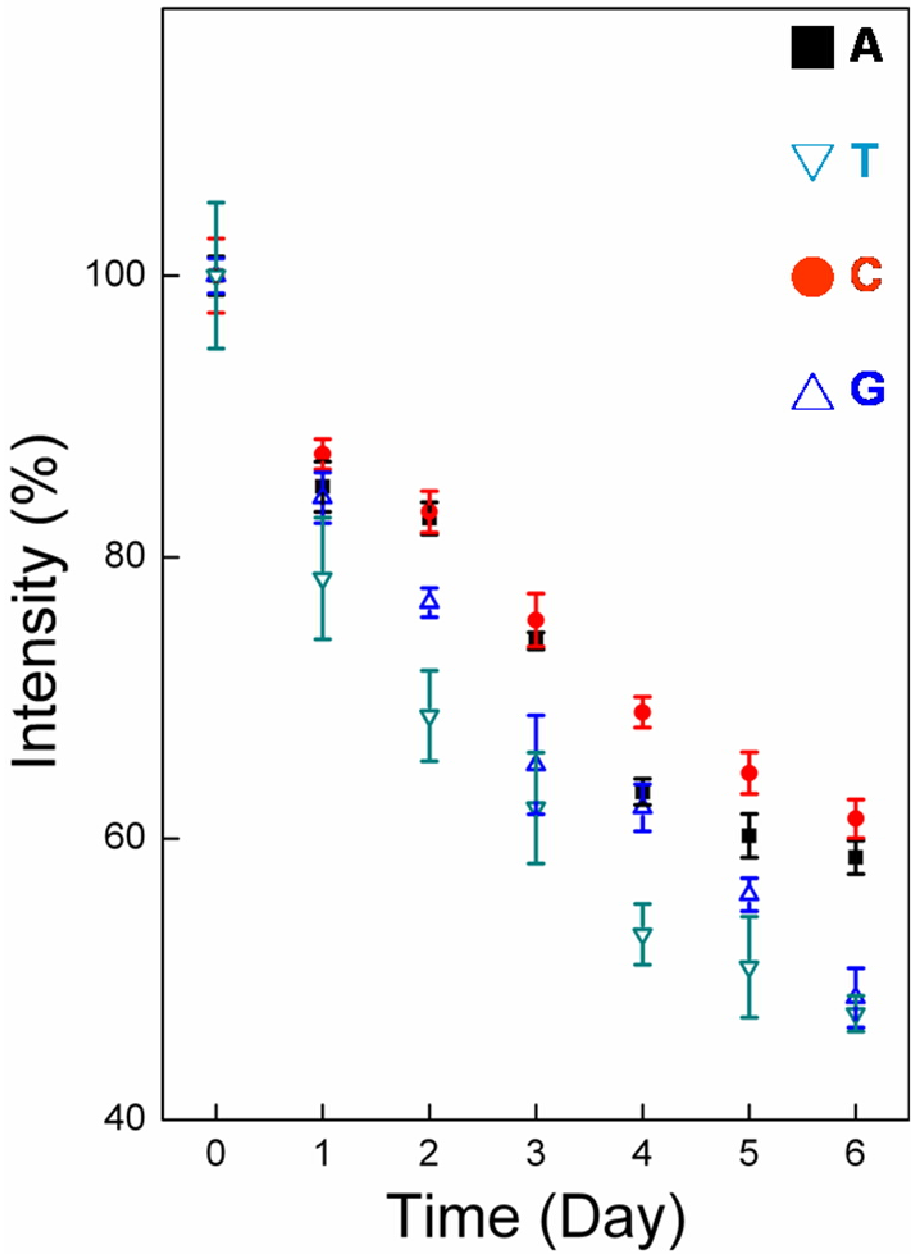

Figure. 7-14. Decay of SERS signals of DNA. Decay of SERS signals of thiolated *ss*-A, T, C and G (1.2 μM each) immobilized on AgNP decorated AuNTs (optimized substrate) as a function of time (Days). Intensity of the 1300, 1359, 1279, and 652 cm^{-1} line is taken as the reference for A, T, C, and G, respectively, (see figure 7-13) in this experiment. The error bar measures the scatter of the data. The data is normalized by setting the mean of the scatter on day 0 to 100 %.

Chapter 8. Geometrically tuned and chemically switched wetting properties of silicon nanotips

8-1 INTRODUCTION

The wetting property is an expression of the surface energy of a material and is crucial for fundamental understanding as well as from the point of view of applications. 'Unfreezable water' can exist at sub-freezing temperatures around a hydrophilic surface due to equilibrium hydration effects [8-1]; this can be contrasted with the super water repellent properties (hydrophobicity) of nanostructured plant surfaces [8-2] that mimic the 'lotus effect'. These both come down to a surface engineering problem of synthesizing 'wetting' (hydrophilic) and 'de-wetting' (hydrophobic) surfaces to meet our technological needs. The need for hydrophobic properties is generally obvious because of the growing importance of bio-electromechanical systems (bio-MEMS) where fluidic reactants are pushed through micrometre-sized channels and reactions made to occur in micrometre sized reactors [8-3]. Properties of low flow resistance [8-4] and high water contact angle can be used in microfluidics and labon-chip devices. It is known that a high degree of surface roughness (geometrical factor) results in solid surfaces having hydrophobic properties [8-5, 8-6]. A super-hydrophobic surface is created when a rough surface is coupled with a self assembled layer of low surface energy fluorinated compounds (chemical factor) [8-4, 8-7~8-10]. Hydrophilic surfaces, on the other hand, are generated mostly by using dry processes [8-11, 8-12] such as corona discharge or a plasma discharge/jet on metal-polymer or metal-metal surfaces to enhance the adhesion and wettability. In contrast to the numerous reports on super-hydrophobicity,

those concerning super- hydrophilicity are scarce. An interesting report demonstrated the super-hydrophilic and oleophilic properties of both anatase and rutile TiO_2 surfaces upon UV irradiation [8-13]. Electrochemical generation of a super-hydrophilic surface on In_2O_3-SnO_2coated glass by the application of high anodic potentials was demonstrated to give an anti-fogging property [8-14]. However, dynamic or reversible wetting-dewetting behaviour seems to be the most attractive of the surface properties. Reversible wetting behaviour caused by the application and removal of an electrical potential on a self-assembled monolayer (SAM) surface has been demonstrated [8-15]. Controlled hydrophobic and hydrophilic domains have also been created in microchannels [8-16, 8-17] or patterned Si substrates [8-18]. This paper reports on the wetting properties of silicon nanotips (SiNTs) as a function of their aspect ratio (α = length (l)/base diameter (D)) and inter-tip distance (β) (geometrical effect), and when the SiNT surface is modified by TiO_2 particles (chemical effect).

8-2 MATERIALS AND METHODS:

Synthesis: Silicon nanotips were prepared from bare untreated p-type Si(100) wafers exposed to an electron cyclotron resonance (ECR) plasma of silane (SiH_4), methane (CH_4), argon (Ar) and hydrogen (H_2) gases. Gas phase reaction between SiH_4 and CH_4 dissociation products resulted in the formation of SiC nanoclusters on the Si surface. Subsequent physico-chemical etching of the Si surface with the SiC acting as a nanomask created the SiNTs. The entire fabrication process for the SiNTs is called a self-masked dry etching (SMDE) technique [8-19, 8-20]. The structural characterizations have already been reported [8-19, 8-20].

Morphology characterization: The length of a SiNT can be very effectively controlled by a single process parameter, namely the substrate temperature. The change in the morphology of a SiNT as a function of the substrate temperature was studied by high resolution scanning electron microscopy (HRSEM) (JEOL JSM 6700F) as shown in figure 1. The ratio of the length and the base diameter of the nanotip indicate its aspect ratio which was determined from cross-sectional HRSEM images.

TiO_2 coating: The TiO_2 coating of the SiNTs was done by Ar ion-beam sputtering (IBS) of a TiO2 target at a pressures of 5 x 10^{-4} Torr at room temperature. Details of the IBS system can be found elsewhere [8-21].

Contact angle measurements: The water contact angles were measured in a standard FACE contact anglemeter setup (model CA-D, Kyowa Interface Science Co. Ltd, Japan) attached to a CCD camera.

8-3 RESULTS AND DISCUSSIONS:

The formation of SiNTs is based on the generation of an SiC nanomask on the Si surface resulting from gas phase reactions between the dissociated products of SiH_4 and CH_4 in the high density ECR plasma [8-19]. Dissociation of SiH_4 and CH_4 into the lower hydrides (MH_x, where M is Si or C, and x = 1, 2, 3) follows via abstraction of hydrogen by thermal, electron or excited Ar impact dissociation. A series of reactions can lead to the formation of SiC nanomasks which deposit on the silicon [8-22, 8-23]. Any addition of SiH_4 can promote the formation of SiC in a plasma environment [8-24]. The length of the SiNT can be very effectively controlled by a single process parameter, namely the substrate temperature. SiNTs were fabricated at different substrate temperatures and their length was found to vary inversely with the substrate temperature (figure 8-1).

The SiNT fabricated at 250 ºC was the longest at ~2 μm; the shortest, 100 nm, was formed when the substrate temperature was 700 ºC. Beyond this temperature formation of SiNTs was inhibited. This is explained as follows. The rate constants for the dissociation of SiH_4 exceed CH_4 by three orders in magnitude at a temperature of 250 ºC, whereas the difference is only one order of magnitude at 700 ºC [8-25]. This signifies efficient formation of SiC at higher temperatures. As a consequence, random deposition of SiC nanomasks on silicon will be favored at lower temperatures and formation of SiC thin film will be promoted at higher temperatures. The etching will be done predominantly by the Ar and H_2 species. We estimated that just physical sputtering, say by Ar, may not result in efficient etching of the silicon substrate. A combination of physico-chemical sputtering that includes ion-assisted chemical etching will be required to bring about such sputtering of the silicon substrate. The high density ECR plasma provides an ideal medium or active etchants such as H, H^+,

H^{+2}, H^{+3}, Ar^{+} and ArH^{+}. In the two extreme substrate temperatures, i.e. 250 and 800 ºC, etching will continue through the SiC nanomask mesh in the former whereas etching will be hindered for the latter, having a continuous SiC thin film. Thereby longer nanotips will result at lower growth temperatures, whereas upon exceeding 700 ºC nanotips formation will be inhibited (figure 8-1). In short, single parameter tunability of the length of the SiNT, and hence α, has been achieved. Similarly, β can be controlled by the gas flow ratios. A higher Ar/H_2 and lower SiH_4/CH_4 will increase β, and vice versa.

Measurements of the water contact angle (θ) performed on SiNTs having different α yielded a very interesting and consistent result (figures 8-1 and 8-2). Apart from the cross sectional SEM images of the SiNTs, the insets in figure 8-1 show optical photographs of the water droplet on corresponding SiNTs. Figures 8-2 and 8-3 show the advancing (θ_{adv}) and receding (θ_{rec}) water contact angles as a function of α and β, respectively. For the high α or β case only θ_{act} is shown, since θ_{adv} and θ_{rec} could not be measured due to the super-hydrophilicity demonstrated in them. θ_{act} is the intrinsic water contact angle measured with a horizontal substrate and fixed droplet volume. A systematic decrease in θ has been observed with increasing α and can reproducibly approach 2º at large α (~15). The larger α (>12) showed super-hydrophilicity (θ_{act} ~ 2º), whereas the smaller α (<5) progressively showed lesser hydrophilicity (increasing θ_{act}) (figure 8-2). In figure 8-2 the inter-tip distance (β) was kept between 100 and 180 nm. The samples with α = 2, 3, had β on the larger side. It is understood that surface energy and adhesion tension that dictate the wetting properties of a solid surface will vary as a function of the roughness of the surface. If we quantify a roughness factor (r) according to Wenzel [8-5], as the ratio of the actual (rough) area to the geometrical (planar) area, then a hydrophilic starting material may result in super-hydrophilicity if the roughness factor is high enough. This condition is achieved with α > 7 and $\theta_{act} \rightarrow$

0. The data points for α=5 (figure 8-2) when fitted according to $\cos \theta_{act} = r \cos \theta$ (Wenzel's equation), yield r ~ 1.41, which is underestimated by a factor of ~16 when the actual surface area is calculated. The actual surface area is calculated from the microscopically determined density (~10^{10} cm^{-2}), length (~0.2-2 μm) and base radius (~100 nm) of the SiNTs, which are assumed to be conical. Hence we agree with Bico et al [8-26] that the roughness is an extremely intricate factor for the Wenzel's equation to hold since the right-hand side cannot exceed 1. However, it has been shown before that for fractal surfaces 'r' can assume large values where the Wenzel equation will no longer be applicable [8-27]. A similar situation arises here too as for the high α case, where the calculated r is close to ~23. But still, the super-hydrophilicity is predicted well for the SiNT surface having high α. Note that the Cassie model [8-6] does not explain this behaviour observed in figure 8-2. Assuming air gaps between these SiNTs, that might support the weight of a water droplet, the Cassie model would predict hydrophobicity as also obtained from vertically aligned carbon nanotube arrays [8-28]. However, a large hysteresis in θ is observed, as seen from the large departures of θ_{adv} and θ_{rec}, the latter being close to bulk silicon θ for each α < 5. Hence, instead of judging each contact angle, θ, θ_{adv} or θ_{rec}, independently, the trend of variation of these taken together, bears more physical significance. The increasing θ with reducing α < 5 can be attributed to an increasing β. At such low α it was difficult to keep a constant density for the SiNTs so that they touched each other at the base, a condition fulfilled for α = 7. The two data points in figure 8-2 for α = 2 and 3, are consistent with figure 3 for SiNT lengths of 250 nm.

The variation of θ as a function of β, measured for very long (7 μm) and short (250 nm) SiNTs is shown in figure 8-3. Interestingly, θ decreased for the shorter SiNTs and increased for the longer ones, and β was increased. For the shorter as well as longer SiNTs, a large β (1/β < 1) implies a morphology close to an intrinsic flat silicon

surface ($r \rightarrow 1$), hence $\theta_{act} \approx 48°$. An increasing roughness instilled by a small β should then drive the surface to hydrophilicity, which it does for the longer SiNTs. However, for the shorter SiNTs the trend is that of an increasing θ, although θ_{rec} stays close to the intrinsic value for flat Si. The results of increasing θ for the low α and β (shorter SiNTs) have been repeated and are reproducible. However, some error in measurement cannot be ruled out. A model by Lenz and Lipowsky [8-29] predicts an increase in θ if the surface has a patterned hydrophilic-hydrophobic domain structure. However, this model is not applicable in this case since the SiC cap and the chemically pure silicon in the body of the SiNT have similar wetting properties. The Cassie model which should be applicable for hydrophobic surfaces or the large 'r' regime seems to fail even if our surfaces have $r > 20$. The Wenzel model succeeds qualitatively, in a limited way, in predicting the super-hydrophilicity.

Consider SiNTs with a high value of α that yields vanishing water contact angles. The SiNTs were coated using Ar ion-beam sputtering [8-21] of a TiO_2 target. The TiO_2 formed particle-like features on the SiNTs. A similar coating of TiO_2 on a polished Si wafer produced θact ≈ 72º (figure 8-4(a)). The amphiphilic (hydrophilic as well as oleophilic) TiO_2 shows super-hydrophilicity when irradiated by UV light [8-13]. However, in this case, when deposited on the SiNTs they exhibited hydrophobicity. Upon coating with TiO_2, the super-hydrophilic SiNT with $\theta_{act} \approx 2º$ (figure 8-1(a)) exhibits $\theta_{act} \approx 140º$ (figure 8-4(b)), with $\theta_{rec} = 74º$, $\theta_{adv} = 110º$. Assuming a similar roughness for the bare SiNTs and those coated with TiO_2, switching from wetting to de-wetting behavior has been observed with the help of a TiO_2 layer. Evidently, a discontinuity exists in the water contact angles, promoted by TiO_2, at a particular roughness value. An increase in θ may be expected due to contamination and impurities in the TiO_2 surface [8-30]. However Wenzel's model predicts a rough TiO_2 surface to be more hydrophilic than the planar one. Hence the

switch from super-hydrophilic (as-grown SiNT with high α) to hydrophobic (TiO_2 coated SiNT) is interesting and is not well understood at present. The result shown in figure 8-4 can only be explained with Cassie's model by assuming air columns to be trapped under the water droplet. This was clearly not the case for the as-grown SiNT ($\theta_{act} \approx 2°$) and hence we have to assume that a nanostructured TiO_2 induced air trapping under the droplet, creating a second line of contact between air and water other than TiO_2 and water. The two roughness scales existing in the SiNTs and that on the nanostructured TiO_2 coating contribute to this unusual hydrophobicity.

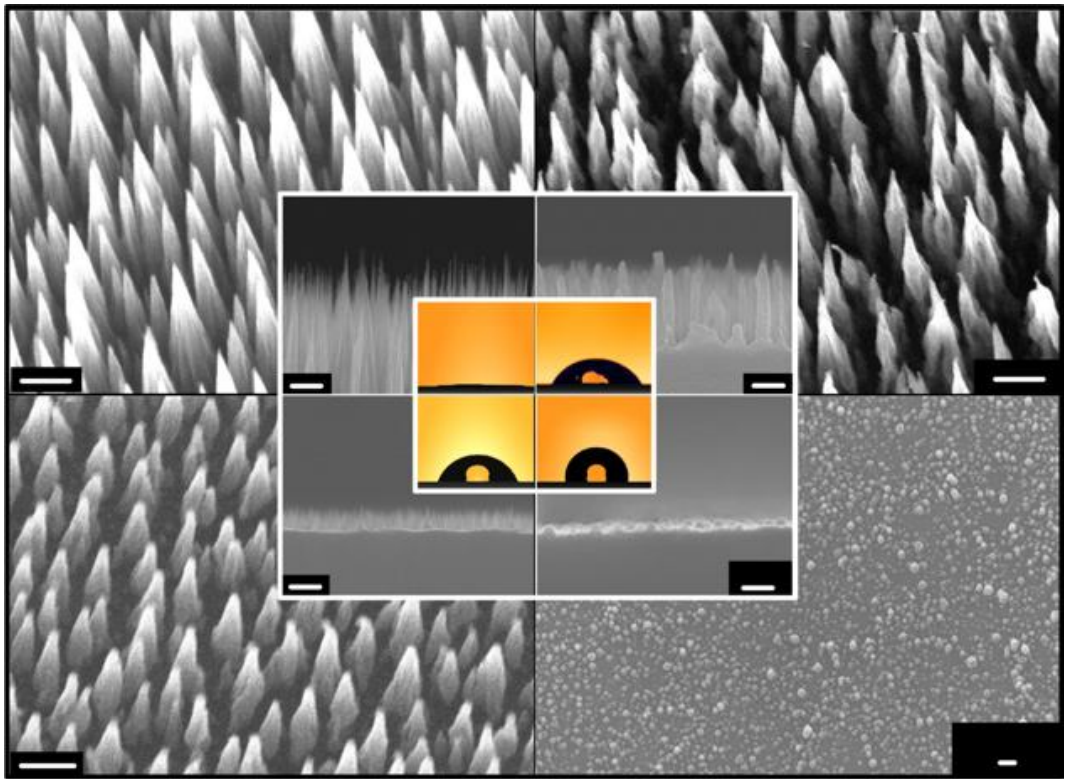

Figure 8-1. Tilted view SEM images of SiNTs grown at different temperatures: (a) 250 °C. (b) 400 °C. (c) 600 °C and (d) 700 °C. The inset in each shows the cross-sectional SEM images and the corresponding optical photograph of a water droplet indicating the contact angle. Scale bars for (a)-(d) are 100 nm and those in the inset are 200 nm.

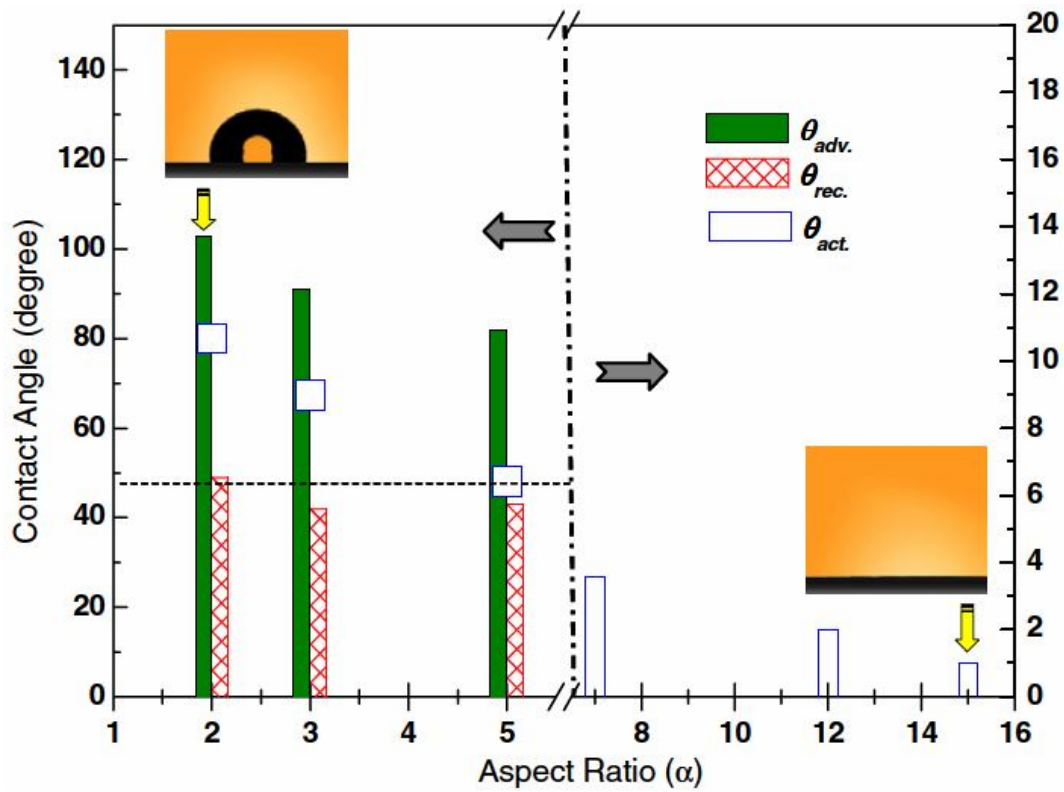

Figure 8-2. Advancing, receding and intrinsic water contact angles as a function of aspect ratios (α) of the silicon nanotips. An optical photograph of a water droplet indicating the contact angle is shown for the two extreme α values. A reference value of the water contact angle at 48° for a polished silicon wafer is indicated by the dashed line.

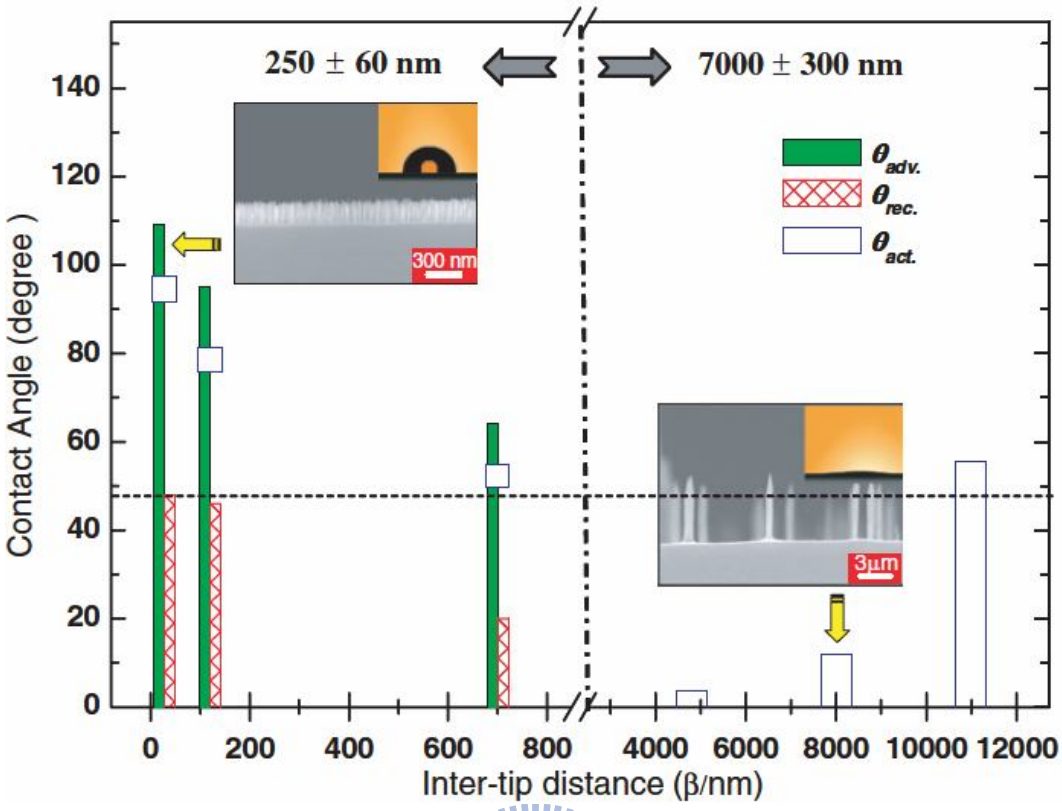

Figure 8-3. Advancing, receding and intrinsic water contact angles as a function of inter-tip distance (β) of the silicon nanotips. A cross-sectional SEM image and corresponding optical photograph of a water droplet indicating the contact angle is shown for the two different β values. A reference value of water contact angle at 48° for polished silicon wafer is indicated by the dashed line.

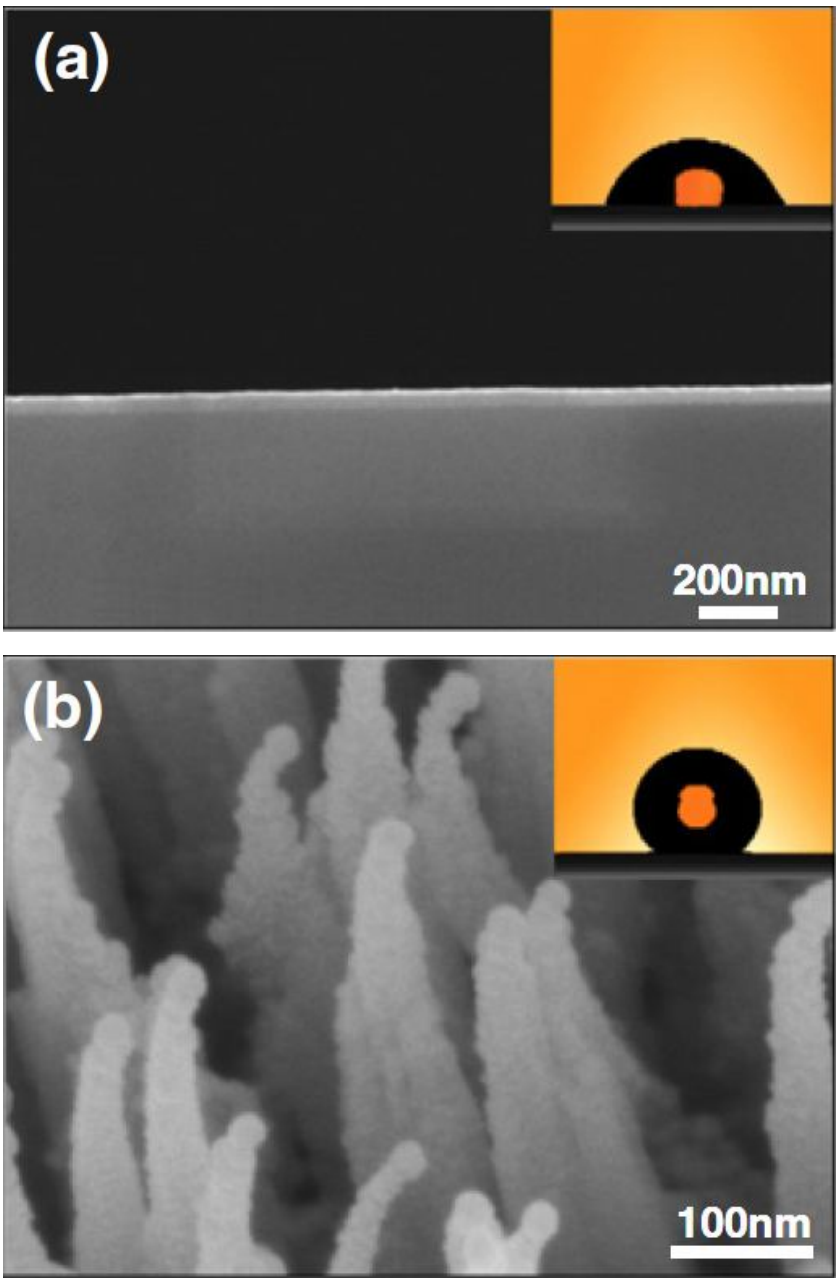

Figure 8-4. (a) Cross-sectional SEM image of a TiO_2 coated polished silicon wafer. (b) Tilted view SEM image of a TiO_2 coated silicon nanotip. The inset shows an optical photograph of a water droplet indicating the contact angles on the respective substrates.

Chapter 9. Conclusion and future prospects

9-1 Conclusion

Systematic investigation of the 1-D nanotip arrays has been carried out in this thesis work. the formation mechanism, control of nanotip density, size, aspect ratio and post processing with additional Au/Ag nanoparticle decoration have been demonstrated. For the studies on the field emission, cell culturing, contact angle, and SERS applications has been performed. Major conclusions include:

1. Quantum confinement effects in Si as well as compound semiconductors (GaN, GaP, Al, Al_2O_3 and Glass) arising from reduction in dimensions have been widely investigated via new developed SMDE technique.
2. The field emission property of such sharp Si nanotip arrays in a simple diode structure reveals an ultralow turn-on field (defined as the field at which an emission current density of 10 uA/cm^2 is obtained) of 0.35 V/um.
3. The neuron cell cultivated on SMDE made Au nanotip arrays revealed that, regardless of the surface structure of the template, neuron cell viability and proliferation could be manipulated by changing the surface charge of the template, which we accomplished via Au coating of the template. Such an approach could be applied to a variety of different cell culture as well as template surface structures and coatings, enabling the study of a vast realm of different cell cultures and potential applications.
4. The self-assembled silver nanoparticles mono-dispersed on silicon nanotips, formed by self-masked dry etching of crystalline silicon substrates, demonstrated high activity for surface-enhanced Raman scattering. Molecules such as R6G, BPE and DNA with concentrations as low as sub-picomole could be detected in a

reproducible and stable fashion with the help of these substrates.

5. Nanoscale surface texturing and designs can be achieved reproducibly to tailor the hydrophilicity of the silicon nanotips. Super-hydrophilicity has been achieved for nanotips with a high aspect ratio which can only be predicted qualitatively by the Wenzel model. An unusual switching of the wetting properties has been observed upon chemical modification of the surface of the nanotip by coating with TiO_2 that renders it hydrophobic.
6. The excellent anti-reflection properties observed in the SiNTs with gradient reflective index are close to near-ideal anti-reflection coatings.

9-2 Future prospects

1. Fabricate the nanotip structure on hard material need to be investigated for the other applications such as gas ionization was required.
2. Self assembled nanostructure on nanotip arrays via electron emission technique was required for further application such as CO/CO_2 transformation.
3. The guided growth of neuron cell culture was required for next generation bio computer development.
4. The development of bio sensing template via nanotip arrays with suitable post treatment was required for medical engineering applications.
5. Tunable wetting properties were valuable to develop for humid adsorption from atmosphere environment which may solve the drinking issue of specific area such as desert.

References and Notes

Chapter 1

[1-1] Merkoci, A. *Biosensing Using Nanomaterials*. Wiley. **2009**.

[1-2] Krug, H. *Nanotechnology*, **2008**, *2*: Environmental Aspects. Wiley-VCH.

[1-3] Janasek, D.; Franzke, J.; Manz, A. *Nature*, **2006**, *442*, 374.

[1-4] Yager, P.; Edwards, T.; Fu, E.; Helton, K.; Nelson, K.; Tam, M. R.; Weigl, B. R. *Nature*, **2006**, *442*, 412.

[1-5] Lee, M.; Baik, K. Y.; Noah, M.; Kwon, Y. K.; Lee, J. O.; Hong, S. *Lab Chip*, **2009**, *9*, 2267.

[1-6] Sears, G. W. *Acta. Met.*, **1953**, *1*, 457.

[1-7] Wagner, R. S.; Ellis, W. C. *Appl. Phys. Lett.*, **1964**, *4*, 89.

[1-8] Sasaki, H. *Jpn. J. Appl. Phys.*, **1980**, *19*, L735.

[1-9] Hiruma, K.; Yazawa, M.; Katsuyama, T.; Ogawa, K.; Haraguchi, K.; Koguchi, M. *J. Appl. Phys.*, **1995**, *77*, 447.

[1-10] Morales, A. M.; Lieber, C. M. *Science*, **1998**, *279*, 208.

[1-11] Burton, W. K.; Cabrera, N.; Frank, F. C. *Nature*, **1949**, *163*, 398.

[1-12] Burton, W. K.; Cabrera, N.; Frank, F. C. *Phil. Trans. Roy. Soc. London*, **1951**, *243*, 299.

[1-13] Sears, G. W. *Acta. Met.*, **1955**, *3*, 361.

[1-14] Sears, G. W. *Acta. Met.*, **1955**, *3*, 367.

[1-15] Brenner, S. S. *Acta. Met.*, **1956**, *4*, 62.

[1-16] Coleman, R. V.; Sears, G. W. *Acta. Met.*, **1957**, *5*, 131.

[1-17] Morelock, C. R.; Sears, G. W. *J. Chem. Phys.*, **1959**, *31*, 926.

[1-18] Brenner, S. S.; Sears, G. W. *Acta. Met.*, **1956**, *4*, 268.

[1-19] Gomer, R.; *J. Chem. Phys.*, **1958**, *28*, 457.

[1-20] Parker, R. L.; Anderson, R. L.; Hardy, S. C. *Appl. Phys. Lett.*, **1963**, *3*, 93.

[1-21] Hirth, J. P.; Pound, G. M. *J. Phys. Chem.*, **1960**, *64*, 619.

[1-22] Parker, R. L.; Hardy, S. C. *J. Chem. Phys.*, **1962**, *37*, 1606.

[1-23] Blakkly, J. M.; Jackson, K. A. *J. Chem. Phys.*, **1962**, *37*, 428.

[1-24] Ruth, V.; Hirth, J. P. *J. Chem. Phys.*, **1964**, *41*, 3139.

[1-25] Gomer, R. *J. Chem. Phys.*, **1963**, *38*, 273.

[1-26] Bierman, M. J.; Lau, Y. K. A.; Kvit, A. V.; Schmitt, A. L.; Jin, S. *Science*, **2008**, *320*, 1060.

[1-27] Zhu, J.; Peng, H. L.; Marshall, A. F.; Barnett, D. M.; Nix, W. D.; Cui, Y. *Nat. Nanotechnol.*, **2008**, *3*, 477.

[1-28] Lau, A. Y. K.; Chernak, D. J.; Bierman, M. J.; Jin, S. *J. Am. Chem. Soc.*, **2009**, *131*, 16461.

[1-29] Eshelby, J. D. *J. Appl. Phys.*, **1953**, *24*, 176.

[1-30] Drum, C. M.; Mitchell, J. W. *Appl. Phys. Lett.*, **1964**, *4*, 164.

[1-31] Webb, W. W.; Dragsdorf, R. D.; Forgeng, W. D. *Phys. Rev.*, **1957**, *108*, 498.

[1-32] Herring, C. *Phys. Rev.*, **1951**, *82*, 87.

[1-33] Kaldis, E. *J. Cryst. Growth*, **1969**, *5*, 376.

[1-34] Sears, G. W. *J. Chem. Phys.*, **1956**, *25*, 154.

[1-35] Givargizov, E. I. *J. Cryst. Growth*, **1975**, *31*, 20.

[1-36] Givargizov, E. I. *Highly Anisotropic Crystals*, Reidel, Dordrecht, **1987**, p.100.

[1-37] Bootsma, G. A.; Gassen, H. J. *J. Cryst. Growth*, **1971**, *10*, 223.

[1-38] Pan, Z. W.; Dai, S.; Rouleau, C. M.; Lowndes, D. H. *Angew. Chem. Int. Ed.*, **2005**, *44*, 274.

[1-39] Ding, Y.; Gao, P. X.; Wang, Z. L. *J. Am. Chem. Soc.*, **2004**, *126*, 2066.

[1-40] Parker, R. L. *J. Chem. Phys.*, **1962**, *37*, 1600.

[1-41] Dick, K. A.; Deppert, K.; Martensson, T.; Mandl, B.; Samuelson, L.; Seifert,

W. *Nano Lett.*, **2005**, *5*, 761.

[1-42] Dick, K. A.; Deppert, K.; Karlsson, L. S.; Wallenberg, L. R.; Samuelson, L.; Seifert, W. *Adv. Funct. Mater*, **2005**, *15*, 1603.

[1-43] Kamins, T. I. *J. Appl. Phys.*, **2001**, *89*, 1008.

[1-44] Hofmann, R.; Sharma, S.; Wirth, C. T.; Cervantes-Sodi, F.; Ducati, C.; Kasama, T.; Dunin-Borkowski, R. E.; Drucker, J.; Bennett, P.; Robertson, J. *Nat. Mater.*, **2008**, *7*, 372.

[1-45] Harmand, J. C.; Patriarche, G.; Pere-Laperne, N., Merat-Combes, M. N.; Travers, L.; Glas, F. *Appl. Phys. Lett.*, **2005**, *87*, 203101.

[1-46] Campos, L. C.; Tonezzer, M.; Ferlauto, A. S.; Grillo, V.; Magalhaes-Paniago, R.; Oliveira, S.; Lacerda, R. G. *Adv. Mater.*, **2008**, *20*, 1499.

[1-47] Wang, Y. W.; Schmidt, V.; Senz, S.; Goesele, U. *Nat. Nanotechnol.*, **2006**, *1*, 186.

[1-48] Persson, A. I.; Larsson, M. W.; Stenstrom, S.; Ohlsson, B. J.; Samuelson, L.; Wallenberg, L. R. *Nat. Mat.*, **2004**, *3*, 677.

[1-49] Kodambaka, S.; Tersoff, J.; Reuter, M. C.; Ross, F. M. *Science*, **2007**, *316*, 729.

[1-50] Mohammad, S. N. *J. Chem. Phys.*, **2009**, *131*, 224702.

[1-51] Uhlir, A. *Bell Syst. Technol. J*, **1956**, *35*, 333.

[1-52] Turner, D. R. *J. Electrochem. Soc.*, **1958**, *105*, 402.

[1-53] Archer, R. J. *J. Phys. Chem. Solids*, **1960**, *14*, 104.

[1-54] Hummel, R. E.; Chang, S. S. *Appl. Phys. Lett.*, **1992**, *61*, 1965.

[1-55] Saadoun, M.; Mliki, N.; Kaabi, H.; Daoudi, K.; Bessais, B.; Ezzaouia, H.; Bennaceur, R. *Thin Solid Films*, **2002**, *405*, 29.

[1-56] Carstensen, J.; Christophersen, M.; Lolkes, S.; Ossei-Wusu, E.; Bahr, J.; Langa, S.; Popkirov, G.; Fo¨ll, H. *Phys. Stat. Solid C*, **2005**, *2*, 3339.

[1-57] Rieger, M. M.; Kohl, P. A. *J. Electrochem. Soc.*, **1995**, *142*, 1490.

[1-58] Allongue, P.; Kieling, V.; Guerischer, H. *Electrochim. Acta.*, **1995**, *40*, 1353.

[1-59] Rao, A. V.; Ozanam, F.; Chazalviel, J. N. *J. Electrochem. Soc.*, **1991**, *138*, 153.

[1-60] Gerischer, H. *Electrochem. Acta.*, **1990**, *35*, 1677.

[1-61] Beale, M. I. J.; Benjamin, J. D.; Uren, J.; Chew, N. G.; Cullis, A. G. *J. Cryst. Growth*, **1985**, *73*, 622.

[1-62] Canham, L. T. *Appl. Phys. Lett.*, **1990**, *57*, 1046.

[1-63] Smith, R. L.; Collins, S. D. *J. Appl. Phys.*, **1992**, *71*, R1.

[1-64] Dittrich, Th.; Timoshenko, V.; Rappich, J. *J. Appl. Phys.*, **2001**, *90*, 2310.

[1-65] Berger, M. G.; Dieker, C.; Thonissen, M.; Vescan, L.; Luth, H.; Munder, H. *J. Phys. D*, **1994**, *27*, 1333.

[1-66] Frohnhoff, St,; Berger, M. G.; Tho¨missen, M.; Dieker, C.; Vescan, L.; Mu¨nder, H.; Lu¨th, H. *Thin Solid Films*, **1995**, *255*, 59.

[1-67] Steckl, A.; Xu, J.; Mogul, H.; Prokes, S. *J. Electrochem. Soc.*, **1995**, *142*, L69.

Chapter 2

[2-1] Palumbo, G.; Doyle, D. M.; El-Sherik, A. M.; Erb, U.; Aust, K. T. *Scr. Metall. Mater.,* **1991**, *25*, 679.

[2-2] Bakonyi, I.; Toth-Kada, E.; Tarnoczi, T.; Varga, L. K.; Cziraki, A.; Gerocs, I.; Fogarassy, B. *Nanostruct. Mater.,* **1993**, *3*, 155.

[2-3] Groza, J. R. *Non-equilibrium Processing of Materials* ed C Suryana (Oxford: Pergamon), **1999**, 345.

[2-4] Lee, K. L.; Hatzakis, M. *J. Vac. Sci. Technol.,* **1989**, *B*7, 1941.

[2-5] Lee, K. L.; Abraham D. W.; Secord F.; Landstein, L. *J. Vac. Sci. Technol. B,* **1991**, *9*, 3562.

[2-6] Utke, I.; Hoffman, P.; Dwir, B.; Leifer, K.; Kapon, E.; Doppelt, P. *J. Vac. Sci. Technol. B,* **2000**, *18*, 3168.

[2-7] Weber, M.; Koops, H. W. P.; Rudolph, M.; Kretz, J.; Schmidt, G. *J. Vac. Sci. Technol. B,* **1995**, *13*, 1364.

[2-8] Weber, M. *J. Phys. D,* **1994**, *27*, 1363.

[2-9] Lau, Y. M.; Chee, P. C.; Thong, J. T. L.; Ng, V. *J. Vac. Sci. Technol. A,* **2002**, *20*, 1295.

[2-10] Yavas, O.; Ochiai, C.; Takai, M.; Hosono, A.; Okuda, S. *Appl. Phys. Lett.*, **2000**, *76*, 3319.

[2-11] Liu, Z. Q.; Mitsuishi, K.; Furuya, K. *J. Appl. Phys.*, **2004**, *96*, 3983.

[2-12] Rack, P. D.; Randolph, S.; Deng, Y.; Fowlkes, J.; Choi, Y.; Joy, D. C. *Appl. Phys. Lett.*, **2003**, *82*, 2326.

[2-13] Tanaka, M.; Shimojo, M.; Mitsuishi, K.; Furuya, K. *Appl. Phys. A: Mater. Sci. Process,* **2004**, *78*, 543.

[2-14] Mitsuishi, K.; Shimojo, M.; Han, M.; Furuya, K. *Appl. Phys. Lett.*, **2003**, *83*,

2064.

[2-15] Willmott, P. R.; Huber, J. R. *Reviews of Mod. Phys.*, **2000**, *72*, 315.

[2-16] Himpsel, F. J. *MRS Bulletin*, **1999**, *24*, 20.

[2-17] Duan, X. F. *Nature*, **2001**, *409*, 66.

[2-18] Eason, R.; *Pulsed Laser Deposition of Thin Films: Applications-led Growth of Functional Materials*. **2007**: Wiley-Interscience.

[2-19] Hulteen, J. C.; Martin, C. R. *J. Mater. Chem.*, **1997**, *7*, 1075.

[2-20] Trentler, T. J. *Science*, **1995**, *270*, 1791.

[2-21] Smith, D. L. *Thin-Film Deposition*, **1995**, New York: McGraw-Hill, Inc.

[2-22] Yang, P. D.; Lieber, C. M. *Science*, **1996**, *273*, 1836.

[2-23] Dietz, T. G. *J. Chem. Phys.*, **1981**, *74*, 6511.

[2-24] George, J.; Pradeep, B. *Solid Stat. Commun.*, **1985**, *56*, 117.

[2-25] Seifert, W. *J. Crys. Growth*, **2004**, *272*, 211.

[2-26] Beuret, C.; Akiyama, T.; Staufer, U.; de Rooij, N. F.; Niedermann, P.; Hanni, W. *Appl. Phys. Lett.*, **2000**, *72*, 1621.

[2-27] Givargizov, E. I.; Zhirnov, V. V.; Kuznetsov, A. V.; Plekhanov, P. S. *Mater. Lett.*, **1993**, *18*, 61.

[2-28] Zhirnov, V. V.; Givargizov, E. I.; Plekhanov, P. S. *J. Vac. Sci. Technol.*, **1995**, *B13*, 418.

[2-29] Chen, Y.; Guo, L.; Shaw, D. T. *J. Cryst. Growth,* **2000**, *210*, 527.

[2-30] Bai, X. D.; Zhi, C. Y.; Liu, S.; Wang, E. G.; Wang, Z. L. *Solid Stat. Commun.*, **2003**, *125*, 185.

[2-31] Remskar, M.; Mrzel, A.; Skraba, Z.; Jesih, A.; Che, M.; Demˇsar, J.; Stadelmann, P.; L´evy, F.; Mihailovic, D. *Science,* **2001**, *292*, 479.

[2-32] Nath, M.; Rao, C. N. R. *Chem. Comm.*, **2001**, *21*, 2236.

[2-33] Li, Y.; Bando, Y.; Goldberg, D. *Adv. Mater.*, **2003**, *15*, 581.

[2-34] Li, Y.; Bando, Y.; Goldberg, D. *Adv. Mater.*, **2004**, *16*, 37.

[2-35] Wu, Q.; Hu, Z.; Wang, X.; Lu, Y.; Chen, X.; Xu, H.; Chen, Y. *J. Am. Chem. Soc.*, **2003**, *125*, 10176.

[2-36] Wu, J. J.; Liu, S. C. *Adv. Mater.*, **2002**, *14*, 215.

[2-37] Zhang, Y.; Zhu, J.; Zhang, Q.; Yan, Y.; Wang, N.; Zhang, X. *Chem. Phys. Lett.*, **2000**, *317*, 504.

[2-38] Han, W.; Fan, S.; Li, Q.; Hu, Y. *Science,* **1997**, *277*, 1287.

[2-39] Chattopadhyay, S.; Shi, S. C.; Lan, Z. H.; Chen, C. F.; Chen, L. C.; Chen, K. H. *J. Am. Chem. Soc.*, **2005**, *127*, 2820.

[2-40] Shi, S. C.; Chattopadhyay, S.; Lan, Z. H.; Chen, C. F.; Chen, K. H.; Chen, L. C. *Chem. Phys. Lett.,* **2006**, *418*, 152.

[2-41] Bai, Z. G.; Yu, D. P.; Zhang, H. Z.; Ding, Y.; Wang, Y. P.; Gai, X. Z.; Hang, Q. L.; Xiong, G. C.; Feng, S. Q. *Chem. Phys. Lett.*, **1999**, *303*, 311.

[2-42] Chen, Y.; Cui, X.; Zhang, K.; Pan, D.; Zhang, S.; Wang, B.; Hou, J. G. *Chem. Phys. Lett.*, **2003**, *369*, 16.

[2-43] Lao, J.; Huang, J.; Wang, D.; Ren, Z. *Adv. Mater.*, **2004**, *16*, 65.

[2-44] Chang, K. W.; Wu, J. J. *Adv. Mater.*, **2004**, *16*, 545.

[2-45] Liang, C. H.; Chen, L. C.; Hwang, J. S.; Chen, K. H.; Hung, Y. T.; Chen, Y. F. *Appl. Phys. Lett.*, **2002**, *81*, 22.

[2-46] Lan, Z. H.; Wang, W. M.; Sun, C. L.; Shi, S. C.; Hsu, C. W.; Chen, T. T.; Chen, K. H.; Chen, C. C.; Chen, Y. F.; Chen, L. C. *J. Cryst. Growth,* **2004**, *269*, 87.

[2-47] Dhara, S.; Datta, A.; Wu, C. T.; Lan, Z. H.; Chen, K. H.; Wang, Y. L.; Hsu, C. W.; Shen, C. H.; Chen, L. C.; Chen, C. C. *Appl. Phys. Lett.*, **2004**, *84*, 5473.

[2-48] Ronning, C.; Gao, P. X.; Ding, Y.; Wang, Z. L.; Schwen, D. *Appl. Phys. Lett.*, **2004**, *84*, 783.

[2-49] Ding, Y.; Wang, Z. L. *J. Phys. Chem. B,* **2004**, *108*, 12280.

[2-50] Geng, B.; Zhang, L.; Meng, G.; Xie, T.; Peng, X.; Lin, Y. *J. Cryst. Growth,* **2003**, *259*, 291.

[2-51] Dai, R.; Pan, Z. W.; Wang, Z. L. *Solid Stat. Commun*., **2001**, *118*, 351.

[2-52] Ma, C.; Moore, D.; Ding, Y.; Li, J.; Wang, Z. L. *Int. J. Nanotech*., **2004**, *1*, 431.

[2-53] Kong, X. Y.; Wang, Z. L. *Appl. Phys. Lett*., **2004**, *84*, 975.

[2-54] Jost, O.; Gorbunov, A.A.; Moller, J.; Pompe, W. *J. Phys. Chem.* B, **2002**. *11*, 2875.

[2-55] Manasevi, Hm. *Appl. Phys. Lett.,* **1968**, *12,* 156.

[2-56] Shaw, D. W. *J. Phys. Chem. Solids*, **1975**, *36*, 111.

[2-57] Reep, D. H.; Ghandhi, S. K. *J. Electrochem. Soc.*, **1983**, *130*, 675.

[2-58] Duchemin, J. P. *J Electrochem. Soc.*, **1979**, *126*, 1134.

[2-59] Coleman, J. J. *Proceedings of the IEEE*, **1997**, *85*, 1715.

[2-60] Kondo, M. *J. Cryst. Growth*, **1994**, *141*, 1.

[2-61] Parry, C. P. *Appl. Phys. Lett.*, **1991**, *58*, 481.

[2-62] Cho, A. Y. *J. Vac. Sci. Technol.*, **1971**, *8*, S31.

[2-63] Cho, A. Y.; Ballamy, W. C. *J. Appl. Phys.*, **1975**, *46*, 783.

[2-64] Qin, L. C.; Zhou, D.; Krauss, A. R.; Gruen, D. M. *Appl. Phys. Lett.*, **1998**, *72*, 3437.

[2-65] Bower, C.; Zhu, W.; Jin, S. H.; Zhou, O. *Appl. Phys. Lett.*, **2000**, *77*, 830.

[2-66] Delzeit, L.; McAninch, I.; Cruden, B. A.; Hash, D. *J. Appl. Phys.*, **2002**, *91*, 6027.

[2-67] Han, J. H.; Choi, S. H.; Lee, T. Y.; Yoo, J. B. *Thin Solid Films*, **2002**, *409*, 126.

[2-68] Merkulov, V. I.; Melechko, A. V.; Guillorn, M. A.; Lowndes, D. H.; Simpson, M. L. *Appl. Phys. Lett.*, **2001**, *79*, 2970.

[2-69] Hsu, C. H.; Lo, H. C.; Chen, C. F.; Wu, C. T.; Hwang, J. S.; Das, D.; Tsai, J.;

Chen, L. C.; Chen, K. H. *Nano Letters,* **2004**, *4*, 471.

[2-70] Hsu, C. H.; Huang, Y. F.; Chen, L. C.; Chattopadhyay, S.; Chen, K. H.; Lo, H. C.; Chen, C. F. *J. Vac. Sci. Technol. B,* **2006**, *24*, 308.

Chapter 4

[4-1] Ravi, T. S.; Marcus, R. B.; Liu, D. *J. Vac. Sci. Technol. B* **1991**, *9*, 2733.

[4-2] Williams, C. C.; Davis, R. C.; Neuzil, P. *U.S. patent* 5,969,345, **1999**.

[4-3] Jung, M. Y.; Kim, D. W.; Choi, S. S. *Microelectron. Eng.* **2000**, *53*, 399.

[4-4] Nishijima, H.; Kamo, S.; Akita, S.; Nakayama, Y. *Appl. Phys. Lett.* **1999**, *74*, 4061.

[4-5] Cho, K.; Joannopoulos, J. D. *Phys. Rev. Lett.* **1993**, *71*, 1387.

[4-6] Eong, S. S.; Woolley, A. T.; Joselevich, E.; Lieber, C. M. *Chem. Phys. Lett.* **1999**, *306*, 219.

[4-7] Asano, T.; Obiuchi, Y.; Katsumata, S. *J. Vac. Sci. Technol. B* **1995**, *13*, 431.

[4-8] Dai, H.; Hafner, J. H.; Rinzler, A. G.; Colbert, D. T.; Smalley, R. E. *Nature* **1996**, *384*, 147.

[4-9] Oon, C. H.; Thong, J. T. L.; Lei, Y.; Chim, W. K. *Appl. Phys. Lett.* **2002**, *81*, 3037.

[4-10] Deheer, W. A.; Chatelain, A.; Ugarte, D. *Science* **1995**, *270*, 1179.

[4-11] Tarntair, F. G.; Chen, L. C.; Wei, S. L.; Hong, W. K.; Chen, K. H.; Cheng, H. C. *J. Vac. Sci. Technol. B* **2000**, *18*, 1207.

[4-12] Kichambare, P. D.; Tarntair, F. G.; Chen, L. C.; Chen, K. H.; Cheng, H. C. *J. Vac. Sci. Technol. B* **2000**, *18*, 2722.

[4-13] Tarntair, F. G.; Wen, C. Y.; Chen, L. C.; Wu, J. J.; Chen, K. H.; Kuo, P. F.; Chang, S. W.; Chen, Y. F.; Hong, W. K.; Cheng, H. C. *Appl. Phys. Lett.* **2000**, *76*, 2630.

[4-14] Chen, C. C.; Yeh, C. C.; Ho, C. H.; Yu, M. Y.; Liu, H. L.; Wu, J. J.; Chen, K. H.; Chen, L. C.; Peng, J. Y.; Chen, Y. F. *J. Am. Chem. Soc.* **2001**, *123*, 2791.

[4-15] Groning, O.; Kuttel, O. M.; Emmenegger, C.; Groning, P.; Schlapbach, L. *J.*

Vac. Sci. Technol. B **2000**, *18*, 665.

[4-16] Chen, K. J.; Hong, W. K.; Lin, C. P.; Chen, K. H.; Chen, L. C.; Cheng, H. C. *Jpn. J. Appl. Phys.* **2002**, *41*, 6132.

[4-17] Bonard, J. M.; Weiss, N.; Kind, H.; Stockli, T.; Forro, L.; Kern, K.; Chatelain, A. *Adv. Mater.* **2001**, *13*, 184.

[4-18] Striemer, C. C.; Fauchet, P. M. *Appl. Phys. Lett.* **2002**, *81*, 2980.

[4-19] Ponce, F. A.; Bour, D. P. *Nature* **1997**, *386*, 351.

[4-20] Nakamura, S. *Science* **1998**, *281*, 956.

[4-21] Lin, V. S. Y.; Motesharei, K.; Dancil, K. P. S.; Sailor, M. J.; Ghadiri, M. R. *Science* **1997**, *278*, 840.

[4-22] Kovalev, D.; Timoshenko, V. Y.; Kunzner, N.; Gross, E.; Koch, F. *Phys. Rev. Lett.* **2001**, *87*, 68301.

[4-23] Hickman, J. J.; Ofer, D.; Laibinis, P. E.; Whitesides, G. M.; Wrighton, M. S. *Science* **1991**, *252*, 688.

[4-24] Tennant, D. M. *In Nanotechnology*; Timp, G., Ed.; Springer-Verlag: New York, 1999; ch 4.

[4-25] Yoshida, H.; Urushido, T.; Miyake, H.; Hiramatsu, K. *Jpn. J. Appl. Phys.* **2001**, *40*, 1301.

[4-26] Lewis, P. A.; Ahmedb, H.; Sato, T. *J. Vac. Sci. Technol. B* **1998**, *16*, 2938.

[4-27] Shang, N. G.; Meng, F. Y.; Au, F. C. K.; Li, Q.; Lee, C. S.; Bello, I.; Lee, S. T. *Adv. Mater*. **2002**, *14*, 1308.

[4-28] Thibault, N. W. *Am. Mineral.* **1944**, *29*, 249.

[4-29] Adamsky, R. F.; Merz, K. M. *Kristallogr.* **1959**, *111*, 350.

[4-30] Lee, W. H.; Lin, J. C.; Lee, C.; Cheng, H. C.; Yew, T. R. *Diamond Relat. Mater.* **2001**, *10*, 2075.

[4-31] Corso, M.; Auwarter, W.; Muntwiler, M.; Tamai, A.; Greber, T.; Osterwalder,

J. *Science* **2004**, *303*, 217.

[4-32] Olshavsky, M. A.; Goldstein, A. N., Alivisatos, A. P. *J. Am. Chem. Soc.* **1990**, *112*, 9438.

[4-33] Allan, G.; Niqute, Y. M., Delerue, C. *Appl. Phys. Lett.* **2000**, *77*, 639.

[4-34] Anedda, A.; Serpi, A.; Karavanskii, V. A.; Tiginyanu, I. M.; Ichizli, V. M. *Appl. Phys. Lett.* **1995**, *67*, 3316.

[4-35] Li, X.; Kim, Y. W.; Bohn, P. W.; Adesida, I. *Appl. Phys. Lett.* **2002**, *80*, 980.

[4-36] Lo, H. C.; Das, D.; Hwang, J. S.; Chen, K. H.; Hsu, C. H.; Chen, C. F.; Chen, L. C. *Appl. Phys. Lett.* **2003**, *83*, 1420.

Chapter 5

[5-1] Yang, P. D.; Wu, Y. Y.; Fan, R. *Int. J. Nanosci.*, **2002**, *1*, 1.

[5-2] Fang, X. S.; Ye, C. H.; Zhang, L. D.; Zhang, J. X.; Zhao, J. W.; Yan, P. *Small*, **2005**, *1*, 422.

[5-3] Lu, J. G.; Chang, P.; Fan, Z. Y. *Mater. Sci. Eng. R*, **2006**, *52*, 49.

[5-4] Imahori, H.; *J. Mater. Chem.*, **2007**, *17*, 31.

[5-5] Fang, X. S.; Ye, C. H.; Xu, X. X.; Xie, T.; Wu, Y. C.; Zhang, L. D. *J. Phys.: Condens. Matter*, **2004**, *16*, 4157.

[5-6] Zhang, Z. D. *J. Mater. Sci. Technol.*, **2007**, *23*, 1.

[5-7] Sun, S. H. *Adv. Mater.*, **2006**, *18*, 393.

[5-8] Li, L.; Li, G. H.; Fang, X. S. *J. Mater. Sci. Technol.*, **2007**, *23*, 166.

[5-9] Sun, Y. G.; Choi, W. M.; Jiang, H.; Huang, Y. Y.; Roger, J. A. *Nat. Nanotechnol.*, **2006**, *1*, 201.

[5-10] Lai, G. H.; Li, Z. L.; Cheng, L.; Peng, J. B. *J. Mater. Sci. Technol.*, **2006**, *22*, 677.

[5-11] Chiu, J. J.; Kei, C. C.; Perng, T. P.; Wang, W. S. *Adv. Mater.*, **2003**, *15*, 1361.

[5-12] Li, C.; Lei, W.; Zhang, X. B.; Wang, J. X.; Sun, X. W.; Tan, S. T. *J. Vac. Sci. Technol, B*, **2007**, *25*, 590.

[5-13] Wei, L.; Zhang, X. B.; Zhu, Z. Y. *J. Vac. Sci. Technol. B*, **2007**, *25*, 608.

[5-14] Xu, N. S.; Huq, S. E. *Mater. Sci. Eng. R*, **2005**, *48*, 47.

[5-15] Yomaoka, Y. ; Goto, T.; Nakao, M.; Kanemaru, S.; Itoh, *J. Jpn. J. Appl. Phys., Part 1*, **1995**, *34*, 6932.

[5-16] Urayama, M.; Ise, T.; Maruo, Y.; Kishi, A.; Imamoto, R.; Takase, T. *Jpn. J. Appl. Phys., Part 1*, **1993**, *32*, 6293.

[5-17] Thibault, N. W. *Am. Mineral.* **1944**, *29*, 249.

[5-18] Tachibana, A.; Kawarchi, S.; Yano, T.; Yoshida, N.; Yamabe, T. *J. Mol. Struct.*, **1994**, *313*, 121.

[5-19] Sasake, K.; Tomoda, H.; Takada, T. *Vacuum*, **1998**, *51*, 537.

[5-20] Liu, J.; Son, U. T.; Stepanova, A. N.; Christensen, K. N.; Wojak, G. J.; Givargizov, E. I.; Bachmann, K. J.; Hren, J. J. *J. Vac. Sci. Technol. B*, **1994**, *12*, 717.

[5-21] Yi, W.; Jeong, T.; Yu, S.; Heo, J.; Lee, C.; Lee, J.; Kim, W.; Yoo, J. B.; Kim, J. *Adv. Mater.*, **2002,** *14*, 1464.

[5-22] Lee, J. H.; Chung, Y. W.; Hon, M. H.; Leu, I. C. *Appl. Phys. A: Mater. Sci.* Process., 2009, 97, 403.

[5-23] Hsu, C. H.; Lo, H. C.; Chen, C. F.; Wu, C. T.; Hwang, J. S.; Das, D.; Tsai, J.; Chen, L. C. ; Chen, K. H. *Nano Lett.*, **2004**, *4*, 471.

[5-24] Matsumoto, K.; Kinosita, S.; Gotoh, Y.; Uchiyama, T.; Manalis, S.; Quate, C. *Appl. Phys. Lett.* **2001**, *78*, 539.

[5-25] Zhu, W.; Kochanski, G. P.; Jin, S.; Seibles, L.; Jacobson, D. C.; McCormack, M.; White, A. E. *Appl. Phys. Lett.*, **1995**, *67*, 1157.

[5-26] Liu, X. W.; Tsai, S. H.; Lee, L. H.; Yang, M. X.; Yang, A. C. M.; Lin, I. N.; Shih, H. C. *J. Vac. Sci. Technol. B*, **2000**, *18*, 1840.

Chapter 6

[6-1] Chen, C. C.; Liu, Y. C.; Wu, C. H.; Yeh, C. C.; Su, M. T.; Wu, Y. C. *Adv. Mater.* **2005**, *17*, 404.

[6-2] Kim, W.; Ng, J. K.; Kunitake, M. E.; Conklin, B. R.; Yang, P. D. *J. Am. Chem. Soc.* **2007**, *129*, 7228.

[6-3] Lietz, M.; Dreesmann, L.; Hoss, M.; Oberhoffner, S.; Schlosshauer, B. *Biomaterials* **2006**, *27*, 1425.

[6-4] Patolsky, F.; Timko, B. P.; Yu, G.; Fang, Y.; Greytak, A. B.; Zheng, G.; Lieber, C. M. *Science* **2006**, *313*, 1100.

[6-5] Chattopadhyay, S.; Lo, H. C.; Hsu, C. H.; Chen, L. C.; Chen, K. H. *Chem. Mater.* **2005**, *17*, 553.

[6-6] Chen, C. P.; Ganguly, A.; Wang, C. H.; Hsu, C. H.; Chattopadhyay, S.; Hsu, Y. K.; Chang, Y. C.; Chen, K. H.; Chen, L. C. *Anal. Chem.* **2002**, *81*, 36.

[6-7] Fan, Y. W.; Cui, F. Z.; Hou, S. P.; Xu, Q. Y.; Chen, L. N.; Lee, I. S. *J. Neurosci. Methods* **2002**, *120*, 17.

[6-8] Chin, V.; Collins, B. E.; Sailor, M. J.; Bhatia, S. N. *Adv. Mater.* **2001**, *13*, 1877.

[6-9] Nguyen-Vu, T. D. B.; Chen, H.; Cassell, A. M.; Andrews, R.; Meyyappan, M.; Li, J. *Small* **2006**, *1*, 89.

[6-10] McKenzie, J. L.; Waid, M. C.; Shi, R.; Webster, T. J. *Biomaterials* **2004**, *25*, 1309.

[6-11] Mattson, M. P.; Haddon, R. C.; Rao, A. M. *J. Mol. Neurosci.* **2000**, *14*, 175.

[6-12] Zuruzi, A. S.; Butler, B. C.; MacDonald, N. C.; Safinya, C. R. *Nanotechnology* **2006**, *17*, 531.

[6-13] Webster, T. J.; Waid, M. C.; MaKenzie, J. L.; Price, R. L.; Ejiofor, J. U. *Nanotechnology* **2004**, *15*, 48.

[6-14] Kim, K. H.; Cho, J. S.; Choi, D. J.; Koh, S. K. *Nucl. Instr. and Meth. in Phys. Res. B* **2001**, *175-177*, 542.

[6-15] Haq, F.; Keith, C.; Zhng, G. *Biotechnol. Prog.* **2006**, *22*, 133.

[6-16] Lee, S. J., Khang. G., Lee, Y. M., Lee, H. B. *J. colloid interface sci.* **2003**, *259*, 228.

[6-17] Khorasani, M. T.; MoemenBellah, S.; Mirzadeh, H.; Sadatnia, B. *Colloids and Surfaces B: Biointerfaces* **2006**, *51*, 112.

[6-18] Engblom, A. C.; Johansen, F. F.; Kristiansen, U. *J. Biol. Chem.* **2003**, *278*, 16543.

[6-19] Liu, S.; Zhong, J. J. *J. Biotechnol.* **1996**, *52*, 121.

[6-20] Laquerriere, P.; Jallot, E.; Kilian, L.; Benhayoune, H.; Balossier, G. *J. Biomed. Materi. Res.* **2003**, *65*, 441.

[6-21] Hsu, C. H.; Lo, H. C.; Chen, C. F.; Wu, C. T.; Hwang, J. S.; Das, D.; Tsai, F.; Chen, L. C.; Chen, K. H. *Nano Lett.* **2004**, *4*, 471.

[6-22] Lo, H. C.; Huang, Y. F.; Chattopadhyay, S.; Hsu, C. H.; Chen, C. F.; Chen, K. H.; Chen, L. C. *Nanotechnology* **2006**, *17*, 2542.

[6-23] Lo, H. C.; Das, D.; Hwang, J. S.; Chen, K. H.; Hsu, C. H.; Chen, C. F.; Chen, L. C. *Appl. Phys. Lett.* **2003**, *83*, 1420.

[6-24] Greene, L. A.; Tischler, A. S. *Proc. Natl. Acad. Sci. U.S.A.* **1976**, *73*, 2424.

[6-25] Smoluchowski, M. *Handbuch der elektrizität und des magnetismus* **1921**.

[6-26] Wenzel, R. N. *L. Phys. Chem.* **1949**, *53*, 1466.

[6-27] Gallo, V.; Kingsbury; Balázs, R.; Jørgensen, O. S. *J. Neurosci.* **1987**, *7*, 2203.

[6-28] Bading, H.; Greenberg, M. E. *Science* **1991**, *253*, 912.

[6-29] Marshall, C. J. *Curr. Opin. Genet. Dev.* **1994**, *4*, 82.

[6-30] Ali, M. B.; Bessueille, F.; Chovelon, J. M.; Abdelghani, A.; Jaffrezic-Renault, N.; Marref, M. A.; Martelet, C. *Mater. Sci. Eng. C* **2008**, *28*, 628.

[6-31] Roco, M. C. *Curr. Opin. Biotechnol.* **2003**, *14*, 337.

[6-32] Dubertret, B.; Skourides, P.; Norris, D. J.; Noireaux, V.; Brivanlou, A. H.; Libchaber, A. *Science* **2002**, *298*, 1759.

[6-33] Ishijima, A.; Yanagida, T. *Trends Biotechnol. Sci.* **2001**, *26*, 438.

[6-34] Curtis, A.; Wilkinson, C. *Trends Biotechnol. Sci.* **2001**, *19*, 97.

[6-35] Bogunia-Kubik, K.; Sugisaka, M. *Biosystems* **2002**, *65*, 123.

[6-36] Seeman, N. C.; Belcher, A. M. *Proc. Natl. Acad. Sci. U.S.A.* **2002**, *99*, 6451.

[6-37] Whitesides, G. M.; Boncheva, M. *Proc. Natl. Acad. Sci. U.S.A.* **2002**, *99*, 4769.

[6-38] Silva, G. A. *Nat. Rev. Neurosci.* **2006**, *7*, 65.

[6-39] Schalwig, J.; Muller, G.; Eickhoff, M.; Ambacher, O.; Stutzmann, M. *Sensors Actuators B* **2002**, *87*, 425.

[6-40] Ambacher, O.; Smart, J.; Shealy, J. R.; Weimann, N. G.; Chu, K.; Murphy, M. *J. Appl. Phys.* **1999**, *85*, 3222.

[6-41] Dimitrow, R.; Murphy, M.; Smart, J.; Schaff, W.; Shealy, J. R.; Eastman, L. F. *J. Appl. Phys.* **2000**, *87*, 3375.

[6-42] Yan, J.; Kappers, M. J.; Barber, Z. H.; Humphreys, C. J. *Appl. Surf. Sci.* **2004**, *234*, 328.

[6-43] Rao, A. M; Richter, E.; Bandow, S.; Chase, B.; Eklund, P. C.; Williams, K. A. *Science* **1997**, *275*, 187.

[6-44] Wong, E. W.; Sheehan, P. E.; Lieber, C. M. *Science* **1997**, *277*, 1971.

[6-45] Tans, S. J.; Vershueren, A. R. M.; Dekker, C. *Nature* **1998**, *393*, 49.

[6-46] Chen, J.; Hamon, M. A.; Hu, H.; Chen, Y.; Rao, A. M.; Eklund, P. C.; Haddon, R. C. *Science* **1998**, *282*, 95.

[6-47] Wong, S. S.; Joselevich, E.; Woolley, A. T.; Caung, C. L.; Lieber, C. M. *Nature* **1998**, *394*, 52.

[6-48] Nakamura, S.; Fasol, G.; *Heidelberg: Springer*, **1997**.

[6-49] Stringfellow, G. B.; Craford, M. G. *High brightness light emitting diodes: semiconductors and semimetals. San Diego, CA, USA: Academic Press*, **1997**.

[6-50] Yang, T. H.; Chen, C. R. *Biomaterials* **2006**, *27*, 3361

[6-51] Kim, W.; Ng, J. K.; Kunitake, M. E.; Conklin, B. R.; Yang, P. *J. Am. Chem. Soc.* **2007**, *129*, 7228.

[6-52] Chen, C.; Liu, Y.; Wu, C.; Yeh, C.; Su, M.; Wu, Y. *Adv. Mater.* **2005**, *17*, 404.

Chapter 7

[7-1] Nie, S.; Emory, S. R. *Science* **1997**, *275*, 1102.

[7-2] Kneipp, K.; Yang, Y.; Kneipp, H.; Parleman, L. T.; Itzkan, I.; Dasari, R. R.; Feld, M. S. *Phys. Rev. Lett.* **1997**, *78*, 1667.

[7-3] Xu, H.; Bjerneld, E. J.; Kall, M.; Borjesson, L. *Phys. Rev. Lett.* **1999**, *83*, 4357.

[7-4] Fleishmann, M.; Hendra, P. J.; McQuillan, A. J. *Chem. Phys. Lett.* **1974**, *26*, 163.

[7-5] Moskovits, M. *Rev. Mod. Phys.* **1985**, *57*, 783.

[7-6] Betzig, E.; Chichester, R. J. *Science* **1993**, *262*, 1422.

[7-7] Xie, X. S.; Dunn, R. C. *Science* **1994**, *265*, 361.

[7-8] Gessner, R.; Winter, C.; Ro¨sch, P.; Schmitt, M.; Petry, R.; Keifer, W.; Lankers, M.; Popp, *J. Chem. Phys. Chem.* **2004**, *5*, 1159.

[7-9] Higgins, D. A.; Kerimo, J. K.; vanden Bout, D. A.; Barbara, P. F. *J. Am. Chem. Soc.* **1996**, *118*, 4049.

[7-10] Birnbaum, D.; Kook, S. K.; Kopelman, R. J. *J. Phys. Chem.* **1993**, *97*, 3091.

[7-11] Tan, W.; Shi, Z. Y.; Smith, S.; Birnbaum, D.; Kopelman, R. *Science* **1992**, *258*, 778.

[7-12] Petry, R.; Schmitt, M.; Popp, J. *Chem. Phys. Chem.* **2003**, *4*, 14.

[7-13] Ni, F.; Cotton, T. M. *Anal. Chem.* **1986**, *58*, 3159.

[7-14] Van Duyne, R. P.; Hulteen, J. C.; Treichel, D. A. *J. Chem. Phys.* **1993**, *99*, 2101.

[7-15] Schlegel, V. L.; Cotton, T. M. *Anal. Chem.* **1991**, *63*, 241.

[7-16] Miller, S.; Baiker, A.; Meier, M.; Wokaun, A. *J. Chem. Soc., Faraday Trans.* **1984**, *I80*, 1305.

[7-17] Sudnik, L. M.; Norrod, K. L.; Rowlen, K. L. *Appl. Spectrosc.* **1996**, *50*, 422.

[7-18] Gunnarsson, L.; Bjerneld, E. J.; Xu, H.; Petronis, S.; Kasemo, B.; Kall, M. *Appl. Phys. Lett.* **2001**, *78*, 802.

[7-19] Green, M.; Liu, F. M. *J. Phys. Chem. B* **2003**, *107*, 13015.

[7-20] Zenobi, R.; Deckert, V. *Angew. Chem., Int. Ed.* **2000**, *39*, 1746.

[7-21] Hsu, C. H.; Lo, H. C.; Chen, C. F.; Wu, C. T.; Hwang, J. S.; Das, D.; Tsai, J.; Chen, L. C.; Chen, K. H. *Nano Lett.* **2004**, *4*, 471.

[7-22] Nikkobakht, B.; Wang, J.; El-Sayed, M. A. *Chem. Phys. Lett.* **2002**, *366*, 17.

[7-23] Hildebrandt, P.; Stockburger, M. *J. Phys. Chem.* **1984**, *88*, 5935.

[7-24] Tao, A.; Kim, F.; Hess, C.; Goldberger, J.; He, R.; Sun, Y.; Xia, Y.; Yang, P. *Nano Lett.* **2003**, *3*, 1229.

[7-25] Maruyama, Y.; Ishikawa, M.; Futamata, M. *Anal. Sci.* **2001**, *17*, i1181.

[7-26] Michaels, A. M.; Nirmal, M.; Brus, L. E. *J. Am. Chem. Soc.* **1999**, *121*, 9932.

[7-27] Garcia-Vidal, F. J.; Pendry, J. B. *Phys. Rev. Lett.* **1996**, *77*, 1163.

[7-28] Otto, A. In Light Scattering in Solids; Cardona, M., Guntherodt, G., *Eds.; Springer: Berlin,* **1984**; *Vol. IV*, Chapter 7.

[7-29] Maxwell, D. J.; Emory, S. R.; Nie, S. *Chem. Mater.* **2001**, *13*, 1082.

[7-30] Glueckstein, J. C.; Evans, M. M. R.; Nogami, J. *Phys. Rev. B* **1996**, *54*, R11066.

[7-31] Mu¨ller, T.; Nienhaus, H. *J. Appl. Phys.* **2003**, *93*, 924.

[7-32] Norrod, K. L.; Sudnik, L. M.; Rousell, D.; Rowlen, K. L. *Appl. Spectrosc.* **1997**, *51*, 994.

[7-33] Aroca, R.; *Surface Enhanced Vibrational Spectroscopy.* John-Wiley & Sons, Toronto, **2006**.

[7-34] Becker, M.; Sivakov, V.; Gosele, U.; Stelzner, T.; Andra, G.; Reich, H. J.; Hoffmann, S.; Michler, J.; Christiansen, S. H. *Small*, **2008**, 4, 398.

[7-35] Brolo, A. G.; Arctander, E.; Gordon, R.; Leathem, B.; Kavanagh, K. L. *Nano*

Lett., **2004**, *4*, 2015.

[7-36] Camden, J. P.; Dieringer, J. A.; Wang, Y.; Masiello, D. J.; Marks, L. D.; Schatz, G. C.; Van Duyne, R. P. *J. Am. Chem. Soc.*, **2008**, *130*, 12616.

[7-37] Chan, S.; Kwon, S.; Koo, T. W.; Lee, L. P.; Berlin, A. A. *Adv. Mater.*, **2003**, *15*, 1595.

[7-38] Chattopadhyay, S.; Shi, S. C.; Lan, Z. H.; Chen, C. F.; Chen, K. H.; Chen, L. C. *J. Am. Chem. Soc.*, **2005a**, *127*, 2820.

[7-39] Chattopadhyay, S.; Lo, H. C.; Hsu, C. H.; Chen, L. C.; Chen, K. H. *Chem. Mater.*, **2005b**, *17*, 553.

[7-40] Chattopadhyay, S.; Chen, L. C.; Chen, K. H. *Crit. Rev. Solid State Mater. Sci.*, **2006**, *31*, 15.

[7-41] Domke, K. F.; Zhang, D.; Pettinger, B. *J. Am. Chem. Soc.*, **2006**, *128*, 14721.

[7-42] Domke, K. F.; Zhang, D.; Pettinger, B. *J. Am. Chem. Soc.*, **2007**, *129*, 6708.

[7-43] Faulds, K.; Smith, W. E.; Graham, D. *Anal. Chem.*, **2004**, *76*, 412.

[7-44] Faulds, K.; Stewart, L.; Smith, W. E.; Graham, D. *Talanta*, **2005**, *67*, 667.

[7-45] Fleischmann, M.; Hendra, P. J.; McQuillan, A. J. *Chem. Phys. Lett.*, **1974**, *26*, 163.

[7-46] Fodor, S. P. A.; Rava, R. P.; Hays, T. R.; Spiro, T. G. *J. Am. Chem. Soc.*, **1985**, *107*, 1520.

[7-47] Garcia-Vidal, F. J.; Pendry, J. B. *Phys. Rev. Lett.*, **1996**, *77*, 1163.

[7-48] Hsu, C. H.; Lo, H. C.; Chen, C. F.; Wu, C. T.; Hwang, J. S.; Das, D.; Tsai, J.; Chen, L. C.; Chen, K. H. *Nano Lett.*, **2004**. *4*, 471.

[7-49] Ichimura, T.; Watanabe, H.; Morita, Y.; Verma, P.; Kawata, S.; Inouye, Y. *J. Phys. Chem. C*, **2007**, *111*, 9460.

[7-50] Kang, S. K.; Bernstein, I. M. *Philos. Mag.,* **1976,** *33*, 709.

[7-51] Kneipp, K.; Wang, Y.; Kneipp, H.; Perelman, L. T.; Itzkan, I.; Dasari, R. R.;

Feld, M. S. *Phys. Rev. Lett.*, **1997**, *78*, 1667.

[7-52] Krug, J. T.; Wang, G. D.; Emory, S. R.; Nie, S. *J. Am. Chem. Soc.*, **1999**, *121*, 9208.

[7-53] Le Ru, E. C.; Blackie, E.; Meyer, M.; Etchegoin, P. G. *J. Phys. Chem. C*, **2007**, *111*, 13794.

[7-54] Lo, H. C.; Das, D.; Hwang, J. S.; Chen, K. H.; Hsu, C. H.; Chen, C. F.; Chen, L. C. *Appl. Phys. Lett.*, **2003**, *83*, 1420.

[7-55] Lo, H. C.; Huang, Y. F.; Chattopadhyay, S.; Hsu, C. H.; Chen, C. F.; Chen, K. H.; Chen, L. C. *Nanotechnology,* **2006**, *17*, 2542.

[7-56] Meyer, S. A.; Le Ru, E. C.; Etchegoin, P. G. *J. Phys. Chem. A*, **2010**, *114*, 5515.

[7-57] Michaels, A. M.; Nirmal, M.; Brus, L. E. *J. Am. Chem. Soc.*, **1999**, *121*, 9932.

[7-58] Moskovits, M. *Rev. Mod. Phys.*, **1985**, *57*, 783.

[7-59] Nie, S.; Emory, S. R. *Science*, **1997**, *275*, 1102.

[7-60] Rasmussen, A.; Deckert, V. *J. Raman Spectrosc.*, **2006**, *37*, 311.

[7-61] Shim, S.; Stuart, C. M.; Mathies, R. A. *Chem. Phys. Chem.*, **2008**, *9*, 697.

[7-62] Stokes, R. J.; Macaskill, A.; Lundahl, P. J.; Smith, W. E.; Faulds, K.; Graham, D. *Small*, **2007**, *3*, 1593.

[7-63] Sun, L.; Yu, C.; Irudayaraj *J. Anal. Chem.*, **2007**, *79*, 3981.

[7-64] Tripp, R. A.; Dluhy, R. A.; Zhao, Y. *Nano Today*, **2008**, *3*, 31.

[7-65] Vo-Dinh, T.; Wang, H. N.; Scaffidi, J. *J. Biophoton.*, **2010**, *3*, 89.

[7-66] Wei, H.; Xu, H. *Appl. Phys. A*, **2007**, *89*, 273.

[7-67] Wenzel, R. N. *J. Phys. Chem.*, **1949**, *53*, 1466.

[7-68] Yeo, B. S.; Stadler, J.; Schmid, T.; Zenobi, R.; Zhang, W. *Chem. Phys. Lett.*, **2009**, *472*, 1.

[7-69] Zhang, X.; Young, M. A.; Lyandres, O.; Duyne, R. P. V. *J. Am. Chem. Soc.*,

2005, *127*, 4484.

Chapter 8

[8-1] Wolfe, J.; Bryant, G.; Koster, K. L. *Cryo Lett.*, **2002**, *23*, 157.

[8-2] Neinhuis, C.; Barthlott, W. *Ann. Bot.*, **1997**, *79*, 667.

[8-3] Madou, M.; Florkey, J. *Chem. Rev.*, **2000**, *100*, 2679.

[8-4] Patankar, N. A. *Langmuir*, **2003**, *19*, 1249.

[8-5] Wenzel, R. N. *J. Phys. Colloid Chem.*, **1949**, *53*, 1466.

[8-6] Cassie, A. B. D.; Baxter, S. *Trans. Faraday Soc.*, **1944**, *40*, 546.

[8-7] Gu, Z. Z.; Uetsuka, H.; Takahashi, K.; Nakajima, R.; Onishi, H.; Fujishima, A.; Sato, O. *Angew. Chem. Int. Ed,* **2003**, *42*, 894.

[8-8] Shiu, J. Y.; Kuo, C. W.; Chen, P.; Mou, C. Y. *Chem. Mater.*, **2004**, *16*, 561.

[8-9] Erbil, H. Y.; Demirel, A. L.; Avci, Y.; Mert, O. *Science*, **2003**, *299*, 1377.

[8-10] Woodward, I.; Schofield, W. C. E.; Roucoules, V.; Badyal, J. P. S. *Langmuir*, **2003**, *19*, 3432.

[8-11] Kim, M. C.; Song, D. K.; Shin, H. S.; Baeg, S. H.; Kim, G. S.; Boo, J. H.; Han, J. G.; Yang, S. H. *Surf. Coat. Technol.*, **2003**, *171*, 312.

[8-12] Kim, K. H.; Cho, J. S.; Han, S.; Beag, Y. W.; Kang, B. H.; Ha, S.; Koh, S. K. *Proc. 2003 ECI Conf. on Heat Exchanger Fouling and Cleaning: Fundamentals and Applications (Santa Fe, NM, USA) ed P Watkinson*, **2004**, H Muller-Steinhagen and M Reza Malayeri, p 107

[8-13] Wang, R.; Hashimoto, K.; Fujishima, A.; Chikuni, M.; Kojima, E.; Kitamura, A.; Shimohigoshi, M.; Watanabe, T. *Nature*, **1997**, *388*, 431.

[8-14] Premkumar, J. R.; Khoo, S. B. *Chem. Commun.* **2005**, *5*, 640.

[8-15] Lahann, J.; Mitragotri, S.; Tran, T. N.; Kaido, H.; Sundaram, J.; Choi, I. S.; Hoffer, S.; Somorjai, G. A.; Langer, R. *Science*, **2003**, *299*, 371.

[8-16] Zhao, B.; Moore, J. S.; Beebe, D. J. *Science*, **2001**, *291*, 1023.

[8-17] Gleiche, M.; Chi, L. F.; Fuchs, H. *Nature*, **2000**, *403*, 173.

[8-18] Wojtyk, J. T. C.; Tomietto, M.; Boukherroub, R.; Wayner, D. D. M. *J. Am. Chem. Soc.*, **2001**, *123*, 1535.

[8-19] Hsu, C. H.; Lo, H. C.; Chen, C. F.; Wu, C. T.; Hwang, J. S.; Das, D.; Tsai, J.; Chen, L. C.; Chen, K. H. *Nano Lett.*, **2004**, *4*, 471.

[8-20] Lo, H. C.; Das, D.; Hwang, J. S.; Chen, K. H.; Hsu, C. H.; Chen, C. F.; Chen, L. C. *Appl. Phys. Lett.*, **2003**, *83*, 1420.

[8-21] Wu, J. J.; Lu, T. R.; Wu, C. T.; Wang, T. Y.; Chen, L. C.; Chen, K. H.; Kuo, C. T.; Chen, T. M. *Diamond Relat. Mater.*, **1999**, *8*, 605.

[8-22] Hsu, W. L. *J. Appl. Phys.*, **1992**, *72*, 310.

[8-23] Lee, W. H.; Lin, J. C.; Lee, C.; Cheng, H. C.; Yew, T. R. *Diamond Relat. Mater.*, **2001**, *10*, 2075.

[8-24] Solomon, I. M.; Schmidt, P.; Tran-Quoa, H. *Phys. Rev. B*, **1988**, *38*, 9895.

[8-25] Rabinowitz, M. J.; Sutherland, J. W.; Patterson, P. M.; Klemm, R. B. *J. Phys. Chem.*, **1991**, *95*, 674.

[8-26] Bico, J.; Tordeux, C.; Qu´er´e, D. *Rough wetting Europhys. Lett.*, **2001**, *55*, 214.

[8-27] Shibuichi, S.; Onda, T.; Satoh, N.; Tsuji, K. *J. Phys. Chem.*, **1996**, *100*, 19512.

[8-28] Sun, T.; Wang, G.; Liu, H.; Feng, L.; Jiang, L.; Zhu, D. *J. Am. Chem. Soc.*, **2003**, *125*, 14996.

[8-29] Lenz, P.; Lipowsky, R. *Phys. Rev. Lett.*, **1998**, *80*, 1920.

[8-30] Gao, Y.; Masuda, Y.; Koumoto, K. *Langmuir*, **2004**, *20*, 3188.

Publication lists

A. Journal Paper

1. Hung-Chun Lo; Hsin-I Hsiung; Surojit Chattopadhyay; Hsieh-Cheng Han; Chia-Fu Chen; Jih Perng Leu; Kuei-Hsien Chen; Li-Chyong Chen *Biosensors and Bioelectronics*, **2011**, *26*, 2413.
2. Hung-Chun Lo; Jeff T. H. Tsai; Jih-Perng Leu; Chia-Fu Chen *J. Vac. Sci. Technol. B*, **2010**, *28*, 1284.
3. Hung-Chun Lo; Yi-Fan Huang; Surojit Chattopadhyay; Chih-Hsun Hsu; Chia-Fu Chen; Kuei-Hsien Chen; Li-Chyong Chen *Nanotechnology*, **2006**, *17*, 2542.
4. Yi-Fan Huang; Surojit Chattopadhyay; Yi-Jun Jen; Cheng-Yu Peng; Tze-An Liu; Yu-Kuei Hsu; Ci-Ling Pan; Hung-Chun Lo; Chih-Hsun Hsu; Yuan-Huei Chang; Chih-Shan Lee; Kuei-Hsien Chen; Li-Chyong Chen *Nature Nanotechnology*, **2007**, *2*, 770.
5. C. H. Hsu; Y. F. Huang; L. C. Chen; S. Chattopadhyay; K. H. Chen; H. C. Lo; C. F. Chen *J. Vac. Sci. Technol. B*, **2006**, *24*, 308.
6. Surojit Chattopadhyay; Hung-Chun Lo; Chih-Hsun Hsu; Li-Chyong Chen; Kuei-Hsien Chen *Chem. Mater.*, **2005**, *17*, 553.
7. Chih-Hsun Hsu; Hung-Chun Lo; Chia-Fu Chen; Chien Ting Wu; Jih-Shang Hwang; Debajyoti Das; Jeff Tsai; Li-Chyong Chen; Kuei-Hsien Chen *Nano Lett.*, **2004**, *4*, 471.

B. Conference Paper

1. Hung-Chun Lo; Chih-Hsun Hsu;, Jih-Shieng Hwang; Li-Chyong Chen; Chia-Fu Chen; Kuei-Hsien Chen "Fabrication of ultra sharp silicon tips as a stable field emitter" *Material Research Society Spring Meeting*, **2003**, April 9-13, San Francisco, California.
2. C. F. Chen; H. C. Lo; D. Das; J. S. Hwang; K. H. Chen; C. H. Hsu; L. C. Chen "SiC-capped Nanotip Arrays for Excellent Field Emission" *Taiwan Nano Tech.* **2003**, September 6-8, Hsin-Chu, Taiwan.
3. Kuei-Hsien Chen; Hung-Chun Lo; Chia-Fu Chen; Chih-Hsun. Hsu; Yi-Fang Hwang, Surojit Chattopadhyay; Li-Chyong Chen "Generally Applicable Nanotip Arrays Fabrication and Their Applications" *NanoMaterials for Defense Applications Symposium*, **2004**, February 19-26, Maui, Hawaii.
4. K. H. Chen; H. C. Lo; C. F. Chen; S. Chattopadhyay, C. H. Hsu; L. C. Chen; Y. F. Huang; C. R. Lin; J. S. Huang "The glory of the unassuming silicon nanotips" *Taiwan Nano Tech.,* **2004**, September 6-8, Taipei, Taiwan.
5. H. C. Lo; C. F. Chen; S. Chattopadhyay; K. H. Chen; L. C. Chen; Y. F. Huang; C. R. Lin "Geometrically and chemically tuned wetting properties of Silicon NanoTips" *Taiwan Nano Tech.,* **2005**, September 21-23, Taipei, Taiwan.
6. H. C. Lo; C. F. Chen; C. J. Huang; Y. C. Chang; L. C. Chen; K. H. Chen "Neuron development in PC12 cells on nano-textured silicon surface" *Physics Annual Meeting,* **2007**, January 23-25, TaoYuan, Taiwan.
7. Hung-Chun Lo; Hsin-I Hsiung; Surojit Chattopadhyay; Chia-Fu Chen; Jim Leu; Kuei-Hsien Chen; Li-Chyong Chen "High-Sensitivity SERS of Sub-Picomole Level of Adenine and Thymine Species at Ag Nanoparticle Modified Gold Nanotip Arrays" *AVS 55th International Symposium and Exibition*, **2008**, October 30-November 4, Boston, Massachusetts.
8. Hung-Chun Lo; Hsin-I Hsiung; Surojit Chattopadhyay; Chia-Fu Chen; Kuei-Hsien Chen; Li-Chyong Chen "Ultrahigh sensitive biomolecule detection via surface enhanced Raman scattering with antireflective silicon nanotip arrays" *Material Research Society Fall Meeting*, **2009**, November 30-December 4, Boston, Massachusetts.